DOE/ER-0045/5

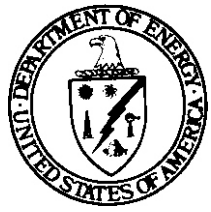

Alloy Development for Irradiation Performance

Quarterly Progress Report
For Period Ending December 31,1980

U.S. Department of Energy
Office of Fusion Energy

Printed in the United States of America. Available from
National Technical Information Service
U.S. Department of Commerce
5285 Port Royal Road, Springfield, Virginia 22161
NTIS price codes — Printed **Copy:** A13 Microfiche A01

DOE/ER-0045/5
Distribution
Category
UC-20, 20c

ALLOY DEVELOPMENT FOR IRRADIATION PERFORMANCE QUARTERLY PROGRESS REPORT FOR PERIOD ENDING DECEMBER 31,1980

ARGONNE NATIONAL LABORATORY

GENERAL ATOMIC COMPANY

HANFORD ENGINEERING DEVELOPMENT LABORATORY

McDONNELL DOUGLAS ASTRONAUTICS COMPANY

MASSACHUSETTS INSTITUTE OF TECHNOLOGY

NAVAL RESEARCH LABORATORY

OAK RIDGE NATIONAL LABORATORY

SANDIA NATIONAL LABORATORIES

WESTINGHOUSE FUSION POWER SYSTEMS

Date Published: April 1981

Prepared by
OAK RIDGE NATIONAL LABORATORY
Oak Ridge, Tennessee 37830
operated by
UNION CARBIDE CORPORATION
for the
DEPARTMENT OF ENERGY
Under Contract No. W-7405-eng-26

Reports previously issued in this series are as follows:

DOE/ET-0058/1	Period Ending March 31, 1978
DOE/ET-0058/2	Period Ending June 30, 1978
DOE/ET-0058/3	Period Ending September 30, 1978
DOE/ET-0058/4	Period Ending December 31, 1978
DOE/ET-0058/5	Period Ending March 31, 1979
DOE/ET-0058/6	Period Ending June 30, 1979
DOE/ET-0058/7	Period Ending September 30, 1979
DOE/ER-0045/1	Period Ending December 31, 1979
DOE/ER-0045/2	Period Ending March 31, 1980
DOE/ER-0045/3	Period Ending June 30, 1980
DOE/ER-0045/4	Period Ending September 30, 1980

FOREWORD

This report is the twelfth in a series of Quarterly Technical Progress Reports on *"Alloy Development for Irradiation Performance"* (ADIP), which is one element of the Fusion Reactor Materials Program, conducted in support of the Magnetic Fusion Energy Program of the U.S. Department of Energy. Other elements of the Materials Program are

- *Damage Analysis and Fundamental Studies (DAFS)*
- *Plasma-Materials Interaction (PMI)*
- *Special-Purpose Materials (SPM)*

The first seven reports in this series are numbered DOE/ET-0058/1 through 7. This report is the fifth in a new numbering sequence that begins with DOE/ER-0045/1.

The ADIP program element is a national effort composed of contributions from a number of National Laboratories and other government laboratories, universities, and industrial laboratories. It was organized by the Materials and Radiation Effects Branch, Office of Fusion Energy, DOE, and a Task Group on *Alloy Development for Irradiation Performance*, which operates under the auspices of that Branch. The purpose of this series of reports is to provide a working technical record of that effort for the use of the program participants, for the fusion energy program in general, and for the Department of Energy.

This report is organized along topical lines in parallel to a Program Plan of the same title so that activities and accomplishments may be followed readily relative to that Program Plan. Thus, the work of a given laboratory may appear throughout the report. Chapters 1, 2, 8, and 9 review activities on analysis and evaluation, test methods development, status of irradiation experiments, and corrosion testing and hydrogen permeation studies, respectively. These activities relate to each of the alloy development paths. Chapters 3, 4, 5, 6, and 7 present the ongoing work on each alloy development path. The Table of Contents is annotated for the convenience of the reader.

This report has been compiled and edited under the guidance of the Chairman of the Task Group on *Alloy Development for Irradiation Performance*. E. E. Bloom, Oak Ridge National Laboratory, and his efforts and those of the supporting staff of ORNL and the many persons who made technical contributions are gratefully acknowledged. T. C. Reuther, Materials and Radiation Effects Branch, is the Department of Energy Counterpart to the Task Group Chairman and has responsibility for the ADIP Program within DOE.

Klaus M. Zwilsky, Chief
Materials and Radiation Effects Branch
Office of Fusion Energy

CONTENTS

1. ANALYSIS AND EVALUATION STUDIES

MATERIALS **HANDBOOK** FOR FUSION ENERGY SYSTEM - J. W. Davis (MCDONNELL DOUGLAS ASTRONAUTICS COMPANY–ST. LOUIS) AND T. K. BIERLEIN (HANFORD ENGINEERING DEVELOPMENT LABORATORY)

1.1.1 ADIP Task

Task Number 1.A.1 - **Define** material property requirements and make structural life predictions.

1.1.2 Objective

To provide an authoritative and consistent source of material property data for use by the fusion energy community in conceptual designs, safety analysis, and performance/verification.

1.1.3 Summary

The data sheets and the revision of the existing pages in the handbook are proceeding satisfactorily. The bulk of the property sheets relate to properties of type 316 austenitic stainless steel which were prepared in support of the ETF design. Data sheets covering fatigue crack growth, swelling, and physical properties have been submitted to the ADIP task group for review. The data sheets describing the effects of irradiation in elevated temperature fatigue strength of 20% cold worked 316 have been reviewed and approved by both ADIP and A&E task groups and will be included in the first publication package of the MHFES. Data sheets in preparation but not submitted to the respective task groups for approval are: effect of irradiation on the mechanical properties of 20% cold worked 316; Structural properties of stainless steel alloys for magnet cases; and properties of glass laminates for superconducting magnet insulators.

1.1.4 Progress and Status

The function of the Materials Handbook for Fusion Energy Systems (MHFES) is to provide a data source which meets the design requirements of near term and longer range conceptual fusion reactor designs. To accomplish this the handbook must be readily available to all personnel in the fusion community actively involved in either fusion research or

conceptual designs. Towards this goal we have assigned the handbook to roughly 30 different organizations in an effort to get as wide a coverage as possible. These organizations consist of national laboratories, universities, and private industries. Within these organizations the handbook has been assigned to specific individuals who have agreed to accept the responsibility of maintaining these handbooks and to keep them up to date. This handbook is not to be construed as the personal desk-top copy of the assigned individual, which unfortunately has been the case in some instances. In the past there have been instances where individuals have left the organization where the handbook is assigned and taken the handbook with them or arbitrarily given the handbook to someone else without informing either the MHFES Chairman or the HEDL MHFES publications group. If this practice continues there will be no way to maintain control of the handbook or keeping it up to date. Accordingly a survey was made of all organizations receiving the handbook in an effort to identify the individuals who are responsible for the book. The survey is now complete with 100%response and all issued copies accounted for. To prevent a reoccurrence of this the following ground rules have been established relative to the handbook. The MHFES is the property of the Office of Fusion Energy who has assigned the Hanford Engineering Development Laboratory (HEDL) the responsibility of distributing the handbook and the data pages. The handbook group at HEDL then assigns the handbook to the appropriate individuals within organizations active in the field of fusion energy based on recommendations from OFE and the Chairman of MHFES. When the individual assigned the handbook no longer has need of it or changes jobs he or she is to notify HEDL in writing of the change in circumstances, HEDL will then decide if the handbook is to be recalled or reassigned. Under no circumstances is the handbook to be reassigned or taken from the assigned organization without the concurrence of the HEDL group. Failure to comply will result in that copy of the handbook being removed from the distribution list and no longer kept up to date. Also to ensure that the update packages are received in a timely manner the holder of the handbook is requested to notify the HEDL group of any errors in the mailing address or any additions to the address which will improve the distribution. Please remember that the handbook should be readily available to a wide

variety of people working in fusion. Towards this end the handbook should be displayed in a prominent place where it is readily accessible.

The first update package is in preparation and will be released shortly. In the update package will be an outline of the various major chapters for the handbook and tentative identification of materials to be included in the handbook. Our goal is to include data for at least one material in every chapter before the end of the year. Also included in the update package will be minor revisions to the existing informational pages on stainless steel and new data sheets relating the effects of irradiation on the elevated temperature fatigue strength of 20% cold worked 316 stainless steel. These latter data sheets include both the effects of displacement damage and helium transmutation. The second update package is planned to contain data sheets on swelling and irradiation creep both covering the effects of displacements and helium, the unirradiated fatigue crack growth, tritium permeability, and electrical resistivity of stainless steel. These data sheets have been prepared by personnel from HEDL and ANL and were submitted to the Austenitic Stainless Steel working group of ADIP for review.

Data sheets are currently in preparation on the properties of magnet case materials by the National Bureau of Standards, and fiberglass laminates (G-10 insulators) for magnet insulators by McDonnell Douglas. A request has also been made to the solid breeder working group requesting inputs to the handbook however these contributions will not be available until later this year.

2. TEST MATRICES AND TEST METHODS DEVELOPMENT

2.1 STATUS OF MFE-5 IN-REACTOR FATIGUE CRACK GROWTH EXPERIMENT - A. M. Ermi (Hanford Engineering Development Laboratory).

2.1.1 ADIP Task

ADIP Task I.B.l, "Fatigue Crack Growth in Austenitic Alloys" (Path A).

2.1.2 Objectives

An apparatus has been developed to perform an in-reactor fatigue crack propagation test on the Path A Reference Alloy. Effects of dynamic irradiation on crack growth behavior will be evaluated by comparing the results with those of unirradiated and postirradiated tests.

2.1.3 Summary

The in-reactor fatigue machine has been inserted into the ORR and cycling on a chain of 20% cold-worked 316 stainless steel specimens has commenced. Because of the uncertainties in the y-heating profile, the temperature profile across the specimen chain could not be optimized. However, this temperature profile was duplicated for the thermal control test, and cycling on this second chain of specimens has been initiated at HEDL.

2.1.4 Progress and Status

2.1.4.1 Introduction

Fatigue crack propagation (FCP) in the first wall of a magnetic fusion reactor may be a limiting quantity governing reactor lifetimes. Previous studies of irradiation effects on FCP have all be conducted out of reactor on materials preirradiated in the unstressed condition. The ORR-MFE-5 experiment will investigate FCP during irradiation, where dynamic irradiation may effect crack growth characteristics.

2.1.4.2 In-Reactor FCP Test at ORNL

The in-reacotr fatigue machine[1,2] was inserted into the ORR during the reactor shutdown period in November. After the reactor was brought up to full power, a large temperature gradient existed across the 58cm (23 in) specimen chain. After adjustments to the helium-neon mixtures through the three annular regions surrounding the capsule were made, the temperature profile did improve; but it was apparent that a flat temperature profile would not be attainable.

The temperature profile which was ultimately selected for MFE-5 is shown in Figure 2.1.1. The peak temperature of 460°C (860°F) can be easily controlled, while slight variations in the outermost temperatures occur during burnup and after refueling. The original target temperature was 425°C (797°F) over the entire length of the capsule. The large gradient can be explained in terms of uncertainties in the y-heating profile which was used in the design of the capsule. In addition, a finite amount of mixing of the gas blends across the sliding seals which separate the three regions is believed to have prevented the good independent temperature control anticipated for the regions.

Since the test is being conducted in sodium, the direct effects of temperature on growth rate should be minimal since FCP in sodium is not strongly thermally activated up to about 0.5 T_m [3] Nevertheless, the temperature gradient observed for the in-reactor test was duplicated for the thermal control test.

Cycling of the in-reactor test was begun on December 4, 1980, and has achieved 58,000 cycles to date.

2.1.4.3 Thermal Control Test at **HEDL**

In order to duplicate the temperature profile of the in-reactor test, a furnace arrangement different from that which was previously described[4] was used. A 1000 watt heating element was coiled around the central part of the assembly to provide the primary heating. The bottom of the assembly was inserted into a heated furnace, while the top was loosely wrapped with foil and exposed to the air. The resulting temperature profile is very similar to that of Figure 2.1.1.

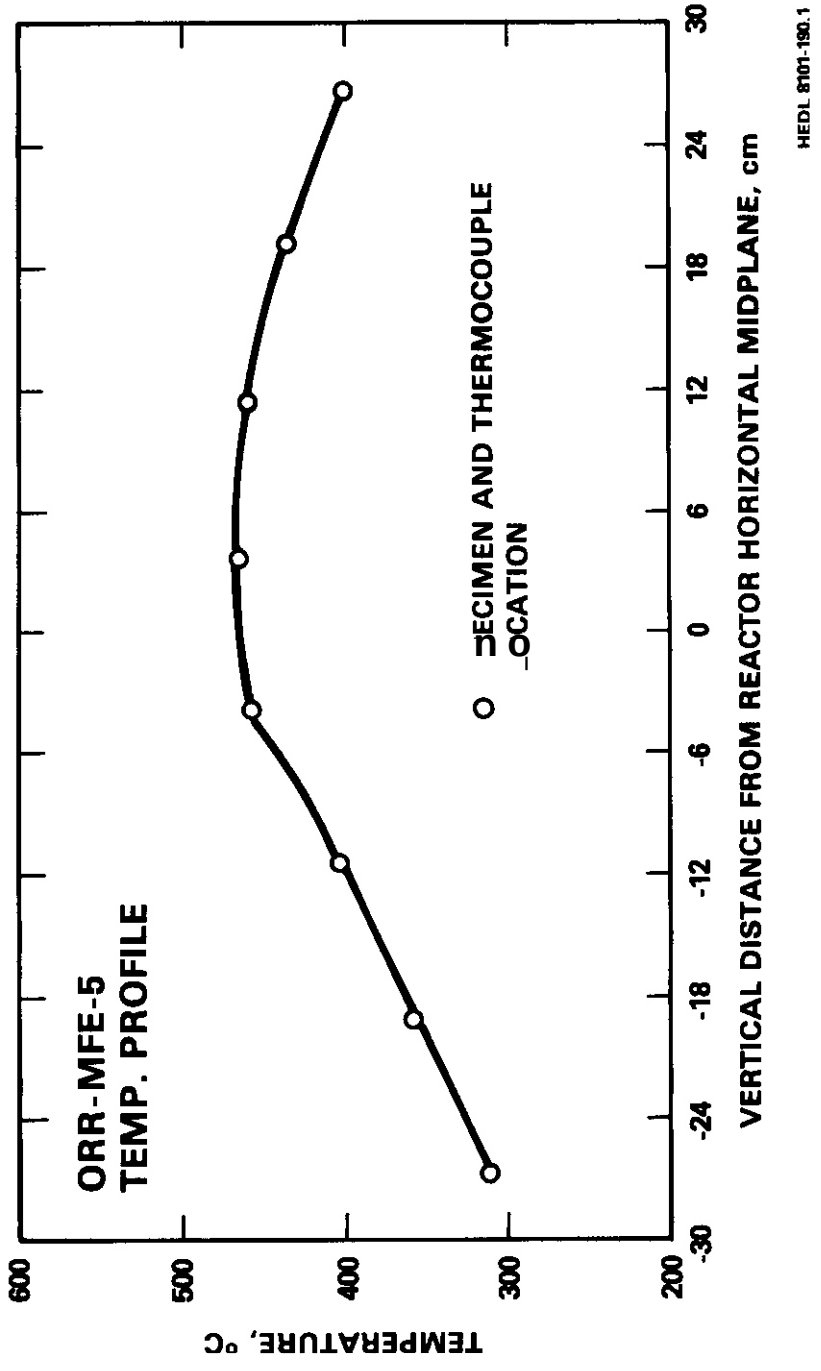

FIGURE 2.1.1 Temperature Profile for the MFE-5 In-Reactor FCP Experiment.

Cycling of the test has been initiated, with shutdowns scheduled to coincide with those of the in-reactor test.

2.1.5 Conclusions

(a) The MFE-5 in-reactor FCP test has been initiated in the ORR. The test has attained 58,000 cycles.

(b) The MFE-5 thermal control test has been initiated, duplicating the temperature and cycle history of the in-reactor test.

2.1.6 References

1. A. M. Ermi, "Status of an In-Reactor Fatigue Crack Growth Experiment", *ADIP Quarterly Progress Report, June 30, 1979*, DOE/ET-005816, pp. 28-34.
2. A. M. Ermi, "Results of Prototypic Testing for the MFE-5 In-Reactor Fatigue Crack Propagation Experiment", *ADIP Quarterly Progress Report, September 30, 1979*, DOE/ET-0058/7, pp. 50-65.
3. A. M. Ermi, "Fatigue Crack Growth Testing of 316SS for MFE-5", *ADIP Quarterly Progress Report, June 30, 1980*, DOE/ER-0045/3, pp. 42-47.
4. L. A. James, "Fatigue-Crack Propagation in Austenitic Stainless Steels", Atomic Energy Review, 14, 1(1976) pp. 53-57.

2.2 NEUTRONIC CALCULATIONS FOR THE CONCEPTUAL DESIGN OF AN IN-REACTOR SOLID BREEDER EXPERIMENT, TRIO-01 — R. A. Lillie, R. L. Childs, and T. A. Gabriel (ORNL)

2.2.1 ADIP Task

ADIP Task I.A.2, Define Test Matrices and Test Procedures.

2.2.2 Objective

The objective of these neutronic calculations is to provide tritium production and heat generation rates for the irradiation of solid tritium breeding materials in the Oak Ridge Research Reactor (ORR). These calculations will guide the design of the reactor irradiation experiment.

2.2.3 Summary

Two-dimensional transport[1] calculations of the TRIO-01 breeder experiment have been performed and the results of these calculations have been compared with previously generated one-dimensional[2-4] results. The two-dimensional results indicate approximately 5% decrease in the tritium production and less than 20% decrease in the heating rates within the experimental materials.

The change in the thermal flux and the flux above thermal along the poolside face due to the insertion of the TRIO-01 experiment in position A2 of the ORR has been estimated[5] using VENTURE and a simulated model of the experiment. The ^{6}Li and ^{7}Li cross sections needed to adequately describe the experiment using VENTURE have been processed and better estimates of the flux change due to the insertion of the experiment are being obtained.

A report entitled "Neutronics Calculations for the Conceptual Design of an In-Reactor Solid Breeder Experiment, TRIO-01," covering the one-dimensional neutronics calculations has been prepared and is being reviewed.

2.2.4 Progress and Status

Previous one-dimensional calculations were performed to establish the tritium production and nuclear heating rates of an experiment to irradiate lithium containing solids in the ORR core.[3] Refined one-dimensional

calculations were completed and experiment parameters were selected.[4] These formed the basis for the more detailed calculations necessary to scope the expected experimental performance.

The tritium production and heating rates in the TRIO-01 experiment obtained from the two-dimensional calculations are given in Tables 2.2.1 and 2.2.2, respectively. Also given for comparison are the previously generated one-dimensional results. These calculations were performed using the modified experimental geometry in which the experiment capsule diameter is about 25 mm. All the results in these tables, both the two- and one-dimensional results, represent zone-averaged quantities. The difference between the tritium production rates predicted by the two models is minimal, and less than 20% change in the heating rates results from the use of a two-dimensional model. These changes occur since the representation of the breeder as finite rather than infinite in height reduces absorptions in ^6Li to the real extent of the material and compensates for the axial variation of the neutron flux.

Table 2.2.1. Calculated Tritium Production Rates in $LiAlO_2$ for the TRIO-01 Experiment

Tritium Source[a]	Tritium Production Rates, atoms/(m^3·s)	
	2-D Calculation[b]	1-D Calculation[b]
^6Li	2.03×10^{19}	2.11×10^{19}
^7Li	0.0094	0.0104

[a]Density of $LiAlO_2$ has been taken to be 70% of 3.4 Mg/m^3. Composition of the lithium is 0.5% ^6Li and 99.5% ^7Li. Rates are averaged over the breeder zone.

[b]The calculational model of the experiment and surrounding reactor core is described by T. A. Gabriel, R. A. Lillie, and B. L. Bishop, "Neutronic Calculations for the Conceptual Design of an 'In-Pile' Solid Breeder Experiment IPSB-01," *ADIP Quart. Prog. Rep. Mar. 31, 1980,* DOE/ER-0045/2, pp. 16-18 and T. A. Gabriel, R. A. Lillie, and R. L. Childs, "Neutronic Calculations for the Conceptual Design of an In-Reactor Solid Breeder Experiment, TRIO-01," *ADIP Quart. Prog. Rep. Sept. 30, 1980,* DOE/ER-0045/4, pp. 8-13.

Table 2.2.2. Calculated Heating Rates for the TRIO-01 Experiment, Using a Two-Dimensional Transport Calculation

Zone[a,b]	Zone Material	Heating Rates,'? MW/m^3		
		Neutron	Gamma	Total
2	Stainless steel	*0.54* (0.68)	77.5 (92.3)	78.0 (93.0)
3	Breeder	12.8 (13.4)	19.7 (23.6)	32.5 (37.0)
4	Stainless steel	0.62 (0.69)	78.5 (93.7)	79.1 (94.4)
5	Aluminum	1.11 (1.21)	25.1 (29.9)	26.2 (31.1)

[a]Average fuel loading of elements around capsule, 140 g. Gamma heating rates include reflected gammas. Percent ^{6}Li, 0.5; percent ^{7}Li, 99.5.

[b]The calculational model of the experiment and the surrounding reactor core **is** described by T. A. Gabriel, R. A. Lillie, and B. L. Bishop, "Neutronic Calculations for the Conceptual Design of an 'In-Pile' Solid Breeder Experiment IPSE-01," ***ADIP Quart. Prog. Rep. Mar. 31, 1980,*** DOE/ER-0045/2, pp. 16-18 and T. A. Gabriel, R. A. Lillie, and R. L. Childs, "Neutronic Calculations for the Conceptual Design of an In-Reactor Solid Breeder Experiment, TRIO-01," ***ADIP Quart. Prog. Rep. Sept. 30, 1980,*** DOE/ER-0045/4, pp. 8-13.

[c]All values in parentheses represent previously calculated one-dimensional results.

The introduction of a strongly neutron-absorbing experiment into the ORR core will perturb the flux on experiments close to the absorber. In particular, the effect of the **TRIO-01** experiment in position ***A2*** on experiments at the ORR pool face was of concern and required evaluation.

The effect on the thermal and above thermal 00.414 eV) neutron fluxes along the horizontal midplane of the pool face of the ***ORR*** due to the replacement of beryllium with the **TRIO-01** experiment in core position ***A2*** is illustrated in Fig. 2.2.1. These results represent only estimates of the actual effect since lithium cross sections were not available when these results were generated and cadmium cross sections were used to simulate the ^{6}Li thermal neutron cross section. However, the

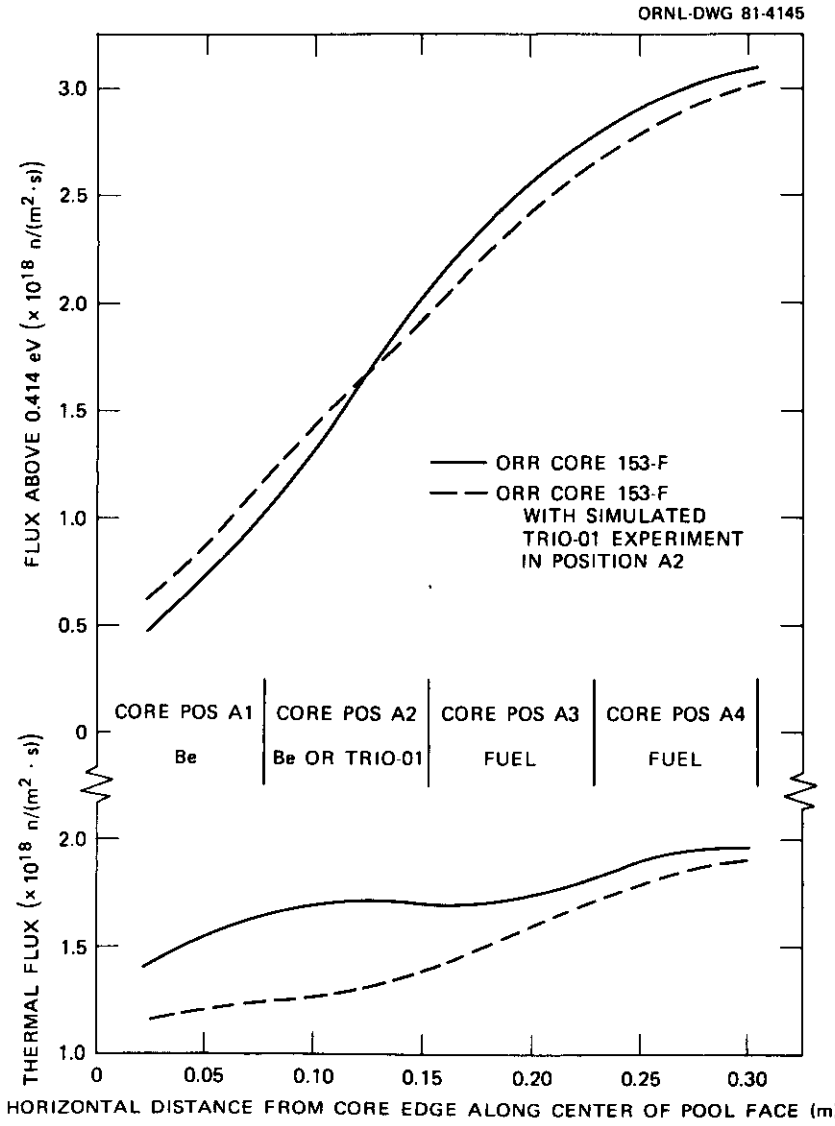

Fig. 2.2.1. Effect of TRIO-01 Experiment on Thermal Flux and Flux Above Thermal Along Oak Ridge Research Reactor Pool Face.

behavior of both the thermal and above-thermal fluxes and the actual magnitude of the thermal flux change are probably fairly indicative of the actual changes that may occur due to the insertion of the experiment in core position A2.

2.2.5 Future Work

The VENTURE calculations to determine the changes in the poolside fluxes due to the presence of the TRIO-01 experiment will be repeated using the recently processed lithium cross sections. These calculations will be performed using the modified geometry' containing γ-$LiAlO_2$ at 60 to 70% of its theoretical density of 2.615 Mg/m^3. In addition to obtaining the poolside flux changes, this calculation will provide better estimates of the neutron fluxes around the experiment. With these results, additional two-dimensional transport calculations will be performed to determine the asymmetric tritium production and heating rates that are expected to occur with the experiment located in core position A2.

2.2.6 References

1. W. A. Rhoades, D. B. Simpson, R. L. Childs, and W. W. Engle, Jr., *The WT 111 Two-Dimensional Discrete Ordinates Transport Code With Space-Dependent Mesh and Quadrature*, ORNL/TM-6529 (January 1979).
2. W. W. Engle, Jr., *A User's Manual for ANISN, A One-Dimensional Discrete Ordinates Code With Anisotropic Scattering*, K-1693 (1967).
3. T. A. Gabriel, R. A. Lillie, and B. L. Bishop, "Neutronic Calculations for the Conceptual Design of an 'In-Pile' Solid Breeder Experiment IPSB-01," *ADIP Quart. Prog. Rep. Mar. 31, 1980*, DOE/ER-0045/2, pp. 16–18.
4. T. A. Gabriel, R. A. Lillie, and R. L. Childs, "Neutronic Calculations for the Conceptual Design of an In-Reactor Solid Breeder Experiment, TRIO-01," *ADIP Quart. Prog. Rep. Sept. 30, 1980*, DOE/ER-0045/4, pp. 8–13.
5. D. R. Vondy, T. B. Fowler, and G. W. Cunningham, *VENTURE, A Code Block for Solving Multigroup Neutron Problems Applying Fine-Diffusion-Theory Approximations to Neutron Transport*, OWL-5062 (October 1975).

2.3 NEUTRONIC CALCULATIONS IN SUPPORT OF THE ORR-MFE-4 SPECTRAL TAILORING EXPERIMENT – R. A. Lillie, R. L. Childs, and T. A. Gabriel (ORNL)

2.3.1 ADIP Task

ADIP Task I.A.2, Define Test Matrices and Test Procedures.

2.3.2 Objective

The objective of this work is to provide the neutronic design for materials irradiation experiments in the Oak Ridge Research Reactor (ORR). Spectral tailoring to control the fast and thermal neutron fluxes is required to provide the desired displacement and helium production rates in alloys containing nickel.

2.3.3 Summary

Three-dimensional neutronic calculations[1,2] are being carried out to follow the irradiation environment of the ORR-MFE-4A experiment. These calculatiuons currently cover the 15 ORR reactor cycles completed to December 12, 1980, corresponding to 111,466 MWh, 3.45 x 10^{25} neutrons/m^2 in thermal fluence and 1.03 × 10^{26} neutrons/m^2 in total fluence. This produces 2.61 dpa and 15.75 at. ppm He in type 316 stainless steel (not including 2.0 at. ppm He from ^{10}B). Using these data and previous calculations, real time projections have been made to estimate the dates that the core pieces should be changed and first samples removed.

The preliminary calculations[3,4] to determine the appropriate sizes of the hafnium core pieces have been accomplished, and in addition, the heating rates within the experimental capsules have been obtained. For a given reduction in thermal flux, the decrease in gamma heating due to the use of either hafnium or tungsten core pieces does not drastically differ. Since the thickness of hafnium needed to obtain a specified thermal flux reduction is approximately one-fourth the thickness of tungsten needed, the reduction in gamma heating is most likely due to a loss of fission gammas and not due to gamma attenuation in the core pieces. Calculations are currently in progress to validate this statement.

2.3.4 Progress and Status

A cylindrical geometry model of the OW-MFE-4A experiment and adjacent core regions has been developed[2] and is used to project helium and displacement damage production rates throughout the course of the experiment. The model is also used to identify necessary changes in the reactor core configuration to maintain the desired ratio of helium production to displacement damage production. Previous calculations showed that the tungsten core pieces used to suppress the thermal neutron flux resulted in too much reduction in the nuclear heating rate,[4] and the feasibility of using hafnium core inserts is under study.

The real time projections of the ratio of atomic parts per million helium to displacements per atom level based on current calculated data are given in Fig. 2.3.1. The data reflect all refueling and extended

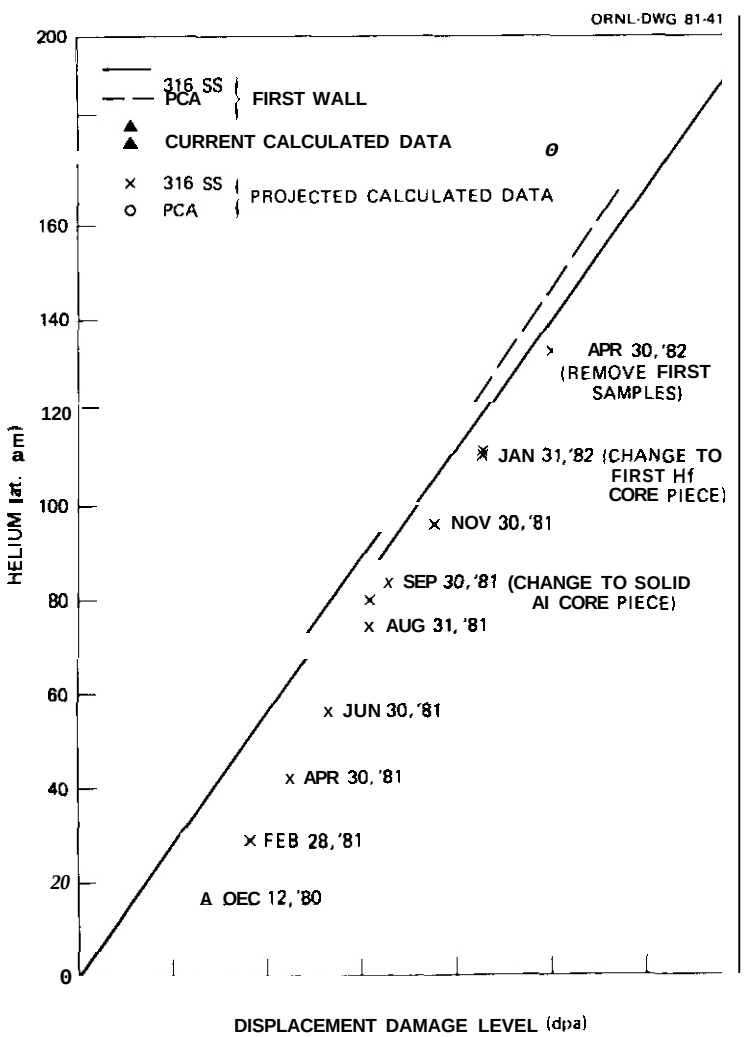

Fig. 2.3.1. Current and Projected Helium and Displacement Damage Levels in the ORR-MFE-4A Experiment.

shutdown times projected as of December 18, 1980. Using these data, the insertion of the solid aluminum core piece will not be required until the end of September 1981. The first samples will be removed sometime around April 30, 1982.

The relative gamma heating as a function of the percent reduction in thermal flux using either hafnium or tungsten core pieces is given in Fig. 2.3.2. For a small reduction in thermal flux, both core pieces yield identical relative gamma heating rates. As the percent reduction in thermal flux increases, the tungsten core piece produces a greater reduction in gamma heating because of the increasing difference in thickness between the two core pieces. However, based on the gamma attenuation properties of tungsten and hafnium and the increased difference in thickness between the two core pieces, a much greater reduction should result from the use of tungsten core pieces. This anomaly strongly suggests that the loss of fissions in the fuel surrounding the experiment due to the thermal flux reduction in the experiment is the primary cause of the reduction in gamma heating.

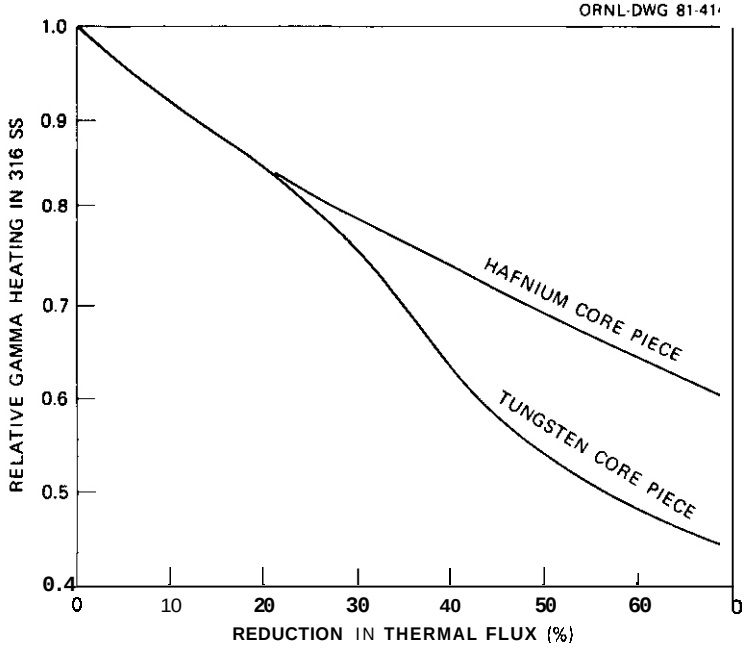

Fig. 2.3.2. Change in Gamma Heating in the ORR-MFE-4A Experiment Due to Use of Tungsten OK Hafnium Core Pieces to Reduce Thermal Flux.

2.3.5 Future Work

The one-dimensional model employed to estimate the effects of hafnium and tungsten core pieces cannot properly account for changes in the fission rate due to thermal flux reductions in the ORR-MFE-4A experiment. For this reason, the use of a two-dimensional model is being contemplated to obtain better estimates of the reduction in gamma heating due to the use of hafnium or tungsten core pieces. Since the total fission rate for the full reactor core must be constant, the loss of fissions in the fuel surrounding the experiment will be made up elsewhere and the changes in gamma heating due to the use of various core pieces will likely be much less than the current one-dimensional calculations indicate.

The three-dimensional calculations that monitor the radiation environment of the ORR-MFE-4A experiment will continue with each ORR reactor cycle.

2.3.6 References

1. D. R. Vondy, T. B. Fowler, and G. W. Cunningham, VENTURE, *A Code Block for Solving Muttigroup Neutron Problems Applying Fine-Diffusion-Theory Approximations to Neutron Transport,* OWL-5062 (October 1975).
2. T. A. Gabriel, R. A. Lillie, B. L. Bishop, and R. L. Childs, "Neutronic Calculations in Support of the ORR-MFE-4A Spectral Tailoring Experiment," *ADIP Quart. Prog. Rep. June 30, 1980,* DOE/ER-0045/3, pp. 7-9.
3. W. W. Engle, Jr. *A User's Manual for ANISN, A One-Dimensional Discrete Ordinates Code with Anisotropic Scattering,* K-1693 (1967).
4. T. A. Gabriel, R. A. Lillie, B. L. Bishop, and R. L. Childs, "Neutronic Calculations in Support of the ORR-MFE-4A Spectral Tailoring Experiment." *ADIP Quart. Prog. Rep. Sept. 30, 1980,* DOE/ER-0045/4, pp. 14-19.

3. PATH A ALLOY DEVELOPMENT — AUSTENITIC STAINLESS STEELS

3.1 HIGH TEMPERATURE FATIGUE CRACK PROPAGATION of TYPE 316 STAINLESS STEEL IN VACUUM - H. H. Smith and D. J. Michel (Naval Research Laboratory)

3.1.1 ADIP Task

Task I.B.l. Fatigue Crack Growth in Austenitic Alloys (Path A).

3.1.2 Objective

To evaluate the influence of neutron irradiation and vacuum environment on the elevated temperature fatigue crack propagation properties of alloys of interest to the MFE alloy development program.

3.1.3 Summary

Elevated temperature fatigue crack propagation tests have been conducted in vacuum on specimens of MFE and FBR reference annealed Type 316 stainless steel. The MFE alloy was tested at 550°C and the FBR alloy at 550 and 593°C. For the levels of ΔK employed in these experiments ($\Delta K < 33$ MPa$\sqrt{m}$), the rates of fatigue crack propagation in vacuum were significantly lower than those of the FBR steel tested in air at 593°C.

3.1.4 Progress and Status

3.1.4.1 Introduction

Current work is being directed toward the establishment of the necessary unirradiated data base to assess the effect of neutron irradiation on the fatigue crack propagation performance of Type 316 stainless steel. This report describes elevated temperature fatigue crack propagation experiments conducted in vacuum using 12.7 mm thick specimens. These tests were performed to develop a data base of conventionally sized specimens for comparison with future evaluations of 2.54 mm specimens intended for pre- and postirradiation studies of first wall materials.

3.1.4.2 Experimental Procedures

Unirradiated MFE and FBR reference annealed Type 316 stainless steel compact tension specimens, 12.7 mm thick, were tested in a vacuum of 6.7 X 10^{-6} Pa using a servo-hydraulic test machine. Details of the

testing procedure have been previously reported[1,2]. In these tests, sawtooth loading was employed at a frequency of 0.17 Hz using a load ratio of 0.05. Fatigue crack propagation rates were determined by the secant method from optical measurements of crack length taken throughout the test.

3.1.4.3 Results

The results of the vacuum tests are compared with previous results of FBR reference material tested at 593°C in air, Figure 3.1.1. Three major points are apparent from these comparisons. First, the results show that the crack propagation rates of the FBR and MFE material are essentially identical in vacuum at 550°C. Secondly, the crack propagation rates in vacuum are lower at 550°C than 593°C for the FBR materials although this difference may fall within an experimental scatter band. And finally, the results show that for the levels of ΔK employed in these experiments ($\Delta K < 33$ MPa $\sqrt{m}$), fatigue crack propagation rates in the FBR alloy at 593°C were significantly reduced in vacuum when compared to the previous results in air. Further, the results show the air and vacuum data to be converging and that a reversal in behavior may take place at higher ΔK levels. Because of the similarity in fatigue crack propagation properties of the two alloys, it would be expected that fatigue crack propagation rates in the MFE alloy also have been reduced compared to those in air at 550°C. This will be verified when the results for the MFE alloy tested in air become available.

Scanning electron microscope (SEM) investigation of the specimens tested in vacuum at 550°C shows that the mode of crack propagation was ductile and entirely transgranular, Figs. 3.1.2 (c) and (d). The FBR steel tested in vacuum at 593°C exhibited a similar mode of crack propagation, Fig. 3.1.2 (b), while the FBR steel tested in air at 593°C produced a transgranular mode without clear evidence of extensive ductility, Fig. 3.1.2 (a).

3.1.4.4 Conclusion

The results demonstrate that for ΔK levels less than 33 MPa $\sqrt{m}$, MFE and FBR reference Type 316 stainless steel will show reduced

susceptibility to cracking in vacuum as compared to air at 593°C.

3.1.4.5 Future Work

Previous work has demonstrated that the fatigue crack propagation data from 2.54 mm thick specimens was in agreement with data produced by conventional sized specimens when tested in air[3]. Additional pre-irradiation comparisons will be conducted using 2.54 mm thick specimens of both annealed and 20% cold worked MFE material to characterize the fatigue crack propagation properties of specimens of first wall section size in vacuum.

3.1.4.6 References

1. D. J. Michel, H. H. Smith, and H. E. Watson, "Effect of Hold Time on Elevated Temperature Fatigue Crack Propagation in Fast Neutron Irradiated and Unirradited Type 316 Stainless Steel," in Structural Materials for Service at Elevated Temperature in Nuclear Power Generation, A.O. Schaefer, ed., American Society of Mechanical Engineers, New York, MPC-1, 1975, pp. 167-190.

2. D. J. Michel and H. H. Smith, "Effect of Neutron Irradiation on Fatigue Crack Propagation in Type 316 Stainless Steel at 649°C," NRL Memorandum Report 3936, Naval Research Laboratory, Washington, D.C., March 14, 1979.

3. D. J. Michel and H. H. Smith, "Elevated Temperature Fatigue Crack Propagation Testing of 2.54 mm Thick CT Specimens," ADIP Quarterly Progress Report for period ending September 30, 1979, DOE/ET-0058/7, Oak Ridge National Laboratory, April 1980, pp. 43-46.

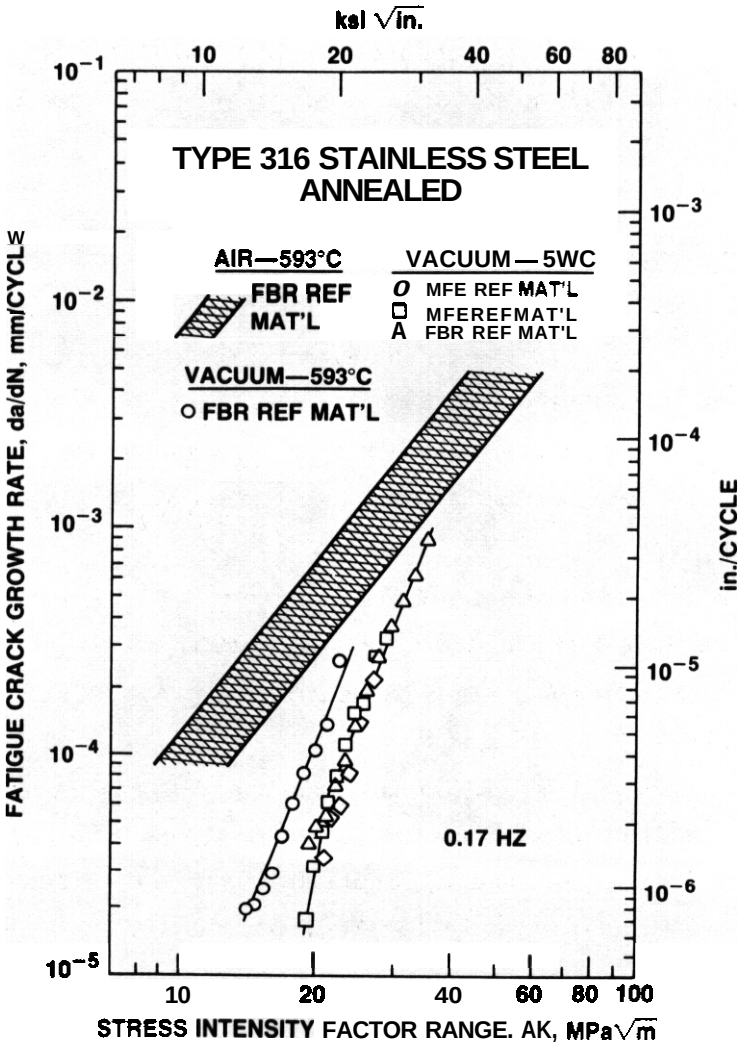

Fig. 3.1.1 Comparison of Fatigue Crack Propagation Rates for 316 Stainless Steel in Air and Vacuum.

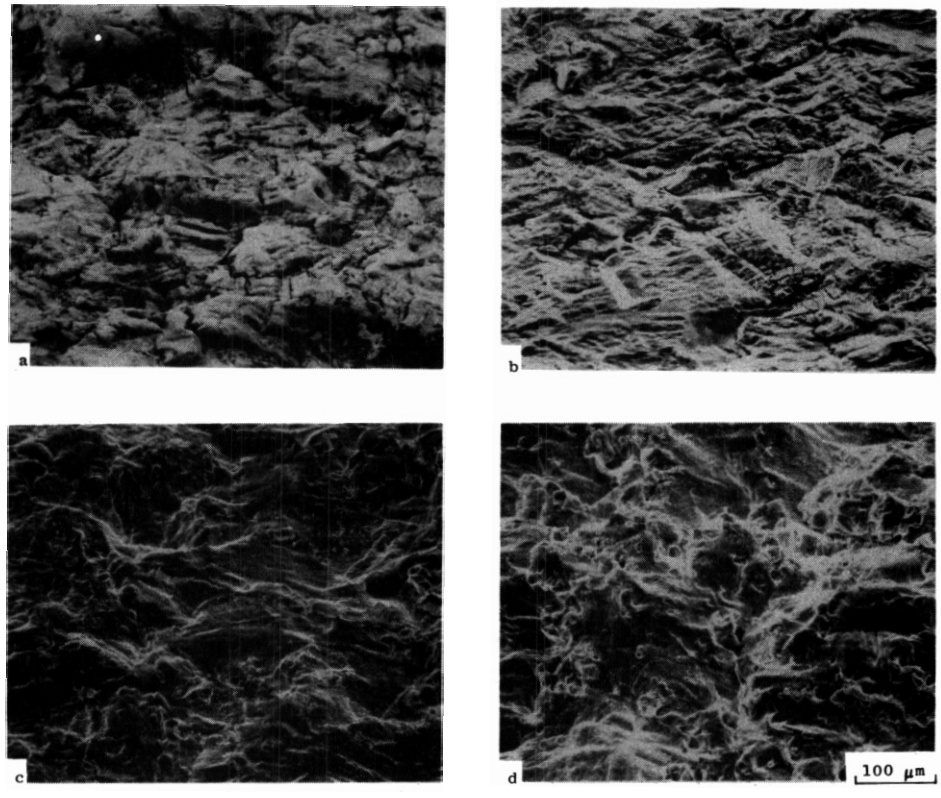

Fig. 3.1.2 Scanning Electron Micrographs of the Crack Propagation Mode in Annealed, Unirradiated MFE and FBR Reference Type 316 Stainless Steels: (a) FBR Reference 316 Stainless steel, Air, 593°C; (b) FBR Reference 316 Stainless Steel, vacuum, 593 C; (c) FBR Reference 316 Stainless Steel, Vacuum 550°C; (d) MFE Reference 316 Stainless Steel, Vacuum, 550°C.

3.2 DESIGN AND FABRICATION OF PREIRRADIATION MICROSTRUCTURES IN PATH A PRIME CANDIDATE ALLOY — P. J. Maziasz and T. K. Roche

3.2.1 ADIP Tasks

ADIP Tasks I.A.5, Perform Fabrication Analysis, and I.C.1 Microstructural Stability.

3.2.2 Objective

The objective of these tasks is to combine microstructural design with fabrication practice and thermal mechanical treatment (TMT) to obtain Path A Prime Candidate Alloy (PCA) specimen material with independently variable grain size and precipitate microstructures.

3.2.3 Summary

Previous work described seven desired preirradiation microstructures and six of these were successfully produced in specimen material with a coarse (ASTM 1–3) grain size. The seventh microstructure, which consists of fine MC precipitates at the grain boundaries and within grains together with a high dislocation density, was not successfully produced initially. However, with modification of the TMTs, this microstructure has been successfully produced in coarse-grain material. Five of the seven microstructures were identified for production in finer grain material (ASTM 7–8). The fabrication sequences and TMTs were adjusted to reduce the grain size without significant MC precipitation prior to the final TMTs and without losing the homogeneity achieved in coarse grained material. A uniform fine grain size was achieved by reducing the temperature of the final 15-min solution anneal from 1175 to 1100°C. The homogeneity was slightly perturbed by this treatment, but the final microstructures with variable distributions of MC precipitate both at the grain boundaries and in the matrix resulted. This completes Phase I of alloy development in Path A PCA.

3.2.4 Progress and Status

Prior work[1] identified a homogeneity problem and titanium rich carbide stringering in as received 13-mm-thick plate stock and 13- and 33-mm-diam bar stocks of Path A PCA. The fabrication behavior of the

PCA was investigated and the reasons established for the development of the inhomogeneous microstructure. Methods were developed to rehomogenize the material and perserve the homogeneity during fabrication.[1,2] Pre-irradiation microstructures for the PCA were designed on the basis of the beneficial effects of interfacial helium trapping at MC precipitates and of cold working on reducing swelling and reducing mechanical properties degradation during HFIR irradiation.[3] These microstructures consisted of various combinations of matrix and grain boundary precipitation with variations in dislocation density. Thermal aging of homogenized PCA in the 0, 10, or 25%-cold-worked conditions established the TMT treatments required to produce the design microstructures.[4] The microstructures are listed and described in Table 3.2.1. The TMTs to produce these microstructures with large grain size are given in Table 3.2.2, and the flow diagram for fabrication is shown in Fig. 3.2.1. Final sheet 0.25 mm thick was produced for microstructures Al, A2, A3, B1, B2, and C and their quality assured by both metallography and transmission electron microscopy (TEM).[5]

Table 3.2.1. Preirradiation Microstructures That Can Be Achieved by Thermal-Mechanical Treatment of the Prime Candidate Alloy

A.	Simple microstructures resulting from: 1. solution annealing, 2. 5 to 10% cold working, or 3. 20 to 25% cold working.
B.	Microstructures with both coarse-grain-boundary MC precipitation and intragranular MC precipitation consisting of: 1. coarse particles or particle clusters or 2. fine matrix precipitation.
C.	Microstructures with both fine-grain-boundary MC precipitation and fine-intragranular MC matrix precipitation.
D.	Microstructures with both fine grain boundary MC precipitation and fine-intragranular MC matrix precipitation plus increased dislocation density.

Table 3.2.2. Recommended Thermal-Mechanical Treatments to Produce Identified Preirradiation Microstructures

Microstructure[a]	Thermal-Mechanical Treatment	
	Initially Suggested	Revised
A1	25% cold work plus 15 min at 1175°C	No change
A2	15 min at 1175°C plus 10% cold work	No change
A3	15 min at 1175°C plus 25% cold work	No change
B1	Solution anneal plus 8 h at 800°C plus 8 h at 900°C	No change
B2	Solution anneal plus 8 h at 800°C plus 25% cold work plus 15 min at 750°C	Solution anneal plus 8 h at 800°C plus 25% cold work plus 2 h at 750°C
C	25% cold work plus 15 min at 750°C	25% cold work plus 2 h at 750°C
D	10% cold work plus 30 min at 750°C plus 10% cold work	10% cold work plus 2 h at 750°C plus 10% cold work

[a]Letter and number codes refer to microstructures defined in Table 3.2.1.

Figure 3.2.2 shows the metallography of coarse-grained specimen material of microstructures A3, B2, and C. The coarser MC at the grain boundaries is visible in Fig. 3.2.2(b) (microstructure B2). Coarse-grained A2 and D are shown in Fig. 3.2.3. The TEM microstructure of coarse-grained D is shown in Fig. 3.2.4. Fine MC precipitation is observed both in the matrix and at the grain boundaries, with particle diameter of about 3 to 5 nm. The significance of microstructure D can be appreciated by comparing Fig. 3.2.4(c) and (d) to Fig. 3.2.5, showing microstructure C in coarse-grained material. Microstructure C, developed by cold working 25% and then aging for 2 h at 750°C, has a dislocation tangle in cellular array, typical of cold deformation, and fine MC particles on all dislocation line segments. By comparison, microstructure D, developed by cold working 10%, precipitating MC and then cold working an additional 10%, has a very high dislocation density in the walls of the cellular array with many dislocations in the tangles. There are few MC particles on dislocations of microstructure D. This demonstrates how the microstructures can be manipulated through homogenization and precipitation control.

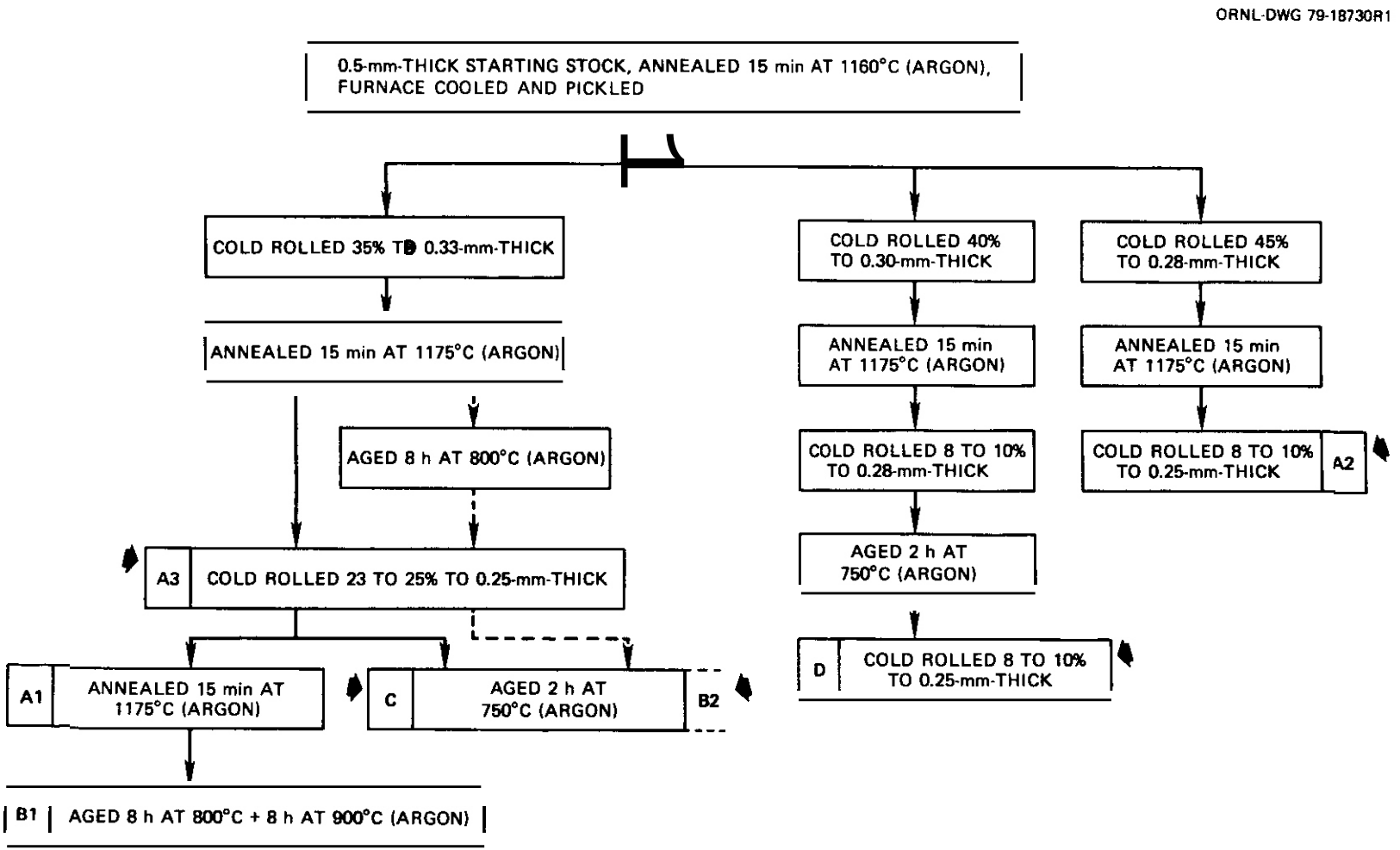

Fig. 3.2.1. Final Processing Steps to Produce Designed Microstructures of the Path A PCA. Number and letter codes refer to the preirradiation microstructures listed in Table 3.2.1. Heavy arrows indicate the points in the sequence at which specimens can be blanked from "hard" material.

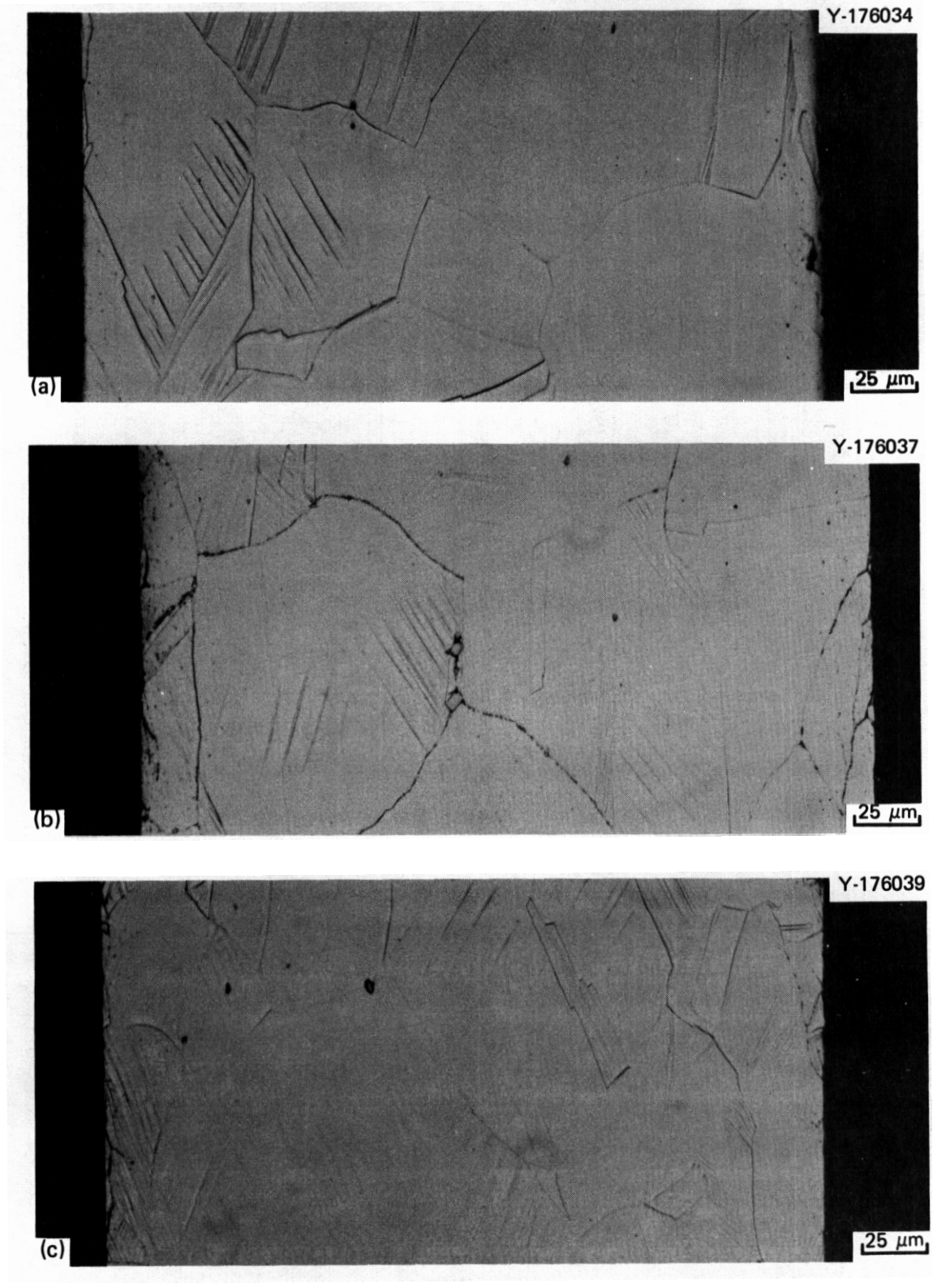

Fig. 3.2.2. Metallography of Coarse-Grained 0.25-mm-Thick Sheet of PCA with Microstructures: (a) A3 — annealed 15 min at 1175°C and cold worked about 25%. (b) B2 — annealed 15 min at 1175°C, aged 8 h at 800°C, cold worked about 25%, and aged 2 h at 750°C. (c) C — annealed 15 min at 1175°C, cold worked about 25%, and aged 2 h at 750°C.

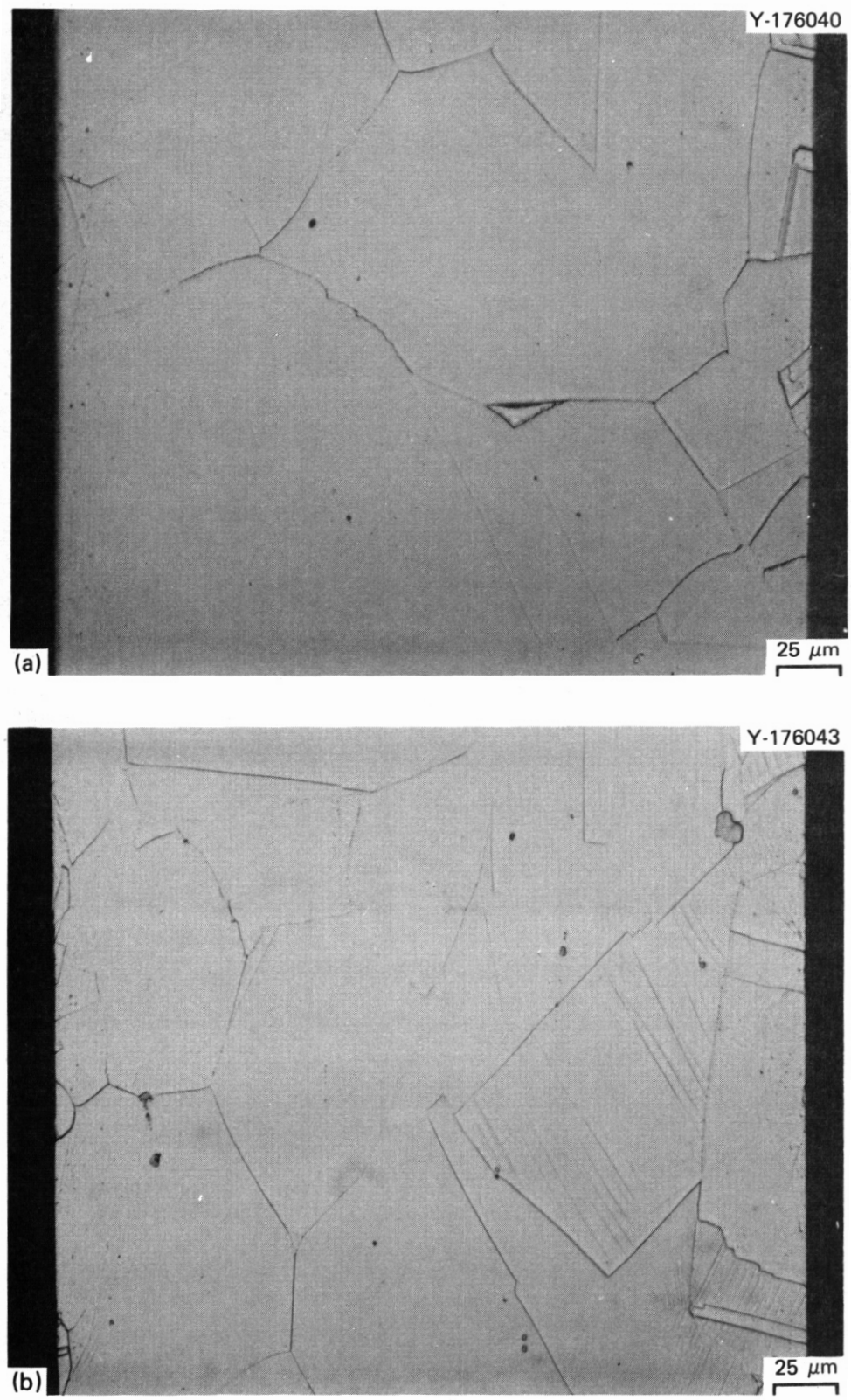

Fig. 3.23. Metallography of Coarse-Grained 0.25-m-Thick Sheet of PCA with Microstructure: (a) A2 — annealed 15 min at 1175°C and cold worked about 10%. (b) D — annealed 15 min at 1175°C, cold worked about 10%. aged for 2 h at 750°C, and cold worked about 10% again.

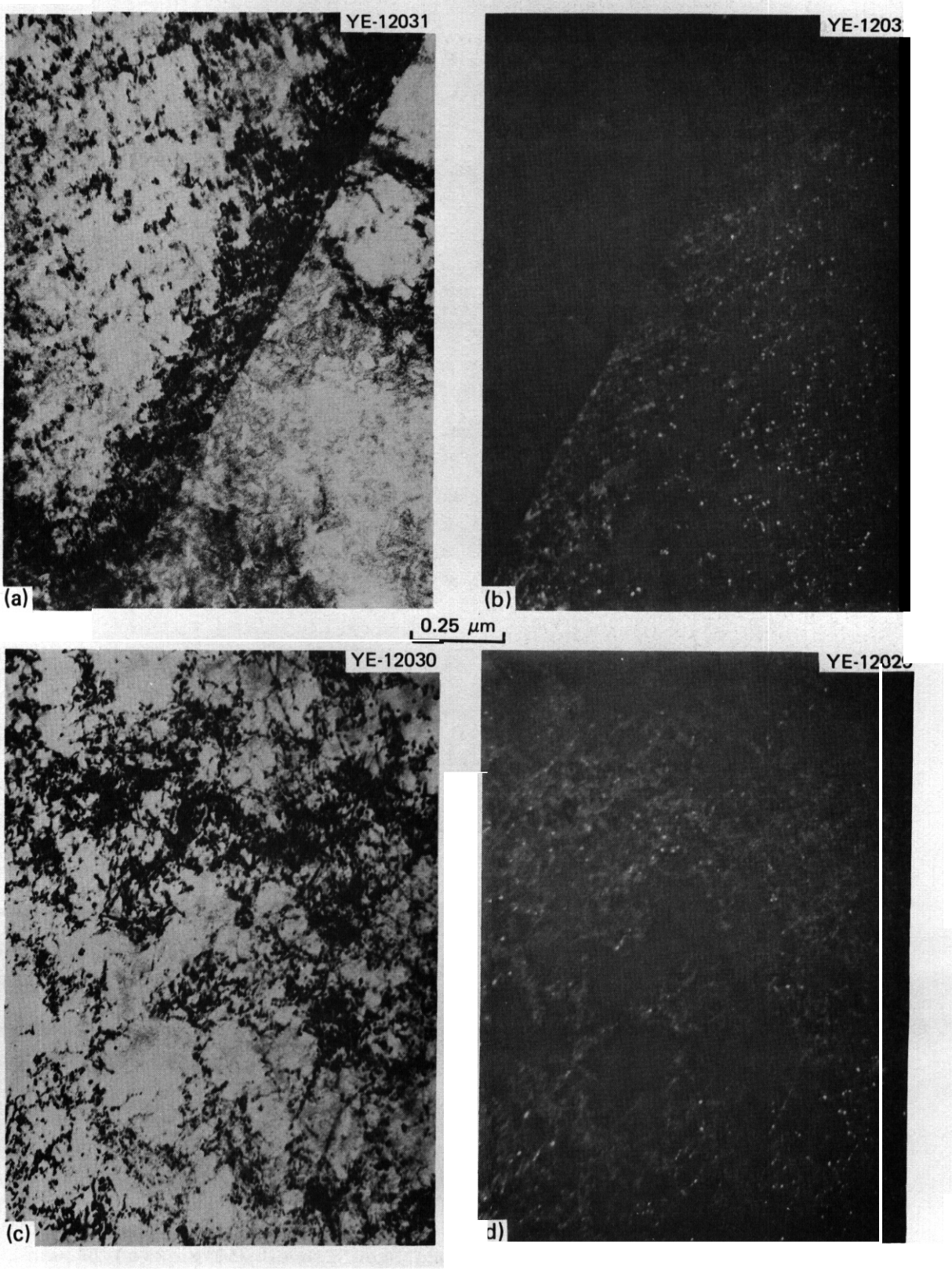

Fig. 3.2.4. Microstructure D of Coarse-Grained **PCA** Annealed 15 min at 1175°C, Cold Worked about 10%. Aged 2 h at 750°C, and Cold Worked about 10%**Again.** (a) Bright Field (BF) and (b) Dark Field (DF) TEM of grain boundaries showing fine MC precipitate and (c) BF and (d) DF TEM of matrix to show fine MC and dislocation structure.

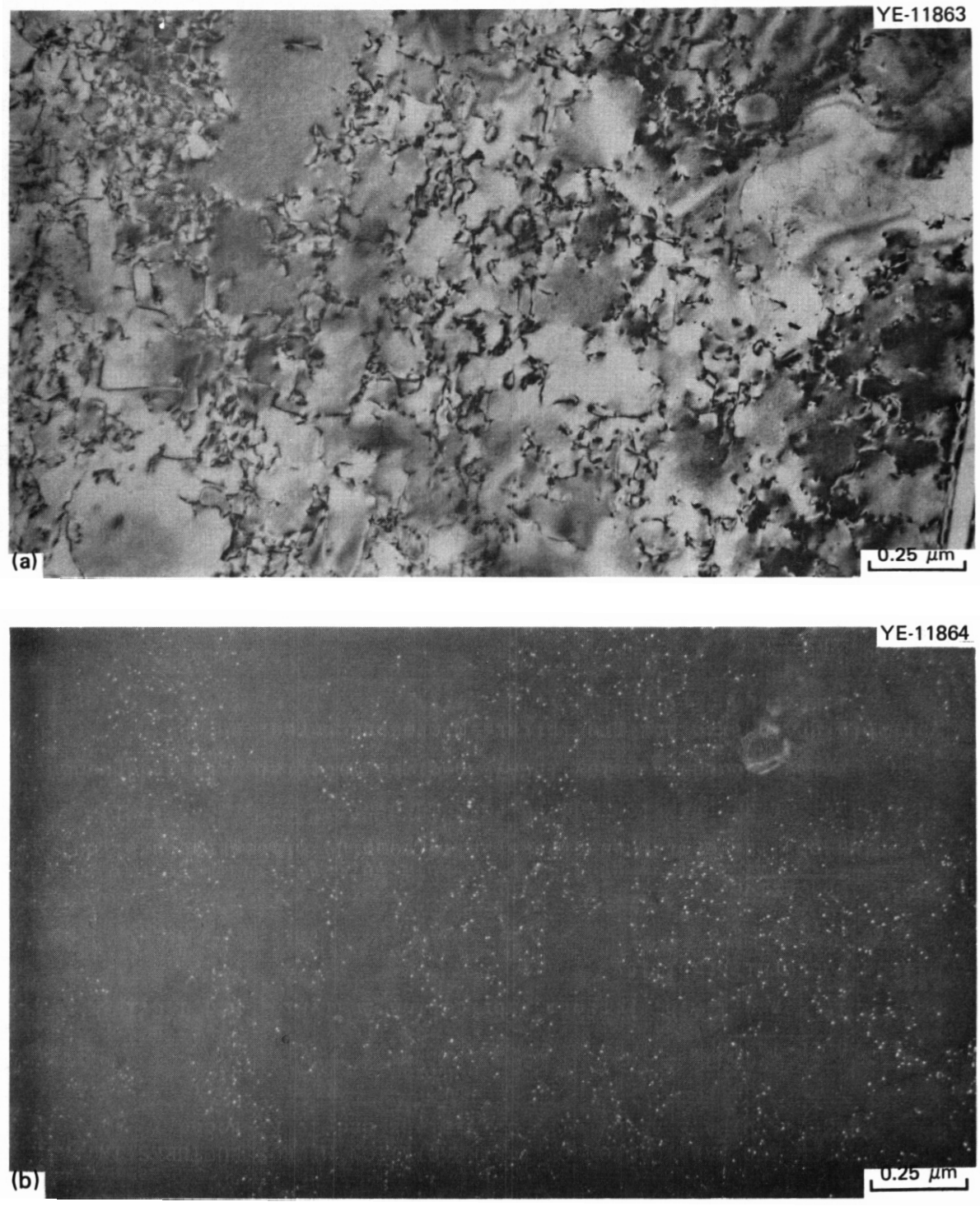

Fig. 3.25. Microstructure C of Coarse-Grained PCA Annealed 15 min at 1175°C, Cold Worked about 25%, and Aged 2 h at 750°C. (a) BF and (b) DF T M of matrix showing fine MC distributed along the dislocation structure.

The very coarse grain size in the above materials was a result of the high temperature (1175°C) used in the last solution annealing step of each fabrication sequence in Fig. 3.2.1. More desirable is a grain size that is controllable and can be varied without ruining the homogeneity or precipitation variability. Trade offs include the better homogeneity in the coarser grained material. A grain size investigation[6] of cold worked PCA revealed that if the material is homogeneous, and the heating rate is fast enough, then MC does not precipitate beforehand, and then the grain size is uniform and simply a function of annealing temperature, as it is in ordinary type 316 stainless steel.[7] A final solution treatment of 15 min at 1100°C was selected to give an ASTM grain size of 7 to 8.

In this work, the fabrication sequence was altered in order to produce sheet stock of 0.25 mm (0.010 in.) final thickness and a fine grain size for microstructures A1, A3, B1, B2, and C (A3 however was not produced). A flow diagram is shown in Fig. 3.2.6. Final sheet stock 0.76 mm (0.030 in.) thick of microstructures A3 for SS-1 tensile specimens was produced according to the flow diagram in Fig. 3.2.7. Metallography of fine grained A1, A3, B2, and C are shown in Fig. 3.2.8. Transmission electron microscopy examination of the finer grained materials shows that microstructures are somewhat perturbed compared to the coarse grained PCA. Figure 3.2.9 shows the TEM of the solution annealed material. Clearly some MC precipitation occurs during recrystallization. In some grains, shown in Fig. 3.2.9(a), it appears that recovery occurred before recrystallization and that the precipitation occurred at grain boundaries that subsequently unpin and migrate. Other grains [Fig. 3.2.9(b)] have precipitation that apparently occurred prior to recrystallization. The grain boundaries in A1 have almost no MC precipitate.

Figure 3.2.10 shows the TEM of B1. The intragranular MC precipitate particles have grown compared to A1 in Fig. 3.2.9. Figure 3.2.10(b) and (c) show coarse MC at a grain boundary of B1. The matrix precipitation in fine grained B1 is more uniformly distributed than the clusters of particles found[5] in coarse grained B1.

Fine MC precipitation was also successfully produced in the cold-worked microstructures of fine grained B2 and C. Figure 3.2.11 shows the

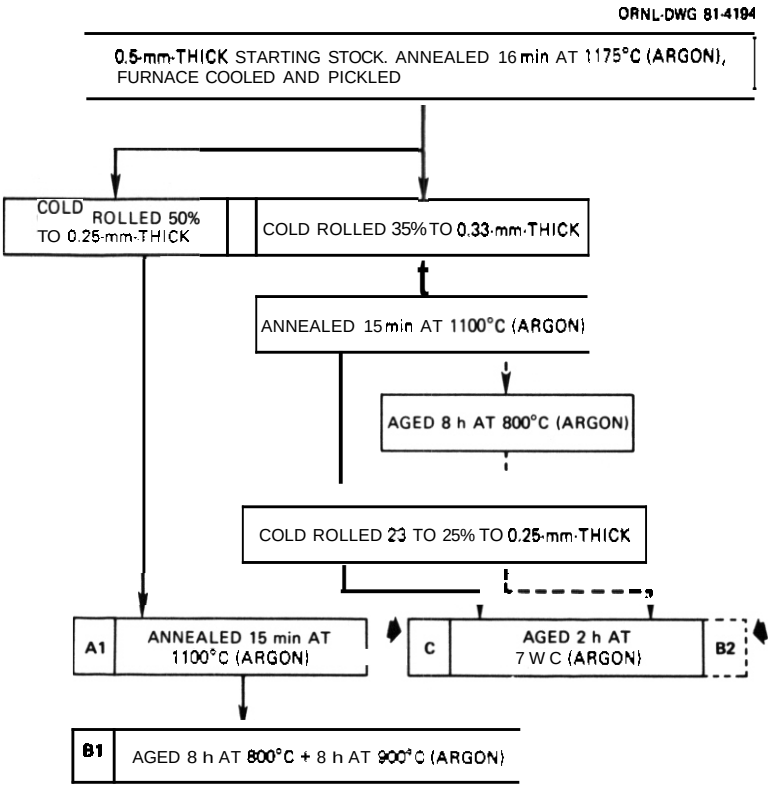

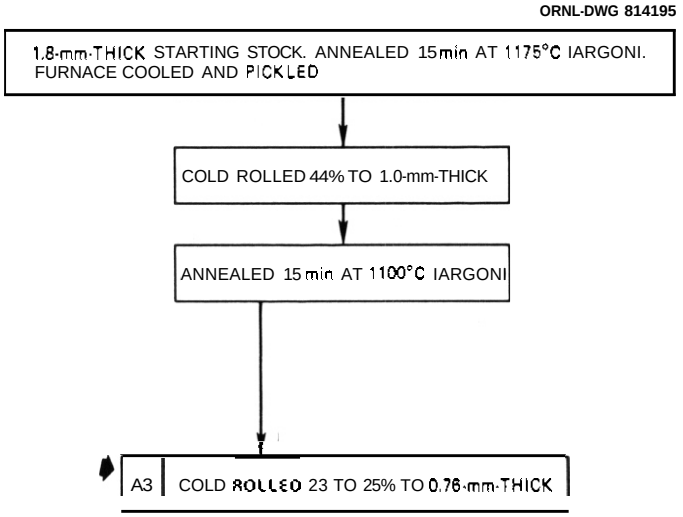

Fig. 3.2.7. Final Processing Steps to Produce Designed Microstructure A3 of the Path A PCA. Number and letter codes refer to the preirradiation microstructures listed in Table 3.2.1. Heavy arrows indicate the points in the sequence at which specimens can be blanked from "hard" material.

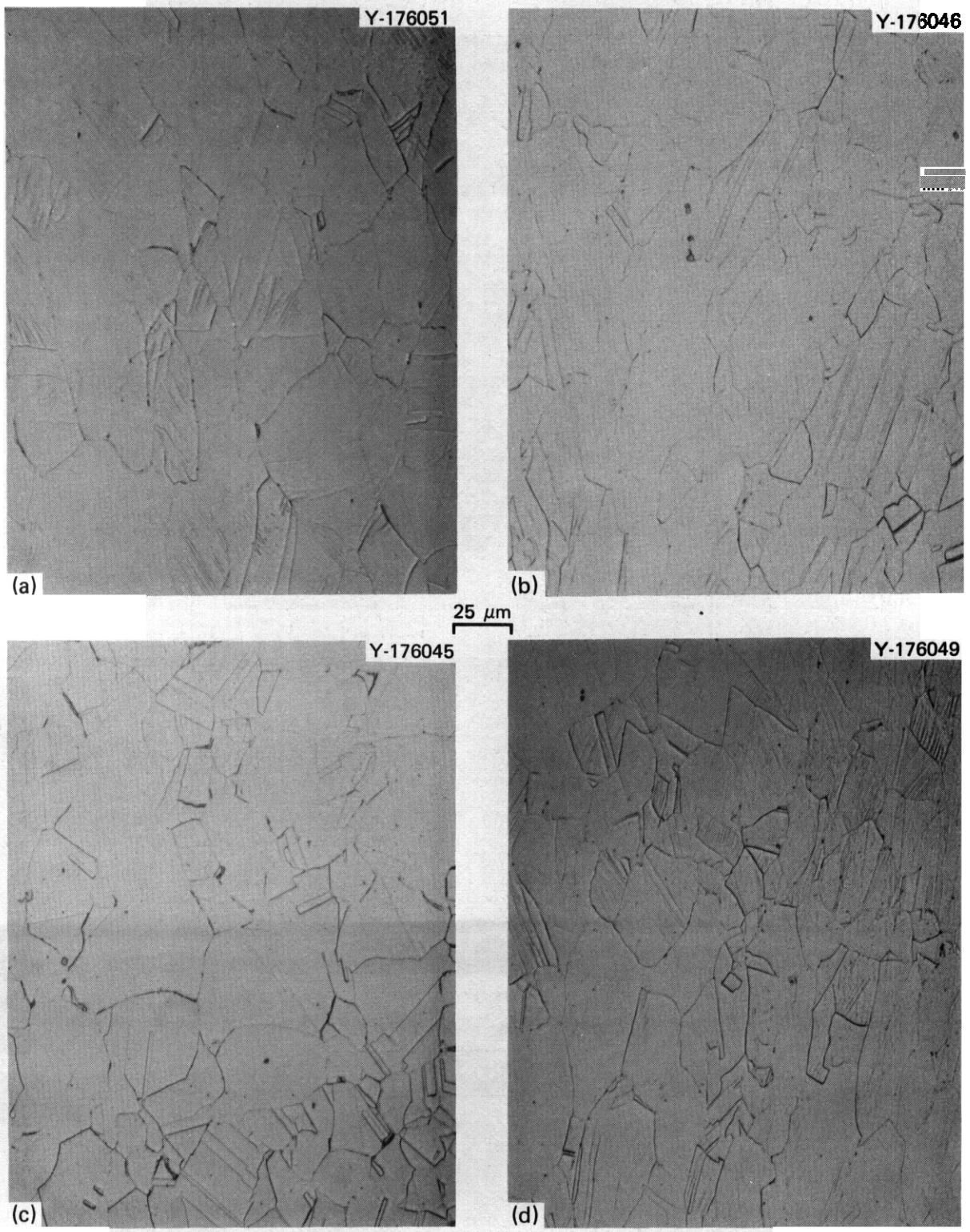

Fig. 3.2.8. Metallography of Fine-Grained PCA of Either 0.76-mm-Thick Sheet (a) or 0.25-mm-Thick Sheet [(b), (c), (d)]. (a) Microstructure A3 — annealed 15 min at 1100°C and cold worked about 25%. (b) Microstructure B2 — annealed 15 min at 1100°C, aged 8 h at 800°C, cold worked about 25%, and aged 2 h at 750°C. (c) Microstructure A1 — annealed 15 min at 1100°C. (d) Microstructure C — annealed 15 min at 1100°C, cold worked about 25%. and aged 2 h at 750°C.

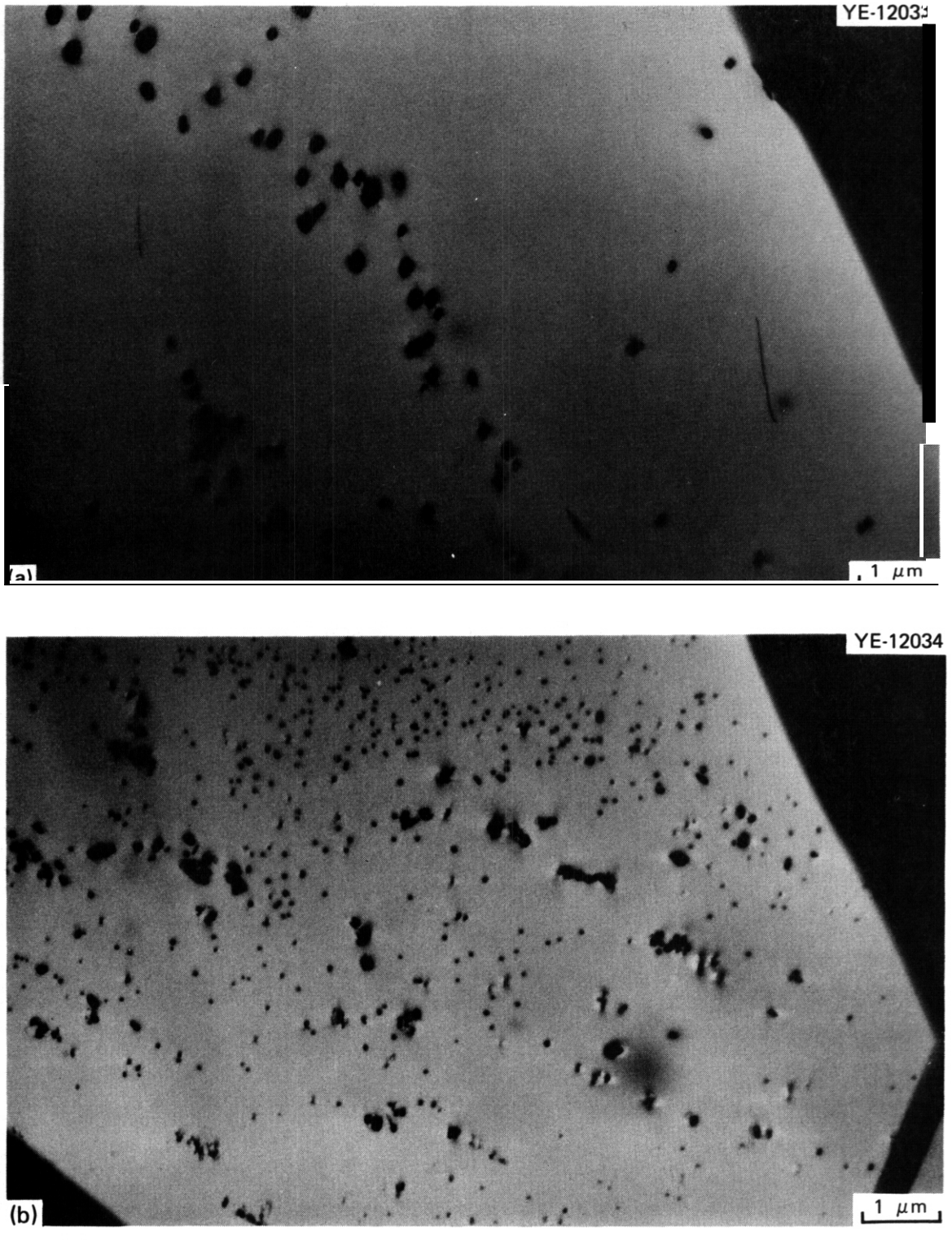

Fig. 3.2.9. Microstructure A1 of Fine-Grained PCA Annealed 15 min at 1100°C. (a) and (b) are TEM of two different areas of grain and grain boundary showing different MC particle distributions.

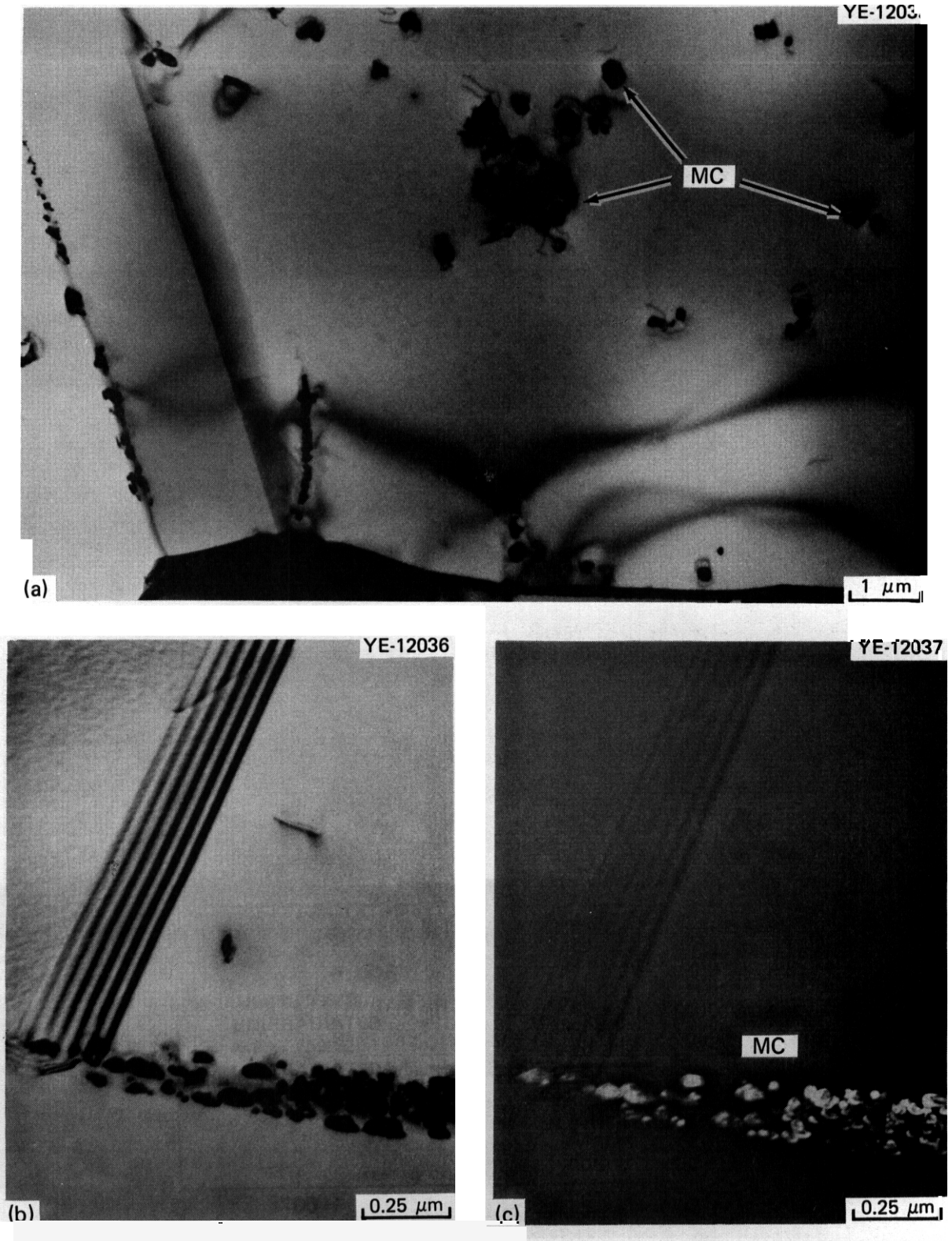

Fig. 3.2.10. Microstructure B1 of Fine-Grained PCA Annealed 15 min at 1100°C then Aged 1 h at 800°C Followed by Aging for 1 h at 900°C. (a) TEM at lower magnification to show matrix carbide dispersion and (b) BF and (c) DF TEM of grain boundaries at higher magnification to show grain boundary MC.

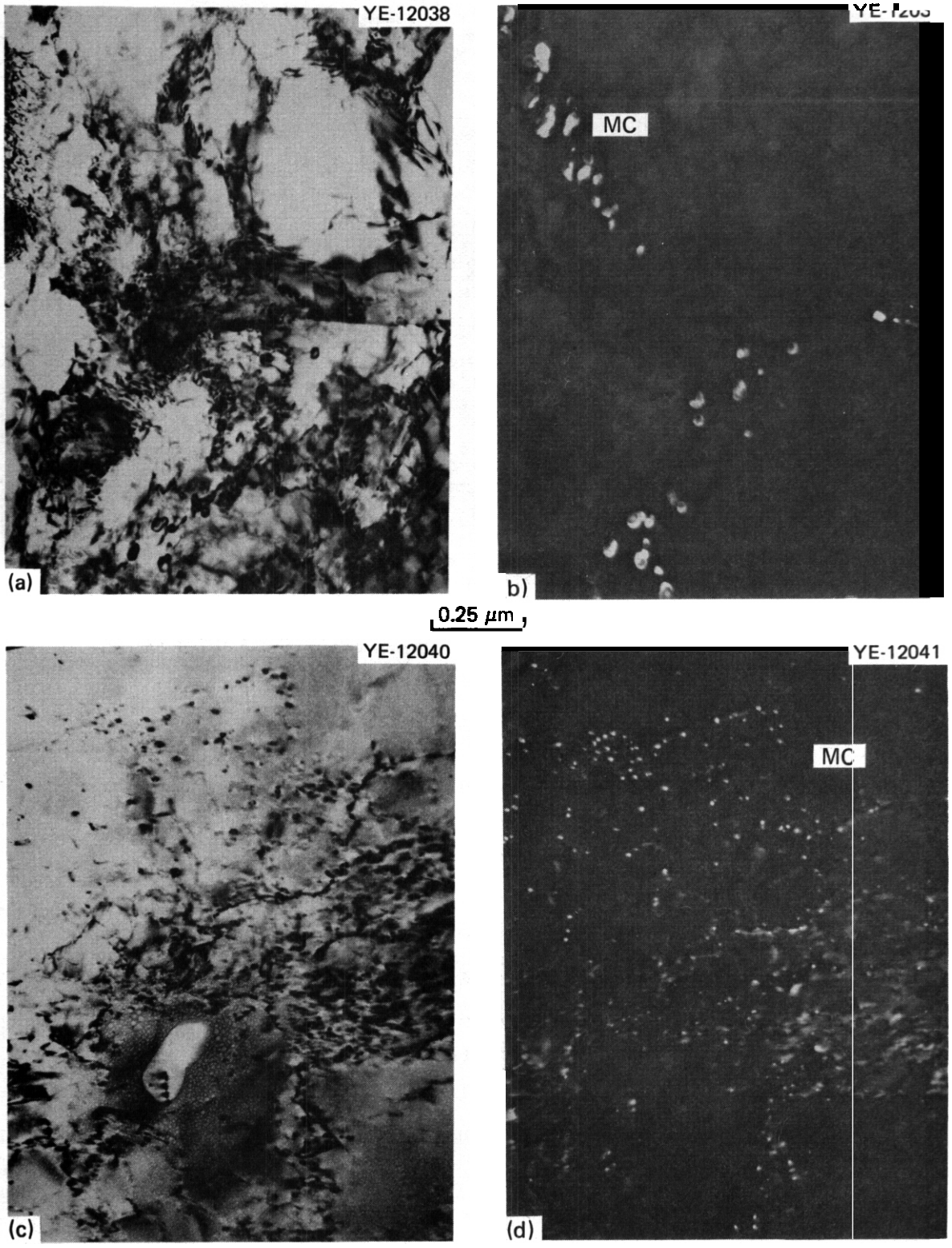

Fig. 3.2.11. Microstructure B2 of Fine-Grained PCA Annealed 15 min at 1100°C, Aged 8 h at 800°C, Cold Worked about 25%, and Aged 2 h at 750°C. (a) BF and (b) DF TEM of MC carbides at the grain boundaries and (c) BF and (d) DF TEM of MC dispersed along dislocations in the matrix.

TEM of the coarse grain boundary and fine matrix MC of microstructure B2. Figure 3.2.12 shows the fine grain boundary and fine matrix MC of microstructure C. Figure 3.2.12(d) clearly shows that fine MC along the cold worked dislocation structure is simply superimposed upon the coarse MC that was produced in the matrix during recrystallization at 1100°C [see Fig. 3.2.9(a)]. The metallography in Fig. 3.2.8 shows that the grain size across the sheet thickness is uniform, so that the post-recrystallization MC does not yield the duplex grain size that results when MC stringers are present. Precipitate stringers apparently result during fabrication from repeated cold work and recrystallization at temperatures that are too low.[1] This work shows that successful microstructural development depends only on preserving homogeneity during the processing until the last few steps. Unprecipitated solution annealed (i.e., the coarse grained PCA) produces the best microstructural results after IMT, but the material is forgiving enough to tolerate some MC precipitation during final solution annealing at lower temperatures and still produce satisfactory microstructures during IMT.

3.2.5 Conclusions and Future Work

This concludes Phase I of Path A PCA alloy development, namely the design and fabrication of preirradiation microstructures. Phase II of the Path A PCA alloy development is the evaluation of the microstructures produced in Phase I. This will include various irradiations, unirradiated and postirradiation mechanical testing, microstructural response, and thermal aging. Reactor experiments to evaluate the response of the various microstructures are already under way in HFIR (HFIR-CTR-30, -31, and -32)[7] and ORR (ORR-MFE-4).[8] The PCA microstructures shown in this work and in other reports[5] serve as the documentation of the preirradiation microstructural condition of these materials. Short-term thermal aging of the PCA after 0, 10, and 25% cold work has already shown the PCA to be more stable than either types 316 stainless steel or 316 + Ti because the grain boundary phase in the PCA is MC whereas the grain boundary phases in 316 or 316 + Ti are tau ($M_{23}C_6$) and eta (M_6C) phases.[9] This is very important because it will allow the mechanism of MC interfacial helium trapping[10] to

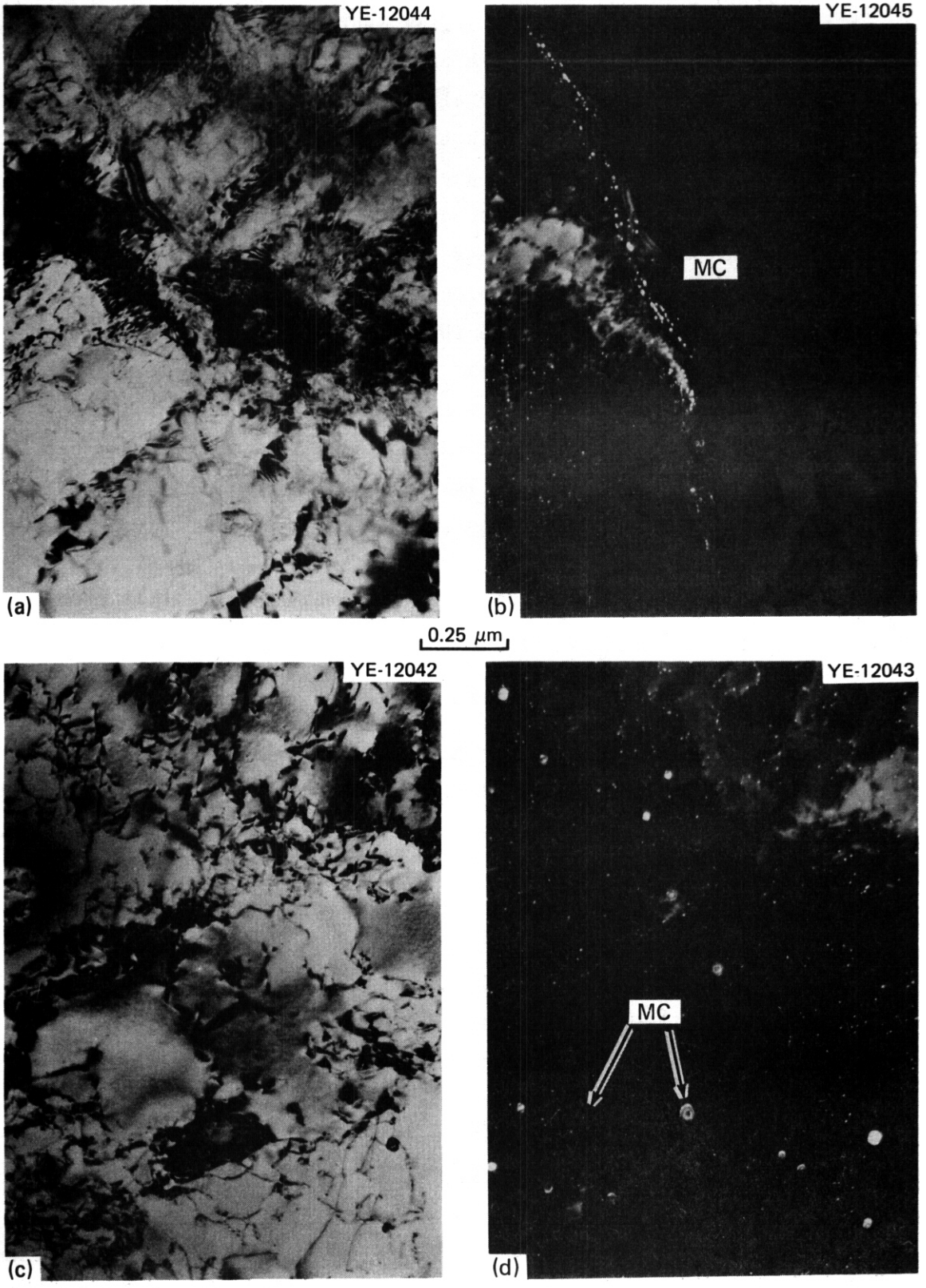

Fig. 3.2.12. Microstructure C of Fine-Grained PCA Annealed 15 min at 1100°C, Cold Worked about 25%, and Aged 2 h at 750°C. (a) BF and (b) DF TEM of MC carbide distribution at the grain boundaries and (c) BF ana (d) DF TEM of fine MC dispersed along dislocations in the matrix.

be effective in the grain boundaries where it is needed most. Stability of MC is an important question to address because helium appears to aid MC formation at lower temperatures, judged from comparison of the results of HFIR and EBR-II irradiation[11,12] and of different He/dpa ratios during dual beam ion irradiation.[13] If MC becomes unstable, the helium trapping mechanism may not work.

Phase III of Path A alloy development will be systematic variation of the composition of the PCA, based on the results of Phase II.

3.2.6 References

1. P. J. Maziasz and T. K. Roche, "Microstructural Characterization of As-Received Prime Candidate Alloy and Examination of Microstructural Sensitivity to Fabrication and Processing Variables," *ADIP Quart. Prog. Rep. Mar. 31, 1979,* DOE/ET-0058/5, pp. 36-52.
2. P. J. Maziasz and T. K. Roche, "Fabrication of Homogeneous Path A Prime Candidate Alloy;" *ADIP Quart. Prog. Rep. Sept. 30, 1979,* DOE/ET-0058/7, pp. 83–102.
3. P. J. Maziasz, "Microstructural Design for Fusion First-Wall Applications and Recommendations for Thermal-Mechanical Preirradiation Treatments," *ADIP Quart. Prog. Rep. June 30, 1979,* DOE/ET-0058/6, pp. 48–56.
4. P. J. Maziasz, B. L. Cox, T. K. Roche, and E. E. Bloom, "Time-Temperature-Precipitation Curve Determination of the Path A Prime Candidate Alloy for Microstructural Design,'' *ADIP Quart. Prog. Rep. Sept. 30, 1979,* DOE/ET-0058/7, pp. 103–27.
5. P. J. Maziasz, T. K. Roche, B. L. Cox, and E. E. Bloom, "Design and Fabrication of Preirradiation Microstructure in Path A Prime Candidate Alloy," *ADIP Quart. Prog. Rep. Mar. 31, 1980,* DOE/ER-0045/2, pp. 20–32.
6. T. K. Roche and P. J. Maziasz, "The Effect of Annealing Temperature on the Grain Size of the Path A Prime Candidate Alloy," *ADIP Quart. Prog. Rep. Sept. 30, 1980,* DOE/ER-0045/4, pp. 73–78.
7. M. L. Grossbeck, J. W. Woods, and G. A. Potter, "Experiments HFIR-CTR-30, -31, and -32 for Irradiation of Transmission Electron Microscopy Disk Specimens," *ADIP Quart. Prog. Rep. Sept. 30, 1980,* DOE/ER-0045/4, pp. 36–44.

8. M. L. Grossbeck and K. R. Thoms, "ORR-MFE-4: A Spectral Tailoring Experiment to Simulate the He/dpa Ratio of a Fusion Reactor in Austenitic Stainless Steel," *ADIP Quart. Prog. Rep. June 30, 1380,* DOE/ER-0045/3, pp. 10–23.

9. P. J. Maziasz, "Composition and Microstructure of Precipitate Phases in Austenitic Stainless Steel," *ADIP Quart. Prog. Rep. June 30, 1380,* DOE/ER-0045/3, pp. 75–129.

10. P. J. Maziasz, "Helium Trapping at Ti-Rich MC Particles in Ti-Modified Austenitic Stainless Steel," paper presented at the Metallurgical Society of AIME Fall Meeting, Pittsburg, October 5–9, 1980, paper to be published in the proceedings.

11. P. J. Maziasz, J. A. Horak, and B. L. Cox, "The Influence of Both Helium and Neutron Irradiation on Precipitation in *20%* Cold-Worked Austenitic Stainless Steel," paper presented at the Metallurgical Society of AIME Fall Meeting, Pittsburg, October 5–9, 1980, paper to be published in the proceedings.

12. E. H. Lee, P. J. Maziasz, and A. F. Rowcliffe, "The Structure and Composition of Phases Occurring in Austenitic Stainless Steels in Thermal and Irradiation Environments," paper presented at the Metallurgical Society of AIME Fall Meeting, Pittsburg, October 5–9, 1980, paper to be published in the proceedings.

13. S. Wood, J. A. Spitznagel, and W. J. Choyke, "Irradiation Response of Materials," to be published in *DAFS Quart. Prog. Rep. Sept. 30, 1980,* DOE/ET-0065/11, p. 143.

3.3 SWELLING AND MICROSTRUCTURE OF HFIR-IRRADIATED 20%-COLD-WORKED TYPES 316 STAINLESS STEEL AND 316 + 0.23 wt % Ti – P. J. Maziasz and M. L. Grossbeck

3.3.1 ADIP Tasks

ADIP Tasks I.C.l, Microstructural Stability, and I.C.2, Microstructure and Swelling in Austenitic Alloys.

3.3.2 Objective

The objective of this work is to characterize the microstructure of standard type 316 stainless steel and titanium-modified type 316 stainless steel after High Flux Isotope Reactor (HFIR) irradiation to determine swelling, microstructure development, and mechanical properties correlation. Together these will reveal some of the principles governing microstructural evolution during neutron irradiation with a high continuous helium generation rate. The immediate objective is to present the microstructural, immersion-density, and cavity swelling data and to compare the behavior of 20%-cold-worked type 316 stainless steel (CW 316) and titanium-modified type 316 stainless steel (CW 316 + Ti).

3.3.3 Summary

Swelling and microstructural results were obtained for CW 316 and CW 316 + Ti after HFIR irradiation at temperatures of 55 to 670°C and to neutron fluences producing 7.7 to 10.8 dpa and 380 to 520 at. ppm He. Cavities and swelling were observed at 285°C and above in CW 316. No cavities could be detected (for $d > 2$ nm) at 55°C. The swelling in all cases is below 0.5%. Within this limit there is considerable temperature dependence of the microstructure. Swelling in CW 316 is maximum at 285°C and minimum at about 450 to 550°C. The cavities are equilibrium bubbles at 375°C and above, but appear to be voidlike at 285°C. Grain-boundary cavities are visible between 475 and 565°C and contribute to swelling at 565°C and above. Immersion density measurements confirm the temperature dependence of the cavity volume fraction swelling but the magnitude is lower, probably reflecting densification. Both measurements indicate less swelling in the CW 316 + Ti at most temperatures. The

MC interfacial helium trapping reduces the swelling at 375°C and above. Trapping by MC precipitate particles results in more smaller cavities and less swelling. We conclude that the helium has a strong effect on microstructural evolution for these irradiation conditions.

3.3.4 Progress and Status

3.3.4.1 Introduction

While it is well established that helium in metals can affect the mechanical properties and can influence the microstructural evolution during irradiation; verified models to predict exact effects are not yet available. This becomes especially important for stainless steel for service in fusion reactors, where approximately 150 at. ppm He and 12 dpa will be produced per 1 MWyr/m^2 of operation. Neither the data to judge the effects of this service nor the facilities to exactly simulate the service are available. The effect of this irradiation must then be studied using facilities that provide partial simulation of the fusion environment. In evaluating fusion reactor materials performance, HFIR irradiation is useful because the displacement damage is accompanied by a high continuous helium generation rate during irradiation. The displacement rate is equivalent to that projected for a first-wall neutron loading of 3.5 MWyr/m^2. The helium-to-displacement ratio is very close to that of a fusion environment up to about 3 to 4 dpa and then diverges nonlinearly with increasing fluence.

The immersion density and cavity swelling of CW 316 and CW 316 + Ti irradiated in HFIR at 55 to 670°C to fluences producing 7.7 to 10 dpa and 380 to 500 at. ppm He are reported and the two alloys are compared.

3.3.4.2 Experimental Details

The compositions of the two steels, CW 316 and CW 316 + Ti, are given in Table 3.3.1. The details of specimen preparation have been presented previously.[1,2] Experiments HFIR-CTR-9 to -13 and -16 were irradiated in equivalent peripheral target positions (PTPs) of HFIR; HFIR-CTR-16 was

Table 3.3.1. Composition of Two Cold-Worked Austenitic Stainless Steels

Alloy	Content,[a] wt %										
	Cr	Ni	Mo	Mn	C	Ti	Si	P	S	N	B
316	18.0	13.0	2.58	1.90	0.05	0.05	0.80	0.013	0.016	0.05	0.0005
316 + Ti	17.0	12.0	2.50	0.5	0.06	0.23	0.40	0.01	0.013	0.0055	0.0007

[a]Balance iron.

irradiated at the reactor coolant water temperature (~55°C). Elevated temperatures in HFIR-CTR-9 through -13 were achieved by insulating the specimens with a helium gas gap. The axial temperature calculated for an irradiation temperature of 600°C is shown in Fig. 3.3.1. This distribution is typical for all specimens in HFIR-CTR-9 through -13. The even temperature distribution in the shoulders of the tensile specimens allowed us to tensile test the specimens and still obtain as-irradiated microstructural information (including dislocation distributions) from transmission electron microscope (TEM) disks cut from the specimen shoulder region.

The production of helium during the irradiation of type 316 stainless steel is shown as a function of displacement damage in Fig. 3.3.2. The irradiation parameters are compared for three cases: HFIR, the first wall of a fusion reactor, and EBR-II. Irradiation in HFIR tracks the projected behavior for fusion for low fluences, up to about 3 dpa, and then diverges to higher helium production levels. (Helium production in a fusion reactor and EBR-II is mainly from single step (n,α) reactions involving energetic neutrons; in HFIR the helium is mainly from a two step reaction between thermal energy neutrons and ^{58}Ni. As a result the helium-to-displacement ratio is constant for EBR-II or fusion, but is nonlinear for HFIR.) The irradiation parameters achieved in experiments HFIR-CTR-9 through -13 are outlined in Fig. 3.3.2.

Disks cut from tested tensile samples were thinned via a standard two step electropolishing procedure. Instruments used for TEM examination

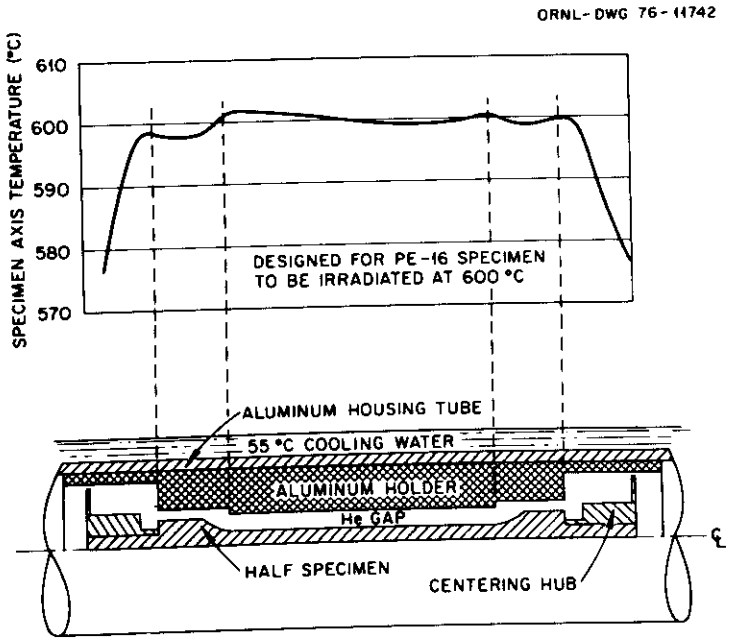

Fig. 3.3.1. Typical Axial Temperature Distributions for a Specimen in the Experiments HFIR-CTR-9 Through -13. Note that the irradiation temperature remains nearly constant across the full specimen, including the grip ends.

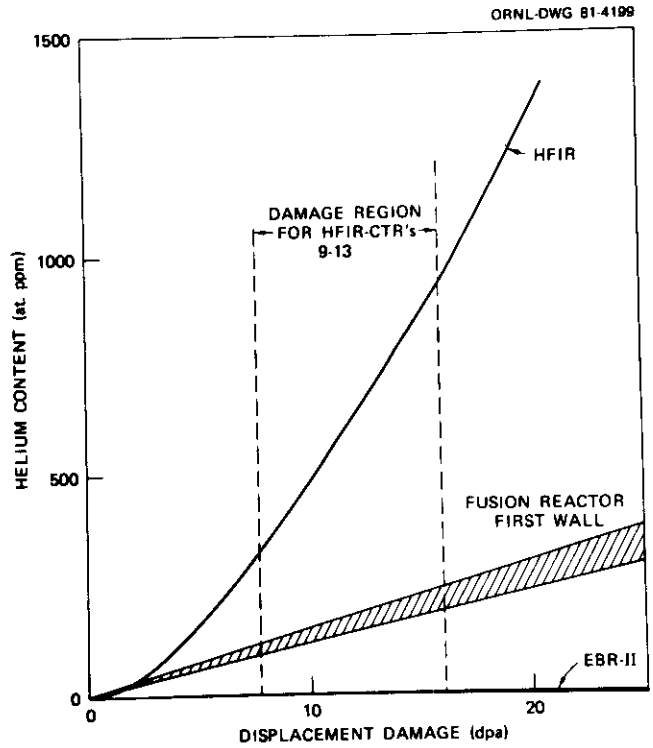

Fig. 3.3.2. Helium Generation During Irradiation as a Function of Displacement Damage for Stainless Steel in HFIR, EBR-II, and a Fusion Reactor First Wall. The damage parameters achieved in experiments HFIR-CTR-9 through -13 are indicated.

included a conventional JEM 100 C and two analytical electron microscopes (AEM) the JEM 100 CX and Phillips EM-400. Foil thicknesses were measured from thickness fringes to obtain the wedge angle using diffracting vectors g_{111} OK g_{200} with $s = 0$ (refs. 3, 4). Values of extinction distance (ξg) were obtained from Muir[5] and Barton et al.[3] This technique is more accurate than thickness measurement by stereo technique. Cavities were imaged in the underfocused condition with weak excitation of low order g for maximum detectability. In some cases multiple disks from the same specimen were examined to evaluate homogeneity of microstructure and reproducibility of the results. These precautions enabled accurate determination of the small values of cavity volume fraction swelling and systematic comparison among samples. Grain boundary cavity swelling was determined by measuring the grain size and computing the area of grain boundary per unit volume of sample, using standard metallographic procedures.[6,7] The cavity volume fraction per unit area of grain boundary was obtained from TEN. The product of the two numbers give the grain boundary component of swelling.

3.3.4.3 Results

The swelling results and cavity statistics for CW 316 and CW 316 + Ti irradiated at 7.7 to 10.8 dpa and 380 to 520 at. ppm He are given in Table 3.3.2. Swelling and cavity statistics for CW 316 irradiated at 40 to 60 dpa from previous experiments' are given in Table 3.3.3 for comparison.

3.3.4.3.1 Temperature Dependence of Microstructural Development in CW 316. Intragranular microstructures for samples of CW 316 irradiated at 55 to 565°C are shown, in cavity contrast, in Figs. 3.3.3 through 3.3.5. Grain-boundary swelling is shown in Fig. 3.3.6 to begin between 475 and 565°C. It correlates with the absence of grain boundary precipitation at 565°C. The total cavity volume fraction swelling is shown as a function of temperature in Fig. 3.3.7, along with the immersion density swelling results. Figures 3.3.3 to 3.3.7 reveal some surprising features. There is considerable microstructural development at all temperatures at these low fluences with cavity formation at 285°C and above. The higher

Table 3.3.2. Swelling and Cavity Statistics for Cold-Worked Stainless Steels Irradiated in HFIR

Irradiation Conditions				Swelling from Immersion Density (%)	Cavity Parameters					
					Matrix Cavities			Grain-Boundary Cavities		Total Cavity Volume Fraction (%)
Temperature (°C)	Neutron Fluence, >0.1 MeV (neutrons/m^2)	Displacement Damage (dpa)	Helium (at. ppm)		Average Diameter (nm)	Concentration (cavities/m^3)	Volume Fraction (%)	Average Diameter (nm)	Volume Fraction (%)	
				20%-Cold-Worked Type 316 Stainless Steel						
55	1.4×10^{26}	10.8	520	−0.03		[a]	0		[a]	0
285	1.0	7.7	390	0.04	12	4×10^{21}	0.46		[a]	0.46
375	1.1	8.5	380	0	2.7 7.6[b]	2×10^{22} 2×10^{21}	0.12		[c]	0.12
475	1.3	10.0	500	−0.1	7	2.6×10^{21}	0.06 ± 0.01[d]		[c]	0.06
565	1.2	9.2	440	0.1	11	5.6×10^{20}	0.04	~35	0.02	0.06
				20%-Cold-Worked Titanium-Modified Type 316 Stainless Steel						
55	1.3	10.5	490			[a]	0		[a]	0
285	1.0	7.7	390	0.17	2.9	2.7×10^{23}	0.36		[a]	0.36
375	1.1	8.5	380	−0.13	3.1	4.6×10^{22}	0.08		[a]	0.08
475	1.3	10.0	500	−0.14	2.2	3.0×10^{22}	0.02		[c]	0.02
565	1.2	9.2	440	−0.14	3.7	5.0×10^{21}	0.02	~18	~0.01	0.03
620	1.3	10.0	500	0.02	5.5	2.0×10^{21}	0.03			0.03
670	1.3	10.0	500	0.18	22.5	1.7×10^{20}	0.09			0.09

[a] None detected.

[b] Bimodal size distribution.

[c] Grain boundary precipitation of eta (M_6C) phase.

[d] Two separate disks with three areas analyzed in one disk and two areas analyzed in the other to show the area-to-area variation in swelling.

Table 3.3.3. Swelling and Cavity Statistics for Cold-Worked Type 316 Stainless Steel Irradiated to High Fluences in HFIR

Irradiation Conditions				Swelling from Immersion Density (%)	Cavity Parameters					
					Matrix Cavities			Grain-Boundary Cavities		
Temperature (°C)	Neutron Fluence, >0.1 MeV (neutrons/m^2)	Displacement Damage (dpa)	Helium (at. ppm)		Average Diameter (nm)	Concentration (cavities/m^3)	Volume Fraction (%)	Average Diameter (nm)	Volume Fraction (%)	Total Cavity Volume Fraction (%)
380	7.05×10^{26}	49	3320	1.6	9.5 111[a]	1.8×10^{22} 4.5×10^{18}	2.2 ± 0.4	[b]		2.2
460	7.69	54	3660	0.8	17	6.6×10^{21}	2.0 ± 0.4			2.0
550	6.18	42	2990	0.0	21	2.4×10^{21}	1.4 ± 0.1	40	0.03	1.4
600[c]	8.71	60	4070	3.3	65	3.3×10^{20}	3.0 ± 0.5	350	0.4	3.4
680[d]	8.74	61	4140	16.8	110	6.5×10^{19}	6.0 ± 2.5	710	2.0	8.0

[a] Bimodal size distribution, large cavities exclusively associated with eta (M_6C) phase particles.

[b] Grain boundary precipitation of eta phase.

[c] Completely recrystallized fine grains.

[d] Completely recrystallized coarse grains.

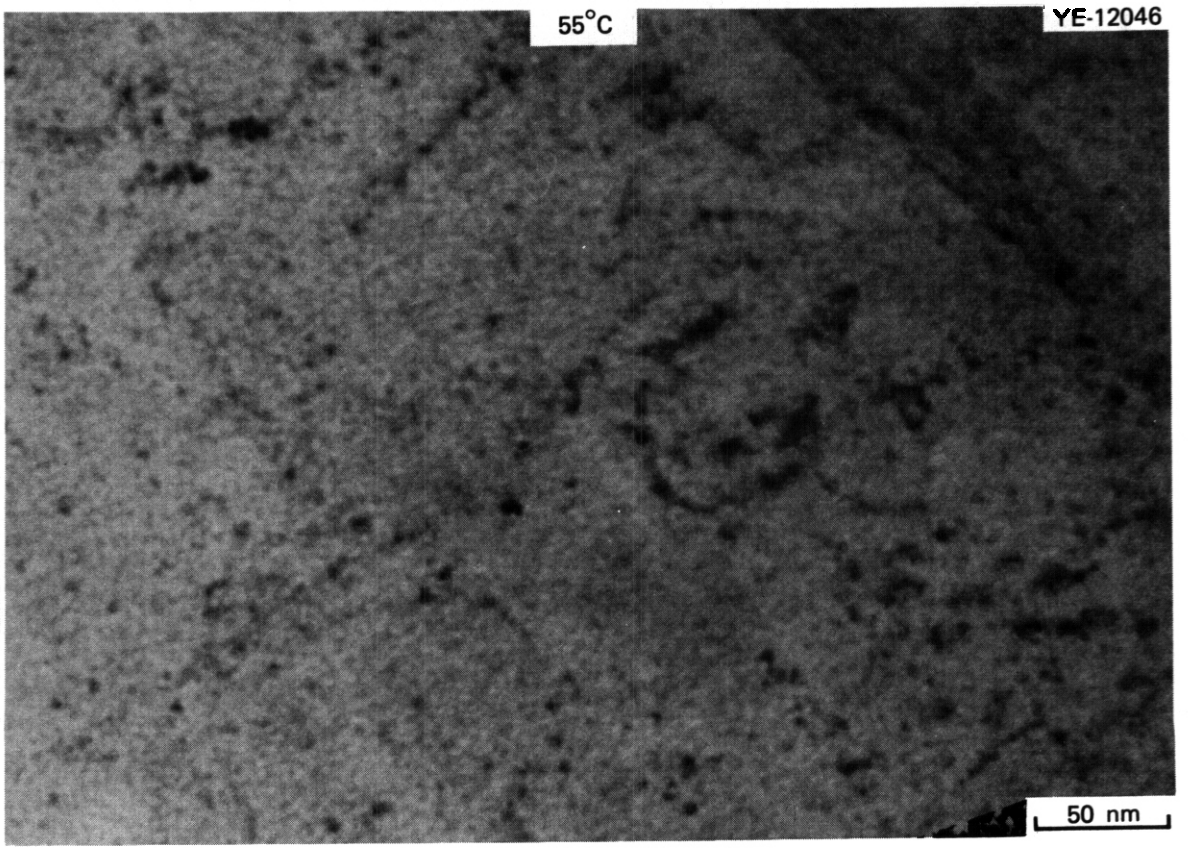

Fig. 3.3.3. Microstructure of CW 316 Irradiated in HFIR at 55°C to 10.8 dpa and 520 at. ppm He. Some small, light features are evident but a high magnification through-focus-series could not confirm these as cavities and they may be artifacts.

fluence swelling results listed in Table 3.3.3 are shown in Fig. 3.3.8 for comparison with Fig. 3.3.7. The temperature dependence of swelling is similar for both fluence ranges, with an apparent minimum at 450 to 550°C and significant grain-boundary swelling at 550 to 565°C and above. The swelling at 7.7 to 10.8 dpa (Fig. 3.3.7) is low, less than 0.1% at most temperatures. Another surprise is the apparent swelling maximum at 285°C or below indicated by this data set. The immersion density change parallels the cavity volume swelling (Fig. 3.3.7), with an offset that indicates a component of densification. This may result from the considerable precipitation at 375°C and above (see Fig. 3.3.5 and ref. 9). However, there is no precipitation at 55 or 285°C to produce densification.

We can better understand the total swelling behavior by considering the cavity size and cavity concentrations. These parameters are shown a8

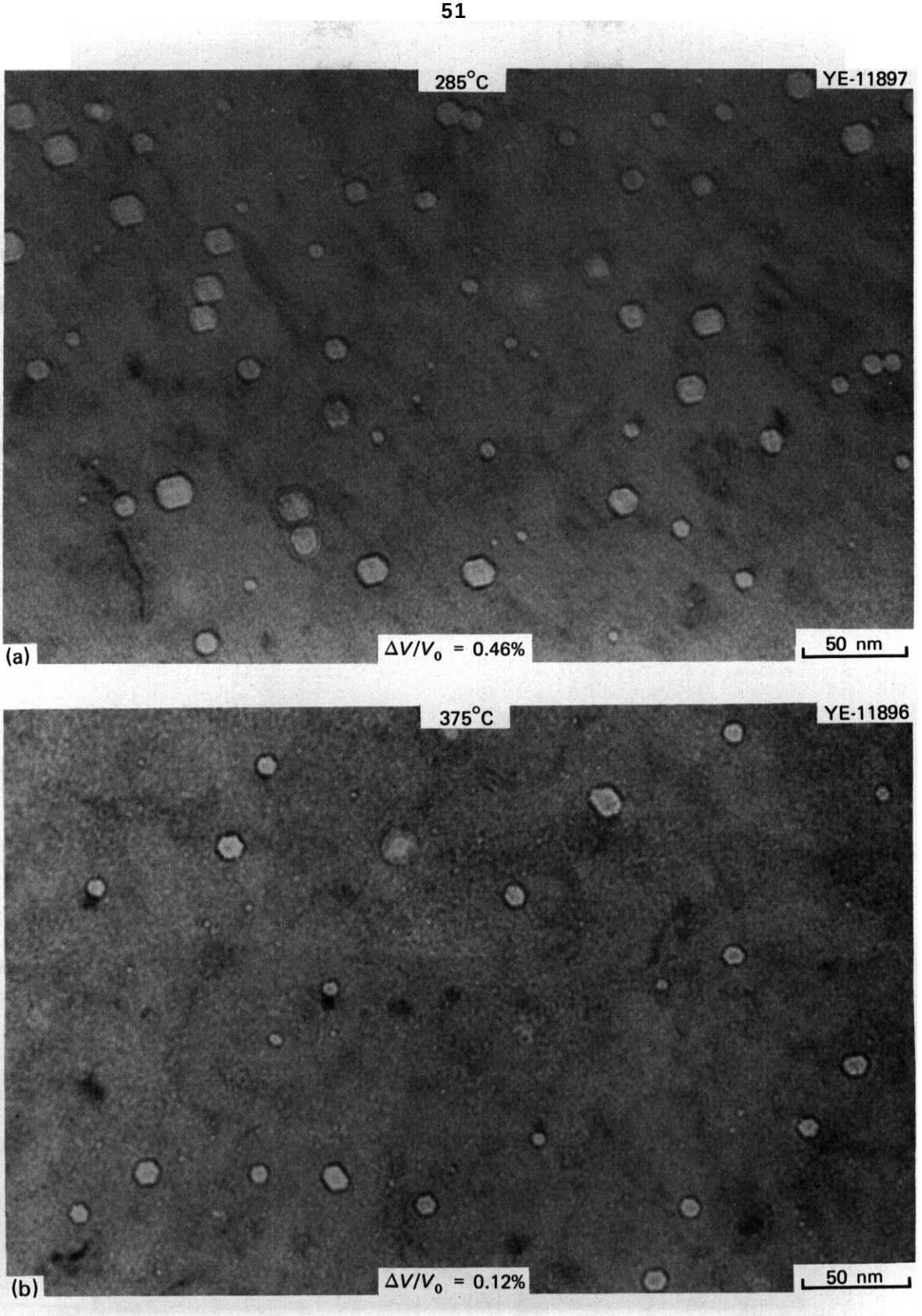

Fig. 3.3.4. Microstructures of CW 316 Irradiated in HFIR at (a) 285°C to 7.7 dpa and 390 at. ppm He and (b) 375°C to 8.5 dpa and 380 at. ppm He. Note the bimodal distribution at 375°C (b) and the apparent lack of small cavities at 285°C (a).

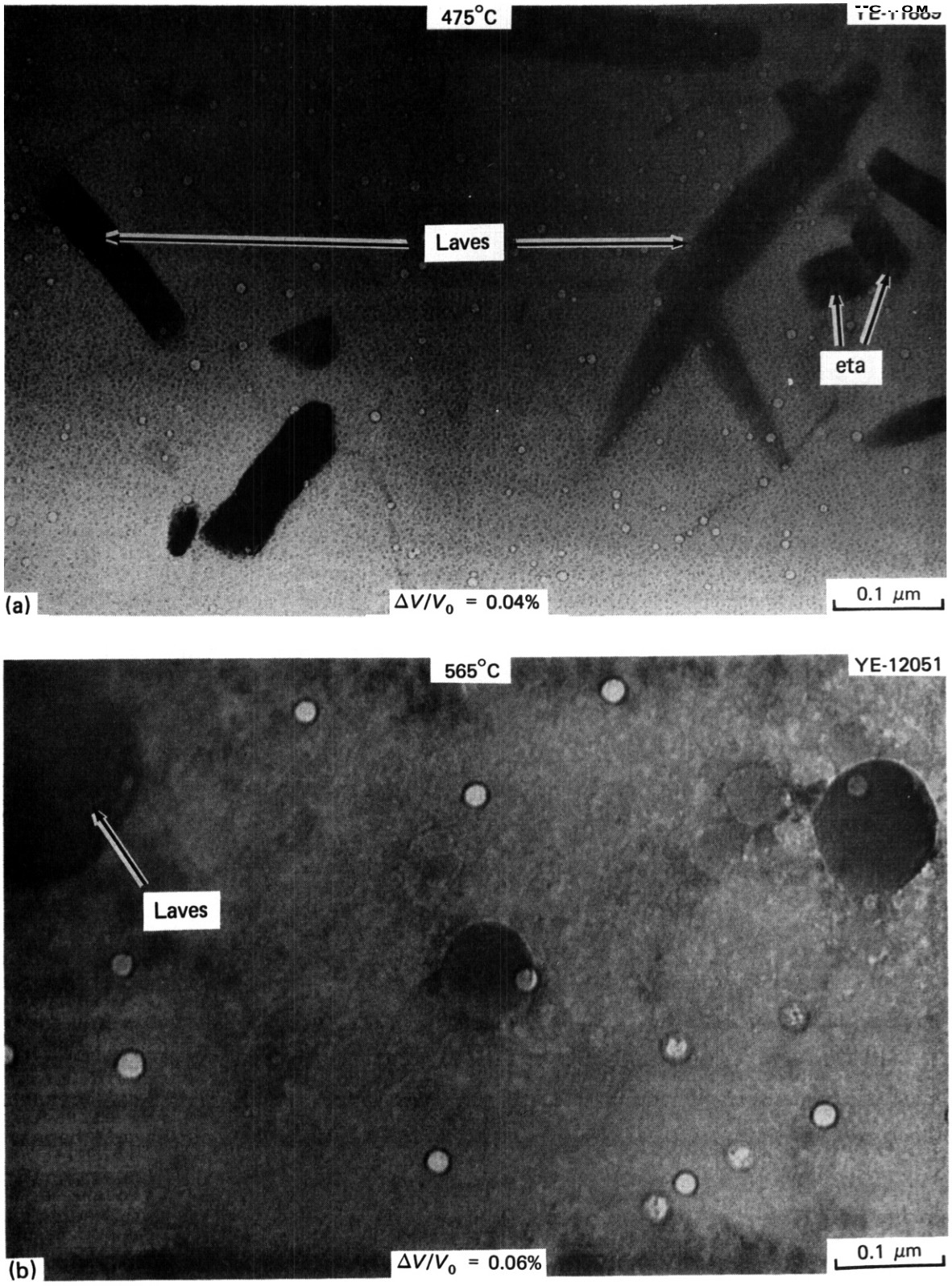

Fig. 3.3.5. Microstructures of CW 316 Irradiated in HFIR at (a) 475°C to 10 dpa and 500 at. ppm He and (b) 565°C to 9.2 dpa and 440 at. ppm He.

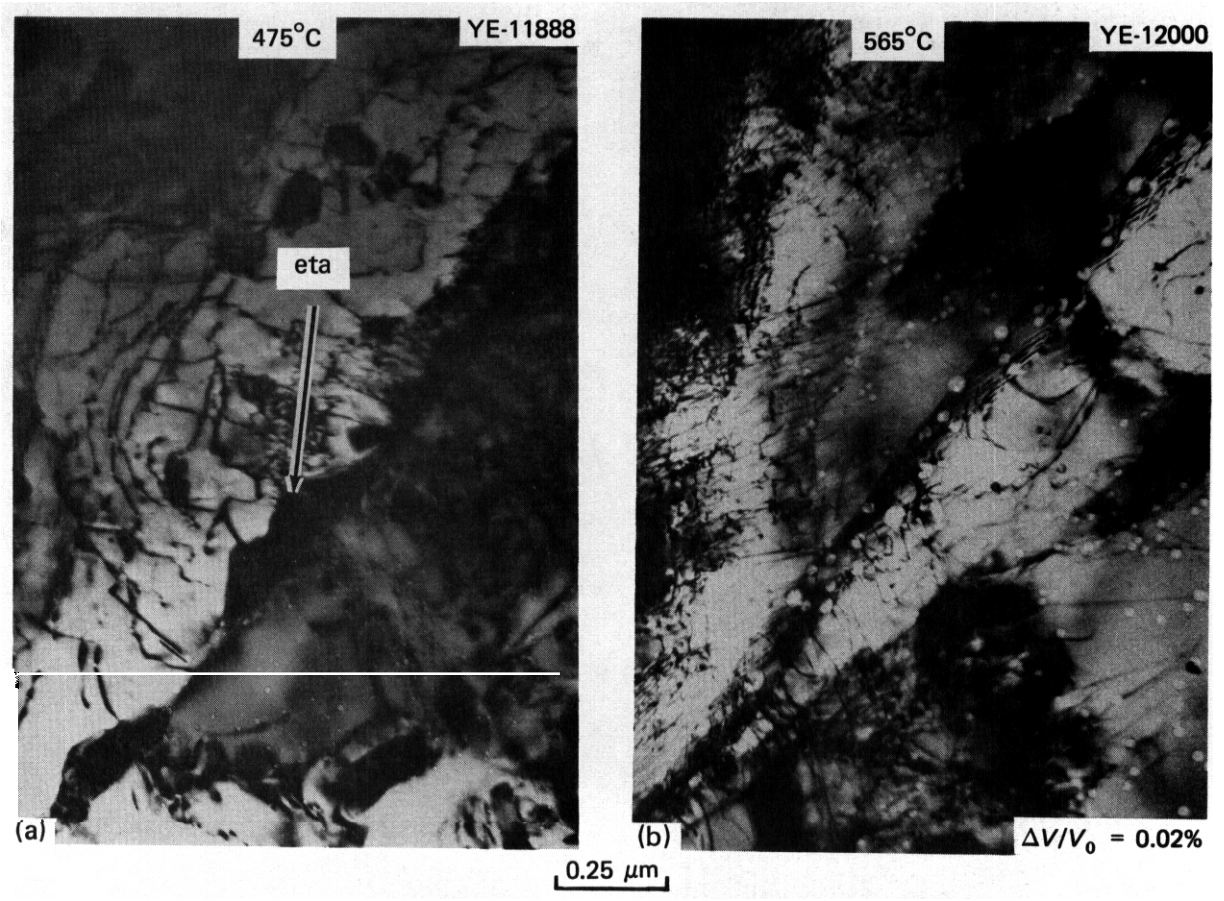

Fig. 3.3.6. Microstructures Including Grain Boundaries for CW 316 Irradiated in HFIR at (a) 475°C to 10 dpa and 500 at. ppm He and (b) 565°C to 9.2 dpa and 440 at. ppm He. Note grain-boundary eta phase in (a) and grain-boundary cavities in (b). The grain boundary cavities in (b) contribute 0.02% to the total calculated swelling of 0.06%.

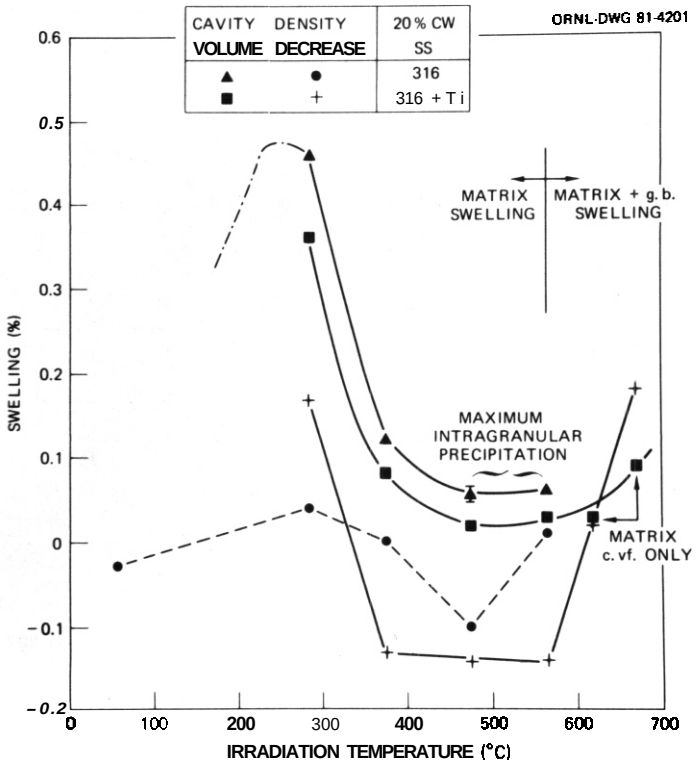

Fig. 3.3.7. Swelling from Cavity Volume Fraction and Immersion Density Changes as a Function of Temperature for CW 316 and CW 316 + Ti. The beginning of grain boundary cavity formation and the temperatures of maximum precipitation (in CW 316) are noted.

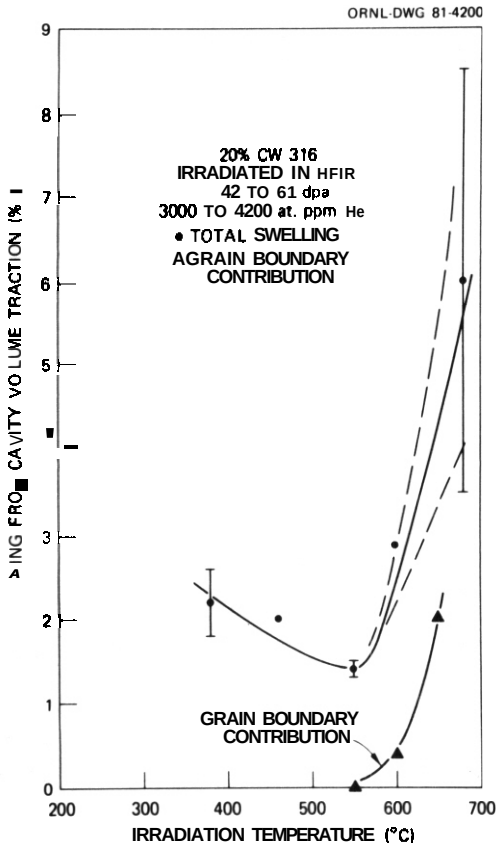

Fig. 3.3.8. Swelling from Cavity Volume Fraction as a Function of Temperature for CW 316 Irradiated in HFIR at the Conditions Indicated Above. The grain-boundary cavity contribution to swelling is also shown.

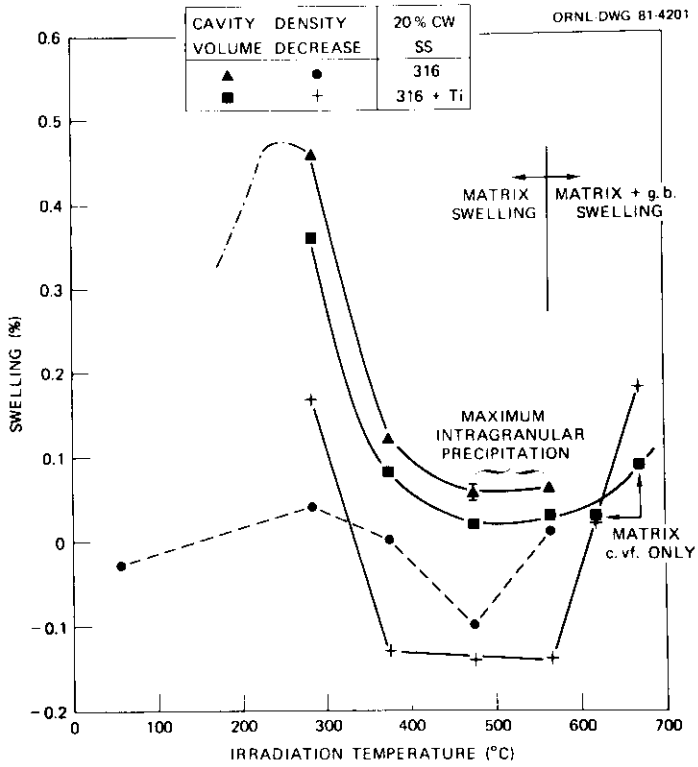

Fig. 3.3.7. Swelling from Cavity Volume Fraction and Immersion Density Changes as a Function of Temperature for CW 316 and CW 316 + Ti. The beginning of grain boundary cavity formation and the temperatures of maximum precipitation (in CW 316) are noted.

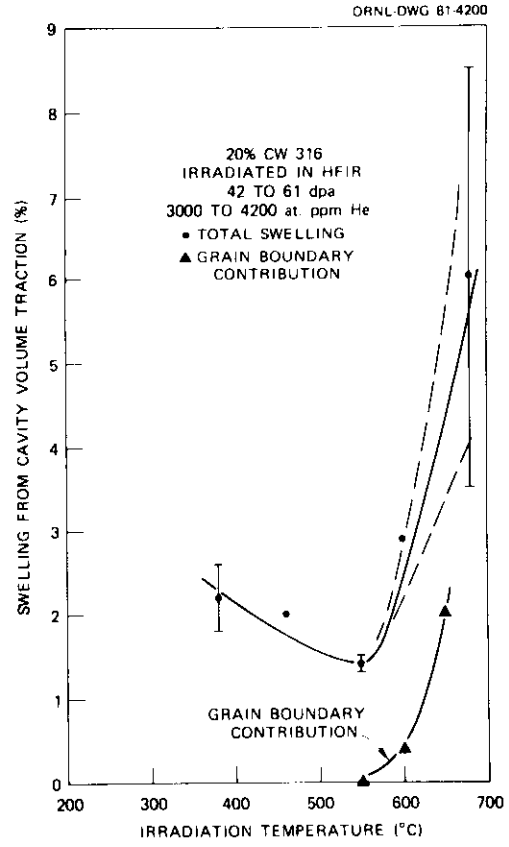

Fig. 3.3.8. Swelling from Cavity Volume Fraction as a Function of Temperature for CW 316 Irradiated in HFIR at the Conditions Indicated Above. The grain-boundary cavity contribution to swelling is also shown.

functions of irradiation temperature in Figs. 3.3.9 and 3.3.10, respectively. The cavity size appears to be well-behaved as a function of temperature above 375°C [see also Figs. 3.3.4(b) and 3.3.5]. However, the cavity size Increases with decreasing temperature from 375 to 285°C was unexpected. Figure 3.3.4(b) shows a bimodal size distribution for the cavities at 375°C and apparently the larger sized mode is favored as the temperature decreases, with very few small cavities observed [compare Fig. 3.3.4(a) and (b)]. The cavity concentration decreases with increasing temperature except for the discontinuity at 375°C, again due to the bimodal cavity distribution. The increase in low temperature swelling thus results because both cavity size and cavity concentration increase in going from 375 to 285°C. We cannot explain why the large size mode is favored as temperature decreases. The microstructure for irradiation at 55°C (Fig. 3.3.3) does not indicate any cavity swelling so the low temperature swelling maximum must be between 55 and 285°C.

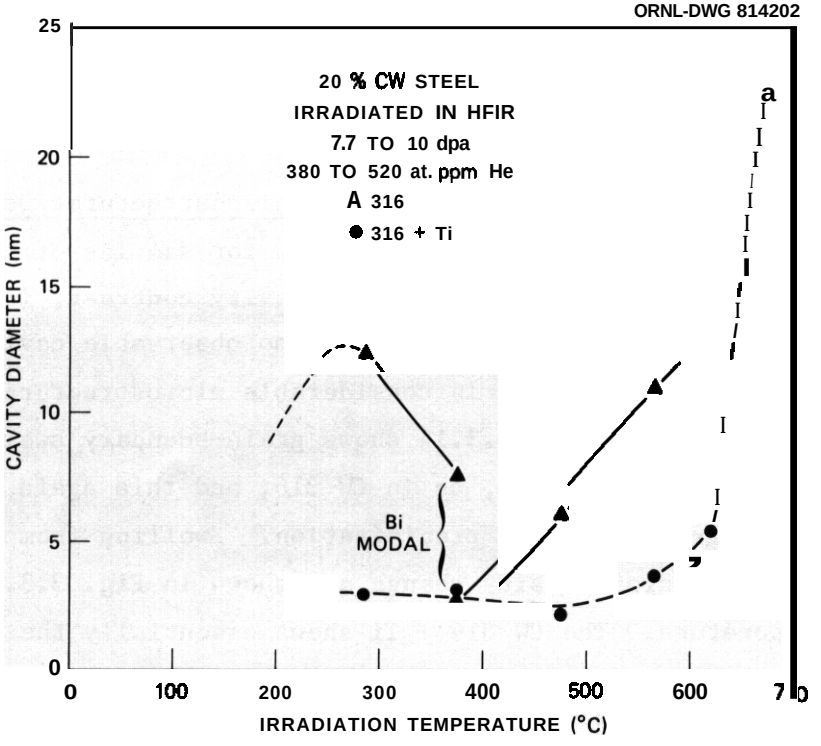

Fig. 3.3.9. Cavity Diameter as a Function of Irradiation Temperature for CW 316 and CW 316 + Ti Irradiated in HFIR to the Conditions Indicated.

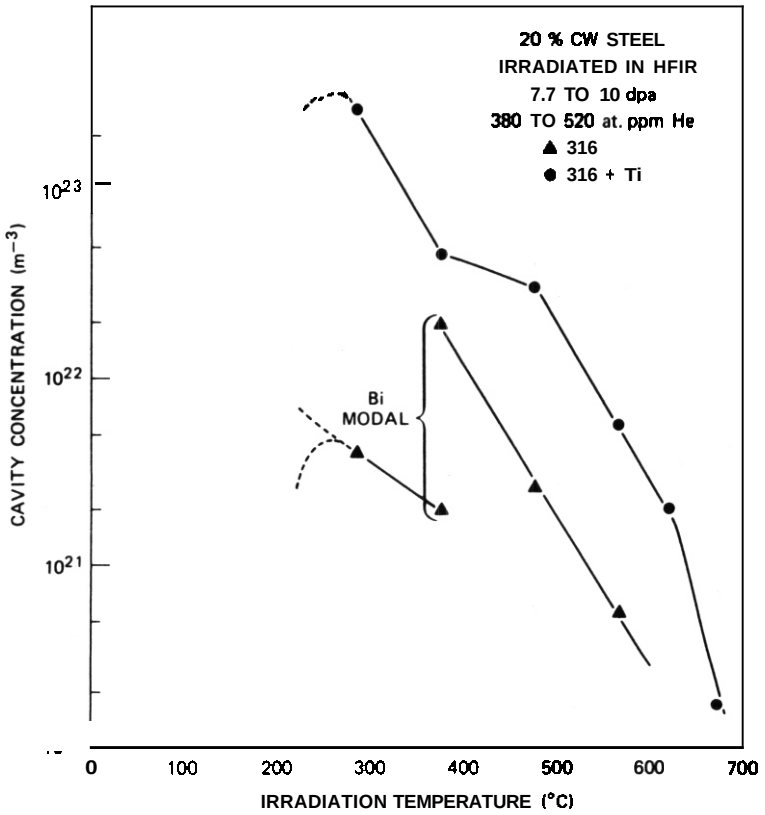

Fig. 3.3.10. Cavity Concentration as a Function of Temperature for CW 316 and CW 316 + Ti Irradiated in HFIR to the Conditions Indicated.

3.3.4.3.2 Temperature Dependence of Microstructural Development in CW 316 + Ti. Intragranular microstructures for samples of CW 316 + Ti irradiated at 285 to 670°C are shown, in cavity contrast, in Figs. 3.3.11 through 3.3.13. The microstructure shows no observable cavity formation at 55°C. As in CW 316, there is considerable microstructural development at 285°C and above. Figure 3.3.14 shows grain-boundary swelling to develop between 475 and 565°C, as in CW 316, and this again coincides with the absence of grain boundary precipitation. Swelling from cavity volume fraction and immersion density change are shown in Fig. 3.3.7 as a function of temperature. The CW 316 + Ti shows essentially the same temperature dependence of swelling as the corresponding curves for CW 316. A maximum is indicated at 285°C or below and a minimum at 450 to 550°C. The cavity volume fraction swelling of CW 316 + Ti is less than CW 316 at all temperatures. This reduction in swelling is also obvious from the microstructures, see by comparing CW 316 in Figs. 3.3.4 and 3.3.5 with

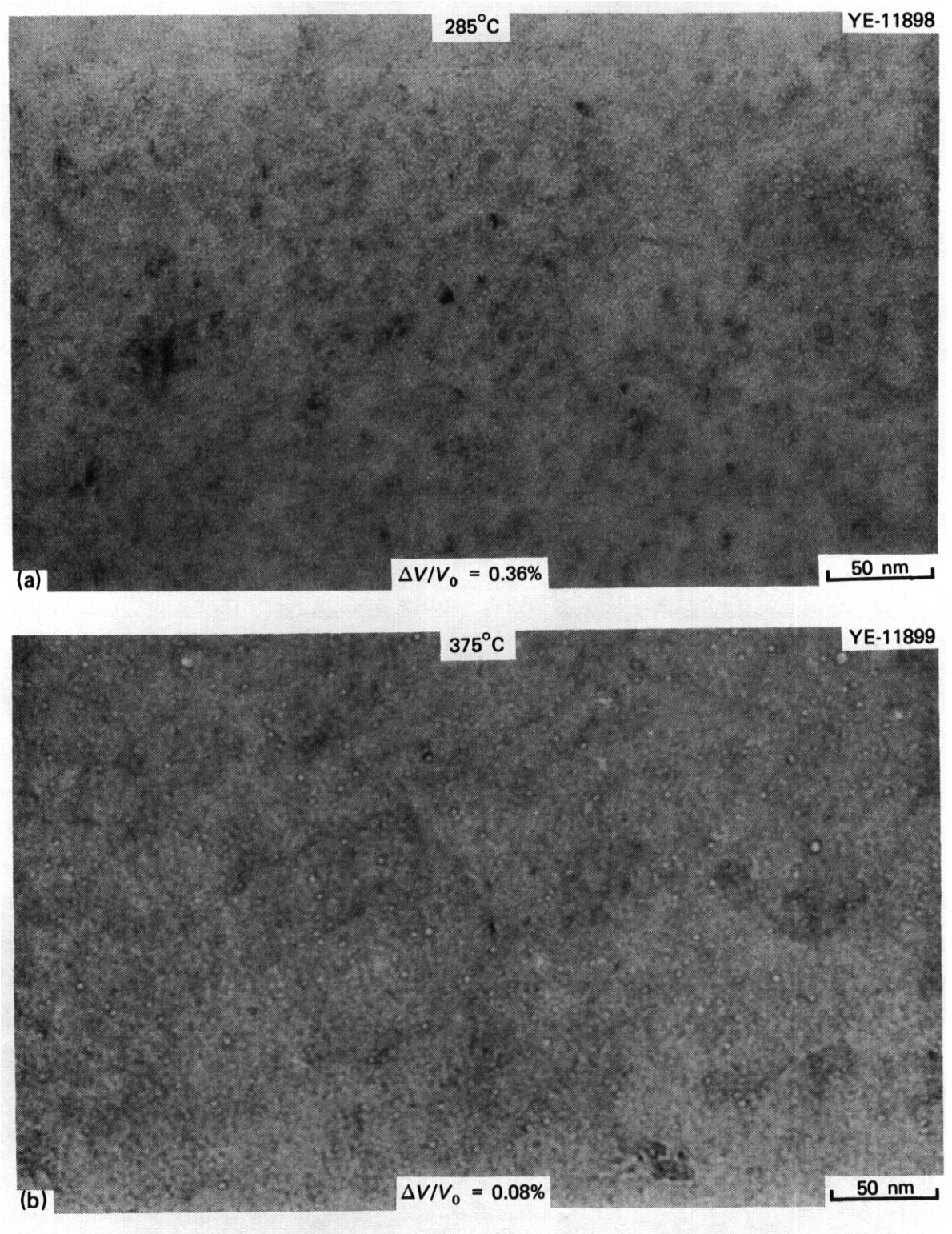

Fig. 3.3.11. Microstructures of CW 316 + Ti Irradiated in HFIR at (a) 285°C to 7.7 dpa and 390 at. ppm He and (b) 375°C to 8.5 dpa and 380 at. ppm He.

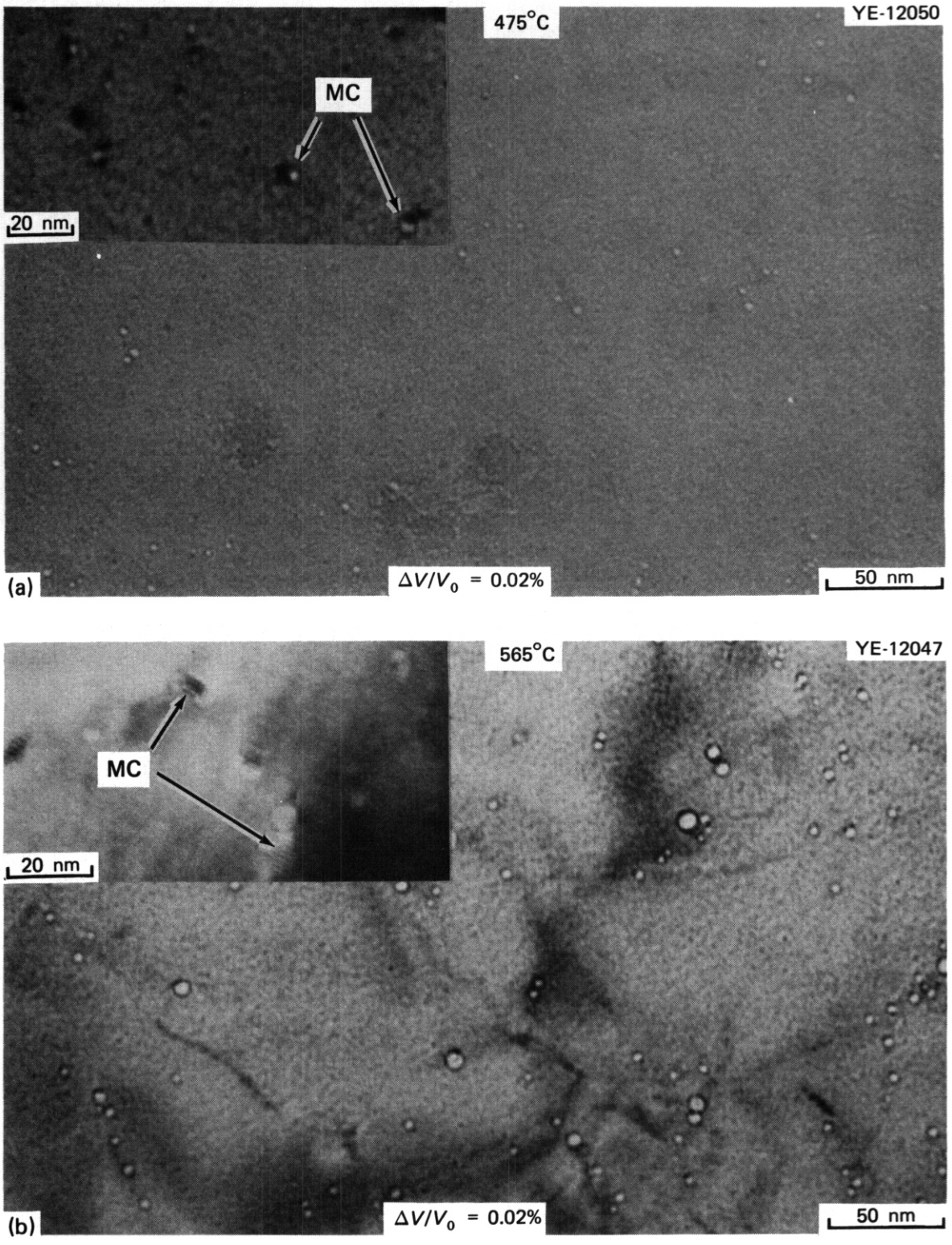

Fig. 3.3.12. Microstructures of CW 316 + Ti Irradiated in HFIR at (a) 475°C to 10 dpa and 500 at. ppm He and (b) 565°C to 9.2 dpa and 440 at. ppm He. High magnification inlays show the exclusive association of the small cavities with fine MC particles.

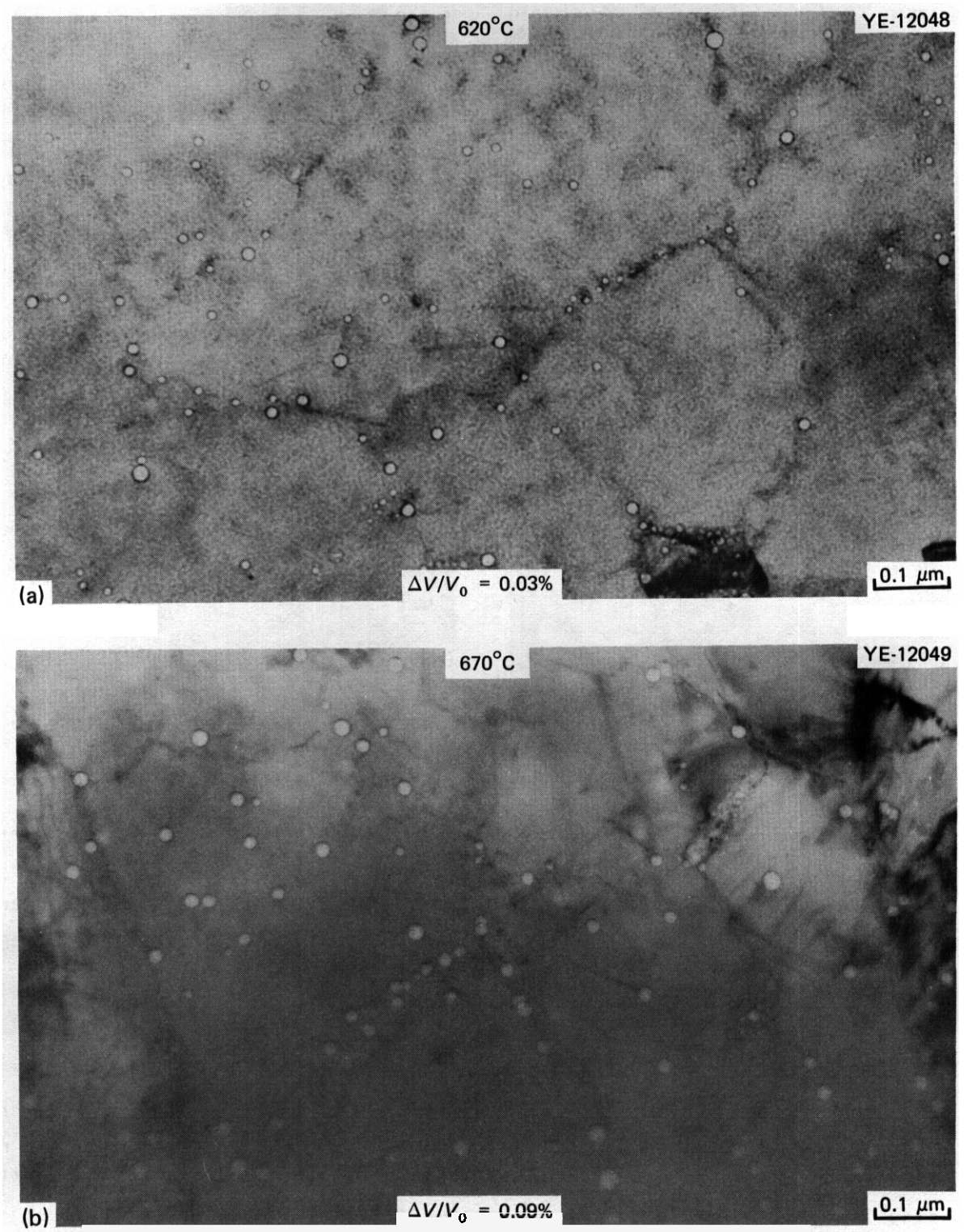

Fig. 3.3.13. Microstructures of CW 316 + Ti Irradiated in HFIR at (a) 620°C to 10 dpa and 500 at. ppm He and (b) 670°C to 10 dpa and 500 at. ppm He.

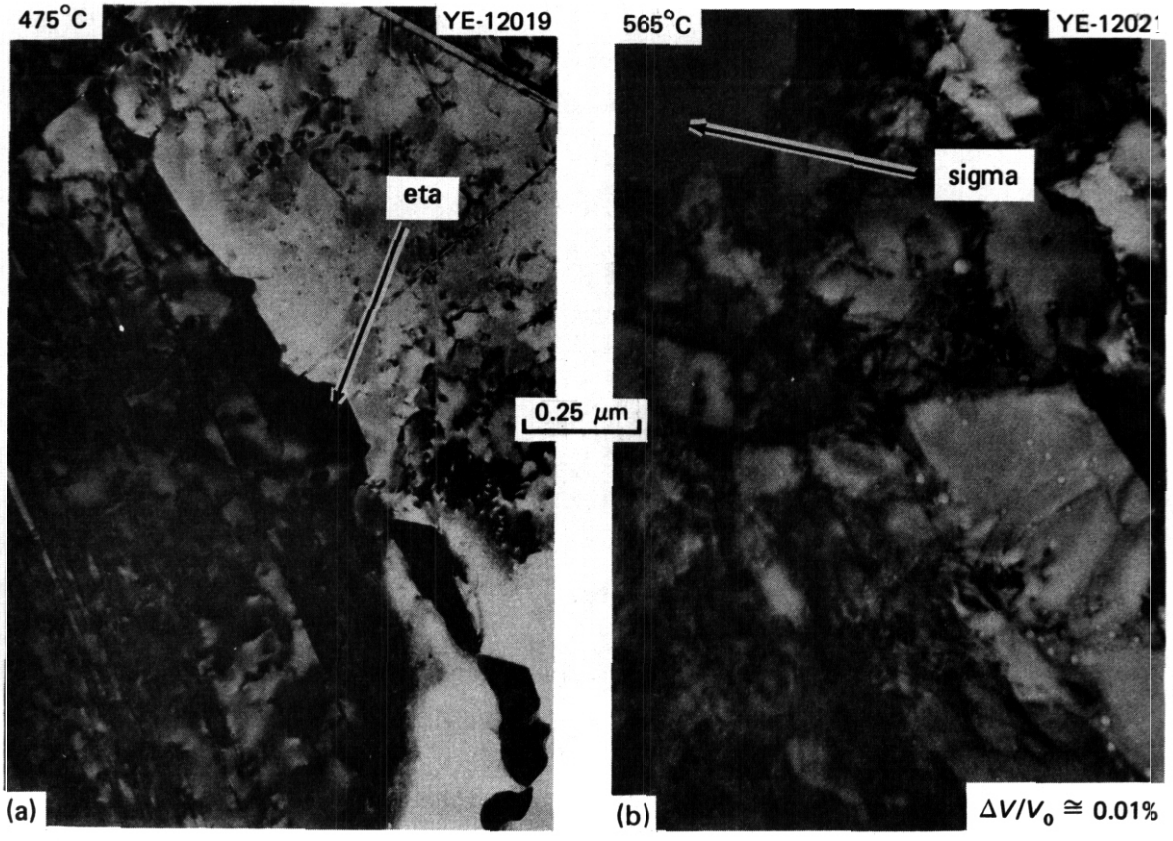

Fig. 3.3.14. Grain Boundary Microstructures of CW 316 + Ti Irradiated in HFIR at (a) 475°C to 10 dpa and 500 at. ppm He and (b) 565°C to 9.2 dpa and 440 at. ppm He. Note grain boundary eta phase in (a) and grain boundary cavities in (b). The grain boundary cavities in (b) contribute approximately 0.01% to the total calculated swelling of 0.03%.

CW 316 + Ti in Figs. 3.3.11 and 3.3.12. As with CW 316 the immersion density change for CW 316 + Ti parallels the cavity volume fraction swelling and appears to indicate a densification component of volume change.

Cavity size and cavity concentration in W 316 + Ti are given as functions of irradiation temperature in Figs. 3.3.9 and 3.3.10, respectively, along with the same data for CW 316. Cavity diameter is nearly constant at 2 to 4 nm from 285 to 565°C and then increases rapidly with temperature above 620°C. This temperature independence of the cavity size is apparently due to the mechanism of MC interfacial helium trapping[10] that is shown in the high magnification inlays of Fig. 3.3.12. The cavity concentration as a function of temperature in the CW 316 + Ti decreases monotonically with increasing temperature. The elbow in this curve toward higher temperatures is a consequence of the MC helium

trapping effect and association of the small cavities with the many fine precipitate particles distributed along the dislocation lines.[9] At 375°C and above, the MC helium trapping reduces the swelling in CW 316 + Ti compared to CW 316 because the cavities are smaller and the concentration is higher in the alloy containing titanium. (This is shown in Figs. 3.3.9 and 3.3.10 and by comparison of Figs. 3.3.4 and 3.3.5 with Figs. 3.3.11 and 3.3.12.) Comparison of the microstructures in Figs. 3.3.6(b) and 3.3.14(b) indicates that grain-boundary cavities are smaller in CW 316 + Ti than in CW 316 and hence the grain-boundary contribution to swelling is less in the former. Swelling increases from 375 to 285°C for CW 316 + Ti as it does for CW 316, but for entirely different microstructural reasons. Figures 3.3.9 through 3.3.11 show that in CW 316 + Ti the microstructure continues to be refined in scale as the temperature decreases and that the increased swelling at 285°C comes from a dramatic increase in cavity concentration. These radically different microstructures giving roughly similar results appear to indicate a stronger dependence of swelling on helium generation rate and migration process, rather than on the exact helium distribution.

3.3.4.3.3 Cavity Character in CW 316 and CW 316 + Ti. The amount of helium necessary to balance the surface tension for a distribution of equilibrium gas bubbles is calculated for the microstructural parameters given in Table 3.3.2. This number is then compared to the amount of gas produced in the sample during irradiation, calculated from empirical equations[11] based on vacuum fusion mass spectrometry measurements. The ratio of measured helium to calculated helium required for stability is 1.0 if all the helium is in the cavities and they are equilibrium bubbles, satisfying $P = 2\gamma/r$, where P = gas pressure in J/m^3, γ = specific surface energy in J/m^2 and r = cavity radius in meters. The ratio will be much less than 1.0 if the cavities are voids. The resulting equation is:

$$nz = 2\pi\gamma d^2/3kT \ , \qquad (1)$$

where

z = compressibility,
n = number of gas atoms (helium),
d = cavity diameter (m),
k = Boltzman's constant (1.38×10^{-23} J/atom K), and
T = irradiation temperature (K).

Equation (1) was used to calculate the number of gas atoms that would be present if these were equilibrium bubbles. The compressibility, z, is a factor that describes the deviation from ideal gas behavior and is 1.0 if the gas is behaving ideally and greater than 1 for a nonideal gas. Cost and Chen[12] pointed out that the ideal gas law seriously overestimated the number of gas atoms in a small bubble ($d < 50$–100 nm) at high pressure and that a reduced Van der Waals equation of state seriously underestimated the number of gas atoms for very small bubbles ($d < 10$ nm). The equation that describes z is called the virial equation and it is formally a power series expansion with the ratio of number of gas atoms (n) to the volume they occupy (V) as the primary parameter. Recently, parallel work by Wolfer[13] and Brearley and MacInnes[14] evaluate z by an alternate procedure that involves treating the gas at high density (high pressure) as a liquid with hard spheres interaction potentials. Both use the same equation for z

$$z = (1 + y + y^2 - y^3)/(1 - y^3) \qquad (2)$$

with

$$y = \pi/6\,\rho d_0^3 = n d_0^3/d^3,$$

where ρ is the number density of gas atoms, d_0 is the hard sphere diameter of the helium atom (0.2637 nm), and y is the atom packing fraction. They differ however in the potential functions that are used to describe the hard sphere diameter, but this is minor and we use the Wolfer equations. Figure 3.1.15 gives curves of z as a function of atom packing fraction (y) at various temperatures, taken from Wolfer.[13] To evaluate z as a function of bubble diameter, d, Wolfer[15] suggests an iterative

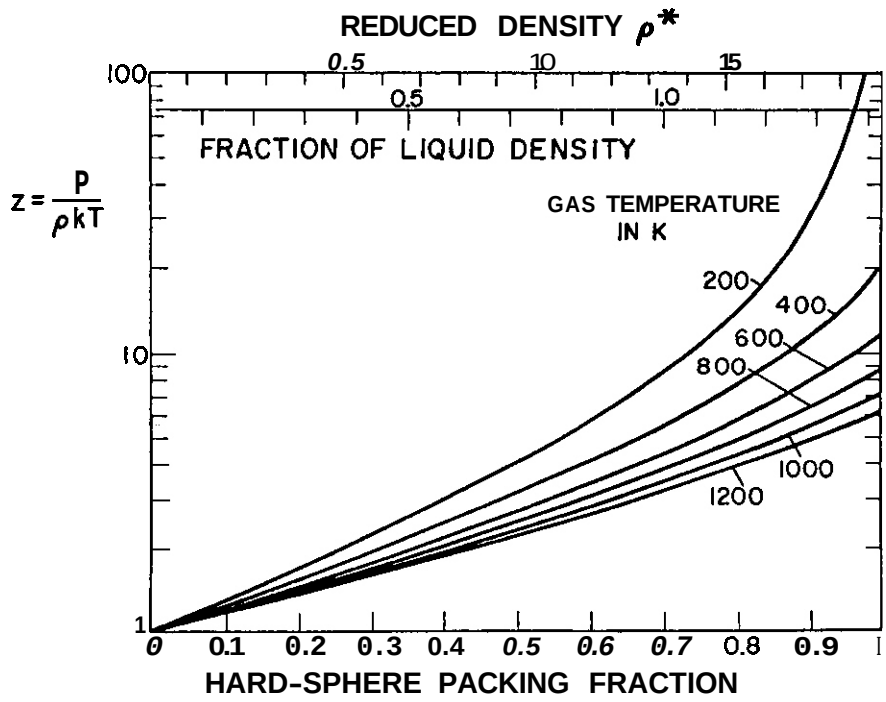

Fig. 3.3.15. High-Density Equation of State for Helium. Reprinted from W. G. Wolfer, *High-Density Equation of State for Helium and Its Application to Bubbles in Solids*, UWFDM-350 (June 1980).

scheme that first calculates n for the ideal case at a microstructurally measured d, and then calculates z to obtain a new n. This quickly converged on a constant value of z and hence n for a given cavity diameter. For very small cavities ($d < 7$ nm) z could range from 1.7 to about 3 for d about 2 nm. At 20 nm and above $z \approx 1$ and is very close to the reduced Van der Waals above about 15 nm, in agreement with Wolfer.[13] This same functional dependence can be seen in the work of Brearley and MacInnes.[14] The cavity character ratios calculated in this way are shown as a function of temperature in Fig. 3.3.16.

Figure 3.3.16 reveals several important features. The cavities are most voidlike at the lowest irradiation temperatures, and most bubblelike at 450 to 600°C. This is consistent with the swelling curves and the temperature locations of maximum and minimum swelling. Large overpressuring of the bubbles is probably not realistic and may indicate that higher

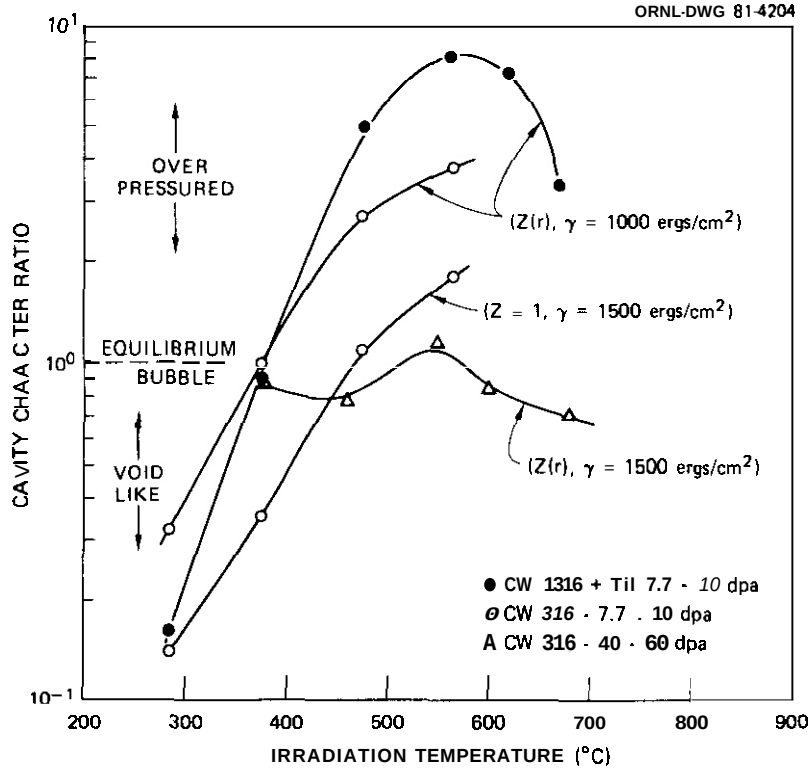

Fig. 3.3.16. Cavity Character Ratio as a Function of Irradiation Temperature for CW 316 and CW 316 + Ti Irradiated in HFIR. The compressibility of helium is z and the specific surface energy of the steel is γ.

surface energies must be used or, as Cost and Chen suggest, $P = 2\gamma/r$ may not be valid for very small bubbles. Another possibility of course is that all the gas is not in the cavities and that some is trapped in vacancies, vacancy clusters, or other sites in the matrix. The temperature dependence of the cavity character ratio, however, is not expected. Letting $z = 1$, as a limiting case, results in the most gas atoms per cavity and the most reasonable cavity character ratios, even though it must be wrong for the small bubbles. Another cause of overpressure could be interstitial absorption by the cavities, due to helium in vacancies reducing bulk recombination as suggested by Maziasz et al.[1] We can conclude only that the unusual temperature dependence of swelling is consistent with unusual temperature dependence of the cavity character, with maximum bubble character where lowest swelling was measured. The cavity character ratio for the high fluence CW 316 data (Fig. 3.3.16 and ref. 8) also showed the largest values at the same temperature as the

minimum of the swelling versus temperature curve of Fig. 3.3.8. This also indicates that bubble behavior persists even to very high fluences. The CW 316 + Ti data in Fig. 3.3.16 are again consistent with the strong trapping of bubbles at an intrinsically vacancy-bias sink like the MC particle interface.[10]

3.3.4.4 Discussion

The microstructural features presented above appear to be internally consistent for both CW 316 and CW 316 + Ti. The previously identified principles of MC interfacial helium trapping[10] result in the observed microstructural differences between CW 316 + Ti and CW 316, and the lower swelling in the alloy containing titanium. An unexpected result is the microstructural and swelling behavior as a function of temperature. The dependence of the cavity character ratio on irradiation temperature was also unexpected. However, these trends are only unexpected because our ideas about swelling and microstructural development come mainly from fast breeder reactor irradiations, where little helium is generated during irradiation. The present results identify a strong role of simultaneous helium generation with displacement damage during irradiation on microstructural evolution and the resulting properties. The few theoretical studies that include helium production during irradiation[16,17] reach similar conclusions.

Both the present work and recent work of Garner et al.[18] are directed at determining the swelling behavior of type 316 stainless steel in fusion reactor service. Both use HFIR data as a basis for the conclusions reached. Garner et al. had only a small portion of the much larger data base now available. They reach a conclusion, with which we agree, that when void swelling develops in EBR-II, the swelling will be greater than the bubble swelling observed in HFIR, and that helium extends the temperature range over which swelling occurs. The equation Garner et al. recommended for fusion reactor design is the fast breeder reactor program swelling equation with tails at high and low temperature for bubble swelling. The temperature dependence of the recommended swelling equation is shown in Fig. 3.3.17. These authors concluded that helium plays a minor role in stainless steel swelling in HFIR and that a smaller role is expected under fusion reactor conditions.

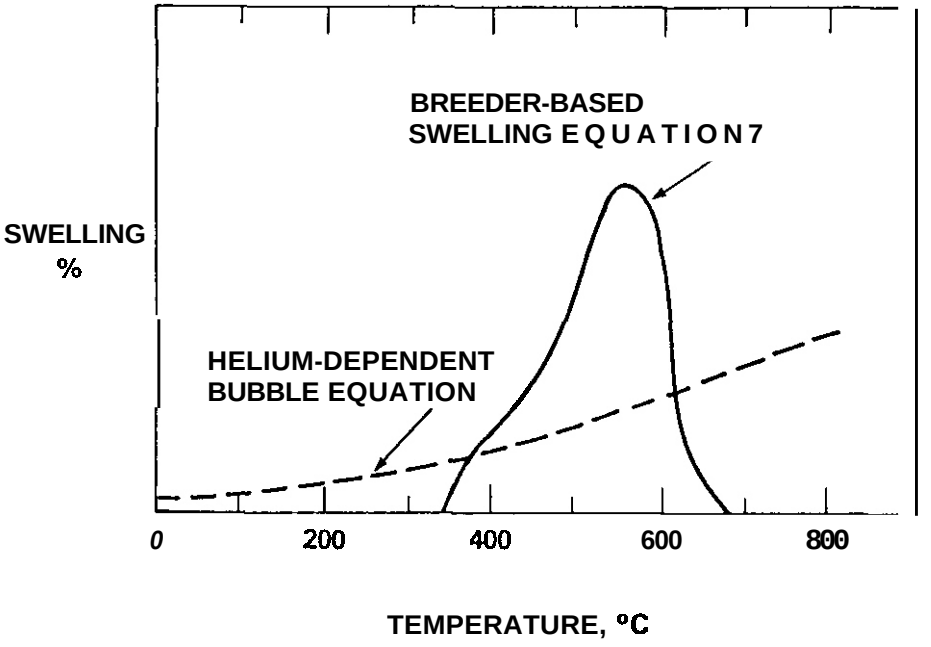

Fig. 3.3.17. Schematic Illustration of Expected Form of Bubble and Void Swelling Equations. Reprinted from: F. A. Garner, P. J. Maziasz, and W. G. Wolfer, "Development of a Swelling Equation for 20%-Cold-Worked AISI 316 in a Fusion Device," DAFS *Quart.* Prog. *Rep.* Sept. 30, 1980, DOE/ET-0065/11, p. 159.

The present results show that helium plays a strong role in microstructural development and that this development governs the swelling behavior. The use of the swelling equation from the fast breeder reactor program for CW 316 does not even assure "conservative" design, since the HFIR data show significant microstructural development and small but measurable swelling at fluences and temperatures where there is little microstructural change and no swelling in EBR-II.[18] In addition, the temperature dependence of swelling shown in Fig. 3.3.17 is quite different than that shown in Figs. 3.3.7 and 3.3.8. The correct shape of the swelling-temperature relationship becomes important in calculating secondary stresses from the differential swelling in a temperature gradient. Figure 3.3.17 indicates that bubble swelling is considerably less than void swelling, but the resulting curve shape is in contradiction to the present results. For the HFIR data, there is a swelling minimum at the temperature corresponding to the swelling peak in the EBR-II data.

3.3.5 Conclusions

1. There is considerable cavity formation and microstructural development in both CW 316 and CW 316 + Ti during HFIR irradiation at 285°C and above and to fluences producing 7.7 to 10 dpa and 380 to 500 at. ppm He. There were no observable cavities in either alloy after irradiation at 55°C to 10.8 dpa and 520 at. ppm He.

2. The level of cavity swelling is small in both CW 316 and CW 316 + Ti for these conditions. It was less than about 0.1% at 375°C and above at these low fluences. However, swelling dramatically increases on decreasing the temperature to 285°C, indicating a low temperature swelling peak near or below this temperature in both alloys.

3. The swelling of CW 316 + Ti is measurably less than in CW 316 at all irradiation temperatures. This is due to a refined cavity microstructure that is a direct consequence of MC precipitate interfacial helium trapping, at least at 375°C and above.

4. Precipitation is the dominant grain boundary process for temperatures up to 475°C; at 565°C and higher grain boundary cavities were common in both alloys and begin to contribute significantly to swelling. As with the matrix swelling, grain-boundary swelling is less in the CW 316 + Ti than in CW 316 due to considerably smaller cavities in the former alloy.

5. Analysis of the bubble-void characters of the cavities produced by irradiation shows the strongest bubblelike behavior at 450 to 600°C, with less bubblelike characteristics at lower or higher temperatures. The strongest bubble characteristics correlate with the swelling minimum at 450 to 500°C, both for irradiation producing 7 to 10 dpa and irradiation to 40 to 60 dpa. The cavity character behavior is similar for CW 316 and CW 316 + Ti, even though quite different microstructures are developed during the irradiation. This may indicate a general dependence on the helium generation rate and migration process, rather than on the ultimate gas location.

6. The very different behavior in the swelling and microstructural development for stainless steel irradiated in HFIR and EBR-II show that

helium plays a dominant role. Continuing effort is needed to elucidate this role of helium, and to develop predictive swelling equations that can be used for fusion reactor service.

3.3.6 References

1. P. J. Maziasz, J. A. Horak, B. L. Cox, and M. L. Grossbeck, "The Influence of Both Helium and Neutron Irradiation on Precipitation in 20%-Cold-Worked Austenitic Stainless Steel," paper presented at the Metallurgical Society of AIME Fall Meeting, Pittsburg, October 5-9, 1980, to be published in the proceedings.
2. P. J. Maziasz, M. L. Grossbeck, and F. W. Wiffen, "The Microstructure and Mechanical Properties of 20%-Cold-Worked Types 316 Stainless Steel and 316 + 0.23 wt % Ti After HFIK Irradiation at 55 to 375°C," *ADIP Quart. Prog. Rep. June 30, 1980,* DOE/ER-0045/3, pp. 48—74.
3. P. J. Barton, B. L. Eyre, and D. A. Stow, "The Structure of Fast-Reactor Irradiated Solution-Treated AISI Type 316 Stainless Steel," *J. Nucl. Mater. 67:* 181—97 (1977).
4. J. W. Edington, "Interpretation of Transmission Electron Micrographs — Monograph Three," *Practical Electron Microscopy in Materials Science,* Macmillan, New York, 1975.
5. L. E. Murr, *Electron Optical Applications in Materials Science,* McGraw-Hill, New York, 1970.
6. J. E. Hilliard, "Measurement of Volume in Volume," pp. 45—76 in *Quantitative Microscopy,* R. T. DeHoff and F. N. Rhines, Eds., McGraw-Hill, New York, 1968.
7. E. E. Underwood, "Surface Area and Length in Volume," pp. 77—125 in *Quantitative Microscopy,* R. T. DeHoff and F. N. Rhines, Eds., McGraw-Hill, New York, 1968.
8. P. J. Maziasz, F. W. Wiffen, and E. E. Bloom, "Swelling and Microstructural Changes in Type 316 Stainless Steel Irradiated Under Simulated CTR Conditions," pp. 259—88 in *Radiation Effects and Tritium Technotogy for Fusion Reactors,* CONF-750989, Vol. I (March 1976); also ORNL/TM-5396 (May 1976).

9. P. J. Maziasz, B. L. Cox, and J. A. Horak, "The Effect of Preinjected Helium on the Microstructure and Tensile Properties of EBR-II-Irradiated 20%-Cold-Worked Type 316 Stainless Steel," *ADIP Quart. Prog. Rep. Mar. 31, 1980*, DOE/ER-0045/2, pp. 35–57.
10. P. J. Maziasz, "Helium Trapping at Ti-Rich MC Particles in Ti-Modified Austenitic Stainless Steel," paper presented at the Metallurgical Society of AIME Fall Meeting, Pittsburg, October 5–9, 1980, to be published in the proceedings.
11. F. W. Wiffen et al., "The Production Rate of Helium During Irradiation of Nickel in Thermal Spectrum Fission Reactors," to be published.
12. J. R. Cost and K. Y. Chen, "The Number of Gas Atoms per Bubble of Inert Gas in a Solid," *J. Nucl. Mater.* 67: 265–72 (1977).
13. W. G. Wolfer, "High-Density Equation of State for Helium and Its Application to Bubbles in Solids," paper presented at Symposium on Effects of Radiation Materials, American Society of Testing and Materials, Savannah, Ga., June 1980, to be published in the proceedings (also in UWFDM-350, June 1980).
14. I. R. Brearley and D. A. MacInnes, "An Improved Equation of State for Inert Gases at High Pressures," *J. Nucl. Mater.* 95: 239–52 (1980).
15. W. G. Wolfer, private communication, January 1981.
16. G. R. Odette and M. W. Frei, "Potential Effects of Interactions Between Transmutants and Displaced Atoms in Controlled Thermonuclear Reactor First Walls," pp. 485–99 in *First Topical Meeting on the Technology of Controlled Nuclear Fusion*, CONF-740402-P2 (1974).
17. M. L. Takata and N. M. Ghoniem, *Intragranular Helium Gas Behavior in Fusion Reactor Structural Materials*, Center for Plasma Physics and Fusion Engineering, UCLA, PPG-519 (October 1980).
18. F. A. Garner, P. J. Maziasz, and W. G. Wolfer, "Development of a Swelling Equation for 20%-Cold-Worked AISI 316 in a Fusion Device, *DAFS Quart. Prog. Rep. Sept. 30, 1980*, DOE/ET-0065/11, p. 159.

4. PATH B ALLOY DEVELOPMENT — HIGHEK STRENGTH Fe–Ni–Cr ALLOYS

5. PATH C ALLOY DEVELOPMENT — REACTIVE AND REFRACTORY ALLOYS

5.1 THE EFFECT OF HYDROGEN ON FLAW GROWTH OF TITANIUM ALLOY Ti-6242s

G. W. Wille and P. S. Pao (McDonnell Douglas Corporation)

5.1.1 ADIP Task

Task 1.B.3, Fatigue Crack Growth in Reactive/Refractory Alloys (Path C).

5.1.2 Objective

The objective of this study is to develop quantitative data to determine the effects of both internal and external hydrogen on fatigue crack growth of Ti-62425 alloy at temperatures and hydrogen pressures of interest for fusion reactors.

5.1.3 Summary

Additional fatigue crack growth rate tests have been conducted at room temperature in a vacuum on Ti-62425 samples with 500 wppm internal hydrogen, At high stress intensities the fatigue crack growth rate increased with decreasing frequency.

5.1.4 Progress and Status

Fatigue crack growth rate tests have been run in a vacuum at room temperature with specimens charged with 500 wppm hydrogen. Test frequencies were 1, 5 and 18 hertz. The results are shown in Figure 5.1.1. Changing the test frequency from 1 to 18 hertz has little effect on the crack growth rates at low stress intensities. At high stress intensities the fatigue crack growth rate increased with decreasing frequency. This characteristic supports the stress assisted hydride formation mechanism that has been proposed by other investigators. In this mechanism, during tensile tests, hydrogen will diffuse and segregate to the region of high triaxial tensile stress near the crack tip. The resultant higher hydrogen concentration promotes hydride precipitation on an extremely small scale at the alpha-beta interfaces. The lower test frequency would thus provide longer periods at high stresses to allow more hydrogen diffusion and segregation. So far, we have not observed any hydride formation on the fracture surface of the specimens.

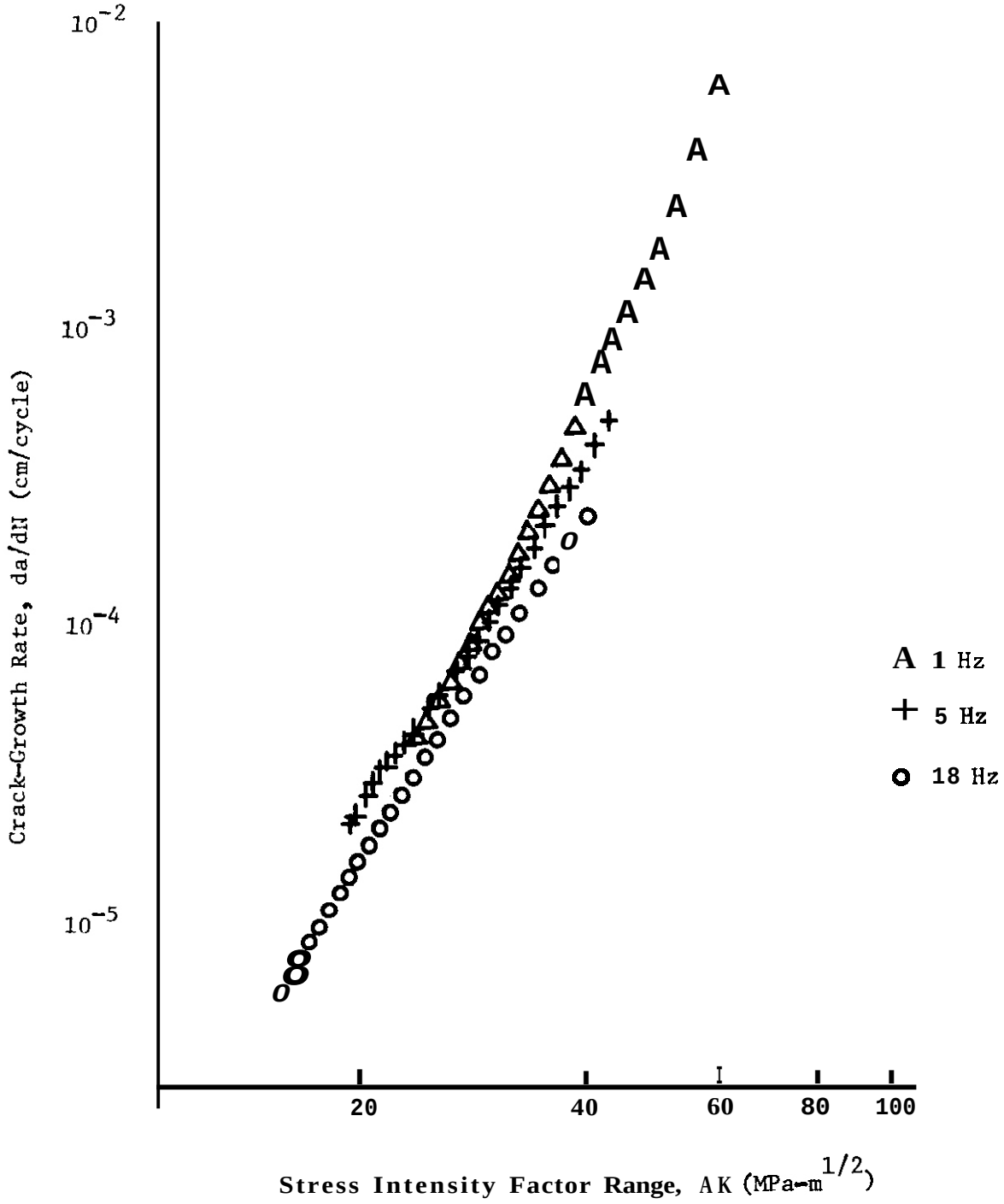

Figure 5.1.1. Effect of Test Frequency on the Fatigue Crack Growth Rates of Ti-6242s with 530 wppm Hydrogen

The fracture surfaces are being examined and will be discussed in the next quarterly.

5.1.5 Conclusions

The fatigue crack growth rate of specimens charged with 500 wppm hydrogen increased with decreasing test cycle frequency. This effect was more pronounced at higher stress intensities.

5.2 TITANIUM ALLOY TENSILE PROPERTIES AFTER NEUTRON IRRADIATION — D. R. Duncan, R. J. Puigh, and E. K. Opperman (Hanford Engineering Development Laboratory)

5.2.1 ADIP Task

The Department of Energy DOE/Office of Fusion Energy (OFE) has cited the need for data under the following ADIP Program Plan Task[1]. I.B.15. Tensile Properties of Reactive/Refractory Alloys.

5.2.2 Objective

The objective of this work is to evaluate the effects of neutron irradiation on the tensile properties of titanium alloys. Assessment of mechanical property response to neutron irradiation will be a necessary step in choosing structural materials for fusion energy systems.

5.2.3 Summary

Irradiated specimens from three titanium alloys (6242S, 5621S, Ti-6A1-4V) were tested in uniaxial tension in air from room temperature to 550°C. Each alloy was in a duplex-annealed condition. The strain rate during testing was $4.2 \times 10^{-5} s^{-1}$. The EBR-II irradiation temperature was 550°C; the maximum fluence was 5×10^{22} n/cm^2 (E>0.1 MeV) or 24 dpa. The specimens were from the first of three capsules from the AD-1 experiment. The remaining two had irradiation temperatures of 394 and 450°C; tensile tests will be performed on material from these capsules in the near future.

Alloy 6242S increased in strength because of reactor exposure by approximately 20% at test temperatures from room to 400°C. Ductility losses of up to 75% were found.

The strength of 5621S seemed to be unaffected by reactor exposure while its ductility was reduced from that of unirradiated material by up to 80%.

Ti-6A1-4V displayed strength reductions at 550°C test temperature with nearly an 80% reduction in total elongation.

While large ductility losses were noted after reactor exposure, reasonable postirradiation ductility remained in the specimens. Total

elongations ranged from ~1-9%.

All of the specimens had some degree of corrosive attack, which probably occurred during cleaning after reactor discharge. The corrosion ranged from discoloration to loss of material. Although specimens with the least corrosion were chosen for testing, the mechanical properties could include corrosion effects as well as irradiation effects. Hence, the ductilities and ultimate strengths obtained in this study are minimum values.

5.2.4 Progress and Status

4.1 Introduction

Titanium alloys are potentially useful in fusion reactor structural applications because of favorable strength to weight ratios, low thermal stresses, and favorable coolant compatibility. In addition, the activity of titanium alloys decreases very rapidly, in comparison to stainless steels. On a strength to weight ratio and creep rupture basis elevated temperature alloys such as 6242S and 5621S are equal to or stronger than cold worked Type 316 stainless steel below 500°C. The effect of radiation to high neutron fluences on mechanical properties is unknown however.

4.2 Materials and Experimental Procedure

The alloys tested are given in Table 1. The alloys 5621S and 6242S were chosen because of their high strength, and Ti-6Al-4V because of its broad industrial usage base. The specimen dimensions are given in Figure 1. Specimens were fabricated from sheet stock supplied by the McDonnell-Douglas Astronautics Company of St. Louis. The alloys were originally manufactured by Reactive Metals Inc. (5621S and Ti-6Al-4V) and Titanium Metals Corporation (6242S).

Samples were irradiated in EBR-II in pin B286 of the AD-1 experiment.[2] The irradiation temperature was 550°C, according to heat balance calculations. The uncertainty in temperature for uninstrumented capsules such as B286 is typically ±30°C. The maximum fluence reached in B286 was ~5 x 10^{22} n/cm^2 (E>0.1 MeV) based on calculations from nominal reactor

TABLE 5.2.1

DESCRIPTION OF MATERIALS

ALLOY	COMPOSITION (%)			HEAT TREATMENT	
6242S (Heat N9882)	A1–5.8 Mo–1.9 N –0.005	Sn–1.9 Si–0.08 O –0.10	Zr–4.0 C –0.018 Fe–0.06	900°C/½hr/Air Cool 785°C/¼hr/Air Cool	Duplex Anneal
5621S (Heat 802881)	A1–4.7 Mo–0.78 N –0.009	Sn–5.9 Si–0.28 O –0.09	Zr–1.8 C –0.02 Fe–0.04	975°C/1hr/Air Cool (vacuum) 595°C/2hr/Air Cool (vacuum)	Duplex Anneal
Ti-6A1-4V (Heat 891352)	A1–6.4 N –0.01	V –3.9 O –0.12	C –0.01 Fe–0.21	940°C/$\frac{1}{6}$hr/Argon Cool 675°C/^{6}4hr/Argon Cool	Duplex Anneal

operating parameters. This is the highest neutron fluence obtained to date on any titanium alloy. The maximum dose was 24 dpa.

Tensile tests were performed in air on an Instron machine with a constant crosshead speed of *8.5* x 10^{-5}cm/s which yielded a strain rate of 4.2 x $10^{-5}s^{-1}$ in the specimen gauge length. Several specimens were given an increase in crosshead speed subsequent to attaining the 0.2% yield load to decrease total test time. This procedure was not continued after a sample fractured during the crosshead speed change.

5.2.4.3 Results

Postirradiation mechanical properties are given in Table 2. Two specimens, one Ti-6A1-4V and one 5621S, broke upon loading during testing at room temperature. This brittle behavior is attributed to corrosion.

Postirradiation strength and elongation results are presented in Figures *2* and 3 for all three alloys. The strongest alloy was 6242S. Its ultimate strength was nearly *40%* stronger than 5621S and almost double that of Ti–6A1–4V. Elongation results were mixed, with 5621S and 6242S exhibiting fairly strong temperature dependencies. The minimum in total elongation for 5621S occurred at 400°C with values of 2.9 and 6.0%, while the minimum for 6242S occurred at 550°C at 3.3%. The elongation at failure of the single Ti–6A1–4V sample was 0.86%, at a test temperature of 550°C.

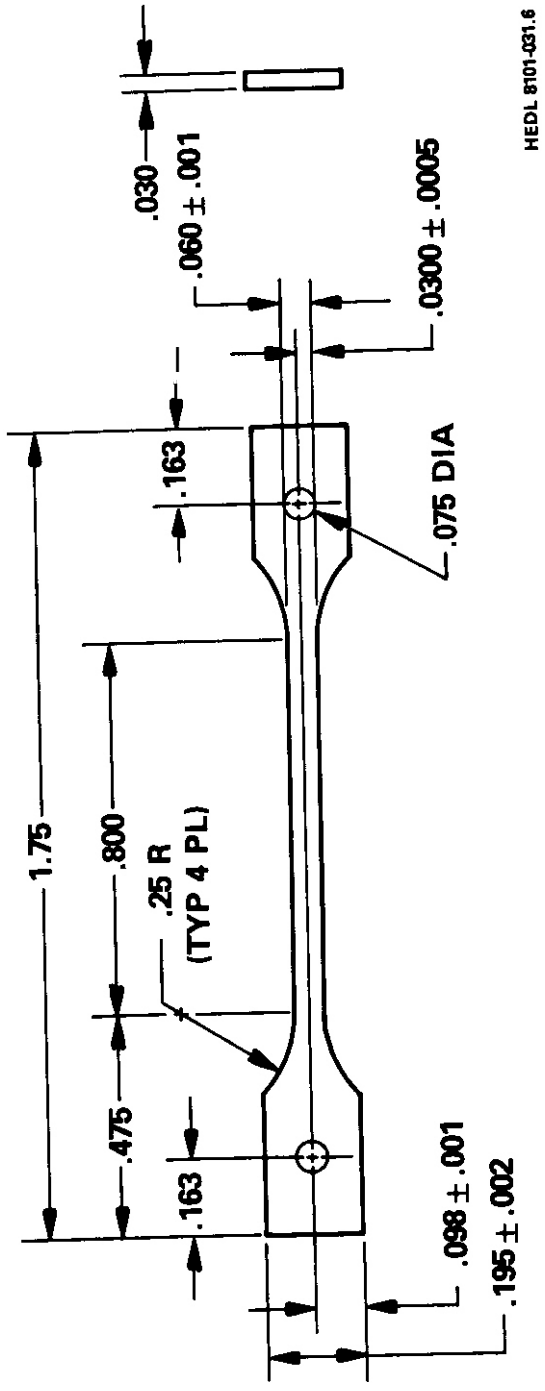

FIGURE 5 2 1 Postirradiation Tensile Specimen

TABLE 5.2.2

POSTIRRADIATION Ti ALLOY TENSILE PROPERTIES
($\dot{\epsilon} = 4.2 \times 10^{-5} s^{-1}$)

Ti-6A1-4V

SPECIMEN ID	TEST TEMP. (°C)	0.2% YIELD STRENGTH (MPa)	ULTIMATE TENSILE STRENGTH (MPa)	UNIFORM ELONG. (%)	TOTAL ELONG. (%)
T2-52	550	394.4	417.8	0.74	0.86

5621S

SPECIMEN ID	TEST TEMP. (°C)	0.2% YIELD STRENGTH (MPa)	ULTIMATE TENSILE STRENGTH (MPa)	UNIFORM ELONG. (%)	TOTAL ELONG. (%)
T5-70	200	659.1	788.8	7.0	8.7
T5-47	400	593.6	728.1	4.3	6.0
T5-58	400	547.4	628.1	1.8	2.9
T5-43	550	459.9	578.5	3.9	5.8

6242S

SPECIMEN ID	TEST TEMP. (°C)	0.2% YIELD STRENGTH (MPa)	ULTIMATE TENSILE STRENGTH (MPa)	UNIFORM ELONG. (%)	TOTAL ELONG. (%)
T4-45	Room Temp.	926.7*	1252.8	5.9	5.9
T4-54	200	873.6*	**	2.4% at fracture	
T4-51	400	743.3	946.0	8.2	8.8
T4-44	550	620.5*	785.3	2.3	3.3

* Crosshead speed increased by 10X between 0.2% yield point and maximum load point.

** Broke during crosshead speed change.

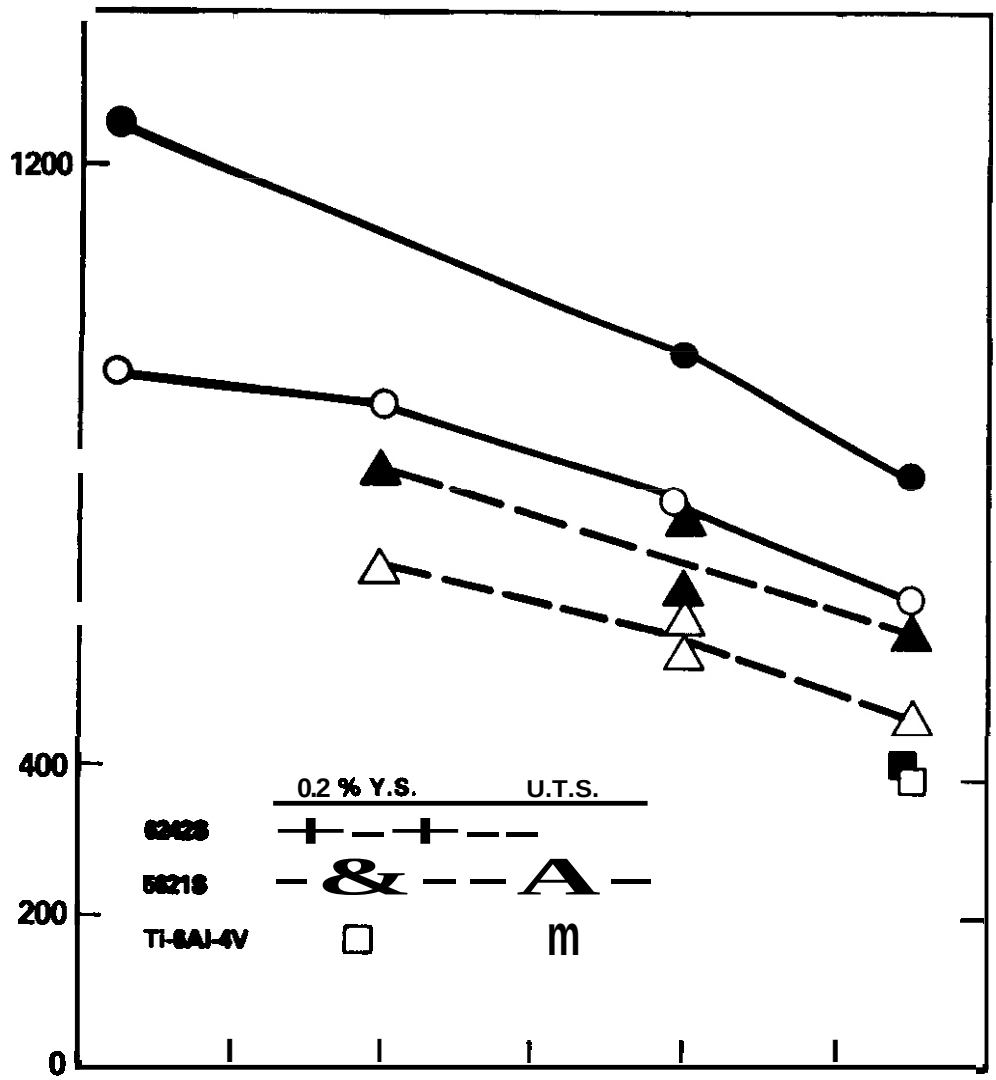

FIGURE 5.2.2 **Postirradiation Yield Strength and Ultimate Strength [Irradiation Temp.= 550°C, ϕt = 5.0 x 10^{22}n/cm^2(E>0.1 MeV)**

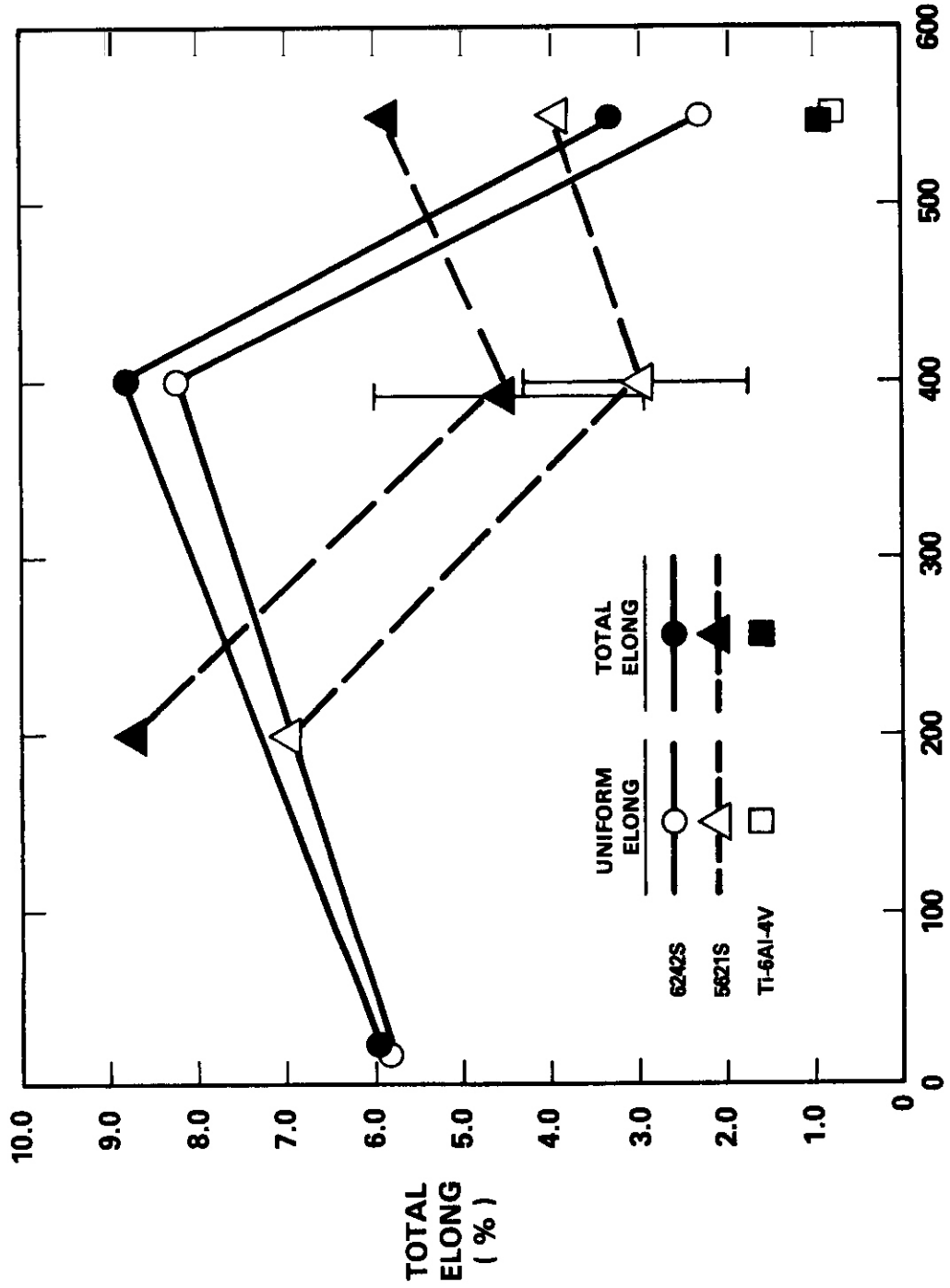

FIGURE 5.2.3 Postirradiation Uniform and Total Elongation [Irradiation Temp. = 550°C, $\phi t = 5.0 \times 10^{22} n/cm^2 (E>0.1\ MeV)$

Comparisons of postirradiation properties with properties of unirradiated material of similar composition and heat treatment are shown next in Figures 4-8. The ultimate strength of 6242S increased due to irradiation by approximately 20% at test temperatures of 400°C and below. The postirradiation yield strength was comparable to that of unirradiated material at room temperature but increased by approximately 20% at 200 and 400°C. Little effect of reactor exposure is apparent at the 550°C test temperature. Significant decreases in ductility were found in 6242S, as shown in Figure 5, although little ductility loss was noted in the test at 400°C. Unirradiated material results were from vendor certification reports and from Dotson.(3) The trend line from Dotson represents an average of 20 tests.

A comparison of postirradiation and unirradiated material 5621S strength in Figure 6 indicates, somewhat surprisingly, no effect of reactor exposure. Yet a consistent trend of ductility loss is apparent in Figure 7. Unirradiated material results were from vendor certification reports and from single data points from Seagle and Bomberger.(4)

The single postirradiation test of Ti-6Al-4V resulted in strength decreases, principally in the ultimate strength, compared to averages from eight heats of unirradiated material, obtained from the Aerospace Structural Materials Handbook,(5) A severe reduction in ductility occurred as a result of reactor exposure.

5.2.4.4 Discussion

Other investigators have irradiated titanium and its alloys with neutrons or heavy ions, but few mechanical property investigations have been undertaken. Hasse and Hartley(6) irradiated Ti-6Al-4V to $\sim 2 \times 10^{21}$ n/cm^2 (E>0.1 MeV) at 70°C. The room temperature ultimate strength increased by 40% and the elongation decreased by 70%. Sastry et al.(7) tested the microhardness of Ti-6A1-4V and 5621S in the unirradiated condition and after irradiation to 3.4×10^{21} n/cm^2 (E>0.1 MeV) at 450°C, and found hardness increases of ~20-35%. Opperman(8) and Nygren(9) investigated the irradiation creep of titanium alloys under proton irradiation and neutron irradiation, respectively. Nygren's specimens had a fluence of 3.4×10^{21}

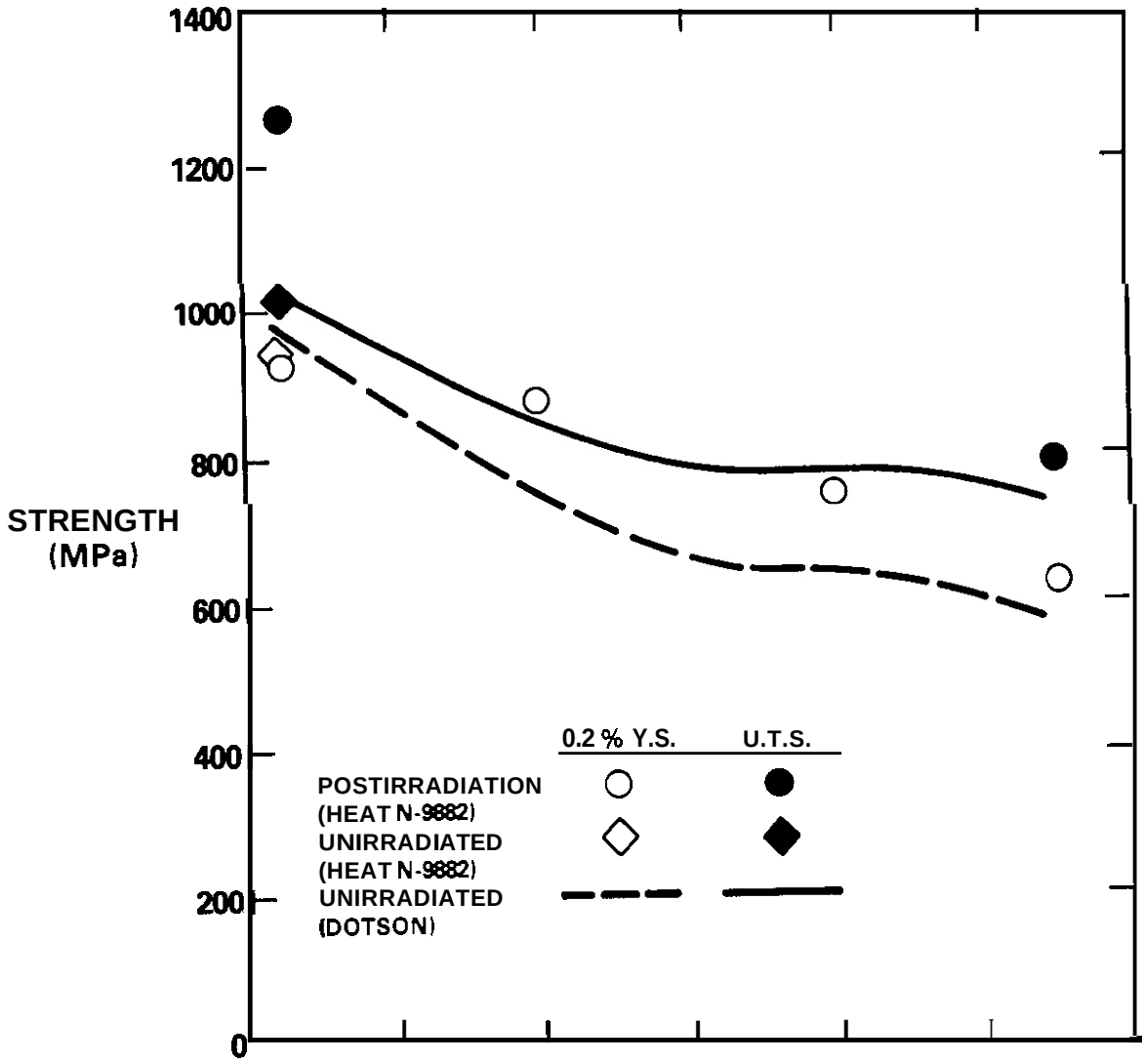
1400
1200
1000
800
600
400
200
0
STRENGTH
(MPa)
0.2 % Y.S.
U.T.S.
POSTIRRADIATION
(HEAT N-9882)
UNIRRADIATED
(HEAT N-9882)
UNIRRADIATED
(DOTSON)

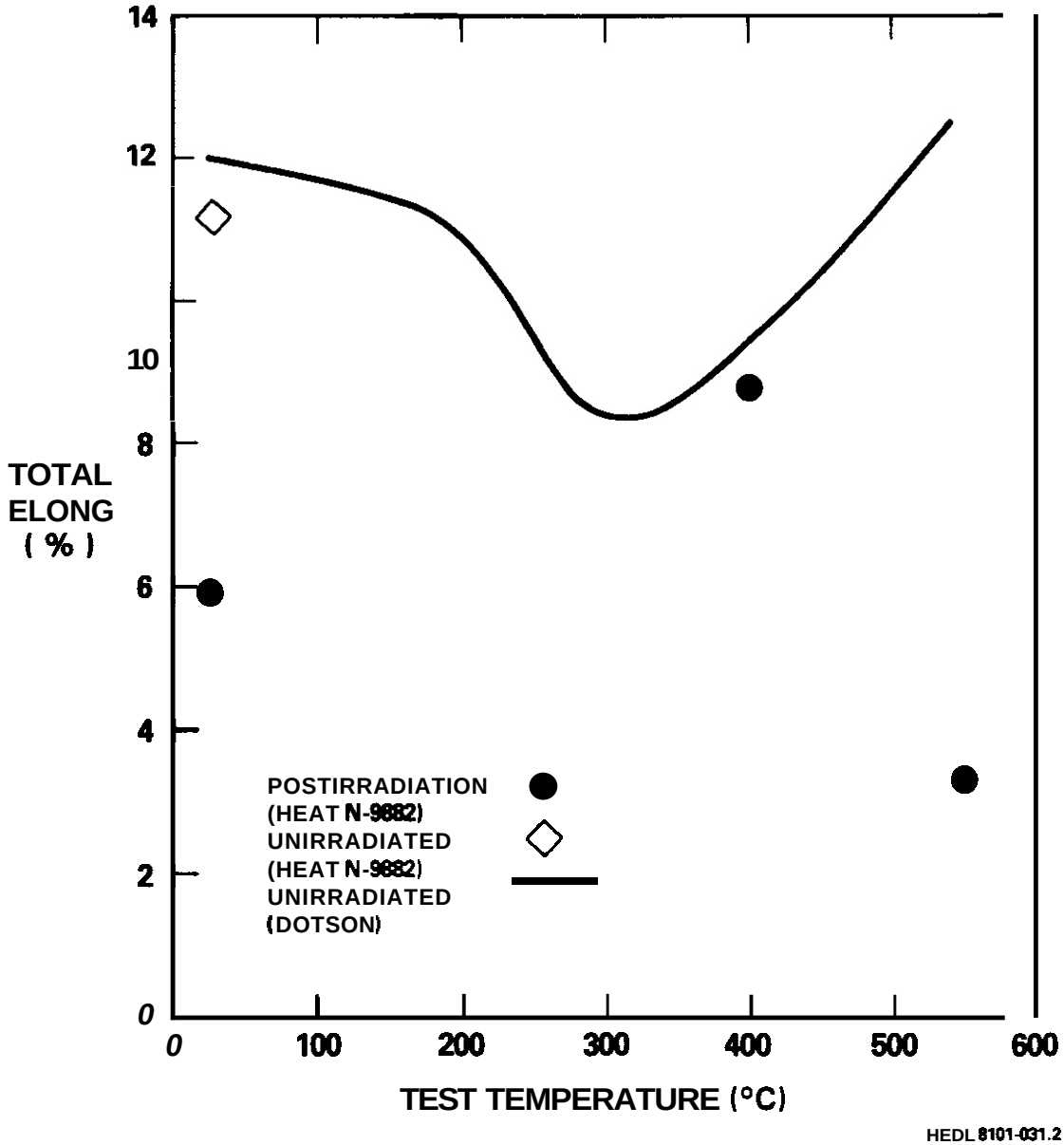

FIGURE 5.2.5 Effect of Neutron Irradiation on the Total Elongation of Alloy 6242S

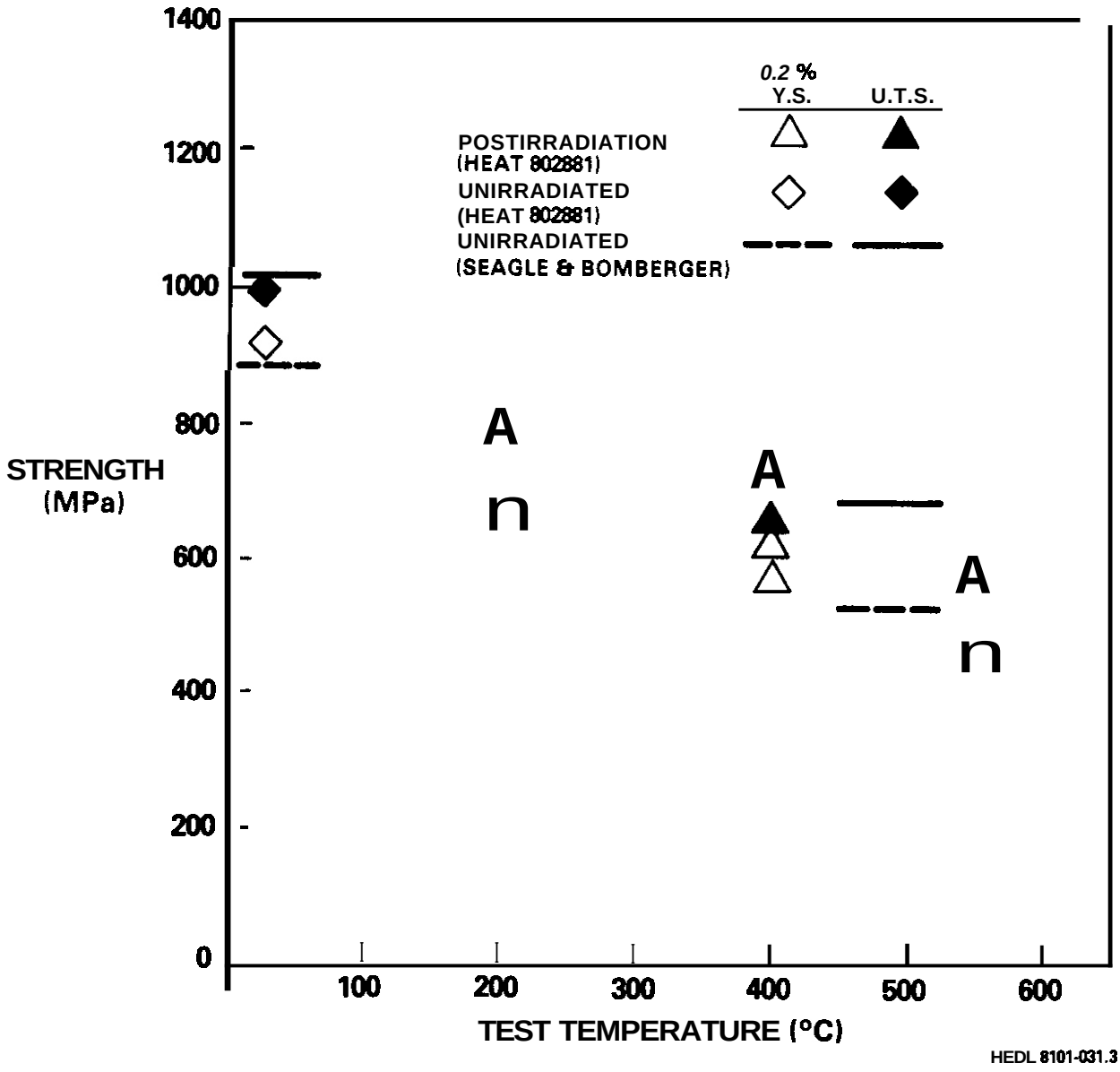

FIGURE 5.2.6 Effect of Neutron Irradiation on Strength of Alloy 5621S.

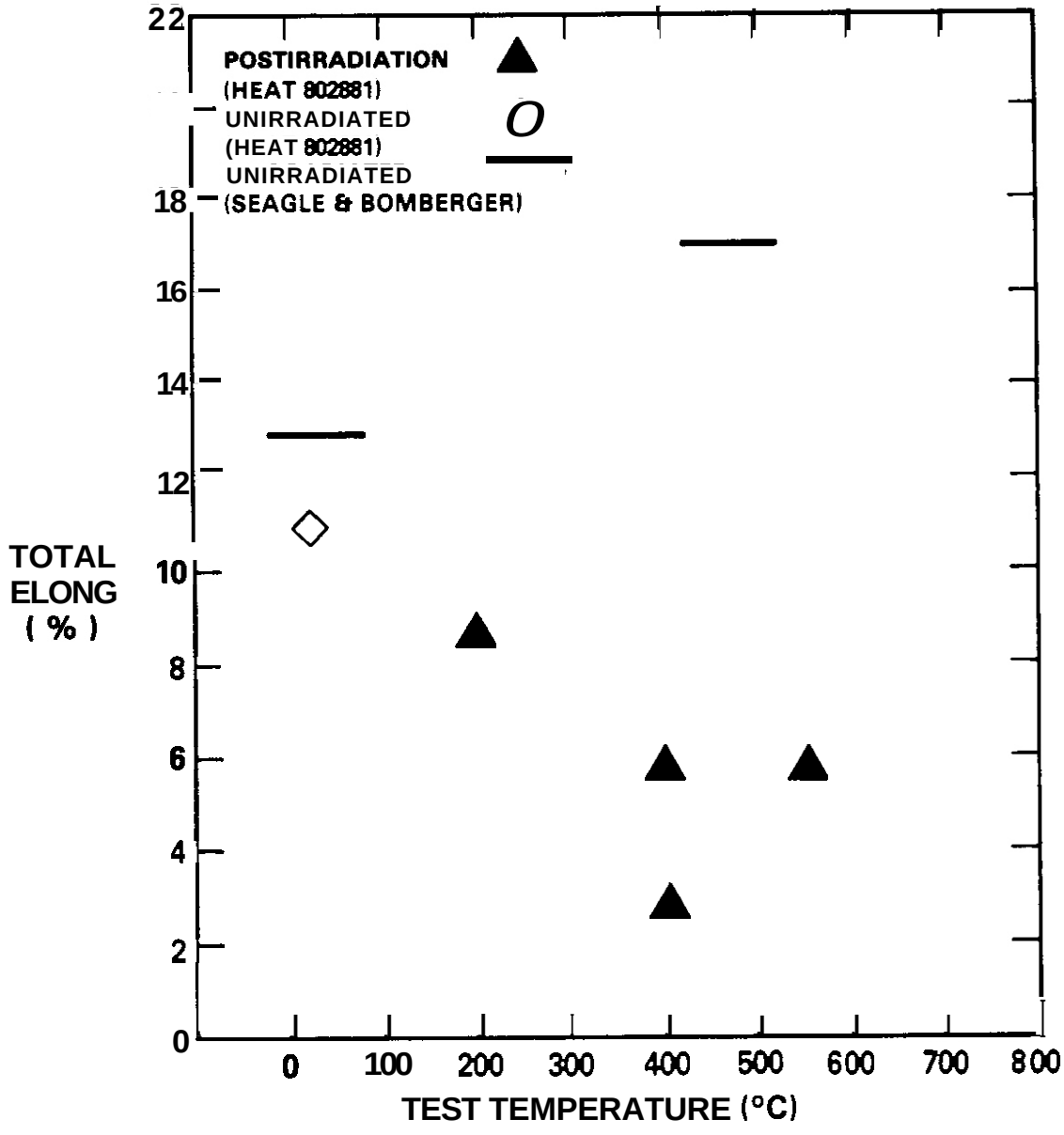

FIGURE 5.2.7 **Effect of Neutron Irradiation on Total Elongation of Alloy** 5621S.

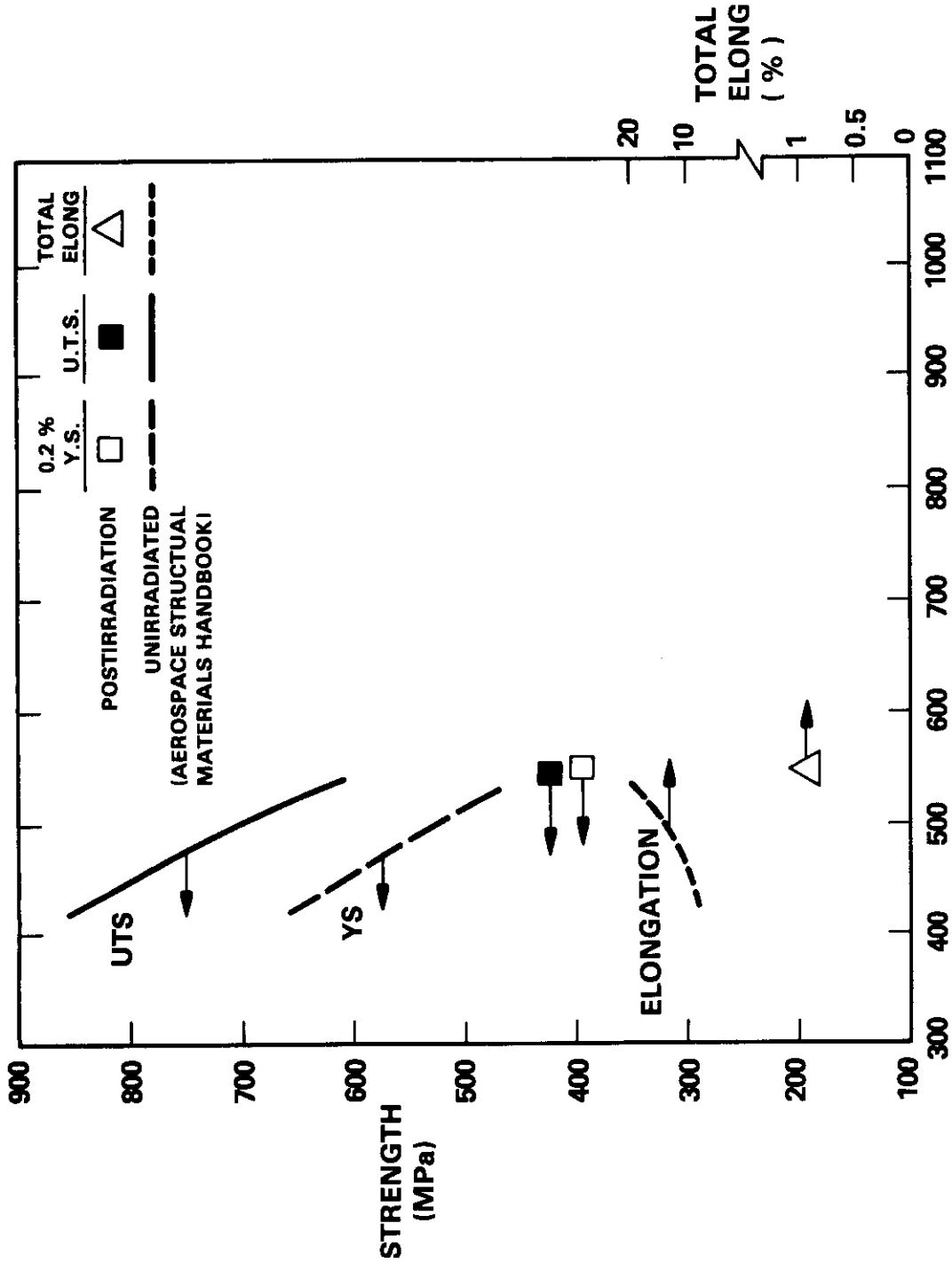

FIGURE 5 2 8 Effect of Neutron Irradiation on Mechanical Properties of Ti-6Al-4V.

n/cm^2 (E>0.1 MeV). The present work thus extends greatly the fluence and temperature range of the mechanical property data base.

Thermal exposure at 550°C, the irradiation temperature of the specimens tested in this work, can strengthen near-a alloys like 6242S and 5621S in subsequent lower temperature tests with little effect on strength at test temperatures near 550°C. An $\alpha + \beta$ alloy like Ti-6Al-4V will in general be softened by exposure at 550°C. Ductility of either type is not greatly affected by 550°C exposure. The strength increases of 6242S upon reactor exposure are thus at least partly due to aging effects. The net effect of irradiation and thermal exposure on 5621S was nil, while the softening observed in the Ti-6Al-4V specimen was undoubtedly a thermal effect. The ductility losses found with all of the alloys cannot be associated with thermal exposure, but must be irradiation or corrosion effects.

The corrosion experienced by the tensile specimens was discovered subsequent to cleaning after removal from the reactor. A significant proportion of the specimens of all alloys discharged from B286 were affected. The corrosion resulted in a dark mottled appearance, localized material removal, and in some cases separation of the specimen into two pieces. The postulated mechanism for the corrosive process was attacked by fused NaK, resulting from reaction with water during cleaning. In-reactor NaK attack was not ruled out, however. A more detailed discussion can be found in Reference 2. The specimens included in the tensile test matrix exhibited the least corrosion, but corrosion cannot be excluded as a possible contributing factor to the postirradiation mechanical properties.

5.2.5 Future Work

Tensile specimens from pins B284 and B285 from AD-1 will be tested next. These pins had irradiation temperatures of 394 and 450°C, respectively, with maximum fluences similar to B286. The corrosion encountered in the specimens from B286 is expected to be minimized. It is highly desirable to isolate the cause of any mechanical property changes to irradiation effects.

5.2.6 References

1. J. O. Stiegler et al., "Alloy Development for Irradiation Performance," *The Fusion Reactor Materials Program Plan,* July 1978.
2. R. J. Puigh and E. K. Opperman, "Examination of Titanium Alloy Specimens Irradiated in EBR-II," *ADIP Quarterly Report,* DOE/ER-0045/1, April 1980.
3. Clifford L. Dotson, "Mechanical and Thermal Properties of High Temperature Titanium Alloys," AFML-TR-67-41, April 1967.
4. S. R. Seagle and H. B. Bomberger, *The Science, Technotogy, and Application of Titanium,* Jaffee and Promisel, eds., Pergamon Press, 1970, p. 1001.
5. *Aerospace Structural Materials Handbook,* 1980 Revision, Code 3707, p. 16.
6. Robert A. Hasse and Charles B. Hartley, "Irradiation Effects on 17-7 PH Stainless Steel, A-201 Carbon Steel, and Ti-6Al-4V Alloy," NASA-TM-X-2678, November 1972.
7. S. M. L. Sastry et al., "Comparison of Titanium Alloy Ti-6A1-4V and 5621S Microstructures After EBR-II Irradiation," *ADIP Quarterly Report,* DOE/ET-0058/4, May 1979.
8. E. K. Opperman, "16 MeV Proton Creep in a Ti-6Al-4V Specimen," *Alloy Development for Irradiation Performance Progress Report,* DOE/ET-0058/1, 1978.
9. R. E. Nygren, "Irradiation Creep Studies of Titanium Alloys," J. *Nucl. Mat.,* 86: 861 (1979).
10. R. H. Jones et al., "Assessment of Titanium Alloys for Fusion Reactor First Wall and Blanket Applications," AP-1433, June 1980.

5.3 MECHANICAL PROPERTY EVALUATIONS OF PATH C VANADIUM SCOPING ALLOYS - R. E. Gold and R. L. Ammon (Westinghouse Electric Corporation)

5.3.1 ADIP Tasks

I.B.11. Stress-Rupture Properties of Reactive/Refractory Metal Alloys (Path C)

I.B.15. Tensile Properties of Reactive/Refractory Metal Alloys (Path C)

5.3.2 Objective

The objective of this program is to develop tensile and creep/stress-rupture data for the unirradiated Path C vanadium Scoping Alloys. In addition, methods will be explored for introducing controlled levels of nonmetallic impurities into test specimens in order to examine their effects on mechanical properties.

5.3.3 Summary

Sheet material of the Path C vanadium Scoping Alloys has been procured from the ETM Research Materials Stockpile and subjected to preliminary recrystallization studies. Based on optical metallography and hardness measurements, a fine, equiaxed ($\sim$ 30 μm grain size) microstructure results from one hour heat treatments at 1100, 1200, and 1350°C for the V-20Ti, V-15Cr-5Ti, and VANSTAR-7 alloys, respectively. Machining of specimens for tensile and creep-rupture testing has been initiated.

5.3.4 Progress and Status

The Path C vanadium-base Scoping Alloys which were prepared for the E M Research Materials Inventory, sited at the Oak Ridge National

Laboratory, are the subject of this evaluation. These include: (compositions in wt. percent)

V-20Ti

V-15Cr-5Ti

VANSTAR-7 (V-9Cr-3.3Fe-1.25Zr-0.054C)

This program was initiated to develop the tensile and stress-rupture data base for the unirradiated alloys. In this respect, it is complementary to the fatigue and crack growth investigations being conducted by K. Liu at the Oak Ridge National Laboratory (see Section 5.4 of this Quarterly and other reports of research in Section 5 of other recent ADIP Quarterly Reports). Because nonmetallic impurities are known to have significant effects on the mechanical behavior of refractory metal alloys, an additional objective of this program is to begin the development of means to introduce controlled levels of impurities such as oxygen and nitrogen into mechanical property specimens.

Specific tasks associated with FY'81 efforts are:

Task 1. Material Procurement

Task 2. Initial Specimen Preparation and Heat Treatments

Task 3. Tensile Evaluations

Task 4. Creep/Stress Rupture Testing

Task 5. Evaluation of the Effects of Nonmetallic Contamination on Mechanical Properties

Task 6. Microstructural Characterizations

Efforts to date have concentrated on Tasks 1 and 2 with some preliminary, supporting efforts on Task 6. These are summarized in the following subsections. In addition a brief review of background information for these alloys is presented.

5.3.4.1 Background

Vanadium Scoping Alloys previously identified for the ADIP Path C activities were prepared as rod and sheet material by Westinghouse for

the ETM Research Materials Inventory.' In FY 1980, Dr. Liu of Oak Ridge National Laboratory began developing fatigue data for these alloys at room and elevated temperatures. To provide similar baseline data for the unirradiated tensile and creep-rupture properties, the present program was initiated in FY 1981.

Compositions identical to the three Scoping Alloys were included in earlier alloy development efforts carried out in support of breeder reactor cladding R&D.[2] The results of microstructural and mechanical property evaluations conducted during those efforts will be of value in interpreting test results for the current program. The densities and melting (solidus) temperatures for these (and similar) alloys were determined; these are tabulated below for general information.

Alloy	Density g/cm^3	Solidus Temperature (°C ± 50°C)
V-20Ti	5.75	1676
V-15Cr-5Ti	6.18	1739
VANSTAR-7	6.32	1728

(Data from Reference 2)

5.3.4.2 Task 1 - Material Procurement

Sheet material for each of the three alloys was requested from the ETM Research Materials Inventory, sited at Oak Ridge. All material was promptly shipped in the form requested - 0.076 cm (0.030 inch) sheet. Approximately 1100 cm^2 (170 in^2) of each alloy was provided.

5.3.4.3 Task 2 - Initial Specimen Preparation

A fully recrystallized, equiaxed (grain size ~ 30-50 μm) microstructure is known to offer optimum time-dependent mechanical properties for the Group V refractory metals and their alloys. Hence, a series of one-hour heat treatments was carried out in order to determine

the appropriate recrystallization temperatures for each of the alloys. The alloys were supplied in a cold-worked (80-90% cold deformation) condition from the EIM Stockpile.

Specimen test coupons, approximately 2 cm x 2 cm, were removed from each alloy, thoroughly cleaned, wrapped in clean tantalum foil, and given 1 hour heat treatments in vacuum (10^{-6} torr) at temperatures from 800°C through 1350°C. Response of the alloys to these heat treatments was determined by optical metallography and hardness measurements. The latter are summarized in Table 5.3.1.

Table 5.3.1.
Results of Hardness Measurements on Path C
Vanadium Alloys Following Heat Treatment*

Annealing Temp., °C	V-20Ti	V-15Cr-5Ti	VANSTAR-7
800	247	305	265
850	224	290	257
900	222	257	197
950	216	221	196
1000	224	216	187
1100	211	-	-
1200	223	215	179
1350	-	-	188

* Hardness Values are for "Vickers Diamond Pyramid Hardness" (DPH) with 10 or 30 kg load. All heat treatments were for 1 hour.

The metallographic examinations indicated the desired ∿ 30 μm grain size was attained in one hour at 1100, 1200, and 1350°C for the V-20Ti, V-15Cr-5Ti, and VANSTAR-7 alloys, respectively. Results of these heat treatments are shown in Figure 5.3.1. Note that these agree very closely with the results of similar heat treatments on rod material of

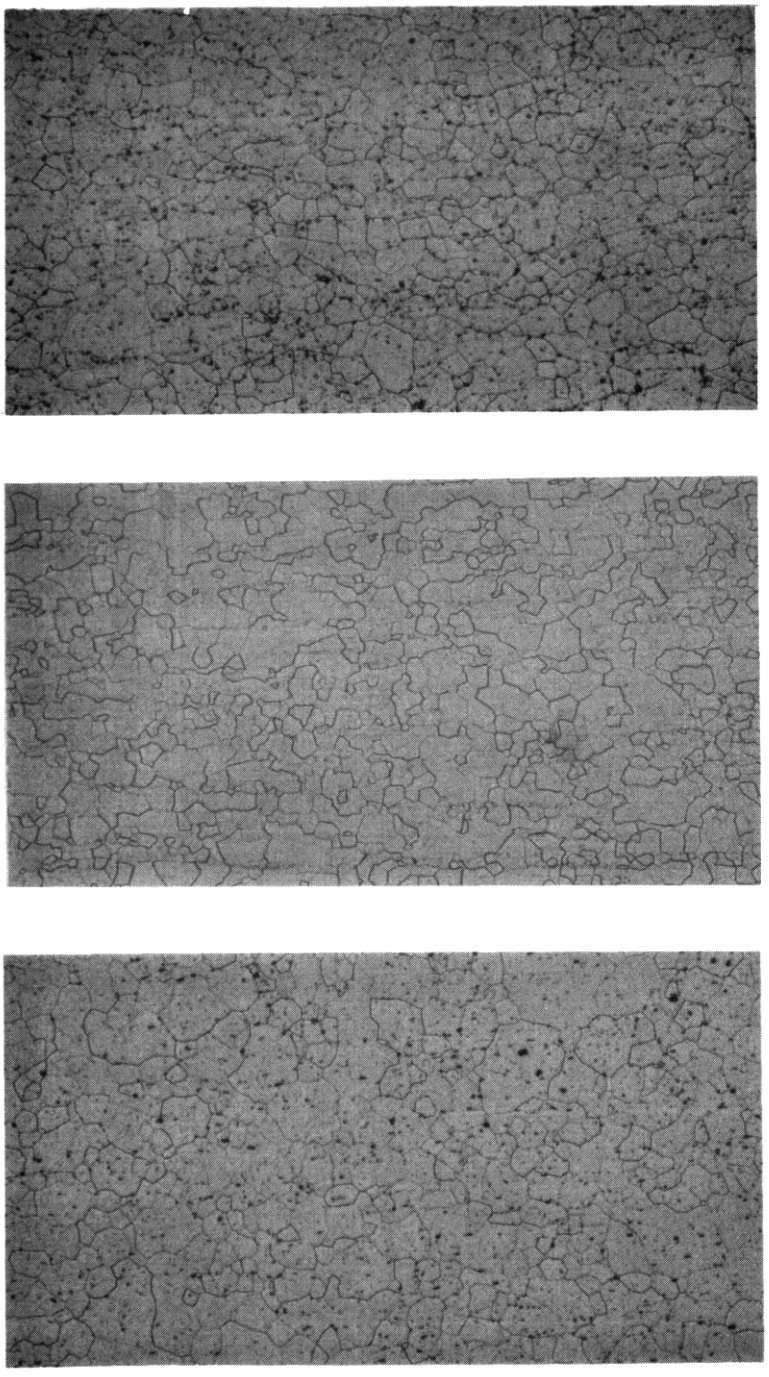

Figure 5.3.1. Optical micrographs of sheet specimens of the Path C Vanadium Scoping Alloys after the one hour heat treatments indicated.

these alloys by K. Liu.[3] The only difference is that Liu finds 1400°C–1 hour preferable for the VANSTAR-7 alloy; the target grain size was again about 30 μm.

Machining of specimens required for Tasks 3 and 4 of this program is currently underway. All material was given the reference recrystallization heat treatments prior to submission for machining.

5.3.6 References

1. R. L. Ammon, "Melting and Processing of Niobium and Vanadium Alloy Sheet and Rod," Report AESD-M-FR-79-004, Westinghouse Advanced Energy Systems Division, Pittsburgh, PA, October 1979.

2. G. A. Whitlow, R. A. Nadler, and R. C. Svedberg, "Vanadium Alloy Cladding Development: Final Report," WARD-3791-47, Westinghouse Advanced Reactors Division, Madison, PA, November 1970.

3. K. C. Liu, Metals and Ceramics Division, Oak Ridge National Laboratory, personal communication, January 1981.

5.4 FATIGUE BEHAVIOR OF PATH C VANADIUM SCOPING ALLOYS — K. C. Liu (ORNL)

5.4.1 ADIP Task

ADIP Task I.B.3, Fatigue Crack Growth in Reactive and Refractory Alloys.

5.4.2 Objective

The objective of this work is to develop baseline fatigue and crack growth data for the Path C refractory metal scoping alloys in the unirradiated condition.

5.4.3 Summary

Limited test data obtained from fully reversed cyclic fatigue tests on unirradiated Vanstar-7 (ADIP heat CAM-836 T-6) at room temperature and 650°C fell consistently below the average trend curves of V–15% Cr–5% Ti tested at the corresponding temperatures. It appears that V–15% Cr–5% Ti has superior fatigue resistance to Vanstar-7.

5.4.4 Progress and Status

5.4.4.1 Fatigue Testing of V–15% Cr–5% Ti

Fully reversed strain-controlled fatigue tests on this alloy were continued, bringing the total number of completed tests to 14. Tests in the low-cycle range, with total cyclic strain range $\Delta\varepsilon_t \geq 1.0\%$, showed consistent results. However, some results obtained from the tests in the high cycle range, $\Delta\varepsilon_t < 1.0\%$, were inconclusive due to a gripping problem discussed below.

The fatigue lifetime data on V–15% Cr–5% Ti tested in vacuum are summarized in Table 5.4.1 and plotted in Fig. 5.4.1. Two of the most recent tests (AV-515 and -520) fall closely on the room temperature $\Delta\varepsilon_t - N_f$ (N_f = cycles to failure) curve established earlier.' However, tests AV-514 and –513 conducted at a strain range of 0.8% and at 550 and 650°C, respectively, ended with fractures outside the gage section. No useful information was obtained and the test failures were apparently due to a problem with the lower grip.

Table 5.4.1. **Fatigue Lifetime Test Data** for V–15% Cr–5% Ti

Specimen[a]	Test Temperature (°C)	Total Strain Range (%)	Maximum Total Cyclic Stress Range, Δσ (MPa)	Cycles to Failure	Mode of Test Control[b]	Comments
AV–53	27	2.0	1340	4,345	SC	
AV–51	27	1.0	1200	109,125	SC	
AV–515	23	0.9	1074	781,200	SC/LC	
AV–520	20	0.8	922	1,860,000	SC/LC	
AV–52	27	0.6	830	>2,047,020	SC/LC	c
AV–510	550	2.0	1240	3,783	SC	
AV–58	550	1.0	1080	43,555	SC	
AV–514	550	0.8	964	>260,220	SC/LC	d
AV–511	550	0.75	920	>1,072,410	SC/LC	d
AV–54	650	2.0	1228	1,874	SC	
AV–56	650	1.0	1080	19,452	SC	
AV–513	650	0.8	892	>16,132	SC	d
AV–55	650	0.6	717	>171,539	SC/LC	d
AV–57	650	0.6	717	>951,302	SC/LC	d

[a] All specimens were annealed 1 h at 1200°C in vacuum.

[b] SC = strain control with $\dot{\varepsilon}_t = 4 \times 10^{-3}$/s; SC/LC = strain control transferred to load control with $\dot{\varepsilon}_t = 4 \times 10^{-2}$/s when the response becomes elastic.

[c] Specimen did not fail; test discontinued.

[d] Specimens ruptured outside the gage section.

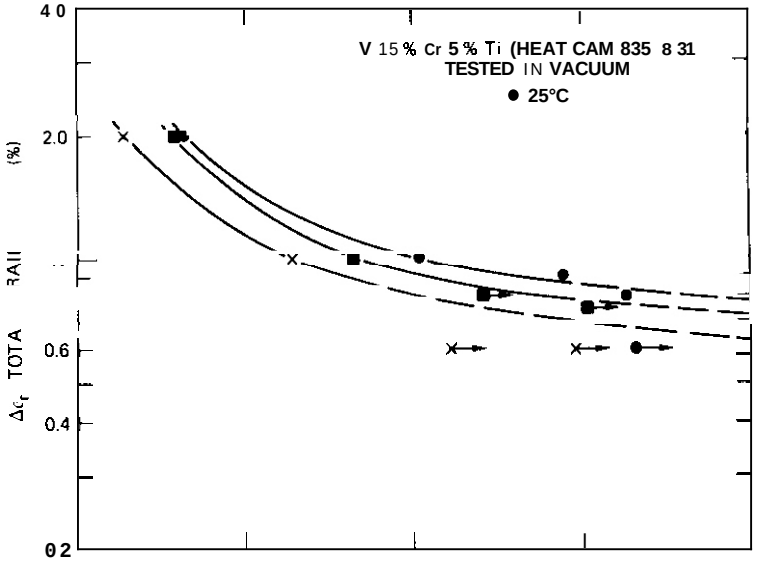

Based on earlier results,' we believed that this alloy might be sensitive to variations in mean stress and/or to the presence of stress risers when cycled in the high-cycle range at high temperature. This conclusion was based on the observation that fatigue failure sometimes occurred outside the gage section of the specimen, either in the threads or on the specimen shoulder at the point of thermocouple attachment.

In recent tests it was determined that excessive strain might have been imposed to the shoulder and threads of the specimen when the jam nuts were torqued down. To avoid recurrence of such failures, considerable care was exercised in specimen preparation and installation in the test rig. Test temperature was controlled through a thermocouple attached to the lower grip. A torque of about 1.5 to 2.5 N•m was used to thread the specimen in the grips and secure them with jam nuts. Following this procedure, two room temperature tests were carried out successfully to specimen failure at a total strain range of 0.9 and 0.8%. However, two other tests at high temperature were not successful. Specimen AV-513, tested at 650°C and $\Delta\varepsilon_t$ = 0.8%, apparently had poor grip connections and the situation worsened as the test progressed. This test was discontinued at 16,132 cycles because the threads galled beyond repair. A second specimen (AV-514), cycled to $\Delta\varepsilon_t$ = 0.8% at 550°C, was carefully installed and secured in the grip by a torque of about 2.5 N•m. This specimen ruptured at the first thread as had an earlier test (AV-511) under similar test conditions.

We conclude that existing grips and/or the specimen configuration need design modifications. Therefore, the remaining high-cycle fatigue tests will be deferred until changes have been made. A realignment of the load column is also scheduled to ensure that the problem was not caused by misalignment.

The additional tests on V-15% Cr-5% Ti support earlier observations' that this alloy has an endurance limit in terms of total strain ranges of about 0.7 and 0.6% at 550 and 650°C, respectively.

5.4.4.2 Fatigue Testing of Vanstar-7

Low-cycle fatigue tests on Vanstar-7 (ADIP heat CAM-836 T-6) have been initiated. Specimens were machined from 6.5-mm-diam rods that had

been annealed 1 h at 1400°C in vacuum. This heat treatment gave the desired grain size, within the range ASTM 6.5 to 7.5. The specimens were stress relieved in vacuum at 1400°C for 0.5 h after machining. The Vanstar-7 specimen geometry was identical to that used for the V-15% Cr-5% Ti.

Five tests have been completed and the results are summarized in Table 5.4.2 and plotted in Fig. 5.4.2. The three trend curves obtained for V-15% Cr-5% Ti are also shown in Fig. 5.4.2, as a basis for comparison of the Vanstar-7 data. All Vanstar-? data fell below the curve for the corresponding test temperature of V-15% Cr-5% Ti. A 'reduction of fatigue lifetime prevailed throughout the test strain range, by a factor of about 2 to 3 in the higher strain range ($\Delta\varepsilon_t \geq 1.0\%$) and by a factor of about 10 OK more in the lower strain range ($\Delta\varepsilon_t < 1.0\%$). The limited data suggest that the V-Cr-Ti alloy has better fatigue properties than does Vanstar-?.

Table 5.4.2. Fatigue Lifetime Test Data for Vanstar-7

Specimen[a]	Test Temperature (°C)	Total Strain Range (%)	Maximum Total Cyclic Stress Range, Aa (MPa)	Cycles to Failure	Mode of Test Control[b]	Comments
vs-72	20	1.0	1172	29,344	SC	
vs-73	25	0.8	958	-290,000	SC	
vs-74	25	0.7	869	2,397,240	SC/LC	c
vs-75	650	2.0	1103	1,703	SC	
vs-71	650	1.0	930	8.938	SC	

[a] All Specimens were annealed 1 h at 1400°C in vacuum.

[b] SC = strain control with $\dot{\varepsilon}_t = 4 \times 10^{-3}$/s; SC/LC = strain control transferred to load control with $\dot{\varepsilon}_t = 4 \times 10^{-2}$/s when the response becomes elastic.

[c] Test switched from strain control to stress control after 24,820 cycles.

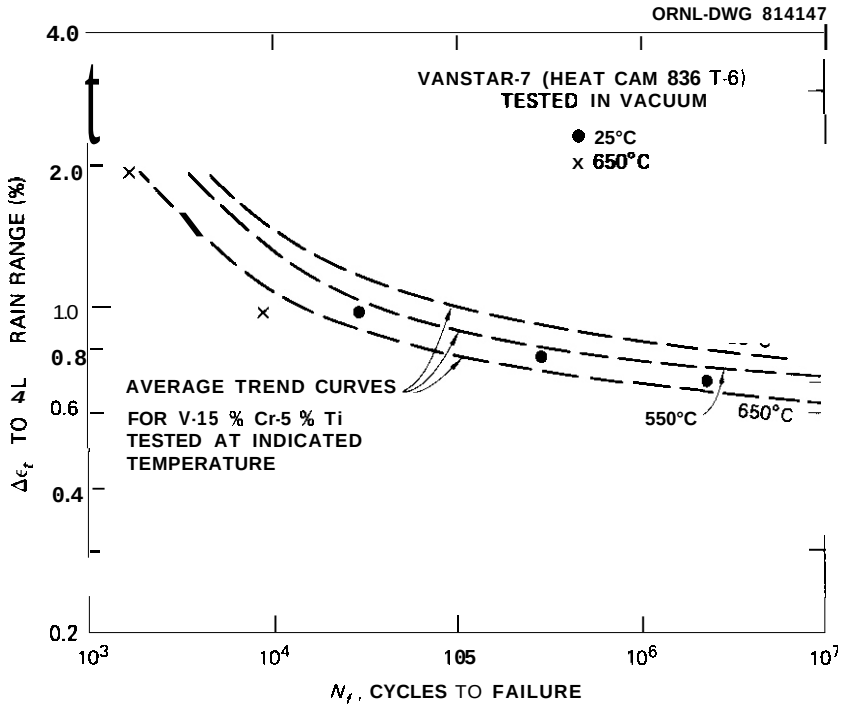

Fig. 5.4.2. Cyclic Fatigue Data for Vanstar-7 Tested at Room Temperature and 650°C in Vacuum. Trend curves for V—15% Cr—5% Ti are included for comparison.

5.4.5 Reference

1. K. C. Liu, "Fatigue Behavior of Unirradiated V—15% Cr—5% Ti," *ADIP Quart. Prog. Rep. Sept. 30, 1980*, DOE/ER-0045/4, pp. 100—04.

5.5 INITIAL OBSERVATION OF VOIDS IN NEUTRON IRRADIATED TITANIUM ALLOYS - D. T. Peterson (Hanford Engineering Development Laboratory).

5.5.1 ADIP Task

Task Number I.C.4 - Microstructures and Swelling in Reactive/Refractory Alloys (Path C).

5.5.2 Objective

The objective of this work is to characterize the swelling and microstructural response of titanium alloys during neutron irradiation.

5.5.3 Summary

A preliminary transmission electron microscopy examination of Ti-6242s irradiated to 5.0 x 10^{22} n/cm^2 (E >0.1 MeV) at 550°C has revealed the presence of voids in this near-alpha alloy. The voids were observed only in the primary alpha grains and do not constitute a large volume fraction.

5.5.4 Progress and Status

5.5.4.1 Introduction

Very little is known about the effect of irradiation on the microstructures and mechanical properties of titanium alloys. The AD-1 experiment was designed to provide such information on a series of titanium alloys consisting of the near-alpha alloys Ti-6Al-2Sn-4Zr-2Mo-0.09Si and Ti-5Al-6Sn-2Zr-1Mo-0.25Si; the alpha-beta alloy Ti-6A1-4V; and the beta alloy Ti-3Al-8V-6Cr-4Mo-4Zr. These materials were irradiated in EBR-II at 394, 450 and 550°C. The 394°C capsule attained a fluence of 4.2 x 10^{22} n/cm^2 (E >0.1 MeV) while the 450 and 550°C capsules attained a fluence of 5.0 x 10^{22} n/cm^2 (E >0.1 MeV). [1] At present only the specimens from the 550°C capsule are available.

5.5.4.2 Preliminary Results

At present only Ti-62425 has been examined, Prior to irradiation this alloy was given a duplex anneal consisting of 900°C/0.5 hr/AC +

788°C/0.25 hr/AC + 718°C in vacuum/4 hr/Argon Cool. This heat treatment produced a structure consisting predominately of equiaxed primary alpha grains with some small regions of transformed beta.

The predominate irradiation induced microstructural changes were the formation of a uniform distribution of fine features and the formation of voids. The fine structure produced is illustrated in Figure 5.5.1 (a). This structure was present in most of the alpha grains. The nature of these features has not yet been determined. Voids were observed only in the alpha grains and are inhomogeneously distributed. Most grains contained very few voids. When voids were present they were usually associated with regions denuded of the fine structure as illustrated in Figure 5.5.1 (b). A few grains were found to have fairly uniform distributions of voids. An example is shown in Figure 5.5.1 (c) (several instances of void coalescence are apparent in this figure). These grains were always found to be devoid of the fine structure observed in the other grains. Overall the void volume fraction is small and does not constitute a significant degree of void swelling.

5.5.4.3 Future Work

The electron microscopy examination will be continued on this material and will be initiated on the other alloys and irradiation conditions. The examination will be expanded to include EDAX analysis to determine if any microchemical segregation has occurred. Immersion density measurements will also be performed on the specimens.

5.5.5 Conclusions

Voids have been observed in Ti-6242s irradiated to 5.0×10^{22} n/cm^2 at 550°C. Although voids have been observed in ion-bombarded Ti-64[2] this is the first observation of voids in neutron irradiated titanium alloys.

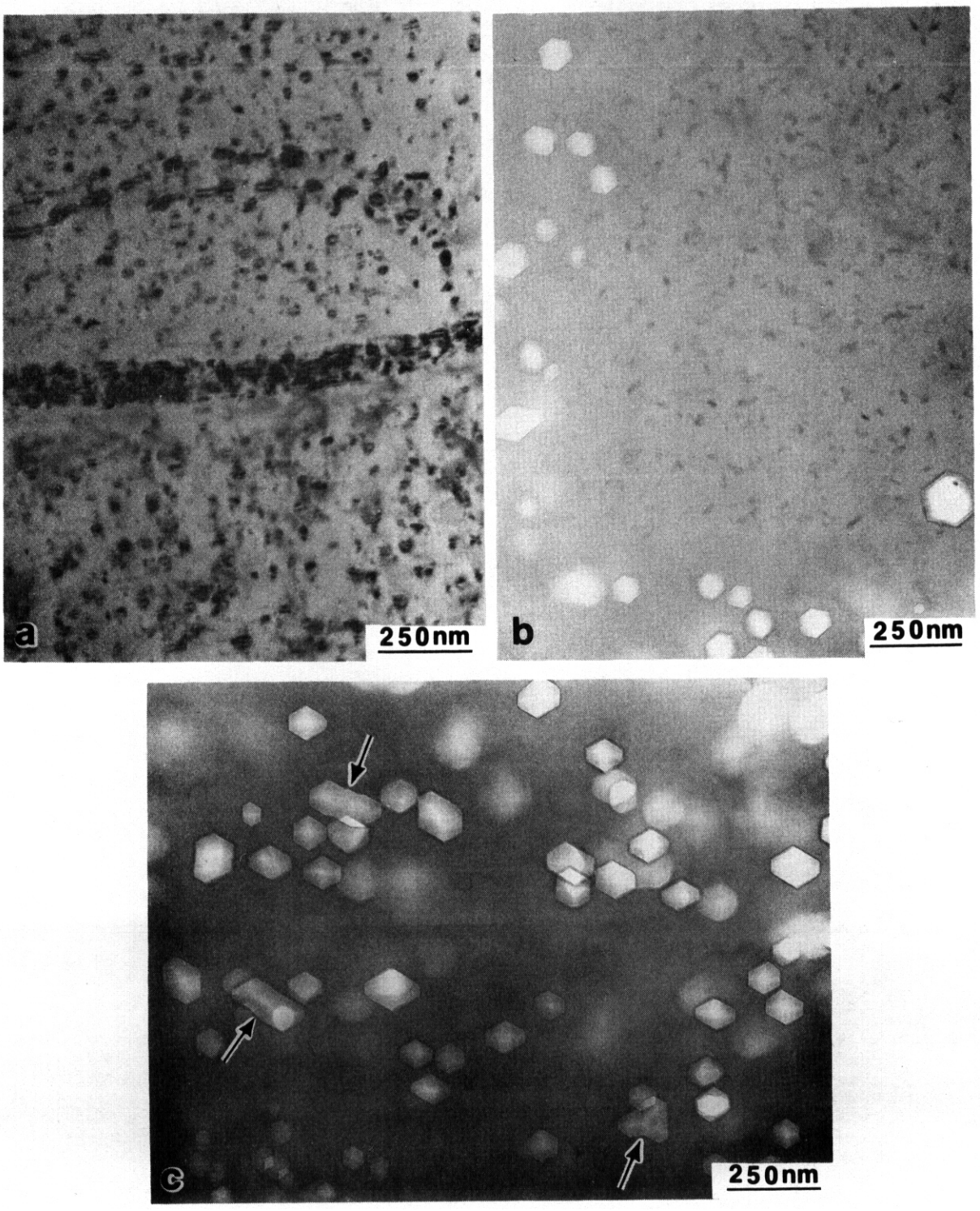

Fig. 5.5.1. The microstructure of Ti-62425 following irradiation at 550°C. (a) Irradiation induced fine structure. (b) Voids formed in a region denuded of the fine structure. (c) Grain with a relatively uniform void distribution. The arrows indicate examples of void coalescence.

5.5.6 References

1. R. J. Puigh and E. K. Opperman, "Examination of Titanium Alloy Specimens Irradiated in EBR-II," *ADIP Quarterly Report*, October-December, 1979.
2. S. C. Agerwal et al, "Microstructure of Single and Dual-Ion Irradiated Fe-20Ni-15Cr and Ti-6A1-4V Alloys," *J. Nuc. Mat.*, 85 and 86 (1979), 653.

6. PATH D ALLOY DEVELOPMENT — INNOVATIVE MATERIAL CONCEPTS

6.1 DEVELOPMENT OF IRON-BASE ALLOYS WITH LONG-RANGE-ORDERED CYRSTAL STRUCTURE — C. T. Liu (ORNL)

6.1.1 ADIP Task

ADIP Task I.B.12, Stress-Rupture Properties of Special and Innovative Materials, Task I.B.16, Tensile Properties of Special and Innovative Materials, and Task I.C.l, Microstructural Stability.

6.1.2 Objective

The objective of this study is to develop a unique class of high-temperature alloys — ductile long-range-ordered (LRO) alloys based on $(Fe,Ni)_3V$ — and to evaluate their potential for use as structural materials for fusion energy systems.

6.1.3 Summary

The iron-base LRO alloys with base compositions $(Fe,Ni)_3V$ are being developed for fusion energy applications. The base alloys are also modified with less than 1% Ti for further improvement in metallurgical and mechanical properties. We have found that the phase relation in the LRO alloys depends strongly on the nickel concentration. The disordered face-centered cubic (fcc) solid solution (gamma phase) starts to precipitate sigma phase at 1000°C in the 32% Ni–0.9% Ti alloy, and $\gamma + \sigma$ phase field extends down to the critical ordering temperature, T_c = 690°C. The existence of the sigma phase (σ), with tetragonal crystal structure, is not desirable, because, in some cases, the retention of the σ phase below T_c lowers the ductility and weakens atomic order in the alloys. The sigma phase region can be eliminated by increasing the nickel content to *40%.* The LRO alloys show excellent creep resistance and structural stability. Long-term aging at 550°C does not cause any significant change in the tensile properties of the LRO alloys. The creep rate of the LRO alloys is lower than that of annealed type 316 stainless steel by more than 3 orders of magnitude. Ingots of the 40% Ni–0.4% Ti alloy were prepared by using commercially produced ferrovanadium, to lower the material cost. The heats prepared from ferrovanadium show finer grain structure and higher yield strength, compared to the heat prepared from pure vanadium. The ferrovanadium heats are ductile, with tensile elongation exceeding 30% at all test temperatures.

6.1.4 Progress and Status

6.1.4.1 Introduction

Long-range-ordered alloys generally offer significant advantages Over conventional or disordered alloys for high-temperature structural applications.[1,2] This is based largely on relatively slow solid-state diffusion processes and unique dislocation dynamics of ordered lattices. The main difficulty limiting the use of LRO alloys is their low ductility and fabricability in the ordered state. Recently, our work on cobalt-base LRO alloys with compositions $(Co,Fe)_3V$ has overcome this limitation.[3] We have demonstrated that the ductility of the ordered alloys can be controlled by adjusting alloy composition and ordered crystal structure. The alloys with cubic ordered structure ($L1_2$-type) are ductile and fabricable with tensile elongation in excess of 30% at room temperature. Alloys with lower cobalt contents would offer the potential of higher tritium breeding ratios, lower levels of structural activation, and lower alloy production costs. For these reasons we are developing cobalt-free, iron-base LRO alloys for fusion applications at temperatures to 700°C.

6.1.4.2 Phase Relationships and Ordered Structure

Several iron-base LRO alloys were prepared based on the compositions $(Fe,Ni)_3V$. Table 6.1.1 lists the nominal composition of the alloys we have prepared. The base alloys $(Fe,Ni)_3V$ are also modified with less than 1% Ti for further improvement in metallurgical and mechanical properties.

The phase relationship and ordered structure in the iron-base LRO alloys were determined by quenching and aging studies, followed by metallographic examination and x-ray diffraction. We have found that the phase relationship in the alloys depends strongly on the nickel concentration. Figure 6.1.1 compares the phase relation in three alloys containing 32% Ni (LRO-39), 36% Ni (LRO-41), and 40% Ni (LRO-38). All the alloys are in the face-centered cubic disordered state, referred as gamma phase (γ) at high temperatures. The gamma phase starts to precipitate sigma phase (σ) at 1000°C in the 32% Ni alloy, and the $\gamma + \alpha$ phase field extends to 690°C, which is the critical ordering temperature (T_o) of the

Table 6.1.1. Nominal Composition of the Iron-Base Long-Range-Ordered Alloys Currently Being Evaluated

Alloy	Composition, wt %		Critical Ordering Temperature (°C)
	Base	Titanium-Modified Alloys	
LRC-16	Fe-31.0 Ni-23.0 V		670
-35		Fe-31.8 Ni-22.5 W . 4 Ti	690
-36		Fe-31.8 Ni-22.0 W . 9 Ti	690
LRC-40	Fe-35.7 Ni-22.9 V		
-41		Fe-35.7 Ni-22.0 W . 9 Ti	700
LRO-20	Fe-39.5 Ni-22.9 V		700
-37		Fe-39.5 Ni-22.4 W . 4 Ti	720
-38		Fe-39.5 Ni-22.0 W . 9 Ti	710

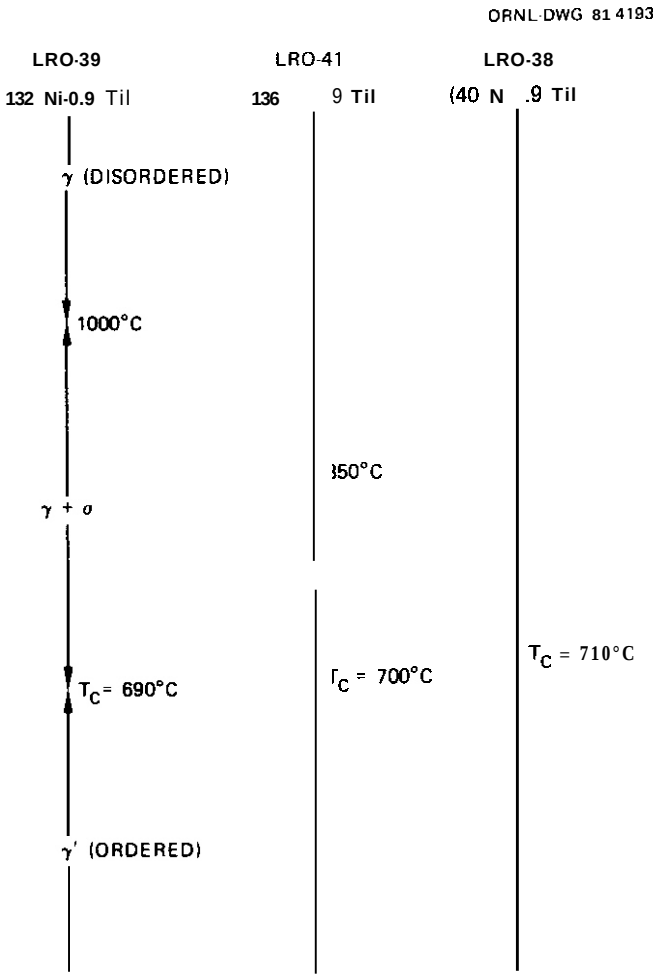

Fig. 6.1.1. Phase Relationship in the LRO Alloys Based on $(Fe,Ni)_3V$, with 32 to 40% Ni, 22% V, and 0.9% Ti.

alloy. Below T_o, atom ordering takes place and the alloy forms a single-phased cubic ordered structure γ' ($L1_2$-type). The existence of sigma phase, with tetragonal crystal structure, is not desirable, because, in some cases, the retention of the sigma phase below T_o (e.g., during slow cooling at temperatures in the $\gamma + \sigma$ phase field) will lower the ductility and weaken atomic order in these alloys. In the 36% Ni alloy the sigma phase starts to form at 850°C, rather than 1000°C in the 32% Ni alloy, resulting in a narrower $\sigma + \gamma$ region in LRO-41. The sigma-phase region is eliminated in the alloy containing 40% Ni, as indicated in Fig. 6.1.1. In this alloy, the disordered gamma transforms directly to the ordered γ' at 710°C (T_o). The elimination of sigma with increase in the nickel content is in agreement with the prediction from the Phacomp procedure[4,5] which is commonly used to predict the stability of sigma phase superalloys. According to the Phacomp procedure, the sigma phase becomes unstable with increasing electron density (e/a) in alloys. The e/a for nickel is 10, and e/a for iron is 8. The average e/a of the LRO alloys increases with increasing nickel content, which reduces the stability of the sigma phase.

The critical ordering temperature, T_o, of the LRO alloys was measured from quenching, x-ray diffraction, and measurement of physical and mechanical properties. The results arse presented in Table 6.1.1 and Fig. 6.1.1. The T_o of the LRO alloys appears to increase slightly as nickel content increases.

6.1.4.3 Tensile Properties

The effect of ordered state and precipitation of sigma phase on tensile properties of the 32% Ni, 36% Ni, and 40% Ni alloys was determined at room temperature at a strain rate of 3.3×10^{-3}/s. The single-phased ordered structure was produced by quenching specimens from 1100°C and then aging at 500 to 650°C. Aging for 500 h at 725°C (>T_o of the alloys) caused a precipitation of sigma phase in the disordered gamma solid solution in the 32% Ni and 36% Ni alloys but not in the 40% Ni alloy. Figure 6.1.2 shows the precipitation of sigma phase in the 32% Ni alloy produced by the heat treatments. The corresponding tensile properties at room temperature are presented in Table 6.1.2. All the alloys in the

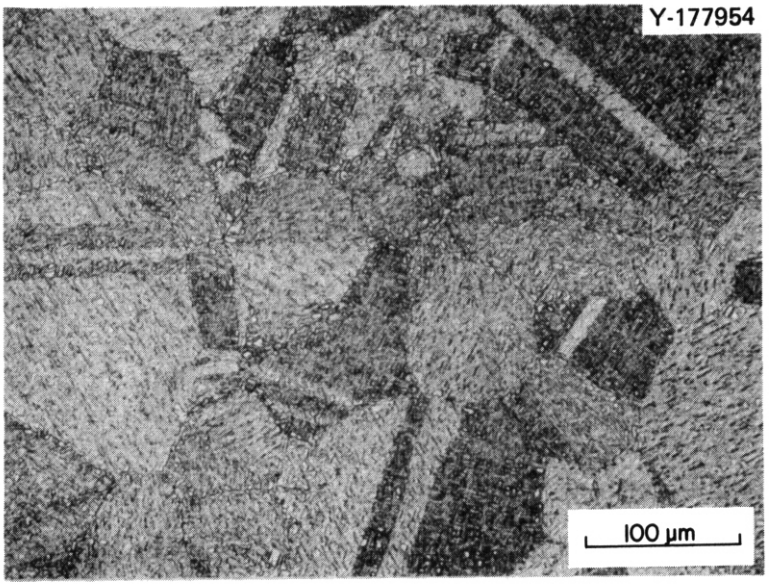

Fig. 6.1.2. Precipitation of Sigma Phase in the 32% Ni Alloy Aged for 500 h at 725°C.

Table 6.1.2. Tensile Properties[a] of LRO-38, -39, and -41 Tested at Approximately 20°C

Alloy Designation and Composition (wt %)	State	Total Elongation (%)	Strength, MPa	
			Yield	Ultimate
LRO-39 (32 Ni-0.9 Ti)	Ordered	44.1	252	1056
-39[b]	Disordered + σ phase[a]	6.1	768	1158
LRO-41 (36 Ni-0.9 Ti)	Ordered	42.0	265	1099
-41[b]	Disordered + σ phase[a]	27.1	435	888
LRO-38 (40 Ni-0.9 Ti)	Ordered	40.5	255	1142
-38[b]	Disordered[a]	48.6	308	758

[a]Strain rate 3.3 x 10^{-3}/s.

[b]Specimens were aged at 725°C for 500 h.

ordered state are ductile with total elongations exceeding 40%. The massive precipitation of sigma phase in the 32% Ni alloy causes a threefold increase in yield strength but a reduction in total elongation to 6.1%. The 36% Ni alloy showed a moderate increase in yield strength and a decrease in ductility. Since no sigma phase is formed during aging of the 40% Ni alloy at 725°C, it exhibited better ductility in the disordered state than in the ordered state. Thus, the precipitation of sigma phase in the LRO alloys increases the yield strength at the expense of ductility.

6.1.4.4 Long-Term Aging Study

Specimens of the base alloy LRO-20 and the titanium-modified alloy LRO-35 were encapsulated in vacuum and aged at 550°C for up to 4000 h to evaluate the long-term structural stability and mechanical property effects. The tensile properties of the aged specimens were determined at room temperature, 550, and 650°C at a strain rate of 3.3×10^{-3}/s. The tensile tests at elevated temperatures were performed in a water-cooled quartz-tube vacuum system, where temperatures were attained in an inductively heated tantalum susceptor. Table 6.1.3 presents the tensile properties of the aged material and compares these with the properties of control material. Both alloys exhibited an increase in yield strength and a decrease in total elongation with increasing test temperature. The comparison between the aged and control materials indicates that long-term aging at 550°C does not cause any significant change in the tensile properties of the base and titanium-modified alloys, demonstrating the structural stability of the LRO alloys.

6.1.4.5 Creep Properties

The creep properties of the LRO alloys were determined at 650°C under stresses of 276 and 414 MPa. Creep tests were performed in vacuum under dead-load arrangement. The results are presented in Table 6.1.4 and compare with those obtained from annealed type 316 stainless steel. The creep rate of the LRO alloys appears to decrease on adding titanium and

Table 6.1.3. Tensile Properties[a] of LRO Alloys Aged at 550°C in Vacuum

Alloy	Aging Time[b] (h)	Total Elongation (%)	Strength, MPa (ksi)	
			Yield	Ultimate
		Tested at Room Temperature		
LRO–20	0	43.8	309 (44.9)	1054 (153)
–20	2000	40.8	336 (48.8)	1188 (173)
–20	4000	41.6	290 (42.1)	1143 (166)
LRO–35	0	42.1	270 (39.2)	1124 (163)
–35	2000	40.3	309 (44.8)	1216 (177)
	4000			
		Tested at 550°C		
LRO–20	0	29.0[c]	356 (51.6)'	792 (115)[c]
–20	2000	33.1	378 (54.9)	909 (132)
	4000			
LRO–35	0	37.0'	355 (51.5)'	854 (124)'
–35	2000	34.2	362 (52.5)	903 (131)
–35	4000	35.3	359 (52.1)	868 (126)
		Tested at 650°C		
LRO–20	0	23.1	377 (54.7)	697 (101)
–20	2000	23.5	443 (64.4)	834 (121)
–20	4000			
LRO–35	0	33.6	391 (56.8)	827 (120)
–35	2000	32.2	392 (57.0)	758 (110)
–35	4000			

[a]Strain rate 3.3 × 10^{-3}/s. Elevated temperature tests in vacuum.

[b]At 550°C.

'Estimated based on plot of tensile properties as a function of test temperature.

nickel content. The minimum creep rate of the LRO alloys is lower than that of solution annealed type 316 stainless steel by more than 3 orders of magnitude. The LRO alloys did not rupture in the test durations of 1000 to 1500 h.

Table 6.1.4. Vacuum Creep Properties of Iron-Base LRO Alloys Tested at 650°C

Alloy Designation and Composition (wt %)	Stress (MPa)	Stress (ksi)	Minimum Creep Rate (10^{-6}/h)	Rupture Life[a] (h)
LRO-16 (31 Ni)	276	40	9.0	>1000
LRO-20 (40 Ni)	276	40	3.0	>1500
LRO-35 (32 Ni-0.4 Ti)	276	40	2.6	>1000
Type 316 stainless Steel[b]	276	40	10,000	~20
LRO-35 (32 [illegible])	[illegible]	60	20	>1000
LRO-37 (40 Ni-0.4 Ti)	414	60	11	>1100

[a]All LRO alloy tests discontinued without rupture.

[b]Solution annealed condition.

6.1.4.6 Preparation of Iron-Base LRO Alloys by Using Ferrovanadium

The iron-base LRO alloys currently being developed contain 22 to 23 wt % V (Table 6.1.1). The material cost of the alloys would be greatly reduced if commercially produced ferrovanadium feedstock could be used in place of pure vanadium. Commercial ferrovanadium generally contains 80 to 85% V and 10 to 15% Fe with impurities including 1 to 4% O and less than 2% Al and Si. The impurities can be significantly lowered by electron-beam melting. Two ingots of the 40% Ni-0.4% Ti alloy were prepared; LRO-37-5 was produced from as-received ferrovanadium, and LRO-37-6 from electron-beam remelted ferrovanadium. The ingots were fabricated into 0.6-mm sheets without difficulty. Figure 6.1.3 compares the grain structure of the 40% Ni-0.4% Ti alloy prepared from pure vanadium (LRO-37) and ferrovanadium (LRO-37-5). Both specimens were annealed for 20 min at 1150°C, followed by aging for 73 h at 750°C. The specimen prepared from pure vanadium shows coarse grain structure while the specimen from ferrovanadium exhibits much finer grain structure. This suggests that some impurities introduced from the ferrovanadium retards grain growth in the alloy.

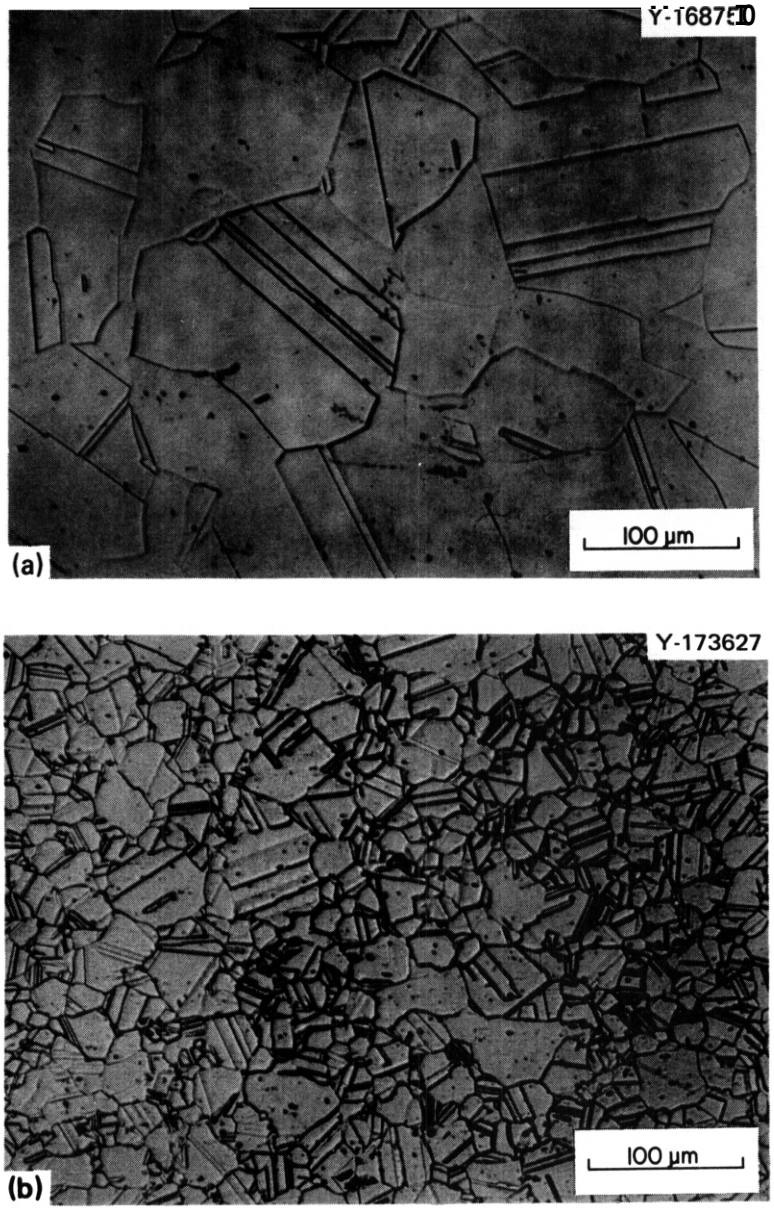

Fig. 613. Comparison of Grain Structure of (a) LRO-37 Prepared from Pure Vanadium, and (b) LRO-37-5 from As-Received Ferrovanadium.

Figure *6.1.4* compares the tensile properties of the 40% Ni–0.4% Ti alloy prepared from pure vanadium and ferrovanadium. All the heats show a positive temperature dependence of the yield strength that reaches a maximum around T_c. However, the heats prepared from ferrovanadium exhibit much higher yield strength, possibly due to greater concentrations of carbide/oxide precipitates in LRO-37-5 and -6. The yield strength of LRO-37-5 reaches 480 MPa at 650°C. The ferrovanadium heats are ductile with total tensile elongation exceeding 30% at all test temperatures (Fig. *6.1.4).* The elongation of the ferrovanadium heat is somewhat lower than that of the pure vanadium heat at temperatures below 700°C; however, there is no major difference in ductility.

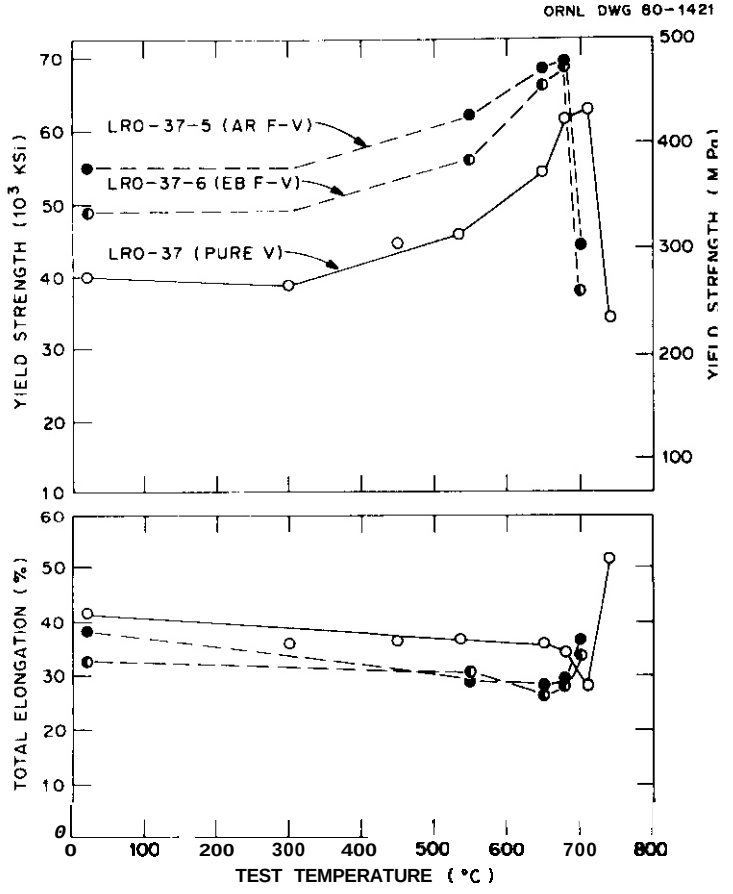

Fig. *6.1.4.* Comparison of the Tensile Properties of the *40%* Ni–*0.4%* Ti Alloy Prepared from Pure Vanadium and As-Received (AR) and Electron-Beam (EB) Melted Ferrovanadium (F-V).

6.1.5 Conclusion and Future Work

The iron-base LRO alloys with compositions listed in Table 6.1.1 are being developed for possible fusion energy applications. Studies of the phase relationship in the LRO alloys indicate that the stability of sigma phase depends strongly on the nickel concentration. The sigma phase region existing in the 32% Ni alloy can be completely eliminated by increasing the nickel content to 40%. This is in agreement with the prediction from the Phacomp procedure, which is commonly used to predict the stability of sigma phase in superalloys. The LRO alloys show excellent creep resistance and structural stability. Long-term aging at 550°C does not cause any significant change in the tensile properties of the LRO alloys. The creep rate of the LRO is lower than that of the annealed type 316 stainless steel by more than 3 orders of magnitude. Ingots of the 40% Ni–0.4% Ti alloy were prepared from commercially produced ferrovanadium. Preliminary evaluation of metallurgical and mechanical properties indicates that preparation of the LRO alloys from ferrovanadium is a promising approach to lowering the alloy production cost.

Our program is continuing to develop and characterize the iron-base ordered alloys for fusion energy applications. Emphasis will be placed on the scaleup of the 40% Ni–0.4% Ti alloy for detailed evaluations. We currently subcontract to Rensselaer Polytechnic Institute (RPI) for primary evaluation of the fatigue properties of the LRO alloys.

6.1.6 References

1. N. S. Stoloff and R. G. David, "The Mechanical Properties of Ordered Alloys," *Prog. Mater. Sci.* 13(1): 1-84 (1966).
2. B. H. Kear, C. T. Sims, N. S. Stoloff, and J. H. Westbrook, **Eds.,** *Ordered Alloys – Structuml and Physical Metallurgy, Proc. 3d Bolton Landing Conference, Lake George, N. Y., Sept. 8–10, 1969,* Claitor's Publishing Division, Baton Rouge, La., 1970.
3. C. T. Liu and H. Inouye, "Control of Ordered Structure and Ductility of $(Fe,Co,Ni)_3V$ Alloys," *Metall. Tmns.* 10A(10): 1515–25 (1979).
4. H. J. Murphy, C. T. Sims, and A. M. Beltran, *J. Metals, 20:* 46 (1968).
5. L. R. Woodyatt, C. T. Sims, and J. H. Beattie, *Tmns. TMS-AIME,* 236: 519 (1966).

6.2 THE EFFECT OF 4-MeV NICKEL ION IRRADIATION ON THE MICROSTRUCTURE OF $(Fe,Ni)_3V$ LONG-RANGE-ORDERED ALLOYS — D. N. Braski (ORNL)

6.2.1 ADIP Task

ADIP Task I.C.5, Microstructure and Swelling in Special and Innovative Materials.

6.2.2 Objective

The objective of this research is to define the response of a new class of $(Fe,Ni)_3V$ long-range-ordered (LRO) alloys to both neutron and ion irradiation. The overall goal is to determine the potential use of this alloy class as a structural material for fusion energy systems.

6.2.3 Summary

Additional data for ion bombarded $(Fe,Ni)_3V$ LRO alloys show convincingly that ordering is an important factor in the resistance of this alloy class to swelling resulting from cavity formation. Relatively low swelling was observed as long as the irradiation temperature was below T_c (~670°C). Swelling increased rapidly above T_c. Small titanium additions improved and the presence of sigma phase degraded the resistance to swelling in the LRO-16/LRO-35 alloy series. Similar effects could not be defined for alloy pairs with a higher nickel content.

6.2.4 Progress and Status

Ion bombardment and microstructural examination of a series of LRO alloys have been performed to determine the swelling behavior of this alloy class. The composition of the alloys investigated is given in Table 6.2.1. Disk specimens of these alloys were solution annealed, quenched in water, and aged below the critical ordering temperature, T_c, to develop fully ordered microstructures. The samples were bombarded in the ORNL dual ion beam facility with 4-MeV nickel ions to a dose of 70 dpa at 525, 570, 625, and 680°C. Helium and hydrogen ions were simultaneously injected at levels of 8 and 28 at. ppm/dpa, respectively. Thinned specimens were examined in a 120-kV electron microscope with a eucentric double-tilt specimen stage. Additional experimental details were reported previously.[1]

Table 6.2.1. The Long-Range-Ordered Alloy Compositions Compared with Type 316 Stainless Steel

Alloy	Content, wt %							
	Fe	Ni	V	Ti	Cr	Mo	Mn	C
LRO-16	46.1	31.0	23.0					[a]
-35	45.3	31.8	22.6	0.4				[a]
-20	37.6	39.5	22.9					[a]
-37	37.6	39.5	22.4	0.4				[a]
DO3 16 stainless steel	Bal	13		0.005	18	2.0	1.9	0.05

[a] Carbon occurs as an impurity with content from 100 to 200 wt ppm.

Previously reported results[2] showed that the LRO alloys bombarded at temperatures below T_c swelled less than 20%-cold-worked type 316 stainless steel.

The swelling behavior of additional specimens of LRO alloys has now been determined by transmission electron microscopy (TEM). Specimens irradiated near the critical ordering temperature were of special interest because swelling data in this region were lacking.[2] Figure 6.2.1 shows the swelling determined by TEM measurements as a function of irradiation temperature for these alloys. Data reported previously are indicated by open symbols and new data by solid points. The values of swelling for LRO-20 at 645°C and LRO-37 at 670°C (very close to T_c) indicate that the shape of the swelling curves drawn previously was probably correct (i.e., swelling tended to increase sharply at or above T_c). An additional data point for the 20%-cold-worked type 316 stainless steel standard shows that swelling has begun to decrease with higher irradiation temperatures and that the peak swelling temperature for this alloy is just below 700°C. The peak swelling temperature is identical to that measured for annealed type 316 stainless steel using 4-MeV nickel ions irradiation and simultaneous helium injection.[3] The swelling value for the LRO-16 alloy at 760°C suggests the dashed shape of the swelling curve for this alloy shown in Fig. 6.2.1. This swelling behavior would also be consistent with

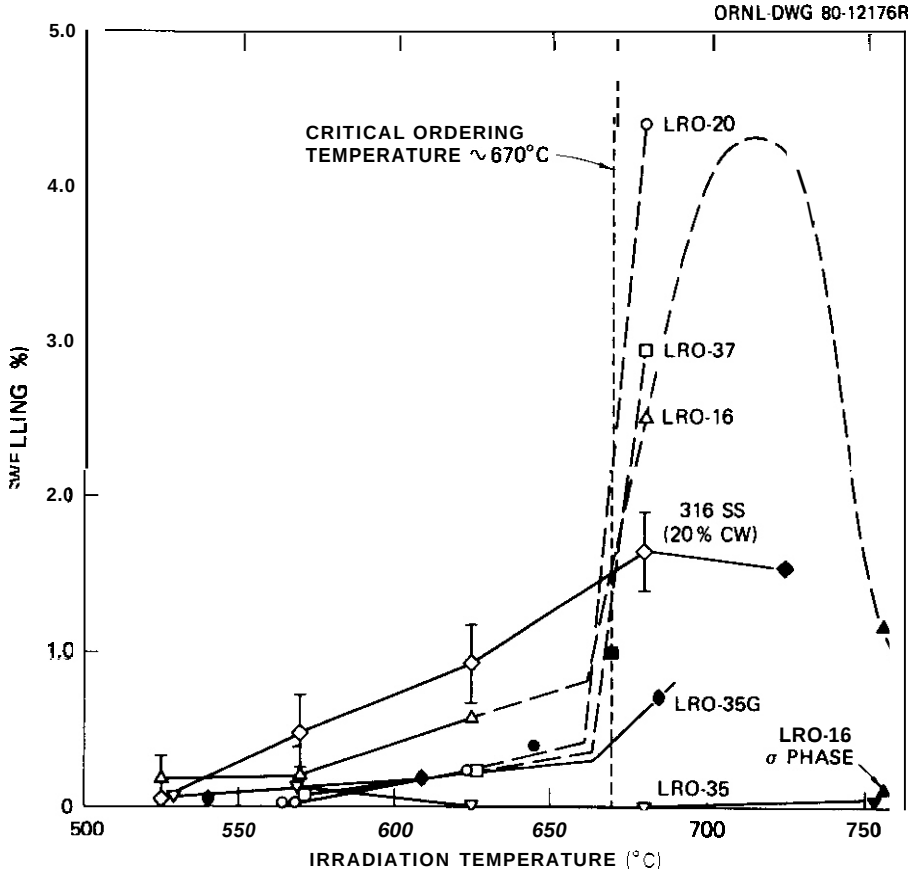

Fig. 6.2.1. Swelling of Iron-Base Long-Range-Ordered Alloys as a Function of Irradiation Temperature. Specimens were irradiated with 4-MeV nickel ions to 70 dpa, with simultaneous injection of 8 at. ppm He and 28 at. ppm D per dpa. Filled symbols indicate previously unreported data.

with the sharp increases observed near T_c. However, more data near 700°C are needed to completely define the swelling behavior of these alloys.

The swelling of the sigma phase in LRO-16 for irradiation at 760°C was measured and is shown in Fig. 6.2.1. This swelling was considerably lower than for the matrix of this alloy at 760°C. Further investigation of the effect of sigma phase in the microstructure was conducted by irradiating two groups of LRO-35 specimens. A series of specimens designated LRO-35G were quenched from 1130°C and aged (3 days at 650°C, 30 h at 600°C, and 60 h at 500°C) to produce a microstructure containing some sigma phase. Although only three specimens were examined, it was found that the swelling was always greater than in the LRO-35 specimen that were heat

treated to avoid sigma phase formation. We can conclude that results on the LRO-16/LRO-35 series are evidence that a small titanium addition improved resistance to swelling while the presence of sigma phase increased the total swelling. When the nickel content was increased, as in the case for the LRO-20/LRO-37 pair, these effects were less clear.

6.2.5 Conclusion and Future Work

Additional data for ion bombarded $(Fe,Ni)_3V$ LRO alloys show convincingly that ordering is an important factor in the resistance of this alloy class to swelling resulting from cavity formation. Relatively low swelling was observed as long as the irradiation temperature was below T_c (~670°C). Swelling increased rapidly above T_c. Small titanium additions improved and the presence of sigma phase degraded the resistance to swelling in the LRO-16/LRO-35 alloy series. Similar effects could not be defined for alloy pairs with a higher nickel content.

The response of two LRO alloys to neutron irradiation in the ORR will be investigated and reported next quarter.

6.2.6 References

1. D. N. Braski, "The Effect of 4-MeV Nickel Ion Irradiation on the Microstructure of $(Fe,Ni)_3V$ Long-Range-Ordered Alloys," *ADIP Quart. Prog. Rep. June 30,* 1980, DOE/ER-0045/3, pp. 162-73.
2. D. N. Braski, "The Effect of 4-MeV Nickel Ion Irradiation on the Microstructure of $(Fe,Ni)_3V$ Long-Range-Ordered Alloys," *ADIP Quart. Prog. Rep. Sept. 30, 1980,* DOE/ER-0045/4, pp. 114-21.
3. E. H. Lee, A. F. Rowcliffe, and E. A. Kenik, "Effects of Silicon and Titanium on Swelling of AISI 316 Stainless Steel," *J. Nucl. Muter.* 83(1): 79-89 (1979).

7. PATH E ALLOY DEVELOPMENT — FERRITIC STEELS

7.1 INITIAL CHARACTERIZATION OF THE 12Cr FUSION FERRITIC PROGRAM HEAT — R. D. Stevenson (General Atomic Company)

7.1.1 ADIP Task

The Department of Energy (DOE)/Office of Fusion Energy (OFE) has stated the need to investigate ferritic alloys under the ADIP program task. Ferritic Steels Development (Path E).

7.1.2 Objective

The objective of this study is to characterize the Fusion-Ferritic 12 Cr program heat melted at Electralloy and converted to plate at Jessop Steel Company (1). As a part of this characterization standard mechanical tests are performed as well as metallurgical analysis on the effect of thermo-mechanical treatments on grain size and decarburization.

7.1.3 Progress and Status

One 3830 Kg slab of 12Cr-1Mo-0.3V steel was converted to plate at Jessop Steel Co. Table 7.1.1 shows the breakdown of plates produced.

Table 7.1.1 Plates Produced from 12Cr Fusion-Ferritic Heat

Thickness (cm)	No. of Plates	Total Area (m^2)
∿ 0.33	13	24.07
∿ 1.00	6	15.20
∿ 1.70	2	5.27
2.86	1	1.78
	22	

Optical microscopy analyses of two sections taken from each of the 22 plates are being done. Inclusion counts are being made for each specimen as well as characterization of grain growth, and decarburization, banding, or other macro-segregation. Tensile and Charpy V-notch test specimens are being machined from all four plate thicknesses. Table 7.1.2 shows the results of initial longitudinal and transverse tensile tests conducted on one of the 1.70cm thick plates.

Table 7.1.2 Room Temperature Tensile Properties From 1.70cm Thick 12Cr-1Mo-0.3V Plate (Fusion-Ferritic Steel Heat)*

Specimen #	UTS MPa(ksi)	0.2 YS MPa(ksi)	Total Tensile Elongation(%)	Reduction in Area
18-1	791 (114.6)	549 (79.5)	22	55.9
18-2	791 (114.5)	553 (80.1)	23	56.1
19-1	795 (115.2)	556 (80.6)	22	56.4
19-2	783 (113.4)	555 (80.4)	23	57.0
Average	790 (114.4)	553 (80.2)	22.5	56.4
Sandvik HT-9 [3]	690-840(100-122)	490 (7/min.)	17(min.)	

* Round dog-bone type specimens, diameter 0.627cm, gauge length 2.54cm.

As can be seen the values compare very favorably with Sandvik HT-9 specifications.

In addition to these characterization tests, studies are being conducted to determine the effect of grain size on mechanical properties. Charpy V-notch bars of three different grain sizes (ASTM 4,6 and 8) will be produced and tested in order to determine their effect on DBTT and fracture energies. Also decarburization kinetics data is being generated for 12Cr-1Mo-0.3V steel. This study involves measuring decarburization depth as a function of time and temperature for exposure in air. Specimens are being exposed at 1100°C and 1200°C.

7.1.4 Conclusions and Future Directions

Tests are planned for the characterization of the 12Cr Fusion-Ferritic Heat by both metallography and mechanical test specimens. Initial tensile results for the 1.70cm plate are promising. Studies are underway to test the fracture strength of 12Cr-1Mo-0.3V as a function of grain size, and to measure decarburization depth as a function of time and temperature.

7.1.5 References

1. Lechtenberg, T. A., R. D. Stevenson, S. N. Rosenwasser, B. E. Thurgood and L. D. Thompson, "Procurement of National 12Cr Heat and Evaluation of Welding Procedures for Irradiation Specimens", from Alloy Development for Irradiation Performance, Quarterly Progress Report for the Period Ending March 31, 1980, DOE/ER-0045/2, pp. 109-131.

2. Stevenson, R. D., B. E. Thurgood and S. N. Rosenwasser, "Procurement and Conversion of the National Fusion-Ferritic Steel Program 12Cr (HT-9) Heat", from Alloy Development for Irradiation Performance, Quarterly Progress Report for the Period Ending June 30, 1980, DOE/ER-0045/3, pp. 192-200.

3. Sandvik Steel Catalog 1.720E, March 1974.

7.2 FRACTURE RESISTANCE TESTING OF ALLOY HT-9 IN THE UNIRRADIATED CONDITION - J.R. Hawthorne (Naval Research Laboratory)

7.2.1 ADIP Task

ADIP tasks are not defined for ferritic stainless steels in the 1978 Program Plan.

7.2.2 Objectives

The objectives of the present investigation were to determine and compare the notch ductility and static fracture toughness properties of two melts of Alloy HT-9 in the unirradiated condition.

7.2.3 Summary

Alloy HT-9, a 12 Cr martensitic stainless steel, is being evaluated for potential applications as a first wall material in magnetic fusion reactors and as a duct material for fast breeder reactors. The present study examined the notch ductility and static fracture toughness of material from two HT-9 melts (melt numbers 91353 and 91354) in the unirradiated condition.

Material comparisons revealed a potential for large differences in Charpy-V (C_v) notch ductility both in terms of upper shelf energy level and in terms of brittle/ductile transition temperature. The transition temperature of one 15.9 mm plate from melt 91353 exceeded 200°C, while the transition temperature for a 33 mm rod from melt 91354 was -18°C. Large variations in J-R curve behavior were also observed, the probable cause of which is inadvertent differences in material heat treatment. The observed material variability may explain why difficulties were encountered in duct fabrication. A reheat treatment of the 15.9 mm plate was found to improve notch ductility properties greatly.

7.2.4 Progress and Status

7.2.4.1 Introduction

Alloy HT-9 currently is being assessed for possible first wall applications in magnetic fusion reactors in the U. S. Magnetic Fusion Materials Program and for duct applications in liquid metal fast breeder reactors in the U. S. Cladding/Duct Alloy Developnent Program of the Department of Energy. For these proposed uses, the fracture

resistance properties before and after elevated temperature irradiation are being investigated. Specimen types employed include Charpy-V (C_v) specimens for notch ductility determinations, fatigue precracked Charpy-V (PCC_V) specimens for dynamic fracture toughness (K_J) determinations, and compact tension (CT) specimens for static fracture toughness determinations.

7.2.4.2 Materials

The test materials are identified in the table. Two melts of Alloy HT-9 are being evaluated. Melt 91353 was in two forms: 6.4 mm thick plate and 15.9 mm thick plate. The plates were obtained from inventory stock of the Magnetic Fusion Materials Program. Melt 91354 was in the form of 33 mm rod and was obtained from the Cladding/Duct Alloy Development Program. Material heat treatment specifications are also indicated in the table. NRL tests of the as-received condition, however, revealed that the two plates from melt 91353 were improperly (or incompletely) heat treated as reported below.

HT-9 Melt	Code	Form[a]
91353	H9T	6.4 mm plate
	H9T	15.9 mm plate
91354[b]	HT9	33 mm rod

[a] Heat Treatment Specification: 1050°C-0.5 hr, air cool, 780°C-2.5 hr, air cool

[b] Supplied by Cladding/Duct Alloy Development Program

7.2.4.3 Specimen Design

The C_v specimens for the study were ASTM Type A (10 mm x 10 mm x 55 mm with a 45°, 2 mm deep notch). The PCC_V specimens were generated by fatigue precracking the C_v notch to an a/W ratio of 0.5. The CT specimen design is shown in Fig. 7.2.1. In both cases, the maximum K_f level for the last 0.70 mm of fatigue crack growth was 22 MPa$\sqrt{m}$ or less.

Details on the PCC_V test procedure and the computation of K_J are

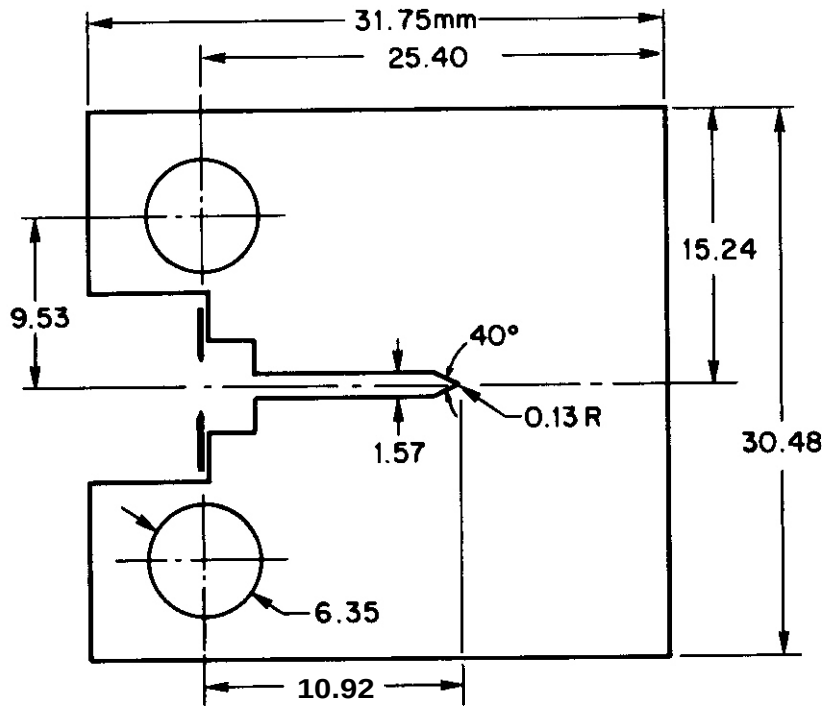

Fig. 7.2.1. Design of the Compact Tension (CT) Specimen. Two specimen thicknesses were used: 2.5 mm (Type 0.1T-CT) and 12.7 mm (Type 0.5 T-CT). A Fatigue Precrack of 1.78 mm Was Added Prior to Testing.

given in Ref. 1. PCC_V tests satisfied EPRI requirements for K_J determinations.[2] The CT specimen tests employed single specimen unloading compliance test procedures and established the J-R curve. Details of the method are given in Refs. 3 and 4. Two specimen thicknesses were used: 2.5 mm and 12.7 mm. The 12.7 mm thick specimens were 20 percent side grooved to aid crack front straightness.

7.2.4.4 Experimental Results

7.2.4.4.1 Notch Ductility Determinations

C_V notch ductility determinations for the 33 mm rod (melt 91354) are illustrated in Fig. 7.2.2. Fig. 7.2.3 indicates a good consistency of test results for two different sections of rod which were heat treated independently (two sites). A brittle/ductile transition temperature of $-18^{\circ}C$ and a high upper shelf energy level are observed. In contrast to the rod, the 15.9 mm plate (melt 91353) showed a C_V energy absorption of only 8J at $216^{\circ}C$. A dissimilarity in transition temperature of at least $234^{\circ}C$ is thus noted.

Hardness tests of the rod and the plate gave values of Rc 23 and Rc 41 respectively which suggest that the dissimilarity in notch ductility was not due to melt variation but to an inadvertent discrepancy in material heat treatment conditions. To help verify this projection, two C_V specimens of the plate were reheat treated to the specifications given in the previous table. The reheat treatment was successful in lowering the transition temperature to below $38^{\circ}C$. That is, a test at $38^{\circ}C$ yielded an energy absorption of 95J. The test at $216^{\circ}C$ showed an energy absorption of 168J, comparable to that of the rod. Hardness was reduced to Rc 20 by the reheat treatment.

Thus far, reexamination of vendor heat treatment records or procedures have not been fruitful. Nonetheless, it has been tentatively concluded that plate tempering was incomplete since no indication of carbide precipiation along martensite lath boundaries was observed in TEM.

7.2.4.4.2 Fracture Toughness Determinations

J-R curve determinations for the 33 mm rod and the 6.4 mm plate are presented in Figs.7.2.4-7.2.7. Insufficient test stock was available

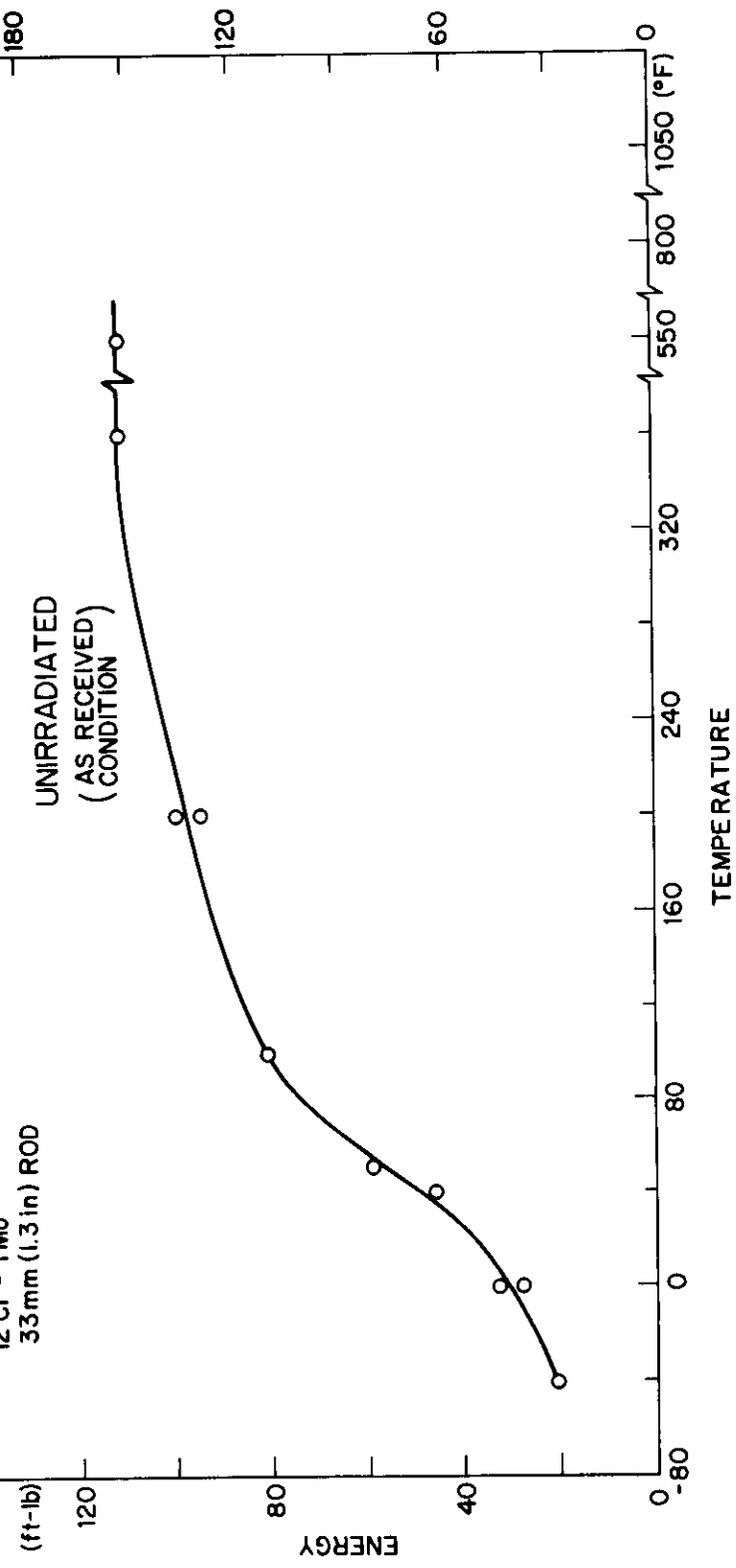

Fig. 7.2.2. Charpy-V Notch Ductility of Alloy HT-9 (33 mm Diameter Rod From Melt 91354) before Irradiation.

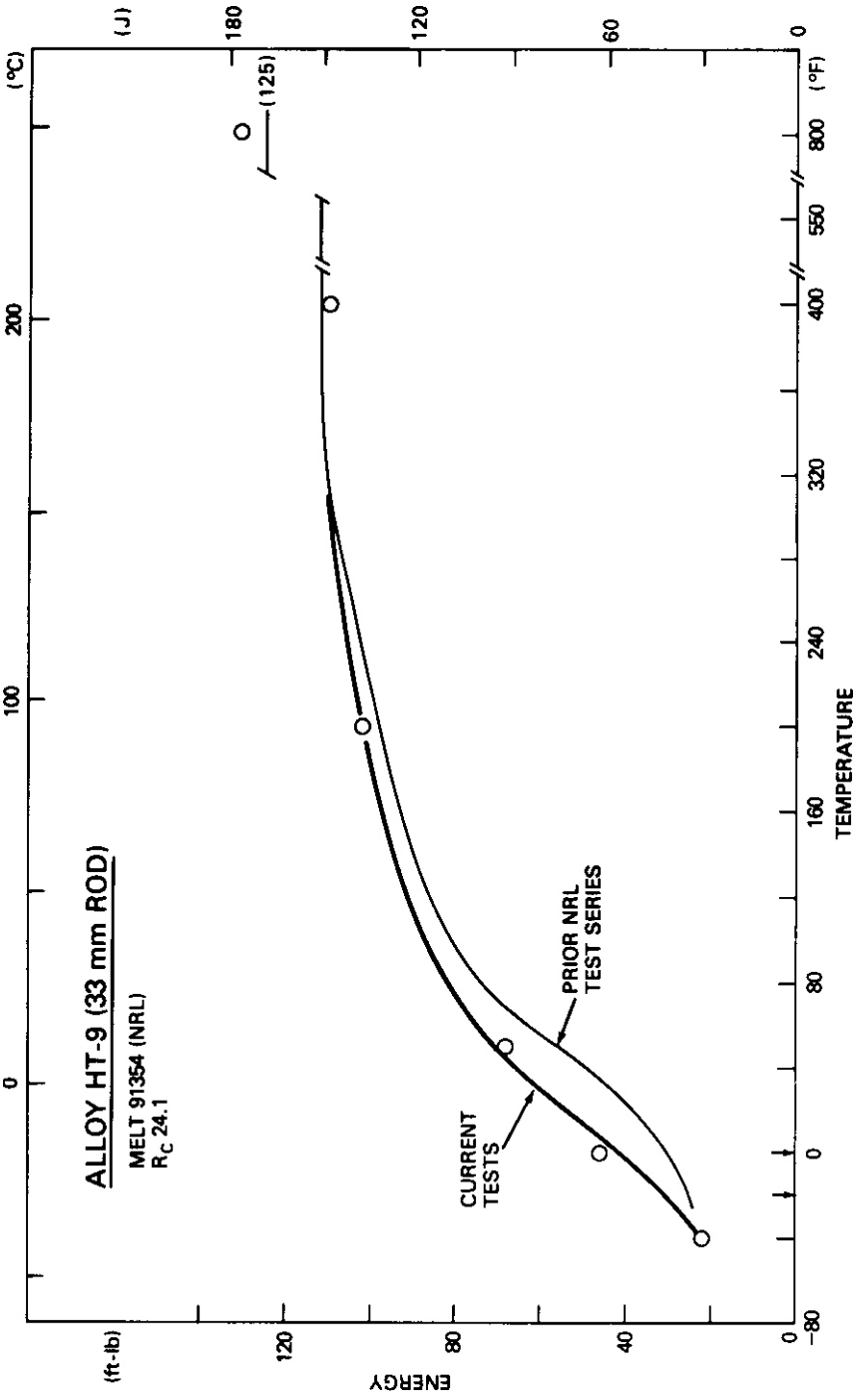

Fig. 7.2.3. Charpy-V Notch Ductility of Alloy HT-9 (33 mm Diameter Rod from Melt 91354) Comparing Properties of Two Rod Sections Heat Treated Independently.

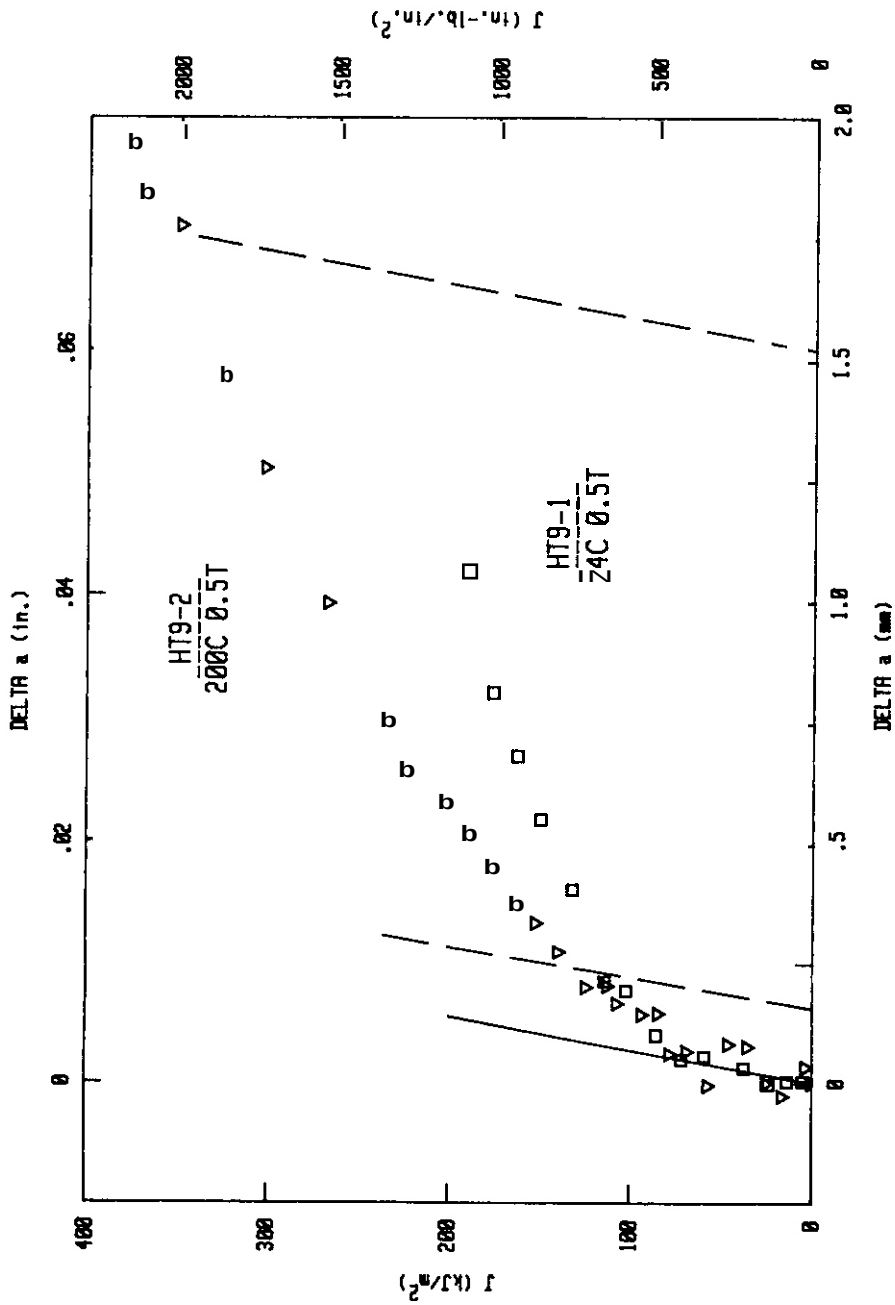

Fig. 7.2.4. Exploratory J-R Curves for Alloy HT-9, Melt 91354 at 24 and 200°C Developed with 20 Percent Side Grooved 12.7 mm Thick (Type 0.5T-CT) Specimens. The Specimen Test at 24°C Exhibited Clevage Instability After 1 mm of Stable Crack Extension.

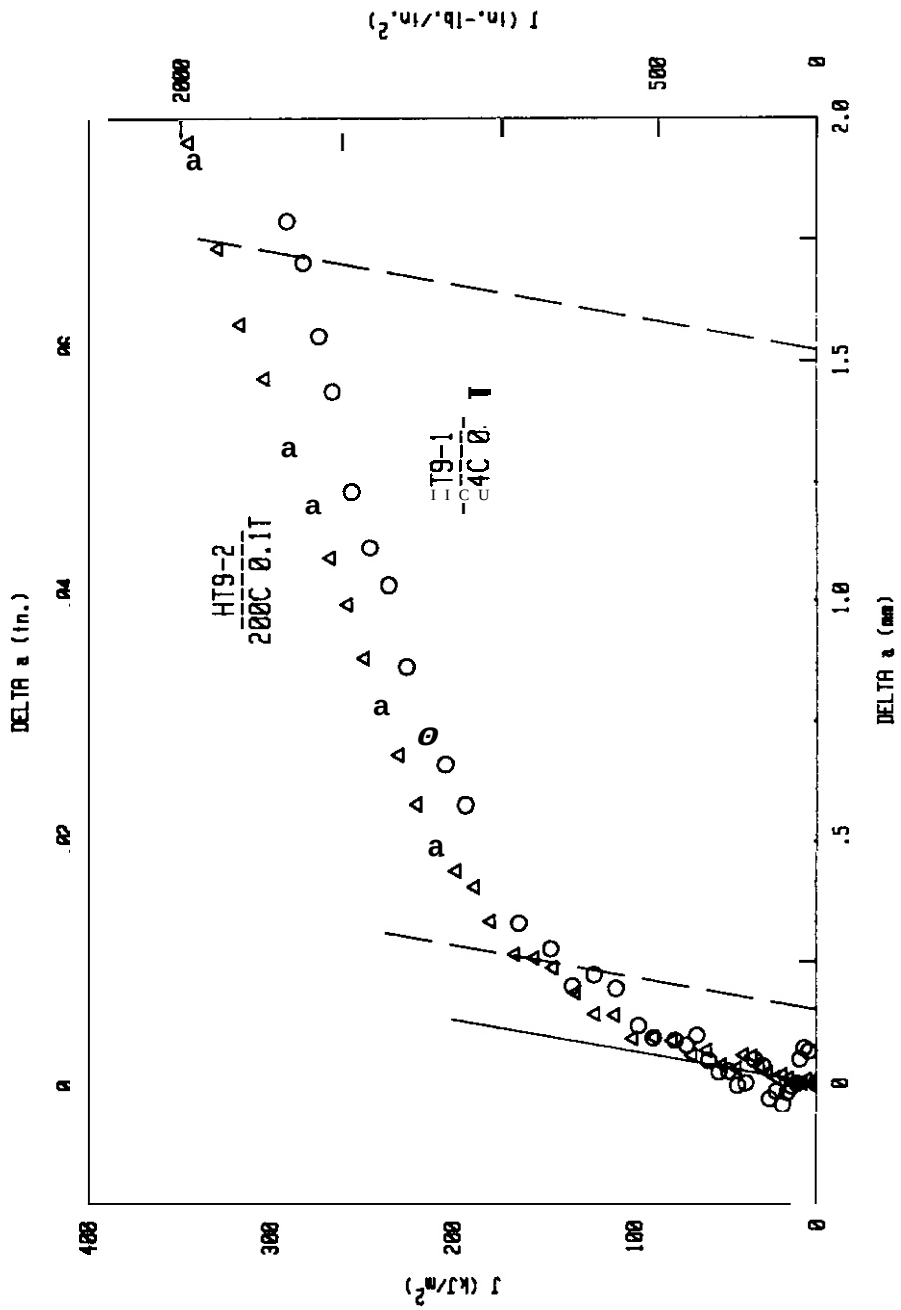

Fig. 7.2.5. Exploratory J-R Curves for Alloy HT-9 Melt 91354 at 24 and 200°C Developed with Zero Percent Side Grooved 2.5 mm Thick (Type 0.1T-CT) Specimens.

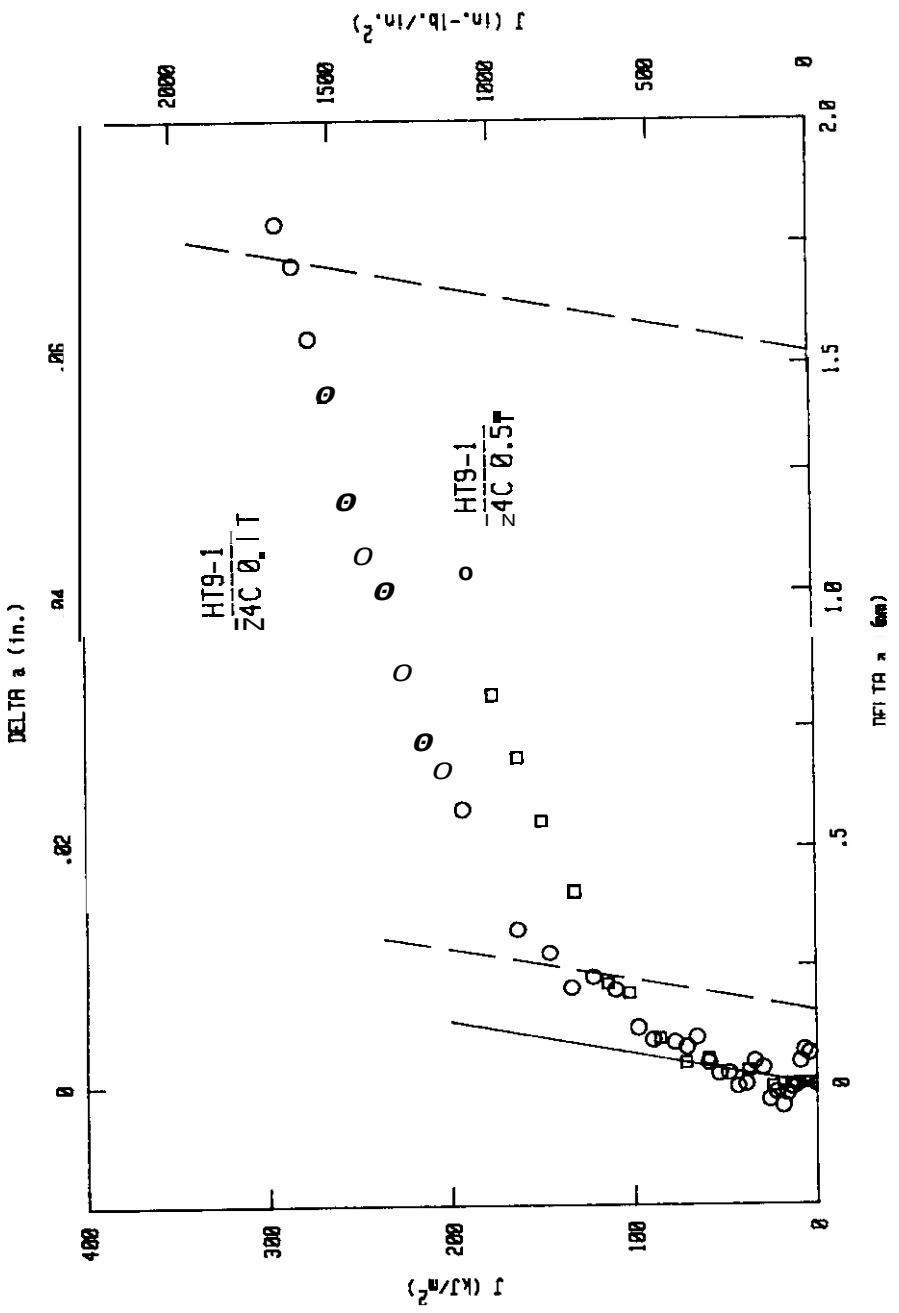

Fig. 7.2.6. Comparison of J-R Curves for Alloy HT-9 Melt 91354 at 24°C Developed With Type 0.1T-CT and Type 0.5T-CT Specimens.

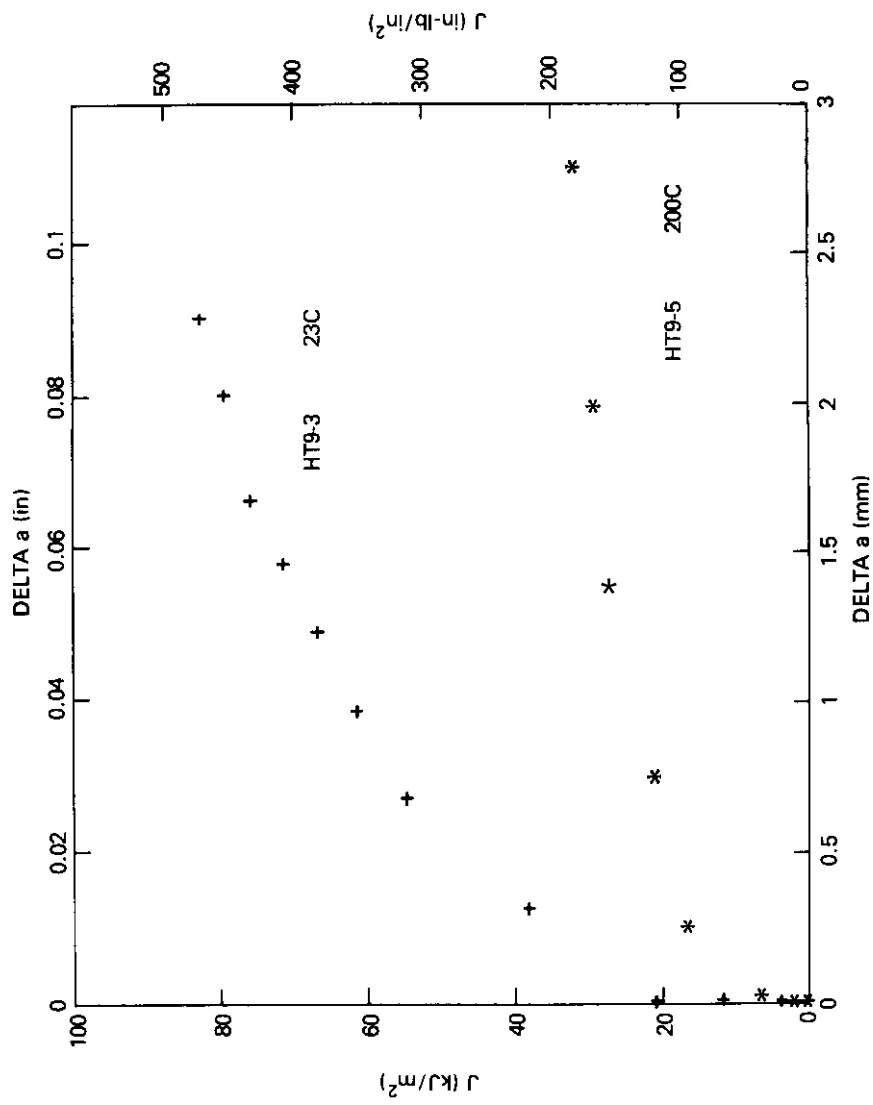

Fig. 7.2.7. Exploratory J-R Curves for Alloy HT-9, Melt 91353, at 24 and 200°C Developed with Zero Percent Side Grooved 2.5 mm Thick (Type 0.1T-CT) Specimens. Fracture Resistance Significantly Lower Than That of Heat 91354 Is Indicated.

for CT testing of the 15.9 mm plate. The CT tests were performed at 24°C and at 200°C. Specimen fractures are illustrated in Figs. 7.2.8-7.2.10.

Paralleling the C_v test indications, large differences between the materials are found. The 6.4 mm plate shows a significantly lower fracture resistance than the 33 mm rod. Heat treatment variability again is the suspected cause. In the case of the plate, large specimen to specimen differences in hardness were also observed which can not be fully explained. More importantly, a potential for low as well as high fracture resistance is indicated and may explain why difficulties were encountered in duct fabrication.

The J-R curves for the 33 mm rod show a higher material toughness at 200°C than at 24°C as expected. The cleavage instability exhibited by the 12.7 mm thick specimen tested at 24°C is also consistent with projections from the C_v data. That is, the 24°C test temperature is just below the minimum temperature for full shear fracture development in the C_v specimens. Finally, the relative positions of the J-R curves for the 12.7 mm thick specimen vs the 2.5 mm thick specimen at 24°C (Fig. 7.2.6) are in accord with prior observations on the effect of specimen side grooving. Specimen fractures, however, indicate that plane stress conditions were present for the 2.5 mm thick specimens but not the 12.7 mm thick specimens. For the 6.4 mm plate, specimen fractures in contrast gave little evidence of metal ductility. Experimental assessments of side groove effects and specimen thickness effects on the J-R curve are continuing.

7.2.5 Discussion

The plate materials of melt 91353 (several specimen types) were irradiated by NRL at 288°C to $7\text{-}8 \times 10^{19}$ n/cm^2, $E > 0.1$ MeV in advance of the present study. The objective was to obtain irradiation data for conditions below the EBR-II data base for this alloy. Because of the typical heat treatment condition(s) of the plates, postirradiation testing for the experiment will not be conducted. A repeat experiment using well documented material from the MFE Program reference heat has been proposed.

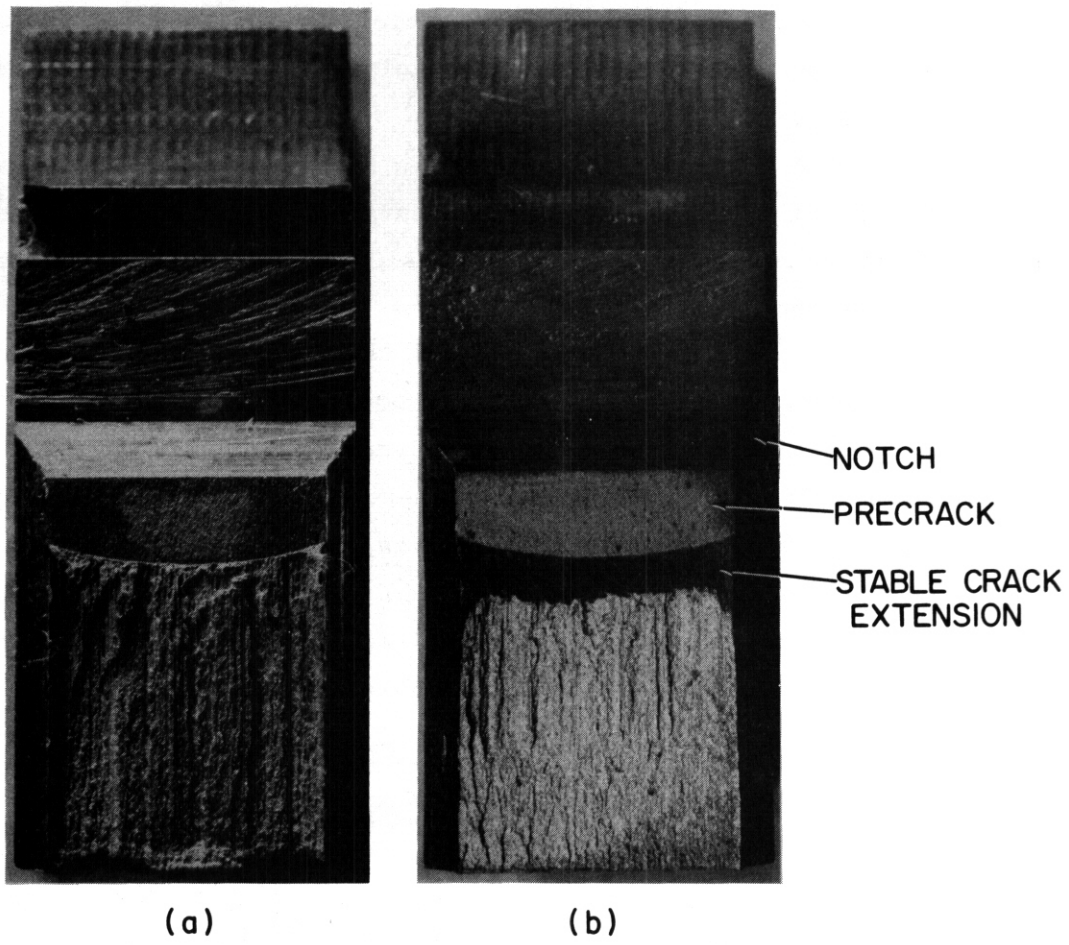

Fig. 7.2.8. Fracture Surfaces of the Type 0.5T-CT Specimens of Alloy HT-9, Melt 91354, Tested At (a) 24, and (b) 200°C. The Region of Stable Crack Extension At 200°C Was Revealed by Post-test Heat Treating.

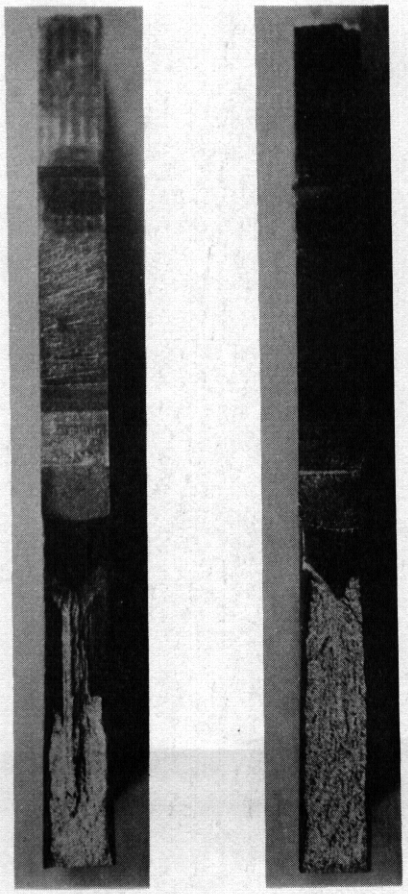

Fig. 7.2.9. Fracture Surfaces of the Type 0.1T-CT Specimens of Alloy HT-9, Melt 91354, Tested At (a) 24, and (b) 200°C. The Thickness Contraction and Slant Fracture Are Evidence of Plane Stress Conditions.

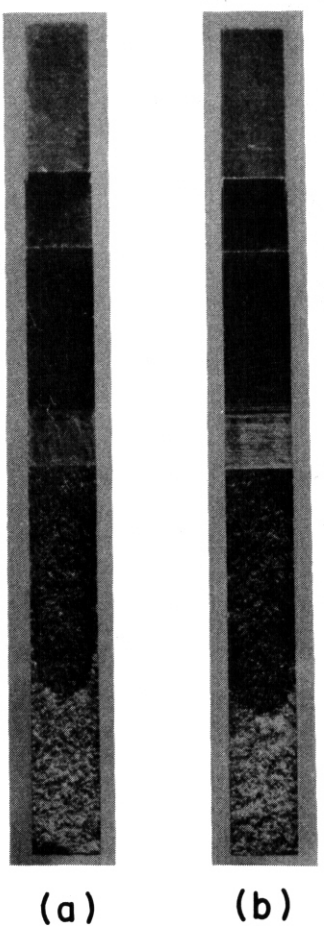

Fig. 7.2.10. Fracture Surfaces of 0.1T-CT specimens of *Alloy* HT-9, Melt 91353, Tested At (a) 24, and (b) 200°C.

7.2.6 Conclusion

The result of this study make it clear that heat treatment documentation and verification will be essential to the confident use of Alloy HT-9 in future fusion or breeder reactor applications. A capability for high fracture resistance in the unirradiated (preservice) condition by the alloy has been demonstrated.

7.2.7 References

1. F. A. Smidt, J. R. Hawthorne, and V. Provenzano, Alloy Development for Irradiation Performance, QPR (Jan-Mar 1980). DOE/ER-0045/2, Oak Ridge National Laboratory, June 1980, pp. 163-180.
2. D. R. Ireland, W. L. Server, R. A. Wullaert, "Procedures for Testing and Data Analysis," Task A, Topical Report, Effects Technology Inc., ETI Technical Report 75-43, October 1975.
3. F. J. Loss (Ed.), "Structural Integrity of Water Reacter Pressure Boundary Components, QPR (Apr-Jun 1979), NUREG/CR-0943, NRL Memorandum Report 4064, Naval Research Laboratory, Sep. 23, 1979.
4. J. R. Hawthorne, (Ed.), "The NRL-EPRI Research Program (RP886-2), Evaluation and Prediction of Neutron Embrittlement in Reactor Pressure Vessel Materials, Annual Progress Report for CY 1978," Aug. 30, 1979.

7.3 PREPARATION OF ALLOY HT-9 REFERENCE PLATE FOR IRRADIATED FRACTURE RESISTANCE STUDIES – J. R. Hawthorne (Naval Research Laboratory)

To be reported in the next quarterly report.

7.4 THE MICROSTRUCTURAL EVALUATION OF EMBRITTLED 12Cr-1Mo-0.3V STEEL

T. A. Lechtenberg (General Atomic Company)

7.4.1 ADIP Task

The Department of Energy (DOE)/Office of Fusion Energy (OFE) has stated the need to investigate ferritic alloys under the ADIP program task, Ferritic Steels Development (Path E).

7.4.2 Objective

This contribution reports the microstructural observations on a 12Cr-1Mo-0.3V steel (HT-9) in the embrittled and non-embrittled conditions whose fracture properties were reported earlier (1).

7.4.3 summary

This section reviews the initial work already reported to determine the effect of embrittlement on the fracture properties (CVN and K_{Id}) of HT-9. Also included is a summary of the new data evaluating the microstructures of the embrittled alloy.

Earlier (1), the dynamic stress intensity factor, K_{Id}, and Charpy impact energy (CVN) transition temperature curves were determined for a 12Cr-1Mo-0.3V steel (HT-9). The specific heat treatment was determined by observing the effect of austenitizing and tempering temperatures on prior austenite grain sizes, hardness, and carbide precipitation. It was concluded that a treatment of 1000°C for an hour followed by an air-cool and subsequent tempering at 650°C for an hour produced a microstructure nearly as stable as the higher temperature industrially recommended heat treatment. Specimens for fracture properties were thus treated, then half were aged at 550°C for 100 hours to induce embrittlement. The ductile-to-brittle transition temperature (DBTT) for each condition was determined. There was an 80°C increase in the DBTT measured by instrumented and precracked CVN, whereas the standard blunt notched CVN showed no shift. The fracture surfaces in both cases were quasi-cleavage along martensite lath boundaries with no indication of intergranular decohesion.

Since the fracture properties were measured, a transmission electron microscopic examination of the microstructures of the as-quenched (AQ), quenched and tempered (Q+T), and Q+T and aged conditions have been performed. It was found that thin films (~200Å) of austenite were retained at the martensite lath boundaries after air-cooling from the austenitizing temperature. Upon tempering, these films transform to $M_{23}C_6$ discontinuous carbide networks (and presumably ferrite), and the martensite laths evidence some sub-grain formation within the laths. Subsequent aging at 550°C for 100 hours produced a small increase in volume percent of stable $M_{23}C_6$ and little change in other fine microstructural details.

7.4.4 Experimental Procedure

The material used in this investigation was obtained from the National Breeder Material Stockpile (heat 891354) at HEDL in the form of 1-5/16" diameter rod. The chemistry is given in Table 7.4.1. The as-received material had been heated to 1100°C for at least an hour, hot worked with reheats to 1150°C between each pass, slow cooled, and tempered at 750°C for 1 hour followed by an air cool.

All heat treatments in this study were done on the same size samples heated in air for the required time after the surface reached temperature, then air-cooled. These were later machined into CVN specimens for mechanical testing. Specimens for transmission electron microscopy were produced by slicing 0.4 mm wafers with a water cooled diamond saw from the room-temperature tested CVN specimens, mechanically thinning the wafers to *40* µm, followed by jet polishing in a solution of 10%$HClO_4$-ethanol cooled to 0°C. The foils were examined on a Phillips 300 transmission electron microscope using a double tilt stage to allow complete diffraction analysis.

Table 7.4.1 Chemistry of 12Cr-1Mo-0.3V Alloy (HT-9) (wt.%)

C	Cr	Mo	V	W	Ni	Mn	Si	P	S	Fe
0.21	12.09	1.02	0.33	0.54	0.58	0.50	0.21	0.008	0.003	Bal.

7.4.5 Results

A careful TEM examination of the as-quenched microstructure showed typical interlocking lath martensite with,

(i) heavily dislocated laths and occasional twinned martensite,

(ii) some auto-tempered laths with intralath precipitates (presumably M_3C) similar in morphology to cementite but with a slightly feathery appearance reminiscent of Haage carbides(2),

(iii) low angle boundaries between the laths as exhibited by close splitting of the martensite reflections,

(iv) laths surrounded by thin films (~200Å) of retained austenite which adopted the Kurdjumov-Sachs (K-S) orientation relationship(3), $(111)_\gamma // (110)_\alpha$; also, the Nishiyama-Wasserman (N-W) (4) relationship was seen less frequently confirming recent results that both can be expected in the same material(5,6), and

(v) spherical $M_{23}C_6$ carbides undissolved during austenitization and uniformly dispersed throughout the microstructure.

Figure 7.4.1 shows a representative area of the microstructure. Figure 7.4.1(a) is a bright field photomicrograph of a typical dislocated lath structure with some undissolved $M_{23}C_6$ carbides (arrow). Part (b) is a dark field image of a $(111)_\gamma$ reflection showing the laths surrounded by thin films of stabilized austenite. Included in the inset is the diffraction analyses showing the K-S relationship. The retention of austenite films at lath boundaries has been reported in several other alloy systems (e.g., refs. 5 and 7). It is thought to be caused by chemical stabilization from interstitial carbon diffusing away from the growing lath, which locally lowers the M_s-M_f temperatures(13) between them. The same TEM foil specimen was subsequently quenched in liquid nitrogen to force the transformation of the austenite. The resulting microstructure is seen in Figure 7.4.2. It shows a dark field image of twinned martensite transformed from retained austenite films emanating

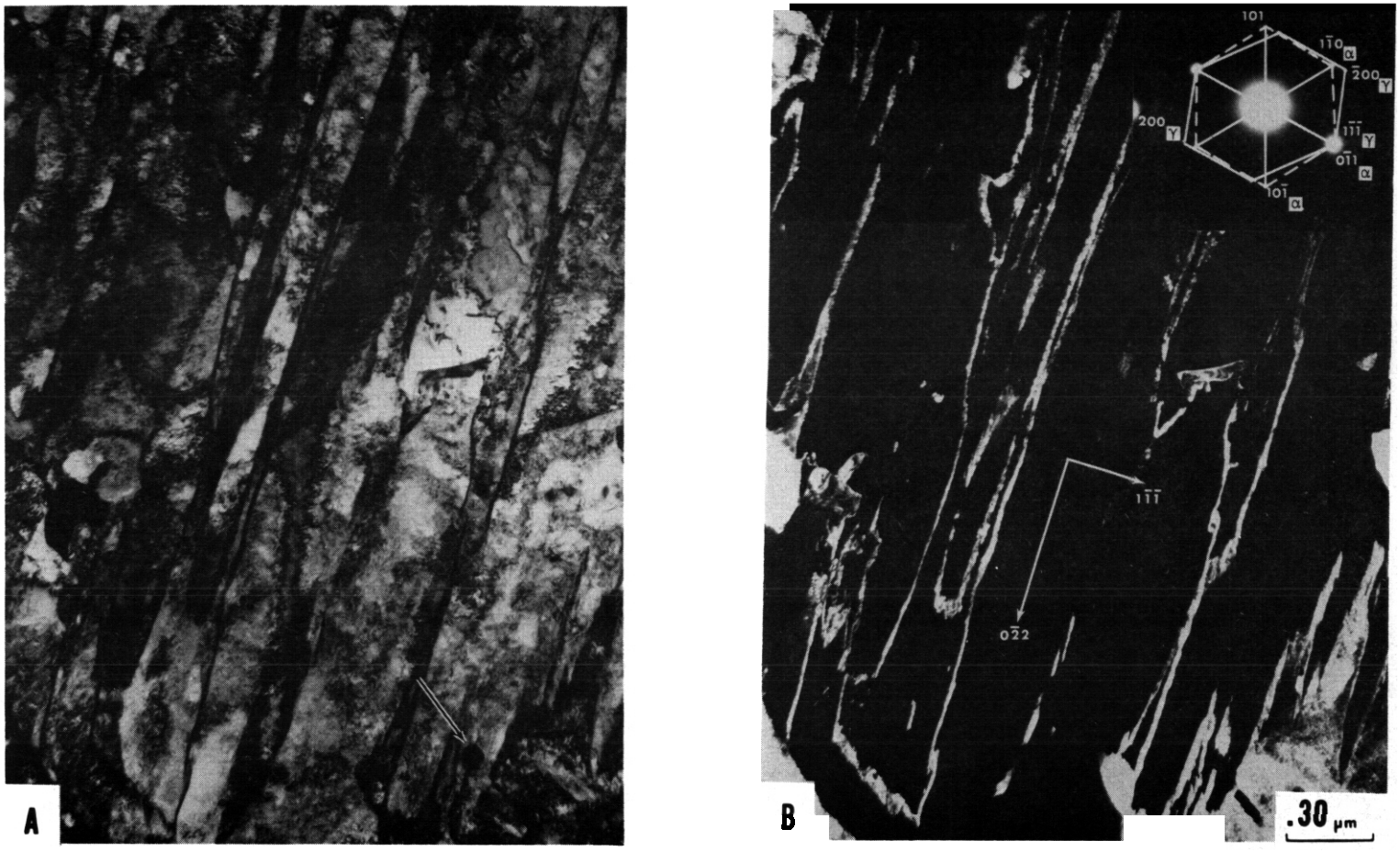

Figure 7.4.1 Transmission electron micrograph of 12Cr-1Mo-0.3V steel (HT-9) after 1000°C for an hour followed by an air-cool. The bright field (A) shows the dislocated lath structure, and (B) shows the dark field image of an austenite reflection. The austenite is retained as thin films surrounding the martensite laths. The diffraction analysis is shown in the inset.

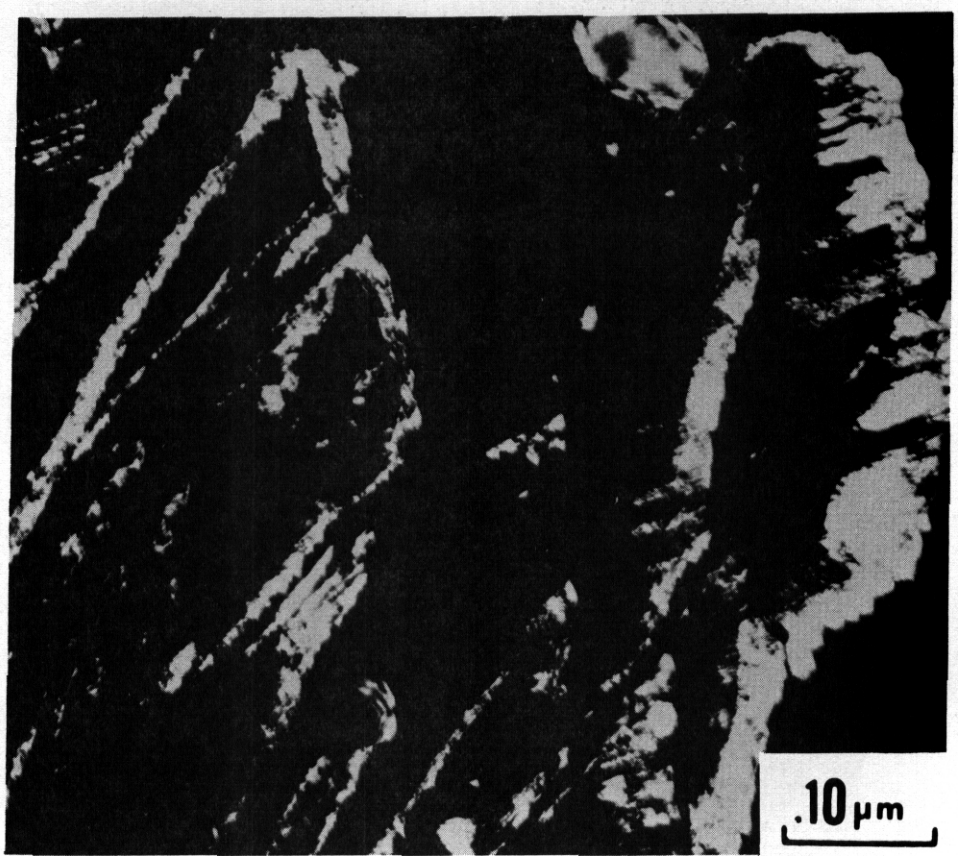

Figure 7.4.2 Dark field image of the same TEM specimen as in Figure 7.4.1 after quenching in liquid nitrogen. Twinned martensite is shown emanating from dislocated lath martensite boundaries. The twinned martensite transformed from carbon enriched retained austenite previously in lath boundaries.

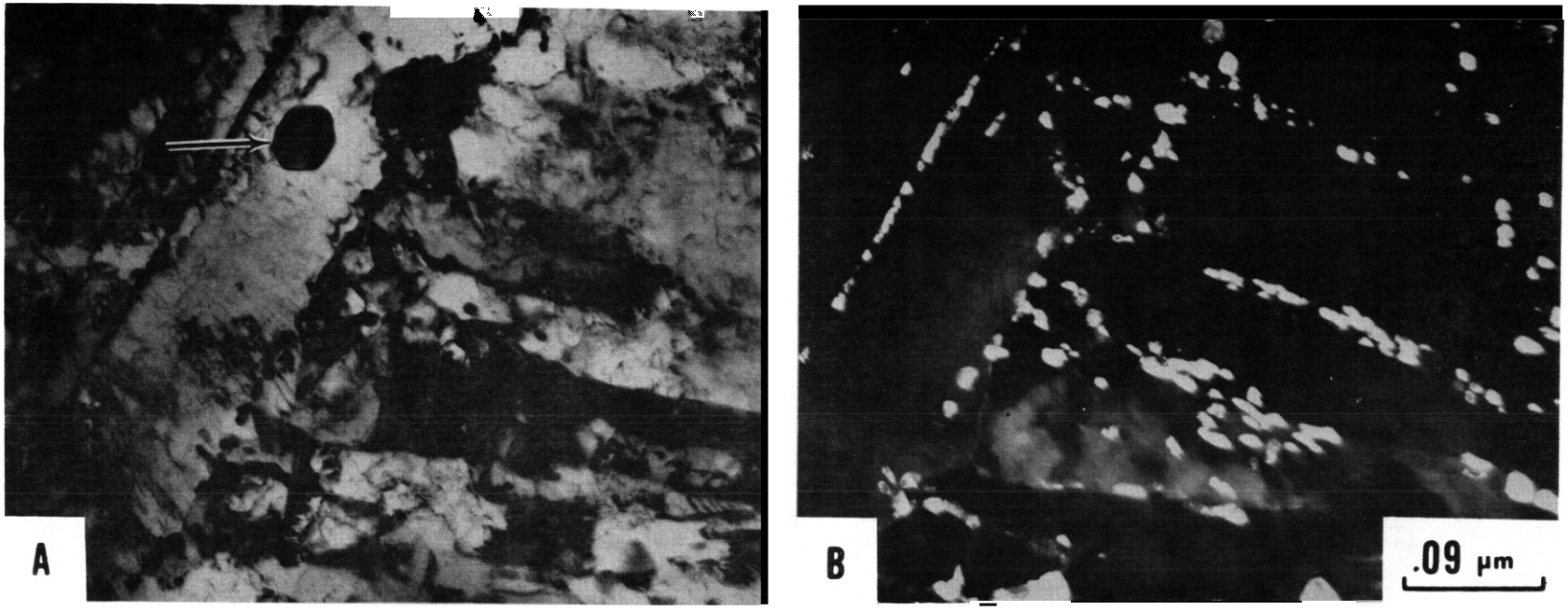

Figure 7 4 m

Transmission electron micrograph of 12Cr-1Mo-0.3V (HT-9) after austenitization at 1000°C for 1 hour followed by an air-cool and tempering at 650°C for an hour. The bright field (A) shows the lath martensite structure with a semi-continuous network of $M_{23}C_6$ carbides at the boundaries and a large undissolved carbide (arrow). The dark field (B) shows the discontinuous carbide networks.

into the dislocated lath from the lath boundaries.

This lends credence to the chemical stabilization of austenite, because it is known that higher carbon austenite has a propensity to transform to twinned martensite *(14-17)*. Figure *7.4.3* shows the microstructure after austenitizing at 1000°C and tempering at 650°C for 1 hour. The martensitic lath structure is still apparent even in this overaged condition, although the dislocation density has decreased and some have arranged themselves into subgrains within the laths. Secondly, the laths are now outlined by a semicontinuous network of $M_{23}C_6$ carbides which precipitated from the high carbon retained austenite. These carbides were found to obey the orientation relationship $(101)_{M_{23}C_6}$ // $(111)_{\alpha}$. The decomposition of thin films of austenite to carbide networks is generally associated with a decrease in notch toughness in many materials when measured as a function of tempering temperature(19). This is called temper martensite embrittlement (TME).

Figure *7.4.4* shows the Q+T condition after thermal aging at 550°C for 100 hours. The $M_{23}C_6$ lath boundary carbides have coarsened slightly, causing the carbide networks to be slightly less continuous. There is no noticeable volume increase of the carbides. This confirms results reported earlier that little additional carbide precipitates after tempering(1). The dislocation density decreased and subgrain formation is more advanced. This micrograph differs little with those reported by Chafey and Thompson(18) on steam generator tubing of the same alloy, HT-9, aged at 600°C for 80,000 hours. This demonstrates the remarkable thermal stability of this material and suggests the 1000°C austenitization an [illegible] ructure as stable as the industrial treatment.

An analysis of the fracture surfaces showed both the Q+T and Q+T+ aged fracture modes to be quasi-cleavage. These are shown in Figure *4.4.5* for both blunt notched Charpy and those fatigue cracked for instrumented impact testing. All were fractured at 25°C. There is

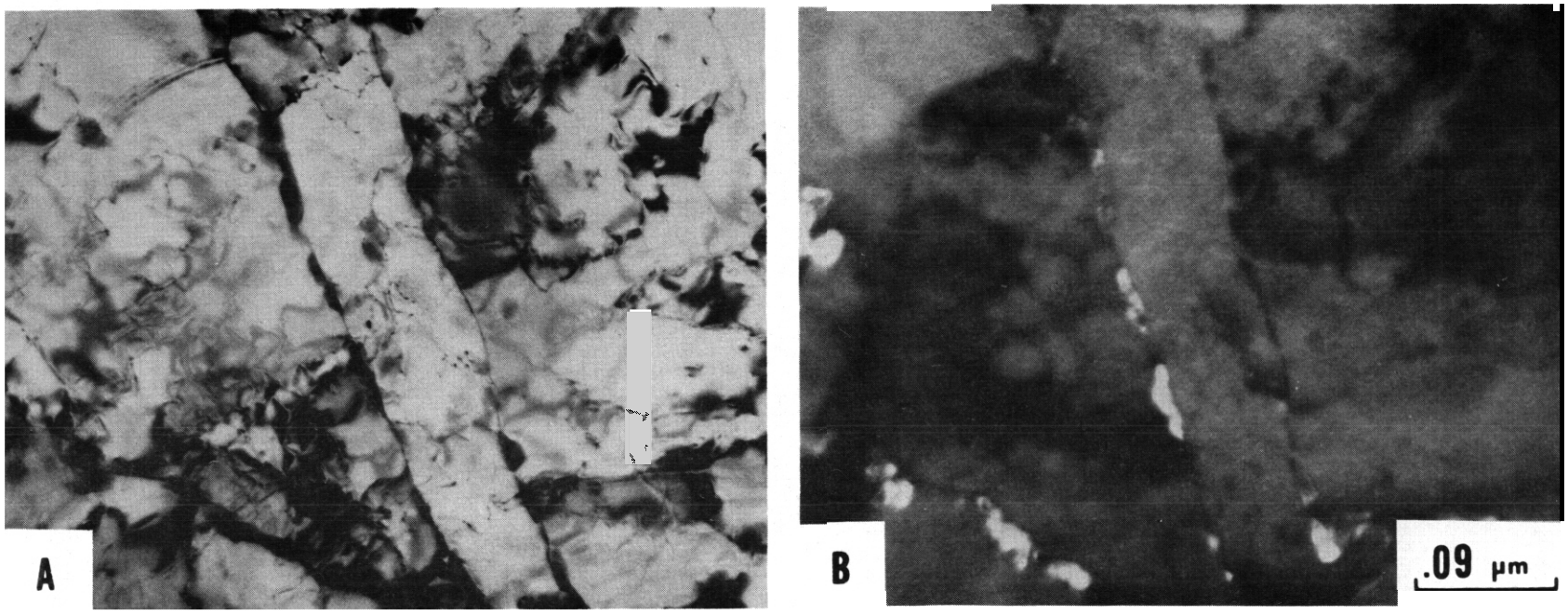

Figure 7.4.4 Transmission electron micrograph of the 1000°C, 1 hour, air-cool, 650°C 1 hour air-cool, 550°C for 100 hours air-cooled condition. Part (A) shows the martensite lath structure still remains, although the dislocations have arranged themselves into subgrains. Also, there is some coalescence of $M_{23}C_6$ carbides at the lath boundaries. This is evident in part (B) when compared to Figure 7.4.3 (B).

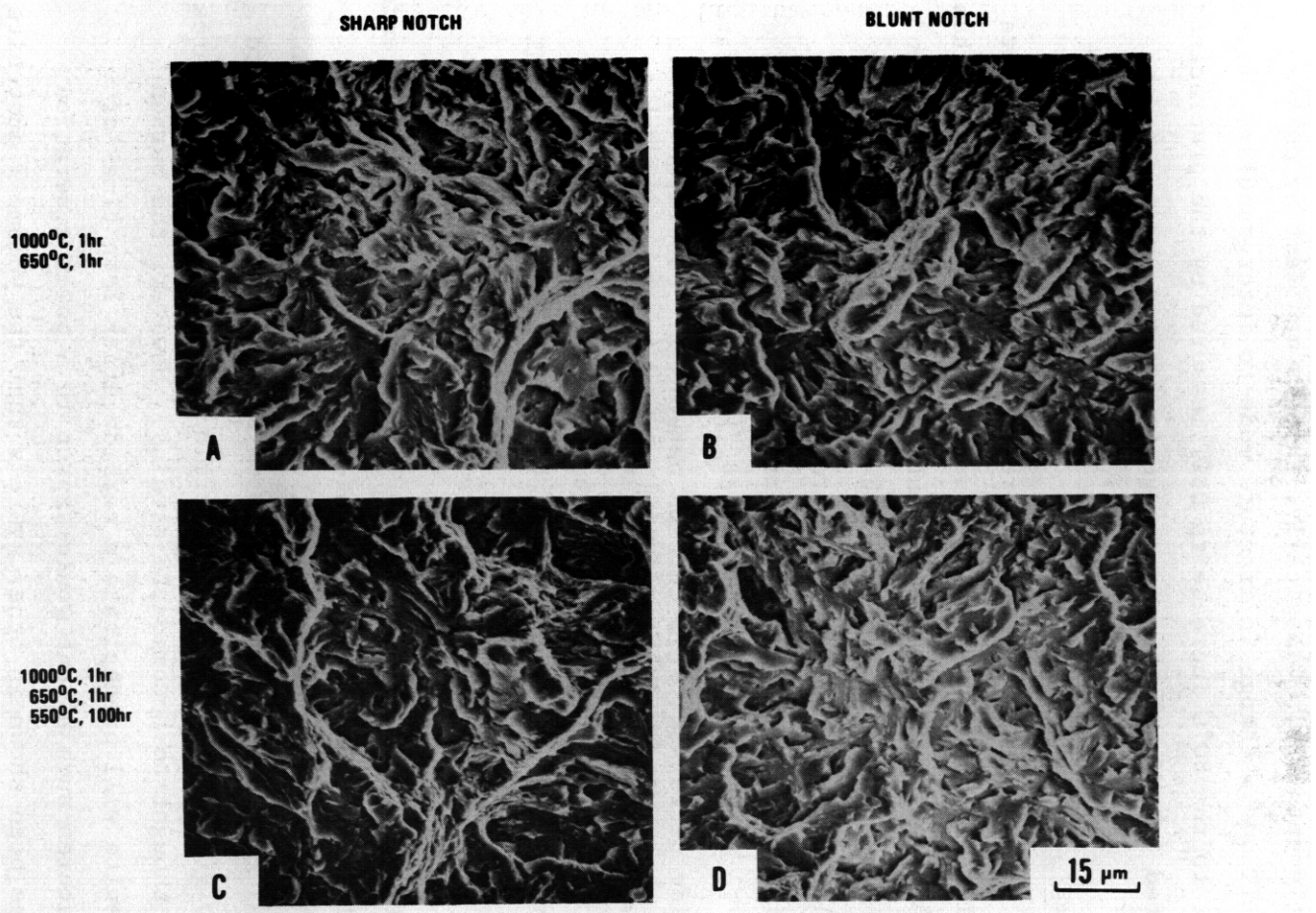

Figure 7 C.5 Scanning electron micrograph of 12Cr-1Mo-0.3V (HT-9) showing the fracture mode at 25°C for blunt and sharp notch and Q+T and Q+T + aged conditions. The fracture mode in all cases was quasi-cleavage along martensite lath boundaries. There was no effect of fatigue pre-cracking or aging at 550°C on the fracture mode.

no difference in fracture mode caused by notch acuity or thermal aging. An increase in DBTT after aging in this temperature range is caused by temper embrittlement (TE). Classically, this is manifest by both an increase in DBTT and a change in fracture mode to intergranular. This is in contrast to the 80°C increase in DBTT measured by the precracked and instrumented impact test but no change in fracture mode.

7.4. Discussion

Based on the results reported here and fracture and other data reported earlier(1), some interesting observations can be made. It has been shown that classical tempered martensite embrittlement occurs in this system. There is strong evidence that it is due to the carbon having sufficient time to diffuse away from the center of the laths, thus stabilizing the austenite as yet untransformed between them. When enough energy is supplied during tempering, the carbon will precipitate in $M_{23}C_6$ carbide networks. This carbide network is associated with a sharp decrease in notch toughness in the tempering regime where the austenite decomposes. In this system the regime probably occurs at temperatures lower than 650°C. Work continues on determining the TME range for the 12Cr-1Mo-0.3V alloy.

The most beneficial heat treatment to be given the material from a vendor would be one in which the amount of austenite was minimized after austenitization and quenching. It is known that austenite films can have beneficial effects on the toughness of some alloys when they are made more stable(7), that is not transforming until higher temperatures. The films are thought to accommodate strains. However, the carbon enriched austenite will precipitate a carbide after long times or higher temperatures such as one would expect in a power generation system. It has been shown in other systems that the volume % austenite can be mitigated. For example, lower austenitizing temperatures have been shown to reduce the amount of austenite in AISI 4340(7). It is also known that a faster quench in some alloys will have the same effect, and it is noted that vendors sometimes cool HT-9 by faster quenches than air-cooling. Work is continuing on these factors, and

preliminary results indicate that the films of austenite were decreased as a result of a warm water quench. Fracture data is being generated to determine if that can increase the as-received toughness. It is this condition from which all other forms of toughness begin degredation, and it is reasonable to assume a higher as-received toughness will result in a higher toughness level in an embrittled structure.

A review of the fracture data shows that aging at 550°C for 100 hours causes an 80°C increase in the DBTT. This is in the temperature regime associated with temper embrittlement (TE) (8,9). When a susceptible material is slowly cooled between 600-400°C, impurity elements segregate to prior austenite grain boundaries causing intergranular fracture(10). Many structures are cooled gradually from operating temperatures during shut-down which provide the environmental requirements for TE. However, there are methods to decrease susceptibility to TE. Cleaner melting practice will decrease the impurity segregation levels thus reducing TE fracture. Lower austenitizing temperatures produce a finer grain size increasing the area required to be embrittled. Recently, TE susceptibility was shown to be decreased by heat treatment of a Ni-Cr-Mo-V steel in the two phased $\alpha + \gamma$ region, and also that this could be done effectively in thick sections(11). This further reduces TE effects. In this investigation, there was no intergranular fracture, although there was a shift in the DBTT. Other investigators also report phenomena such as this(9,12) although no explanation is offered. This data suggests there may be a form of embrittlement with aspects of both TME and TE. That is, the shift in the DBTT may be associated with segregants at martensite lath boundaries. Auger electron spectroscopy of specimens fractured in-situ is being done at Sandia Laboratory to determine if any elements are in higher than nominal concentrations at the lath boundaries.

1.4.1 Conclusions

Based on this data, the following is concluded:

(1) Thin films of austenite retained at martensite

lath boundaries in the austenitized and cooled condition decompose to $M_{23}C_6$ carbide networks upon tempering. This is temper martensite embrittlement, and classically results in a lower notch toughness than would the same microstructure without the networks.

(2) Aging the austenitized and tempered condition at 550°C for 100 hrs. results in an 80°C increase in the DBTT as measured by precracked and instrumental CVN with no significant change in carbide network continuity. This is in the temper embrittlement temperature regime and may be due to impurity segregation at lath boundaries.

(3) The fracture surfaces, Q+T and Q+T and aged, in all cases were quasi-cleavage along the martensite lath boundaries.

(4) Preliminary results indicate the amount of retained austenite can be reduced by utilitizing a faster quench.

7.4.8 References

1. Lechtenberg, T. A. and S. Helfrich, "The Fracture Properties of a Temper Embrittled 12Cr-1Mo-0.3V Steel", Alloy Development for Irradiation Performance, Quarterly Progress Report for the Period Ending June 30, 1980, DOE/ER-0045/3, pp. 201-215.
2. Speich, G. and W. Leslie, Met. Trans A, 3 (1972) 1043.
3. Kurdjumov, G. and G. Sacks, Z. Phys., 64 (1930) 325.
4. Maki, T. and C. Wayman, Acta. Met., 25 (1977) 681.
5. Howell, P., J. Bee, R. Honeycomb, Met. Trans. A, 10A (1979) 1213.
6. Rao, B., Met. Trans A, 10A (1979) 645.
7. Lai, G., W. Wood, R. Clark, V. Zackay, E. Parker, Met. Trans. A, 5 (1974) 1663.
8. Berry, G. and R. Brook, Metals Science, 9 (1975) 286.
9. Edwards, B. and E. Little: Ferritic Steels for Fast Reactor Steam Generators, B.N.E.S., London (1978) 145.
10. McMahon, C., Mat. Sci and Eng., 42 (1980) 215.
11. Woodford, D. and R. Stepien, Met Trans A, 11A (1980) 1951.
12. Druce, S. and B. Edwards, U.K. Atomic Energy Authority, Harwell, Report No. AERE-R9904, September 1980, Oxfordshire, U.K.
13. Rao, B., Ph.D. Thesis, University of California, Lawrence Berkeley Laboratory, LBL Report 7361, February 1979.
14. Krauss, G. and A. Marder, Met. Trans, 2 (1971) 2343.
15. Grange, R., Met. Trans, 2 (1971) 65.
16. Das, S. and G. Thomas, Trans. ASM, 62 (1969) 659.
17. Huang, D. and G. Thomas, Met. Trans, 2 (1971) 1587.
18. Chafey, J. E. and L. D. Thompson, "Post-Service Evaluation of the Properties of a 12Cr-1Mo Steel Superheater Tube", Material-Environment Interactions in Structural and Pressure Containment Service, p. 53, MPC-15, American Society of Mechanical Engineers, NY, (1980).
19. Thomas, G., Met Trans A, 9A (1978) 439.

7.5 ENVIRONMENTAL EFFECTS ON PROPERTIES OF FERRITIC STEELS - O. K. Chopra and D. L. Smith (Argonne National Laboraotry)

7.5.1 ADIP Task

ADIP tasks are not defined for ferritic steels in the 1978 program plan.

7.5.2 Objective

The objective of this program is to investigate the influence of chemical environment on the compatibility, corrosion, and mechanical properties of ferritic steels under conditions of interest in fusion reactors. Test environments to be investigated include lithium, water, and helium as well as candidate solid breeding materials and neutron multipliers. Emphasis will be placed on the combined effect of stress and chemical environment on corrosion and mechanical properties of ferritic steels. Tests have been formulated to determine the (1) effect of a liquid lithium environment on fatigue and creep-fatigue properties of ferritic steels and (2) compatibility of structural materials with liquid lithium and candidate solid tritium-breeding materials.

7.5.3 Summary

Several continuous-cycle fatigue tests have been conducted with 2.5-mm-diameter specimens of HT-9 alloys at 755 K in a lithium environment of controlled purity. However, the fatigue test program was temporarily suspended because of a gradual increase in the nitrogen content of the lithium. The lithium loop was shut down twice owing to plugging of the cold-trap purification loop. Metallographic examination of the cold-trap pipe indicates that plugging was caused by trapping of nickel-manganese and iron-nickel-manganese crystals under the pump coil and flowmeter magnet. The increased nitrogen concentration in the lithium resulted in excessive corrosion and mass transfer. The nitrogen in the lithium also had a large effect on the fatigue behavior of the HT-9 alloy. Metallographic evaluation of HT-9 alloy, Type 316 stainless steel, and Inconel 625 exposed in contact with solid Li_2O, $LiAlO_2$, and

Li_2SiO_3 breeding materials has been completed. Results indicate that Li_2O is the most reactive of the three breeding materials. HT-9 alloy exposed in contact with Li_2O contained Li_5FeO_4 and $LiCrO_2$ compounds, whereas $Li_2Ni_8O_{10}$ and $LiCrO_2$ were observed on Inconel 625. The presence of these volatile compounds may explain the higher reactivity of Li_2O.

7.5.4 Progress and Status

7.5.4.1 Fatigue Tests

The effects of a liquid lithium environment on the fatigue properties of ferritic steels, such as Sandvik HT-9 and developmental Fe-9Cr-1Mo alloy, are being investigated. Tests have been formulated to evaluate the influence of lithium purity, temperature, and test frequency on the fatigue and creep-fatigue behavior of ferritic steels. Several continuous-cycle fatigue tests have been conducted with 2.5-mm-diameter specimens of HT-9 alloy at 755 K in a flowing lithium environment of controlled purity. The facility for conducting fatigue tests and the associated liquid lithium loop were described in an earlier report.[1] The lithium loop was operated at cold-trap temperatures between 474 and 500 K and maximum temperatures between 620 and 760 K. Filtered dip samples of the lithium were taken regularly for analysis of nitrogen and carbon. The concentrations of nitrogen and carbon as a function of loop operating time are given in Table 7.5.1.

Fatigue testing was initiated when the concentration of nitrogen in the lithium was ~100 wppm. However, after ~10.8 Ms (~3000 h), the nitrogen content increased to >1000 wppm and the cold-trap purification loop showed a gradual reduction in lithium flow. The lithium loop was shut down twice, owing to plugging of the cold-trap loop. On each occasion, the flowmeter and pump section of the cold-trap loop was cut out and replaced with a new pipe. X-ray of the pipe showed a plug in the section under the magnetic pump coil. The section of the pipe under the flowmeter magnet was also blocked. After restarting, the maximum temperature in the loop was kept below 620 K to prevent excessive corrosion and mass transfer. Fatigue testing was terminated

to avoid possible contamination of lithium from the fatigue test fixture. Also, calcium metal was added to the lithium to getter nitrogen. Recent analyses indicate nitrogen concentrations between 540 and 570 wppm.

TABLE 7.5.1. Concentrations of Nitrogen and Carbon in Lithium as a Function of Loop Operating Time at Temperatures between 623 and 755 K

Loop Operating Time, Ms (h)	Maximum Temperature, K	Nitrogen, wppm	Carbon, wppm
0.36 (100)	623	475	-
0.54 (150)	623	417	-
2.52 (700)	755	86	-
2.88 (800)		-	9
8.28 (2300)		130	-
8.64 (2400)		-	11
13.14 (3650)		-	19
14.04 (3900)		1220	-
14.76 (4100)	Loop Shut Down		
15.48 (4300)	755	1530	-
17.03 (4730)	Loop Shut Down		
18.32 (5090)	623	1420	-
19.08 (5300)		925	-
19.51 (5420)		1400	-
20.23 (5620)		1380	-
20.74 (5760)		1020	-
22.03 (6120)		898	-
22.32 (6200)		545	-

The plugged pipe removed after the first shutdown was cleaned and examined metallographically to determine the nature and composition of the surface deposits. Lithium from the plugged sections of the pipe was dissolved in a solution of methyl alcohol and water and the residue was analyzed by energy-dispersive x-ray (EDAX) and x-ray diffraction analyses. A strong odor of ammonia was detected during dissolution of the lithium, and the solution turned dark yellow or green. Scanning electron micrographs and EDAX analyses of the surface of pipe sections removed from the pump inlet and under the pump coil are shown in Figs. 7.5.1a and 7.5.1b, respectively. Both surfaces show

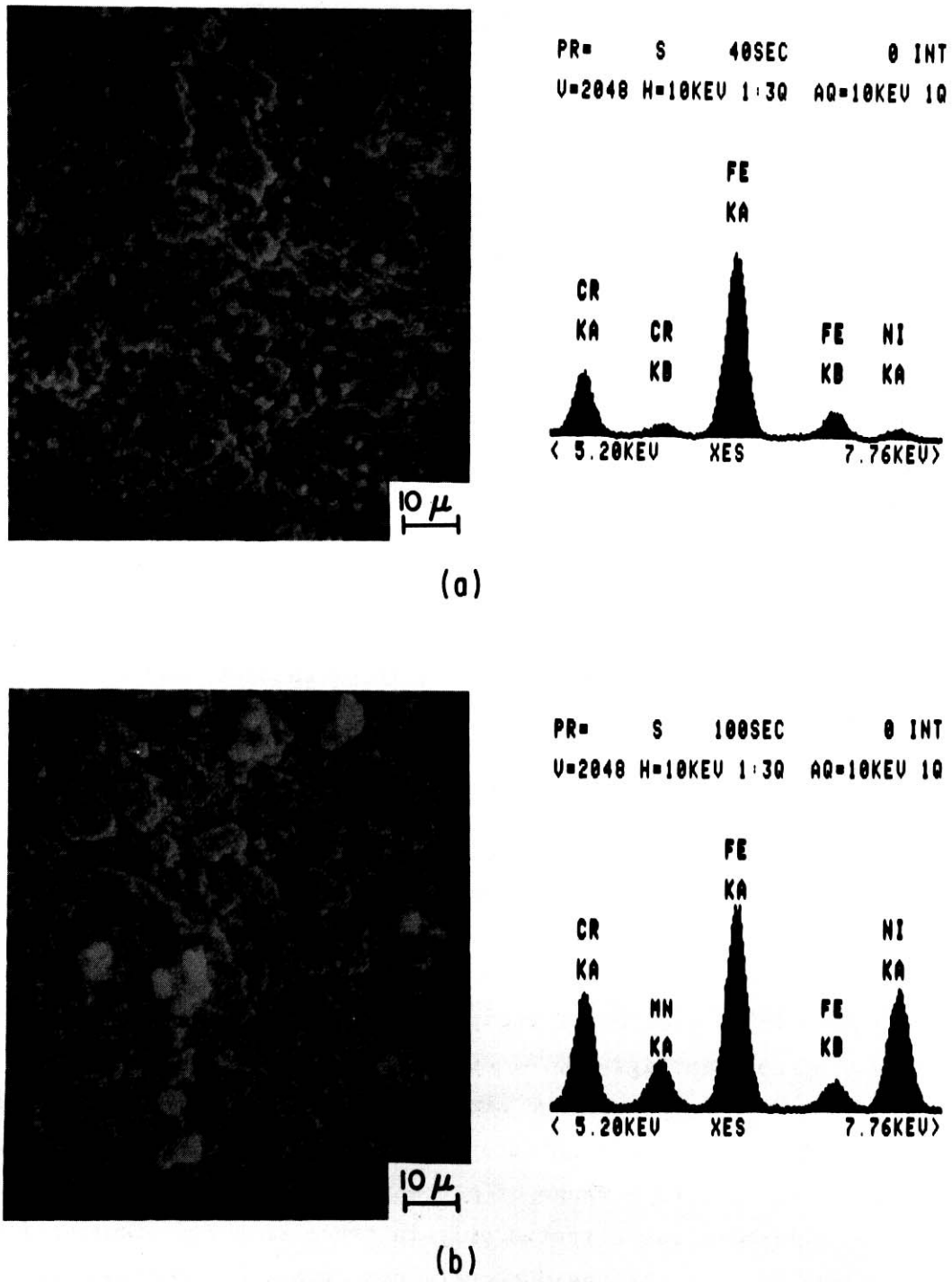

Fig. 7.5.1. Micrographs and EDAX Analyses of the Deposits on the Surface of the Plugged Cold-trap Pipe Removed after the First Shutdown. (a) Pipe section near the pump inlet and (b) pipe section under the pump coil.

globular deposits. EDAX analyses indicate that near the pump inlet, the deposits consist primarily of iron and chromium, whereas an enrichment of nickel, chromium, and manganese is observed on the surface under the pump coil. The large white particles on the surface are chromium oxide.

A scanning electron micrograph of the metallic residue collected from the pump section of the plugged cold-trap pipe is shown in Fig. 7.5.2. The residue consists of large faceted crystals and smaller globular particles. EDAX analyses show that this residue is composed of nickel and manganese; the faceted crystals contain equal amounts of nickel and manganese, whereas a higher concentration of nickel is observed in the globular particles. These particlea were identified by x-ray diffraction as the tetragonal MnNi and cubic $MnNi_3$ phases, respectively. Iron and chromium were not detected in the residue. Figure 7.5.3 shows a micrograph of the residue collected from the flowmeter section of the cold-trap pipe. The residue is similar to that observed in the pump section, i.e., large faceted and small globular crystals. However, the crystals are covered by a chromium-rich opaque phase, which also contains oxygen. These results indicate that chromium was present in the lithium as chromium nitride, and the opaque phase (probably an oxide of lithium and chromium) was formed from the chromium nitride when the lithium was dissolved in methyl alcohol and water.

A micrograph and EDAX analyses of the residue collected from the pump inlet section of the plugged pipe removed after the second shutdown are shown in Pig. 7.5.4. Unlike the residue collected from the pump section of the pipe removed after the first shutdown (Fig. 7.5.2), these particles contain a significant amount of iron. The compositions range from pure iron to a range of concentrations of iron, nickel, and manganese. Chromium was detected only in trace amounts. Examination and identification of the residue collected from other sections of the pipe are currently in progress.

The results of the metallographic examination of the cold-trap pipes indicate that plugging was caused by accumulation of magnetic crystals of nickel-manganese or iron-nickel-manganese phases

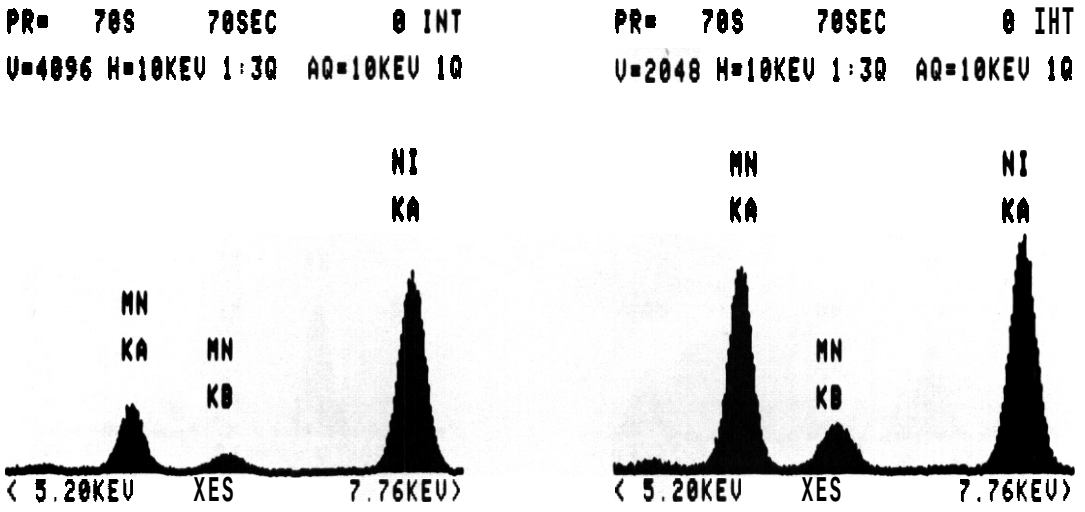

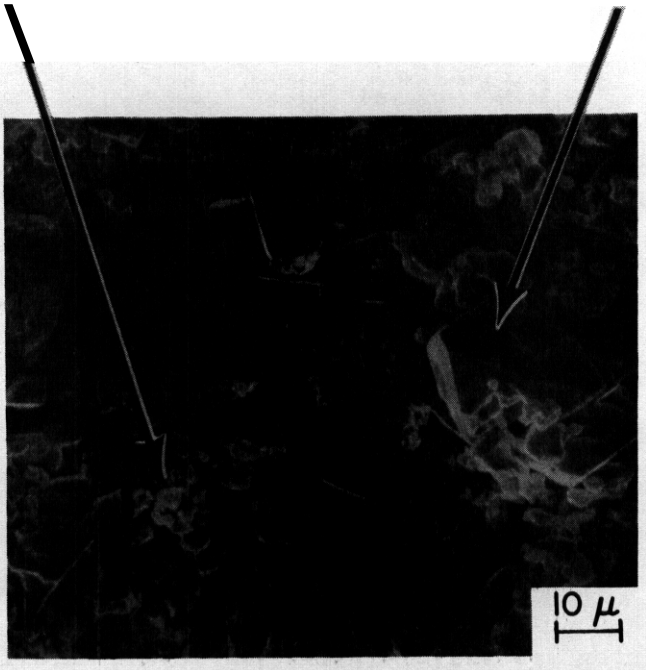

Fig. 7.5.2. Micrograph and EDAX Analyses of the Metallic Residue Collected from the Pump Coil Section of the Plugged Cold-trap Pipe Removed after the First Shutdown.

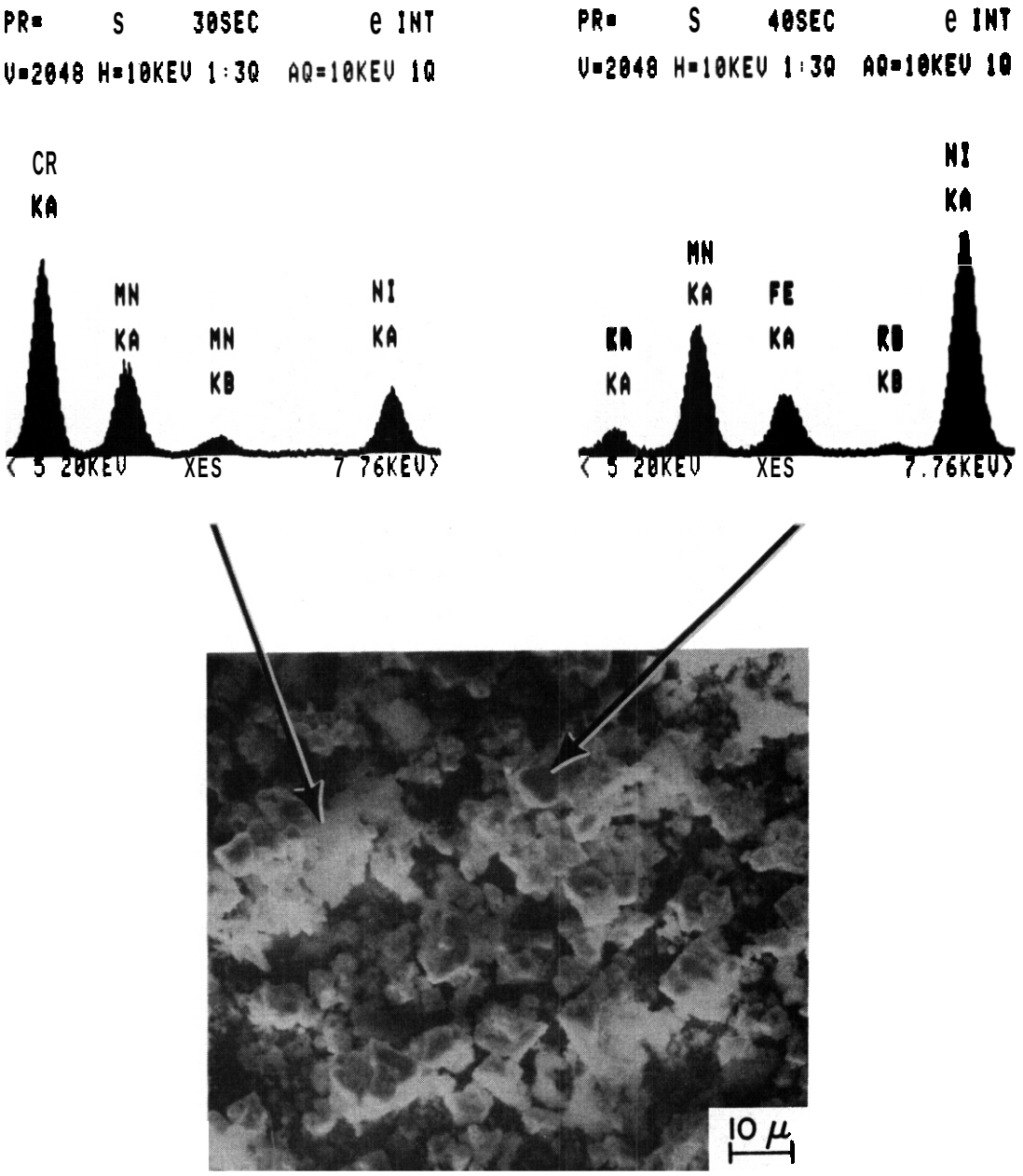

Fig. 7.5.3. Micrograph and EDAX Analyses of the Metallic Residue Collected from the Flowmeter Section of the Plugged Cold-trap Pipe Removed after the First Shutdown.

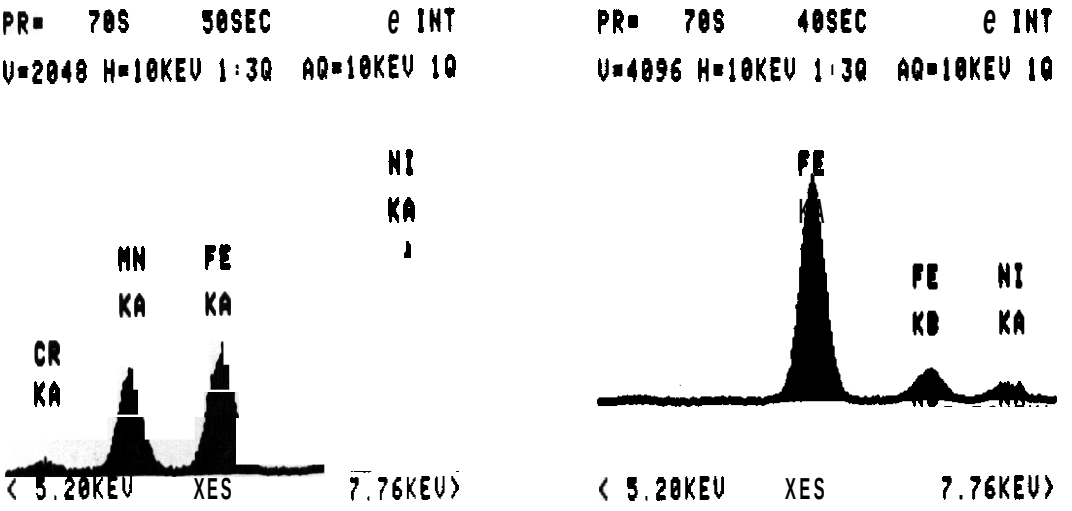

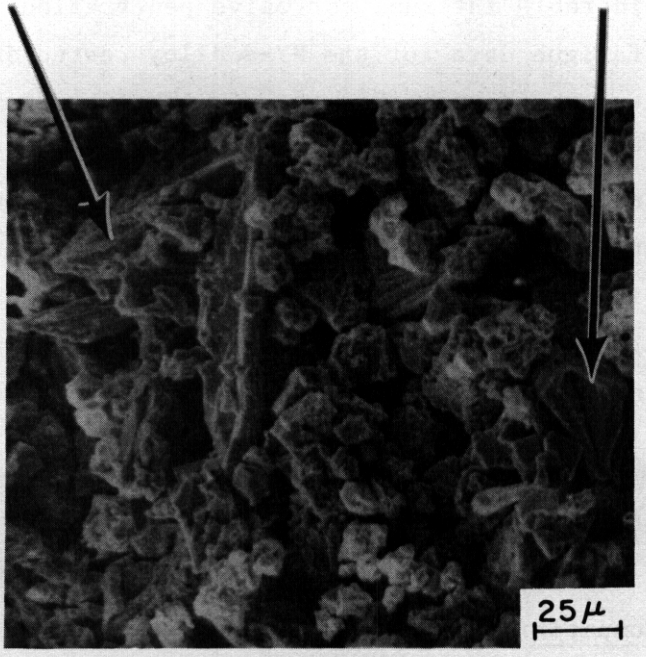

Fig. 7.5.4. Micrograph and EDAX Analyses of the Metallic Residue Collected from the Pump Inlet Section of the Plugged Cold-trap Pipe Removed after the Second Shutdown.

under the pump coil or flowmeter magnet. The increase in nitrogen concentration in the lithium resulted in excessive dissolution and mass transfer of various constituents of the stainless steel vessel. At temperatures below 550 K, crystals of nickel-manganese and iron-nickel-manganese were formed in lithium saturated with nickel, iron, and manganese. Trapping of these crystals by the magnetic field under the pump coil or flowmeter magnet resulted in the plugging of the cold-trap loop.

The fatigue behavior of HT-9 alloy tested at 755 K in a flowing lithium environment was also influenced by the nitrogen concentration in the lithium.[2] At a total strain range of 0.5%, the fatigue life in lithium is a factor of ~5 lower than that in a liquid sodium environment. The specimen teated in lithium shows partial intergranular fracture and considerable internal corrosive penetration. The continuous-cycle fatigue data for the HT-9 alloy tested in lithium and sodium environments are shown in Fig. 7.5.5. The results indicate that the plastic strain and fatigue life follow two different power-law relationships. The fatigue life in tests conducted in lithium containing <500 wppm nitrogen is similar to that in a sodium environment. However, the fatigue life in lithium containing >1000 wppm nitrogen is a factor of 2 to 5 lower than that in sodium. The difference in fatigue life is greater at total strain ranges <0.7%. Fatigue tests at low strain range will be repeated in lithium containing ~100 wppm nitrogen to evaluate the influence of nitrogen and corrosion on the continuous-cycle fatigue behavior of the HT-9 alloy in lithium.

7.5.4.2 Compatibility

Compatibility of structural materials with candidate solid tritium-breeding materials is being investigated. Flat specimens of HT-9 alloy, Type 316 stainless steel, and Inconel 625 in contact with pellets of Li_2O, γ-$LiAlO_2$, and Li_2SiO_3 ceramic material were diffusion annealed for 7.2 Ms (2000 h) at 873 K in a high-purity helium environment. A comparative evaluation of the nature and composition of the surface scales formed on the alloy specimens was presented earlier.[2]

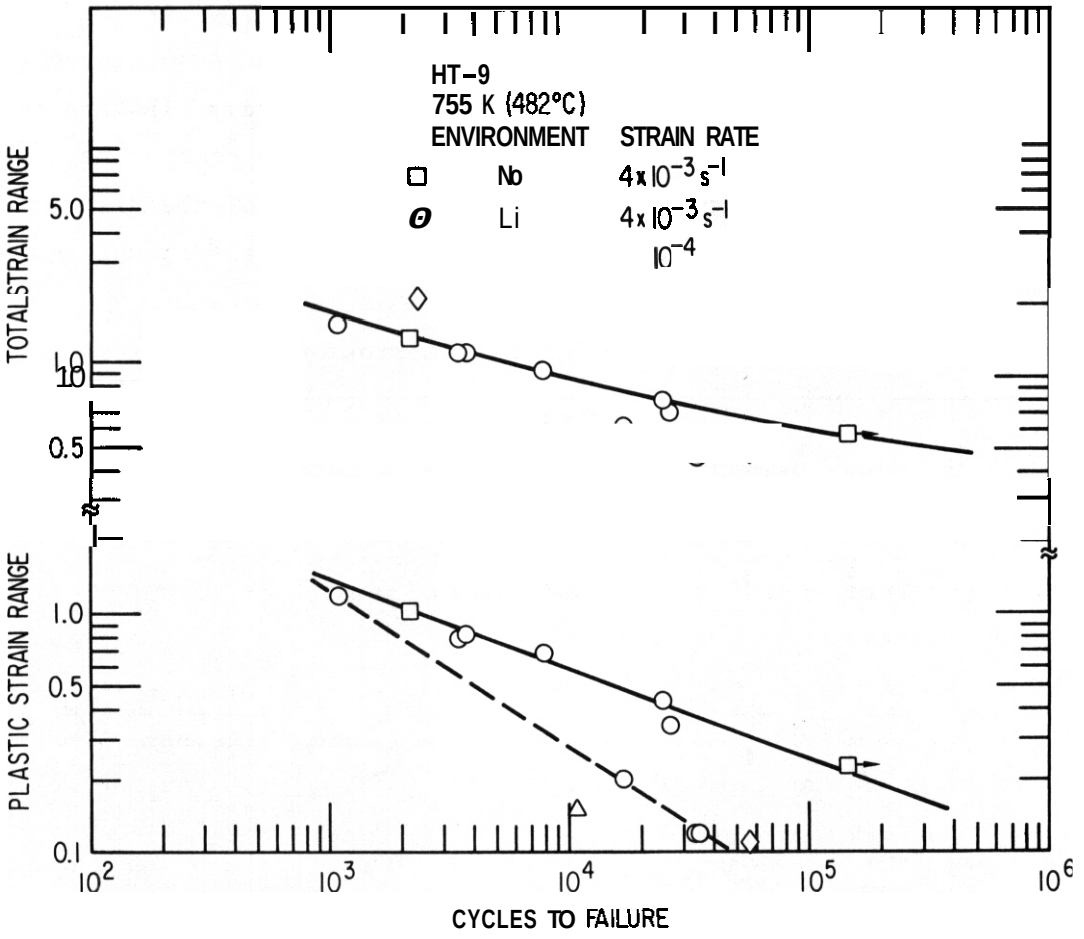

Fig. 7.5.5. Total and Plastic Strain Range vs Cycles to Failure for HT-9 Alloy Tested in Lithium and Sodium at 755 K. Concentration of Nitrogen in lithium: <500 wppm (solid line) and >1000 wppm (dashed line).

Alloy specimens exposed in contact with either $LiAlO_2$ or Li_2SiO_3 showed a weak interaction with the ceramic. The surface scales essentially consisted of chromium and/or iron oxide. However, the alloys in contact with Li_2O showed a strong interaction. The reaction products contain a significant amount of ceramic material.

Specimen cross sections were examined in detail to determine the thickness of the surface scale and the distribution of constituents 'in the scale. The various phases in the scale were identified by x-ray diffraction analysis. A summary of the data is given in Table 7.5.2. The results show that Li_2O is the

TABLE 7.5.2. Summary of Corrosion Data

Ceramic	Alloy	Ceramic/Alloy Interaction	Corrosion Scale Thickness, μm	Corrosion Scale Phases[a]	Remarks
Li_2O	HT-9	Strong	12	Li_5FeO_4, $LiCrO_2$	
	316 SS	↓	54	Li_2CO_3[b]	
	IN 625		116	$Li_2Ni_8O_{10}$, $LiCrO_2$, Li_2O, Li_2CO_3[b]	
$LiAlO_2$	UT-9	Weak	5	Fe_3O_4, $LiCrO_2$	Scale contains ~9% Mn
	316 SS	↓	2	Cr_2O_3, Fe_3O_4, $LiCrO_2$	Scale contains ~3% Mn
	IN 621		<2	Cr_2O_3, $LiCrO_2$	
Li_2SiO_3	HT-9	Weak	6	$LiCrO_2$, $LiFeO_2$	
	316 SS	↓	2	$LiCrO_2$	
	IN 625		<2	$LiCrO_2$	

[a]Phases identified by x-ray diffraction.
[b]Li_2CO_3 formed after the test.

most reactive of the three breeding materials. The thickness of the surface scale for alloys exposed in contact with either $LiAlO_2$ or Li_2SiO_3 is between 2 and 5 μm. However, 150- and 110-μm-thick scales are observed, respectively, for Type 316 stainless steel and Inconel 625 exposed to Li_2O ceramic. Micrographs of the specimens in contact with Li_2O are shown in Fig. 7.5.6. Type 316 stainless steel and Inconel 625 specimens have a thick outer layer of reaction zone, which consists of pieces of the reaction product embedded in the ceramic material. The

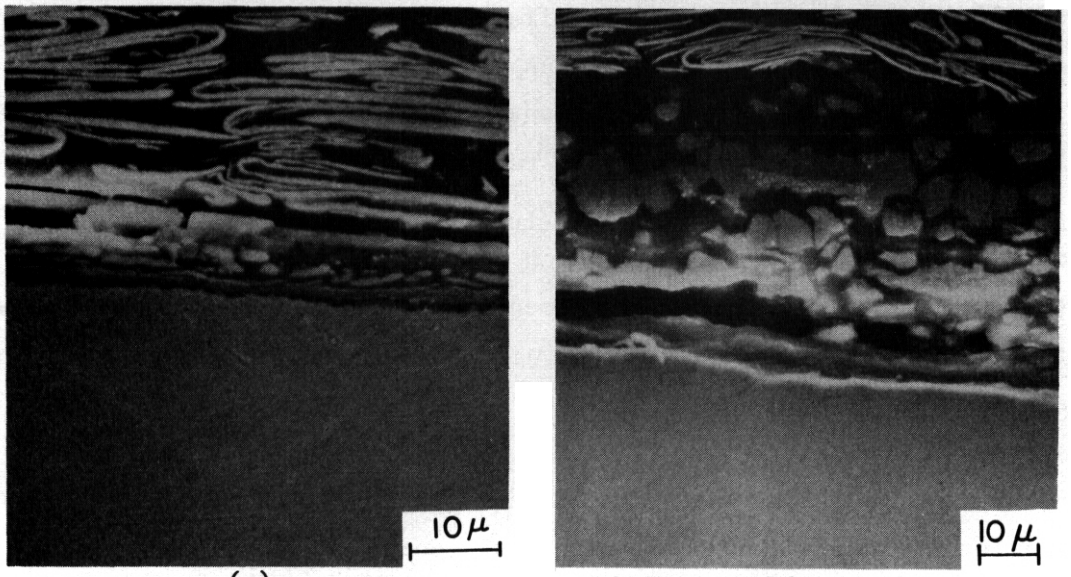

(a) (b)

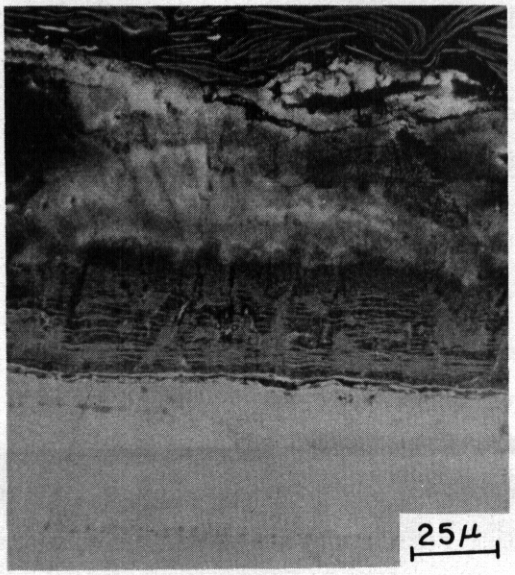

(c)

Fig. 7.5.6. Micrographs of Specimens Exposed in Contact with Li_2O Ceramic for 7.2 Ms at 873 K. (a) HT-9 alloy, (b) Type 316 stainless steel, and (c) Inconel 625.

RT-9 alloy may also have had a similar reaction zone, which broke off when the alloy and ceramic specimens were separated.

X-ray diffraction analysis of the surface scale on AT-9 alloy in contact with Li_2O ceramic revealed two corrosion products, Li_5FeO_4 and $LiCrO_2$, whereas $Li_2Ni_8O_{10}$ and $LiCrO_2$ were observed on the Inconel 625 specimen. Li_2CO_3, which was detected on some of the specimens, is believed to have formed after the test by interaction with moisture and carbon dioxide in the air. The surface scales formed on the specimens in contact with $LiAlO_2$ contained Fe_3O_4 and Cr_2O_3 with trace amounts of $LiCrO_2$. In similar studies on the compatibility of Fe-Ni-Cr alloys with Li_2O ceramic at temperatures between 773 and 1373 K, the formation of volatile Li_5FeO_4 and $LiCrO_2$ compounds was reported.[3,4] The Li_5FeO_4 compound is significantly more volatile than $LiCrO_2$. Consequently, $LiCrO_2$ was predominant in the surface scales at temperatures above 923 K.[4] The formation of volatile Li_5FeO_4 may explain the higher corrosion rates observed for the specimens in contact with the Li_2O ceramic in the present study. Li_5FeO_4 was not observed in the alloys exposed to either $LiAlO_2$ or Li_2SiO_3. Compatibility tests at 973 K are in progress to determine the mechanisms of corrosive attack.

7.5.5 Conclusions

1. Metallographic examination of the cold-trap pipe indicates that plugging was caused by trapping of nickel-manganese or iron-nickel-manganese crystals under the pump coil or flowmeter magnet. The increased nitrogen concentration in the lithium resulted in excessive dissolution and mass transfer of various constituents of the stainless steel vessel.
2. Nitrogen concentration in lithium has a strong effect on the fatigue behavior of HT-9 alloy tested at 755 K in a flowing-lithium environment. The fatigue life of specimens in lithium containing <500 wppm nitrogen is similar to that in s sodium environment, whereas fatigue life in lithium containing >1000 wppm nitrogen is a factor of 2 to 5 lower.

3. Compatibility tests with solid Li_2O, $LiAlO_2$, and Li_2SiO_3 tritium breeding materials indicate that Li_2O is the most reactive of the three breeding materials. HT-9 alloy exposed with Li_2O ceramic contained two reaction products, Li_5FeO_4 and $LiCrO_2$, whereas $Li_2Ni_8O_{10}$ and $LiCrO_2$ were observed on Inconel 625. The formation of volatile Li_5FeO_4 compound may explain the higher corrosion rates for the specimens in contact with Li_2O.

7.5.6. References

1. O. K. Chopra and D. L. Smith, "Environmental Effects on Properties of Ferritic Steels," ADIP Quarterly Progress Report, March 31, 1980, DOE/ER-0045/2, pp. 181-183.
2. O. K. Chopra and D. L. Smith, "Environmental Effects on Properties of Ferritic Steels," ADIP Quarterly Progress Report, September 30, 1980.
3. T. Kurasawa et al., "Reaction of Several Iron and Nickel Based Alloys with Sintered Li_2O Pellets," J. Nucl. Mater. 80 (1979), pp. 48-56.
4. T. Kurasawa et al., "Compatibility between Several Heat Resistant Alloys and Sintered Li_2O in Static Helium Gas Environment," J. Nucl. Mater. 92 (1980), pp. 67-72.

7.6 FABRICATION OF MATERIALS FOR THE RB-1 EXPERIMENT IN HFIR -

R. J. Puigh and R. D. Stevenson
(Hanford Engineering Development Laboratory).

7.6.1 ADIP Task

The Department of Energy (DOE), Office of Fusion Energy (OFE) has cited the need for data on these materials under the ADIP Program Task, Ferritic Material Development (Path E).

7.6.2 Objective

The objective of this work is to provide ferritic materials which are to be used in the fabrication of specimens to be irradiated in the RB-1 and AD-2 experiments.

7.6.3 Summary

Selected ferritic alloys have been mechanically processed for use in the fabrication of specimens for the MFE-RB-1 experiment in HFIR and for the reencapsulation of the AD-2 experiment in EBR-II. Weldments have been fabricated from HT-9, modified 9Cr-1Mo, and 2-1/4Cr-1Mo base metals.

7.6.4 Progress and Status

7.6.4.1 Introduction

The MFE-RB-1 experiment[**]) will provide data on the effects of low energy neutron irradiation at 50°C on the mechanical properties of selected ferritic steels. Specifically, this experiment will contain specimens fabricated from the following alloys: HT-9 (2 heats), 9Cr-1Mo (2 heats), 2-1/4Cr-1Mo, AISI 316SS, weldments of HT-9 (one heat), 9Cr-1Mo (1 heat) and 2-1/4Cr-1Mo, and the nickel doped alloys fabricated by ORNL from HT-9 and 9Cr-1Mo. HEDL and ORNL share responsibility for the fabrication of materials and specimens for this experiment. This report will cover the materials for which HEDL has responsibility: HT-9 (one heat), 9Cr-1Mo (one heat), 2-1/4Cr-1Mo, all weldments, and AISI 316SS.

7.6.4.2 Material Fabrication

The vendor certified compositions for the Carpenter Technology heats of HT-9 and 9Cr-1Mo, for the Cameron Iron Works heat of 2-1/4Cr-1Mo, and for the MHE heat of AISI 316SS are given in Table 7.6.1. This heat of HT-9 is the same material as was used in the fabrication of specimens for the AD-2 experiment.(2) Also, this particular heat of 9Cr-1Mo is from the same melt as the material used in the AD-2 experiment. Since a sufficient quantity of the heat of 2-1/4Cr-1Mo used in the AD-2 experiment was not available, another heat of 2-1/4Cr-1Mo was procured from ORNL. The major chemical difference between this heat and the heat used in the AD-2 experiment is the nickel content.

Figure 7.6.1 outlines the processing steps in the fabrication of the HT-9 specimen material stock from the 33.3 mm diameter bar stock. A decarburized layer as large as 0.25 mm thick forms on the material during the hot forging and rolling at 1038°C. After cold rolling the material approximately 29%, an anneal at 760°C for 2.5 hours was performed to relieve stresses incurred during cold rolling. This anneal and the following two heat treatments were performed in an argon atmosphere furnace to minimize further decarburization of the surfaces. The final heat treatment for the 6.35 and 3.18 mm plate stock was 1038°C/10 min/AC + 760°C/30 min/AC. The decarburized layer was removed from the 6.35 and 3.18mm material during specimen fabrication.

The mechanical processing steps used in the fabrication of the HT-9 sheet stock from which the fatigue crack growth, the flat tensile, and the Grodzinski Fatigue specimens are to be fabricated are shown in Figure 7.6.2. The starting stock was the 3.18 mm plate fabricated using the process outlined in Figure 7.6.1. The surfaces of this plate were ground to remove the decarburized layer. All subsequent heat treatments of this material were performed by encapsulating the material with a strip of Ta getter foil in a quartz tube which was then filled with a one-fourth atmosphere of argon. The final heat treatment for this thin material stock was 1038°C/4 min/AC + 760°C/30 min/AC. This heat treatment produced a microstructure for this material stock which was equivalent to the primary condition (TMT#1) of HT-9 used in the AD-2 experiment.(2)

TABLE 7.6.1

CHEMICAL COMPOSITIONS

Element	HT-9 (91353) Vendor[1]	HT-9 (91353) Overcheck[2]	9Cr-1Mo (30176) Vendor[3]	9Cr-1Mo (30176) Overcheck[4]	2-1/4Cr-1Mo (56447) Vendor[5]	316SS (15893) Vendor[6]	316SS (15893) Overcheck[7]
C	0.21	0.23	0.09	0.092	0.10	0.05	0.057
Mn	0.50	0.39	0.37	0.48	0.40	1.79	1.67
P	0.007		0.011	0.012	0.009	0.031	0.033
S	0.003		0.004	0.004	0.006	0.020	0.015
Si	0.22	0.23	0.16	0.15	0.23	0.65	0.66
Ni	0.58	0.46	0.11	0.09	0.14	12.38	11.84
Cr	11.80	12.34	8.43	8.32	2.16	17.33	16.56
Mo	1.02	0.99	0.89	0.86	1.03	2.14	2.44
V	0.32	0.45	0.24	0.20	0.01		
Nb			0.08	0.06			
Ti	0.003		<0.02	0.001	0.01		<.01
Co			0.02	0.017	0.01		
Cu	0.04	0.07	0.04	0.03	0.03		
Al	0.028		0.016	0.011			
B	<0.0010		<0.001	<0.001			
As	<0.01			<0.001			
Sn				0.002			
Zr				<0.001			
N	0.006			0.055			
O				0.010			
Pb				<0.001			
Sb				<0.001			
Ta	<0.01						
W	0.50			<0.01			
Fe	Bal.	Bal.	Bal.	Bal.	Bal.	Bal.	Bal.

All numbers are weight percents.

1 Carpenter Technology Certificate of Composition dated July 22, 1975.

2 Koon-Hall Test Report dated August 21, 1979.

3 Carpenter Technology (ORNL report, "Modified 9Cr-1Mo Steel Development Progress Report for Period Ending September 30, 1979").

4 Combustion Engineering (ORNL report, "Modified 9Cr-1Mo Steel Development Progress Report for Period Ending September 30, 1979").

5 Cameron Iron Works, Inc. Certificate of Composition dated July 21, 1975.

6 MSI Nuclear Material Certification dated November 4, 1975.

7 National Spectrographic Laboratories, Inc. report dated April 12, 1977.

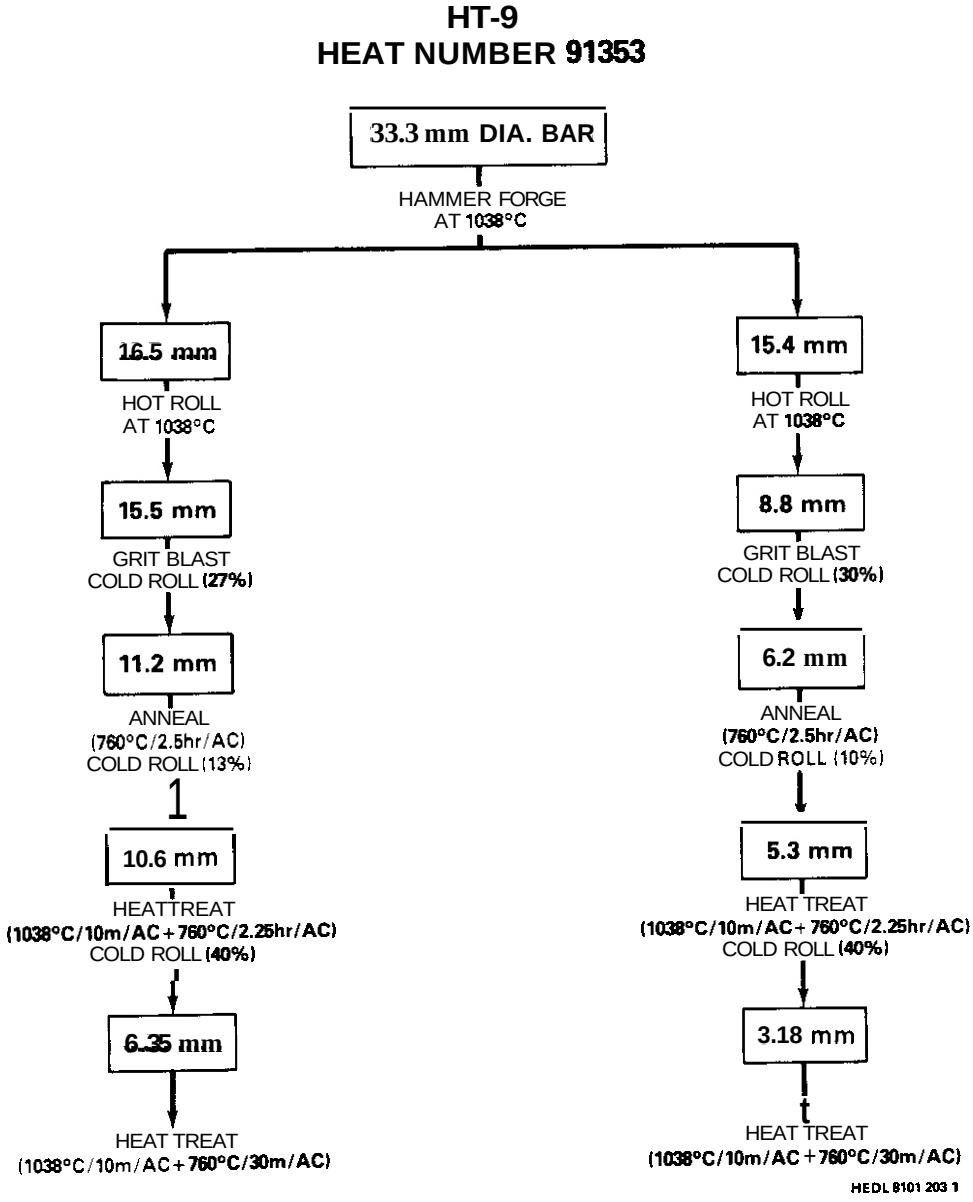

FIGURE 7.6.1 **HT-9** Mechanical Processing Steps for 0.25 and 0.125 inch plate stock.

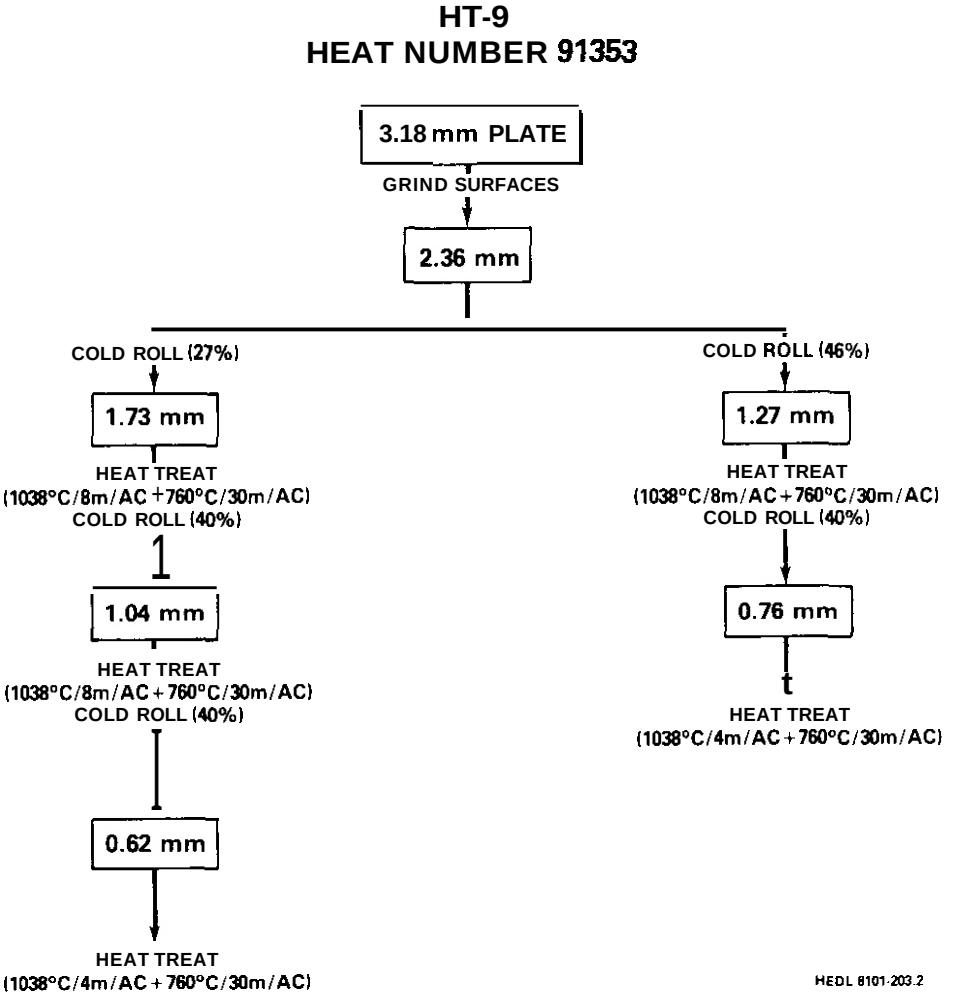

FIGURE **7.6.2** **HT-9 Mechanical Processing Steps** for **0.030 and** *0.024* **inch sheet stock.**

Figure 7.6.3 outlines the processing steps ORNL used in fabricating the 9Cr-1Mo specimen material stock from the 25 mm thick plate. The final heat treatment for this material was chosen to be 1038°C/30 min/AC + 760°C/30 min/AC. This heat treatment was performed in air with the material wrapped in stainless steel foil in order to minimize surface oxidation and decarburization.

Figure 7.6.4 outlines the steps performed at HEDL for processing the 2-1/4Cr-1Mo material into the desired form. The starting material was 51 mm thick plate from a vacuum arc remelt of a Cameron Iron Works, Inc. ingot, heat number 56447. As in the processing of HT-9, a decarburized layer as large as 0.15 mm thick was found on the material after the hot rolling. To minimize further decarbonization of the surface layers the heat treatments were performed in an argon atmosphere. The final heat treatment for this material was 900°C/30 min/AC + 700°C/1 hr/AC. This heat treatment is equivalent to the heat treatment used in the *AD-2* experiment and the breeder program for 2-1/4Cr-1Mo. Again, the decarburized layer was removed during specimen fabrication.

The mechanical processing steps used in the fabrication of the 2-1/4Cr-1Mo sheet stock material for the fatigue crack growth, flat tensile, and Grodzinski fatigue specimens are shown on Figure 7.6.5. The surfaces of the starting 3.18 mm thick stock were ground to remove the decarburized layer. All heat treatments were performed with the material plus a tantalum getter foil encapsulated in a quartz tube filled with a one-fourth atmosphere of argon. The final heat treatment for this material stock was also 900°C/30 min/AC + 700°C/1 hr/AC.

The starting stock for the AISI 316SS material was 7.9 mm thick plate from MFE heat X-15893. This material was sandblasted, wire brushed and pickled, then annealed at 1050°C for one hour in an argon atmosphere. The material was cleaned again and then cold rolled (20% reduction) to a final thickness of 6.35 mm.

Some of the 6.35 mm plate stock from the Carpenter Technology heats of HT-9 and 9Cr-1Mo and the Cameron Iron Works heat of 2-1/4Cr-1Mo were shipped to General Atomic Corporation for the fabrication of welded plate stock from which specimens would be manufactured. The

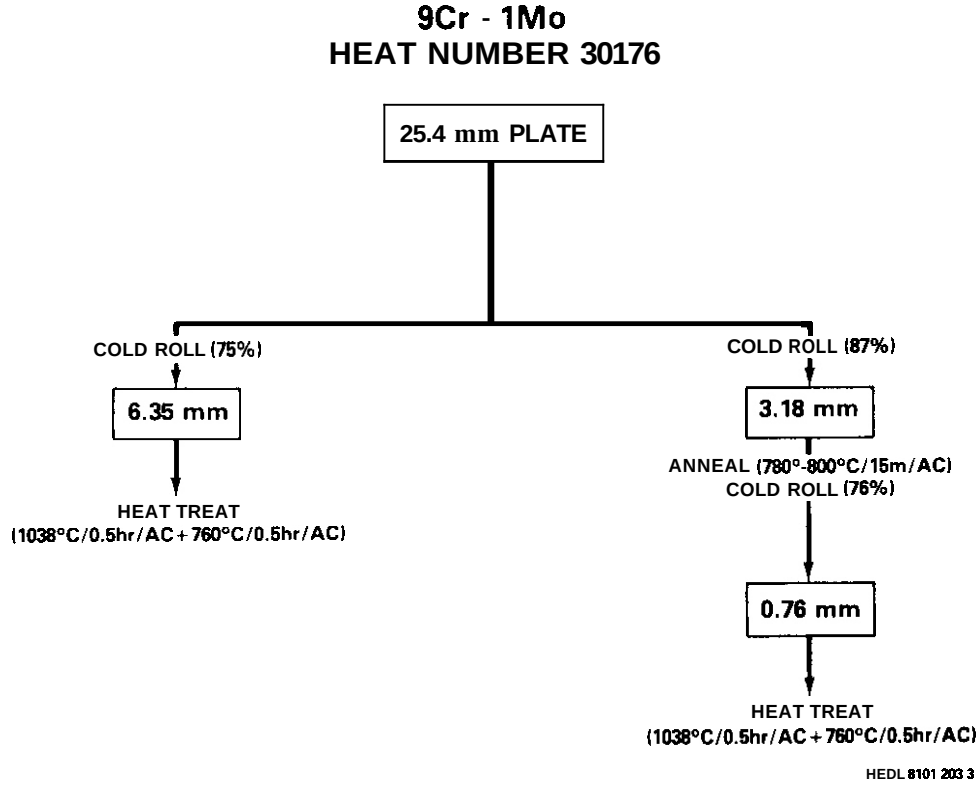

FIGURE **7.6.3 9Cr-1Mo Mechanical Processing Steps** for **0.25, 0.125, and 0.030 inch sheet stock.**

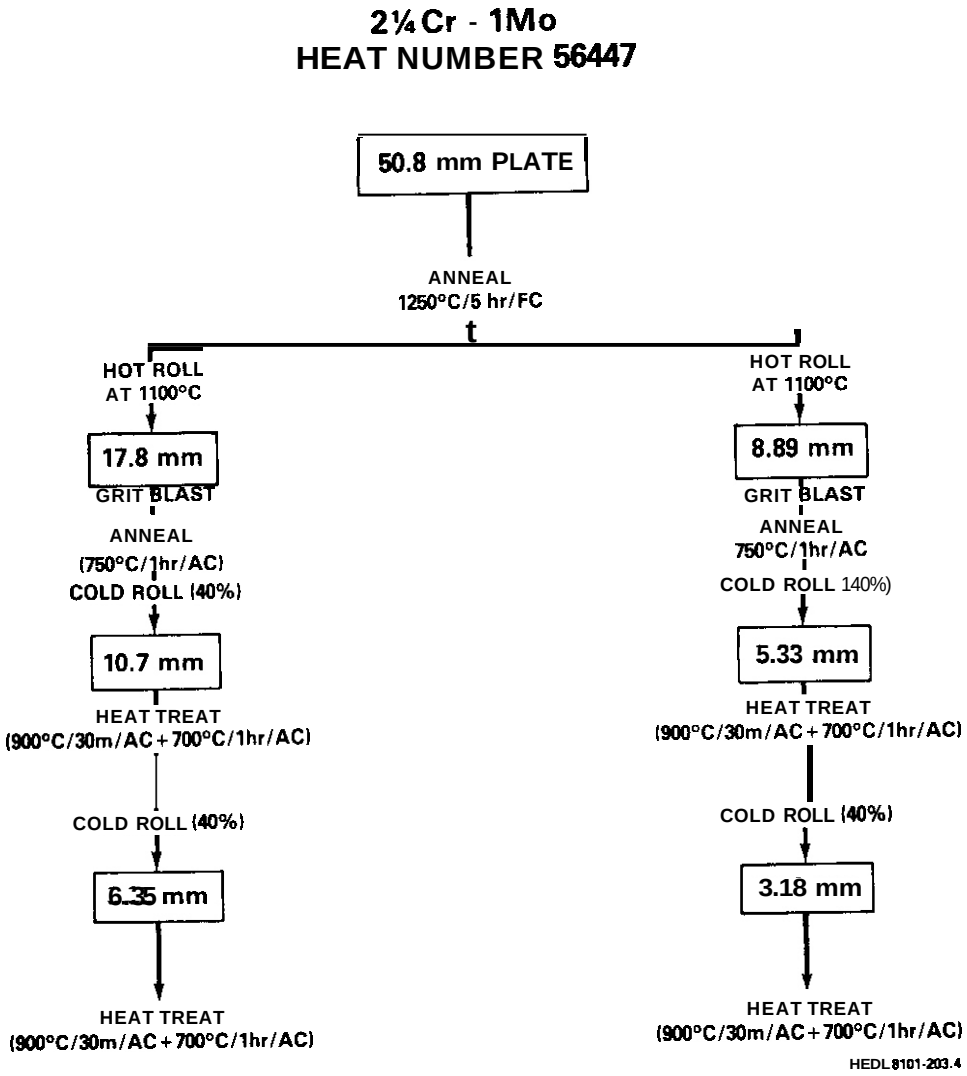

FIGURE *7.6.4* 2-1/4Cr-1Mo Mechanical Processing Steps for 0.25 and 0.125 inch plate stock.

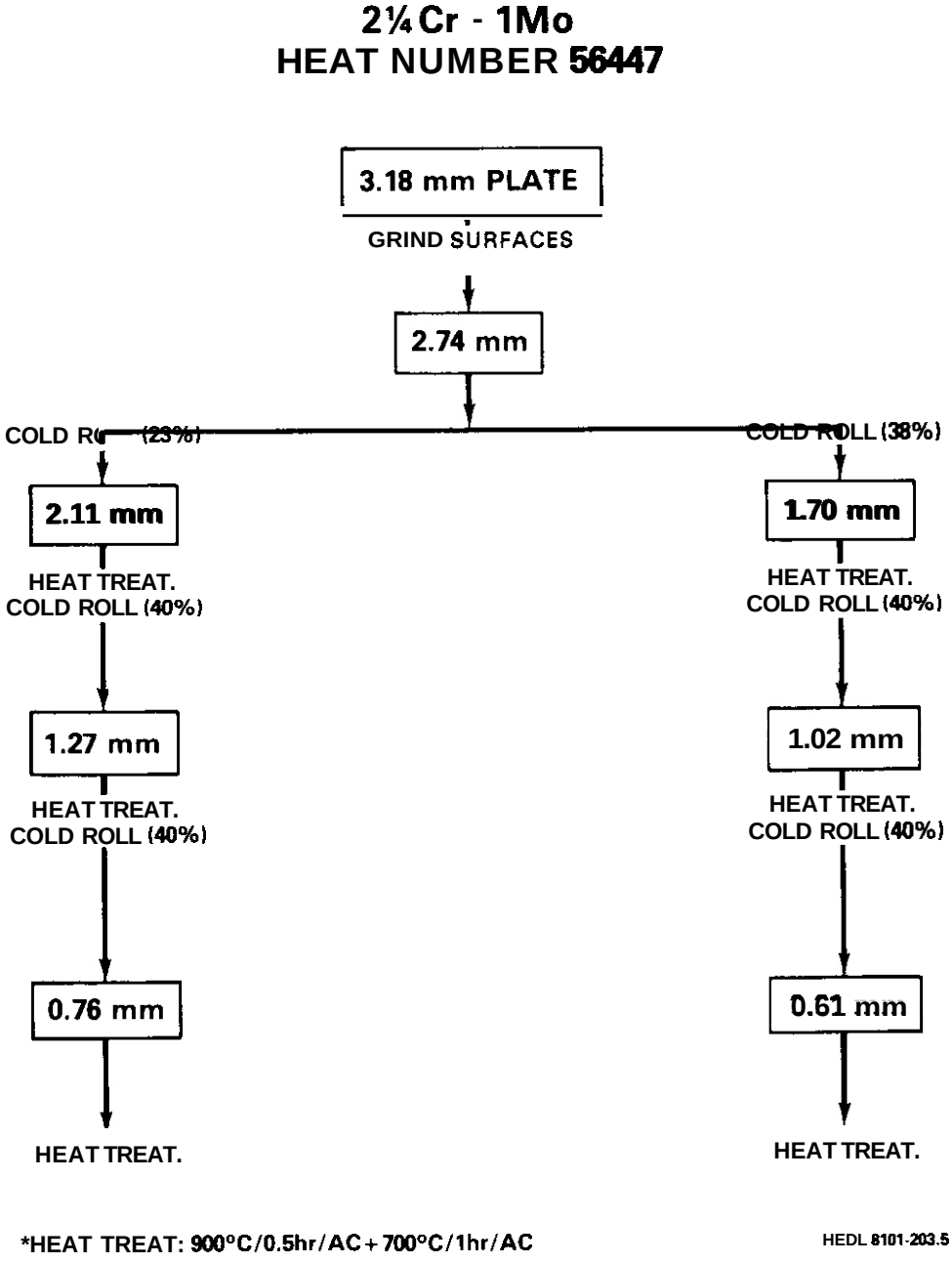

FIGURE 7.6.5 2-1/4Cr-1Mo **Mechanical Processing Steps for 0.030 and** *0.024* **inch sheet stock.**

TABLE 7.6.2

CHEMICAL COMPOSITIONS OF WELD WIRES

ELEMENT	HT-9[1]	9Cr-1Mo[2]	2 1/4Cr-1Mo 3
C	0.26	0.086	0.108
Mn	0.50	0.389	0.65
P	0.011	0.011	0.011
S	0.005	0.015	0.018
Si	0.26	0.32	0.32
Ni	0.62	0.046	0.055
Cr	11.6	8.93	2.53
Mo	0.95	0.98	0.92
V	0.29		
Nb	<0.01		
Ti	<0.01		
Co	0.03	0.020	
Cu	0.04		
Al	0.011		
N	0.024		
Ta	<0.01		
W	0.49		
Fe	Bal.	Bal.	Bal.

All numbers are weight percents.

1 Thyssen Specialty Steels, Inc.

2 San Diego Welders Supply, Inc.

3 **Arcos** Corp., Chromenar 521.

chemical compositions of the weld wire are shown in Table 7.6.2. The welding procedure for the HT-9 and 9Cr-1Mo weldments were equivalent to those previously used for the AD-2 experiment.(3) All the weldments were given a post weld temper of 780°C for one hour. Each plate was radiographed to insure the quality of the weld.

7.6.4.3 Metallographic Characterization of the Materials

Micrographs of the HT-9 material stock from which specimens are to be fabricated are shown in Figure 7.6.6. All thickness exhibited the martensitic structure typical of a 12Cr-1Mo steel. An estimate of the prior austenitic grain size for this HT-9 stock is an ASTM 7-8. Microhardness measurements were made on this material and its hardness was found to be 283 ± 5 DPH (500 gm).

Micrographs of the modified 9Cr-1Mo specimen material stock are shown in Figure 7.6.7. Although there was oxidation and some scaling on the surfaces due to the heat treatment, no evidence of any decarburized layer was found on any of the material stock. The estimated prior austenitic grain size for this material is ASTM 9-10 and the hardness is 218 ± 5 DPH (500 gm).

Micrographs of the 2-1/4Cr-1Mo specimen material stock are shown in Figure 7.6.8. An estimate of the prior austenitic grain size for this material stock is an ASTM 8-9. Microhardness for this material was measured to be 187±1 DPH (500 gm).

The results of metallographic examination of the base materials are summarized in Table 7.6.3.

Micrographs of the weldments of HT-9 and 9Cr-1Mo are shown in Figures 7.6.9 and 7.6.10. Microhardness measurements were performed across both welds. For the HT-9 weldment the hardness varied from 226 ± 2 DPH(500 gm) in the base metal, to 227 ± 11 DPH(500 gm) in the heat affected (HAZ), to 262 ± 5 DPH(500 gm) in the weld metal. For the 9Cr-1Mo weldment the hardness varied from 197 ± 3 DPH(500 gm) in the base metal, to 224 ± 8 DPH(500 gm) in the HAZ, to 261 ±8 DPH(500 gm) in the weld metal.

TABLE 7.6.3

METALLOGRAPHIC CHARACTERIZATION OF FERRITIC ALLOYS

ALLOY	PRIOR HISTORY	MICROHARDNESS 500gm DPH	GRAIN SIZE ASTM
HT-9[†]	40%CW+1038°C/10m/AC+760°C/30m/AC	283±5	7-8
HT-9[††]	40%CW+1038°C/4m/AC+760°C/30m/AC	283±5	7-8
9Cr-1Mo	1038°C/0.5hr/AC+760°C/0.5hr/AC	218±5	9-10
2-1/4Cr-1Mo	40%CW+900°C/0.5hr/AC+700°C/1hr/AC	187±1	7-9

+ Thicknesses of 6.35 and 3.18mm

†† Thicknesses of 0.76 and 0.61mm

(a)

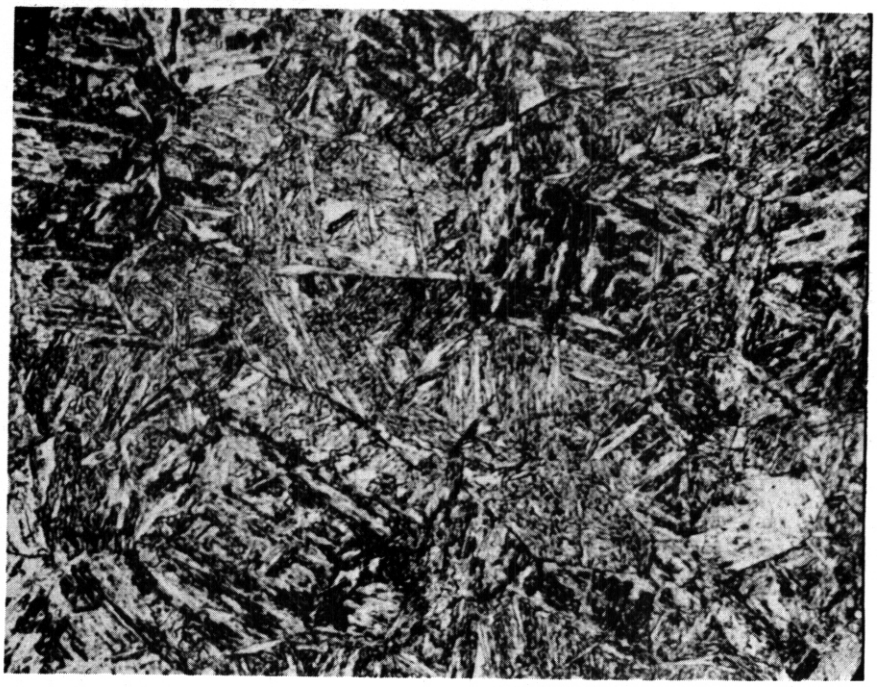

(b)

FIGURE 7.6.6 Micrographs at 400x of HT-9 Material: (a) 0.25 inch plate stock; (b) 0.030 inch sheet stock.

(a)

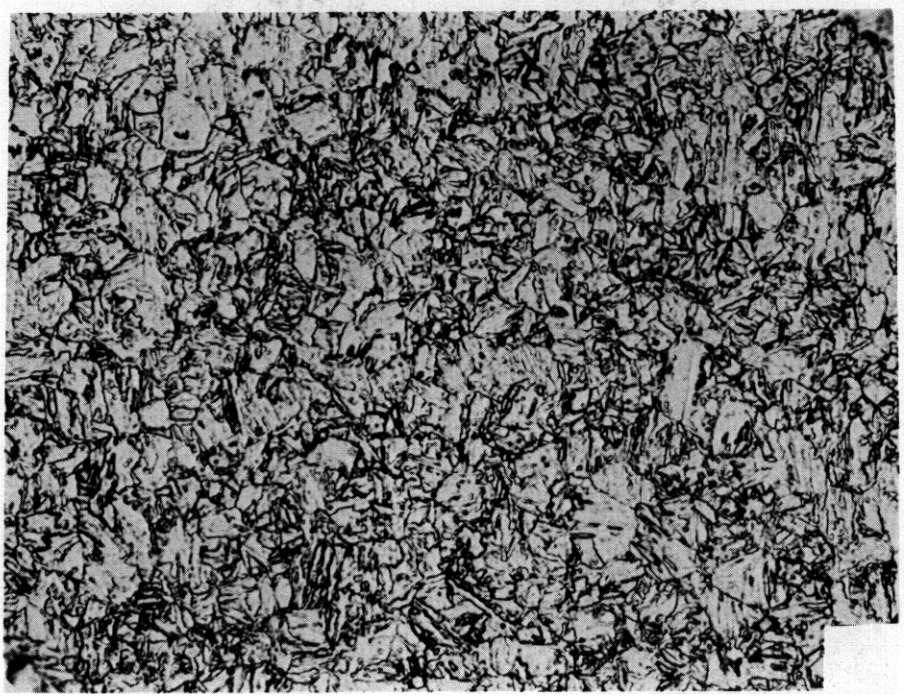

(b)

FIGURE 7.6.7 Micrographs at 400x of 9Cr-1Mo Material: (a) 025 inch plate stock; (b) 0.030 inch sheet stock.

(a)

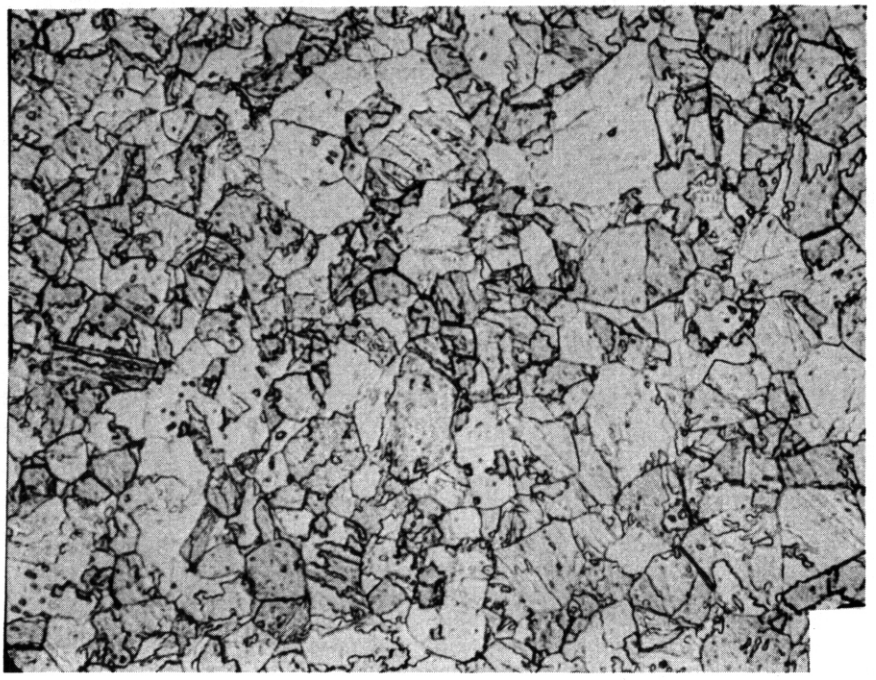

(b)

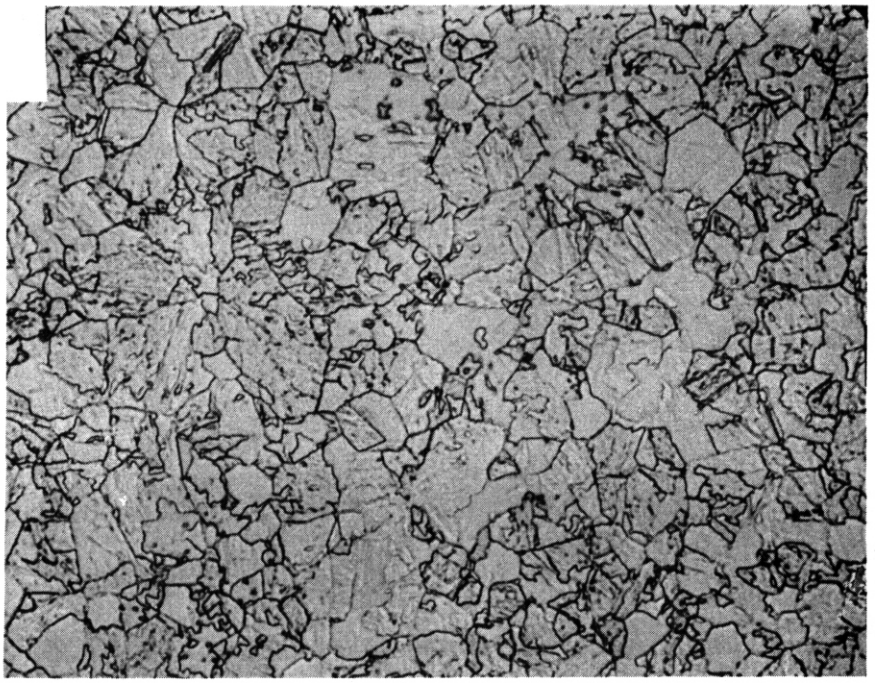

FIGURE *7.6.8* Micrograph at 400x of 2-1/4Cr-1Mo Material: (a) *0.25* inch plate stock; (b) 0.030 inch sheet stock.

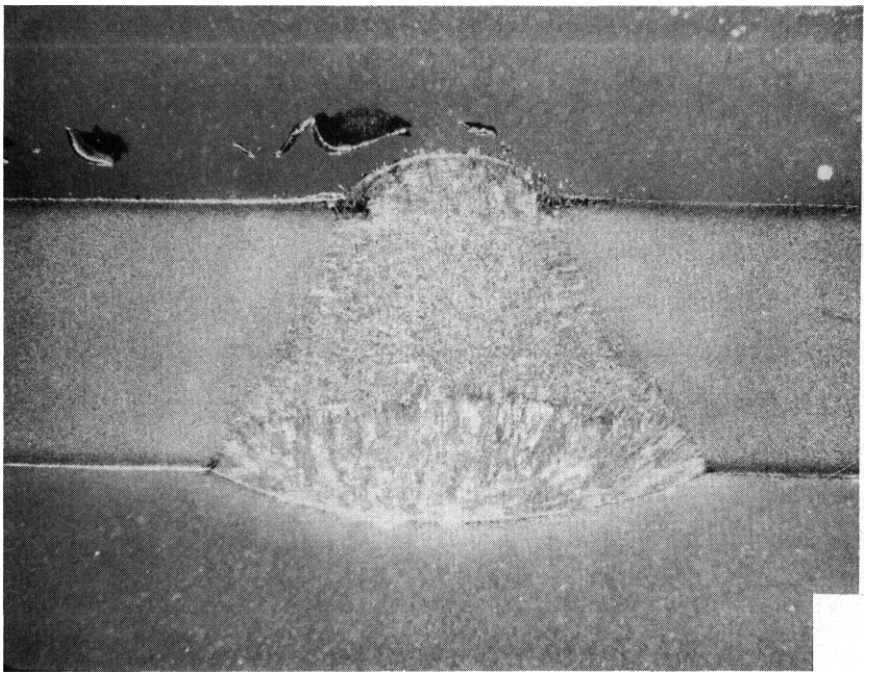

FIGURE 7.6.9 Macrograph at 5-1/2x of HT-9 weldment.

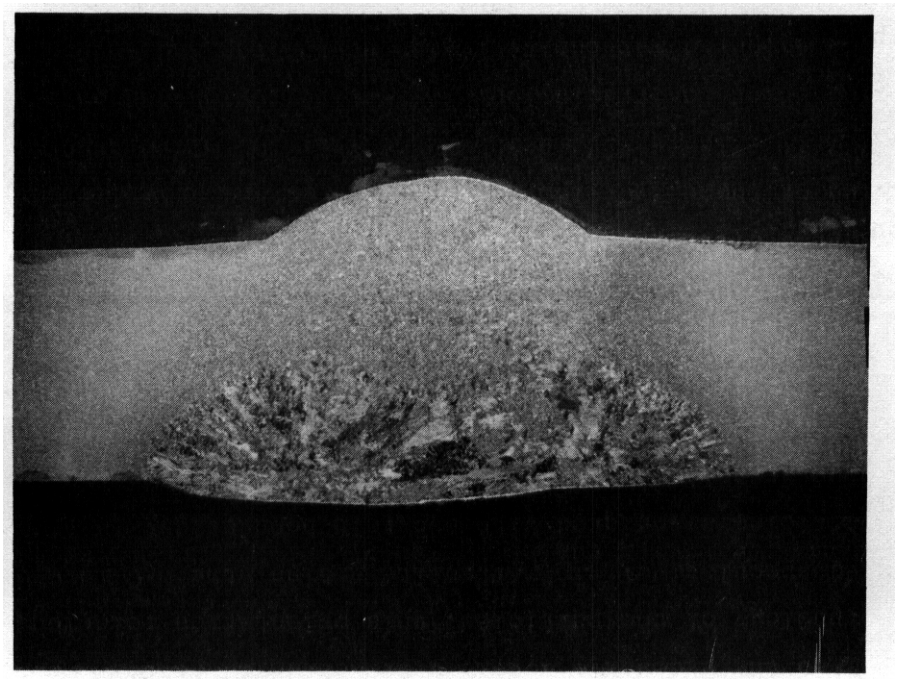

FIGURE 7.6.10 Macrograph at 5-1/2x of 9Cr-1Mo weldment.

7.6.5 Conclusions and Future Work

The fabrication of three ferritic steels to be used in the MFE-RB-1 experiment has been successfully completed. Weldments of HT-9 and 9Cr-1Mo have been successfully fabricated. Weldments of 2-1/4Cr-1Mo are being fabricated now and should be completed by the first week in February, 1981. These materials have been shipped to manufacturers and ORNL for specimen preparation. A TEM examination of these materials is planned to complete the characterization of these materials.

7.6.6 References

1. J. M. Vitek, R. L. Klueh, M. L. Grossbeck and J. W. Woods, "HFIR-MFE-T1, -T2, and RB1: Experiments to Evaluate the Effects of Low-Temperature Irradiation on Ferritic Steels," *ADIP Quarterly Progress Report, September 30, 1980.*

2. R. J. Puigh and N. F. Panayouto, "Specimen Preparation and Loading for the AD-2 Ferritics Experiment," ADIP *Quarterly Progress Report, June* 30, *1980.*

3. T. A. Lechtenburg, R. D. Stevenson, S. N. Rosenwasser, B. E. Thurgood, and L. D. Thompson, "Procurement of National 12Cr Heat and Evaluation of Welding Procedures for Irradiation Specimens," *ADIP Quarterly Progress Report, June 30, 1980.*

7.7 MICROSTRUCTURAL EXAMINATION OF A SERIES OF COMMERCIAL FERRITIC ALLOYS IRRADIATED TO VERY HIGH FLUENCE - D. S. Gelles (Hanford Engineering Development Laboratory).

7.7.1 ADIP Task

The Department of Energy (DOE)/Office of Fusion Energy (OFE) has cited the need to investigate ferritic alloys under the ADIP program task, Ferritic Steels Development (Path E). The tasks involved are akin to task number 1.C.2, Microstructures and Swelling in Austenitic Alloys and task number l.C.l, Microstructural Stability.

7.7.2 Objective

The objective of this work is to provide guidance on the applicability of ferritic stainless steels for fusion reactor structural materials by examining a series of ferritic alloys (not including the Path E candidate alloy) after irradiation to very high fluence in a fast breeder reactor.

7.7.3 Summary

A series of five commercial ferritic alloys, 2¼Cr-1Mo, €I-11, EM-12, 416, and 430F, covering the composition range 2.25 to 17% chromium and including a wide range of preirradiation microstructures has been examined by transmission electron microscopy following irradiation in the EBR-II over the temperature range 400-650°C and to a maximum fluence of **17.6** x 10^{22} n/cm^2 (E >0,1 MeV) or 84 dpa. These materials were confirmed to be low void swelling with maximum swelling of 0.63% measured in EM-12 following irradiation at 400°C to 14.0 **x** 10^{22} **n/cm^2.** **A** wide range of precipitation response was found in these materials both as a function of alloy and irradiation temperature. Precipitates observed included M_6C, Mo_2C, Chi, Laves, $M_{23}C_6$, a' and a low temperature phase **as** yet unidentified. It is predicted, based on these results, that the major impact of irradiation on the ferritic alloy class will be changes in postirradiation mechanical properties due to precipitation.

7.7.4 Progress and Status

7.7.4.1 Introduction

As part of the National Cladding/Duct Materials Development Program (NCD) for LMFBR development, a series of ferritic alloys were included in the AA-I swelling test. As these materials are no longer being studied by the NCD program, they have been made available for fusion related studies. These materials have been irradiated in the EBR-II reactor at a series of temperatures covering the range 400 to 650°C. Irradiations have continued for over 6 years and the fluence levels achieved are now a maximum of 17.8 x 10^{22} n/cm^2 (E >0.1 MeV) or 85 displacements per atom (dpa). As such, these materials provide an unsurpassed opportunity to examine the effects of fast neutron irradiation on the microstructures of the Path E alloy class.

The ferritic alloy series included in the AA-I swelling test consisted of commercial alloys covering a broad composition range. Although the series does not include HT-9, the candidate Path E alloy, alloys similar in composition are included. The alloys chosen for study were 2¼Cr-1Mo, an alloy used for steam generator heat exchangers, H-11 a submarine steel, EM-12 a French ferritic stainless steel, 416 a low alloyed 12Cr ferritic stainless steel and 430F a high chromium alloy used for 'heat exchangers in the petrochemical industry. Alloy compositions may be compared with that for HT-9 in Table 7.7.1. The alloy series covers the broad range of chromium additions for commercial ferritic alloys from 2.25 to 17 percent chromium.

The ferritic alloys examined in the present study are among a series of alloys measured for density change after irradiation to a maximum fluence of 17.8 x 10^{22} n/cm^2 (E >0.1 MeV). [1] Density change measurements demonstrated that these ferritic materials are highly resistant to irradiation induced swelling over the temperature range 400 to 650°C. The maximum swelling observed was 0.57 percent in EM-12 following irradiation at 400°C to 14 x 10^{22} n/cm^2 (E >0.1 MeV) or 67 dpa. But most of the alloys show a slight decrease in density of between 0.10 and 0.20% over the whole temperature range examined.

Table 7.7.1. Compositions (in weight percent) of the ferritic alloys under examination with the HT-9 composition provided for comparison.

Alloy	Cr	Mo	C	Mn	Ni	si	V	Nb	W
2¼Cr-1Mo	2.17	0.93	0.12	0.42	0.16	0.2	-	-	-
H-11	4.97	1.3	0.42	0.37	0.12	0.88	-	-	-
EM-12	9.42	2.0	0.085	1.0	-	0.28	0.27	0.40	-
416	13.5	0.19	0.125	0.45	0.22	0.48	-	0.28	-
430F	17.6	0.04	0.043	0.40	-	0.50	-	-	-
HT-9	12.0	1.03	0.20	0.50	0.47	0.41	0.3	-	0.5

7.7.4.2 Experimental Procedure

Materials were received from various commercial sources. Results of chemistry overchecks for these materials are provided in Table 7.7.1. The materials were heat treated as prescribed in Table 7.7.2 producing the microstructures given in Table 7.7.2. Specimens 0.3 cm diameter by 1.3 cm were machined from the heat treated stock and stamped with a four digit alphanumeric identification code which defines both the material and irradiation history. These specimens were included in the NCD AA-I swelling test which consisted of five irradiation vehicles of B-7a capsule design with eight subcapsules in each constructed to run at eight different temperatures. The temperatures were controlled by gas gap regulation of gamma heat loss. In each subcapsule all specimens were immersed in static sodium to ensure uniform temperature.

Irradiations were performed in Row 2 of the Experimental Breeder Reactor II (EBR-II), Idaho Falls, Idaho. Maximum accumulated fluence was 17.8 x 10^{22} n/cm^2 (E >0.1 MeV) and fluences varied as a function of subcapsule position from core midplane.

Specimens selected for transmission electron microscopy as listed in Table 7.7.2 were prepared by slicing 0.03 cm thick wafers from rod specimens using a slow speed saw with diamond impregnated ganged blades and then by electro-jet polishing the wafers in a Metalthin electropolishing device. The polishing electrolyte was 5% perchloric acid in 95% butyl alcohol and the polishing conditions 90V., 250 to 300 ma. and a moderate

Table 7.7.2. Preirradiation heat treatments and irradiation conditions of ferritic alloy specimens selected for microstructural examination.

Alloy	Heat Treatment	Microstructure*	Selected Specimens**			
			400/14.0	425/15.8	510/17.2	650/17.6
2¼Cr-1Mo	10▯5°C/60 ▯▯n/WQ +≤⊂▯°C/120 min/WQ	α, M, tM		▯4L7	▯4▯	▯4×7
H-11	1005°C/60 ▯▯▯/WQ + ▯65°C/120 ▯i▯/WQ	tM		93L7	▯3▯	
EM-12	10▯0°C/▯0 ▯▯n/AC +755°C/▯▯ m▯▯/AC	α, tM	▯≤M7	▯≤L7	▯8K7	▯≤×7
416	≤▯0°C/c▯▯l 13° ▯er h r t▯ ▯▯5 C/AC	tM		64L7	64▯7	
430F	1065°C/60 ▯i▯/WQ	α, M		▯1L7	▯1K▯	

* α = ferrite
M = martensite
tM = tempered martensite

** x/y where x = irradiation temperature, (°C) and y = flue▯ce▯ ($1▯^{22}$ n/cm^2)
abcd where abcd = alphanumeric specimen identification code

pump speed of 2 to 3. Considerable difficulty was encountered with the lower chromium alloys due to oxide film development. The film was removed by subsequent flash polishing in the same electrolyte. Microscopy was performed on a JEM-200A electron microscope equipped with a side-entry double-tilting goniometer stage and operating at 200 keV. Magnetic effects were overcome by use of the dark-field deflection coils and careful objective stigmator adjustment.

7.7.4.3 Results

7.7.4.3.1 2¼Cr-1Mo. The preirradiation heat treatment given to 2¼Cr-1Mo was non-standard consisting of 1) normalization, 2) water quench, 3) anneal in the two phase ($a + \gamma$) region and 4) water quench. The structure therefore consisted of overtempered martensite, ferrite and untempered martensite. As a result, postirradiation microstructures were quite varied and large area to area differences were encountered which had the advantage of showing what effect these differences had on in-reactor behavior.

Following irradiation at 425°C (condition 94L7), significant effects of irradiation were apparent. Voids were found in both ferrite and tempered martensite, and were slightly truncated octahedra in shape. Swelling was greatest in ferrite regions which developed swelling of 0.2% consisting of voids of 24 nm mean diameter at a number density of 2.4×10^{14} n/cm^3. The dislocation structure consisted of a dislocation tangle typical of an irradiated metal undergoing significant dislocation climb. Precipitates examined in ferrite regions were of two types, equiaxed M_6C and rod shaped Mo_2C both precipitates distributed on a fine scale within ferrite grains. The orientation relationship of the M_6C with the matrix was the same as that identified in the 510°C conditon.

Following Irradiation at 510°C (condition 94K7) 2¼Cr-1Mo was found to have developed quite differently. No void swelling was found and the dislocation structure had relaxed to form subcells typical in martensite of a tempered martensite structure and in ferrite as a much coarser cell size. Most notable however, was the extensive precipitation observed. Isolated regions were found containing Mo_2C but the predominant precipitate was M_6C.

In ferrite grains, M_6C formed as a moderate density of globular 50 nm particles with denuded zones at grain boundaries of 500 nm. These particles were apparently oriented coincident with respect to the ferrite so that

$$\langle 100 \rangle_{M_6C} \parallel \langle 100 \rangle_{\alpha}$$
$$\langle 110 \rangle_{M_6C} \parallel \langle 110 \rangle_{\alpha}$$

However, due to the excessive double diffraction encountered and the non-equiaxed morphology of the particles, this orientation relationship must be considered speculative. In martensite grains, the M_6C formed instead as 200 nm particles associated with subgrain boundaries.

Following irradiation at 650°C (condition 94H7) 2¼Cr-1Mo resembled an overtempered structure. Subgrain cell walls were well developed, with a moderate dislocation density within cells. Precipitation consisted of large blocky precipitate particles at low number density and generally associated with subgrain and grain boundaries. The precipitate was identified by electron diffraction as M_6C.

Examples of these 2¼Cr-1Mo microstructures are provided for comparison in Figure 7.7.1. Figure 7.7.1a shows the 2¼Cr-1Mo microstructure at low magnification prior to irradiation. A ferrite region can be seen at the lower left, a tempered martensite region at the top and several untempered martensite lathes in the center. Figure 7.7.1b shows the 2¼Cr-1Mo microstructure in a ferrite grain following irradiation at 425°C to 15.8 x 10^{22} n/cm^2 (E >0.1 MeV) at much higher magnification. Voids can be seen as white faceted features fairly uniformly distributed. Precipitates appear as dark faint equiaxed particles in the case of M_6C and rod shaped particles in the case of Mo_2C. Figure 7.7.1c shows the 2¼Cr-1Mo microstructure at low magnification following irradiation at 510°C to 17.2 x 10^{22} n/cm^2 (E >0.1 MeV). A ferrite grain containing globular M_6C precipitates can be seen in the lower part of the micrograph and a martensite region is shown at the top. Figure 7.7.1d provides an example of 2¼Cr-1Mo microstructure again at low magnification following irradiation at 650°C

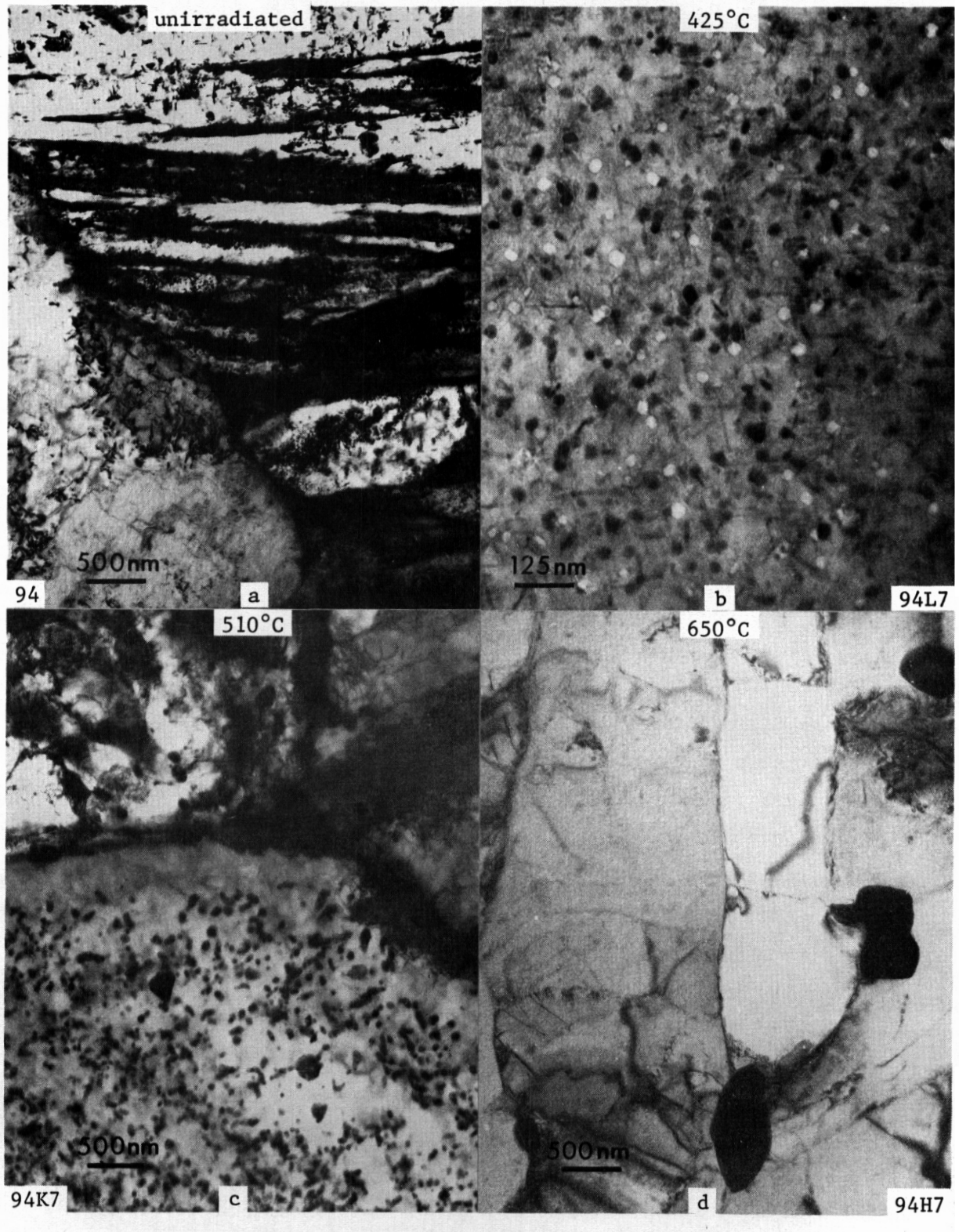

Fig. 7.7.1: Examples of microstructures observed in 2¼Cr-1Mo.

to 17.6 x 10^{22} n/cm^2 (E >0.1 MeV). Large blocky M_6C particles and subgrain development can be identified.

7.7.4.3.2 H-11. The preirradiation treatment given to H-11 produced a fully martensitic structure which was then very lightly tempered. As a result, the martensite lathes were well defined with some acicular precipitate present at lathe and grain boundaries. However, within lathes the dislocation structure was very dense and precipitation could not be resolved.

Following irradiation at 425°C (condition 93L7) the structure of H-11 was altered considerably. No evidence of void swelling was found but extensive precipitation had occurred both within martensite lathes and on martensite lathe boundaries. Precipitate developed both as a globular particles tending to define martensite lathe boundaries and as rod shaped particles at high number density within lathes. The former is identified as M_6C based on analysis of the 510°C structure and the latter is identified as Mo_2C based on its morphology.

Following irradiation of H-11 at 510°C (condition 93K7) the structure was somewhat different. Again no void swelling was observed, but this time the dislocation structure had relaxed into a cell structure more charateristic of tempered martensite. The blocky precipitate was increased in size and positively identified as M_6C based on electron diffraction lattice parameter measurements. The Mo_2C was observed infrequently as small widely separated colonies of rod shaped precipitate. Therefore, the M_6C was determined to be the more stable precipitate phase.

Examples of the H-11 microstructures are provided in Figure 7.7.2. The preirradiation H-11 microstructure is shown in Figure 7.7.2a and may be compared with that following irradiation at 425°C in Figure 7.7.2b and that following irradiation at 510°C in Figure 7.7.2c all at the same magnification. Figure 7.7.2b provides a comparison of rod shaped Mo_2C precipitate and blocky M_6C. Figure 7.7.2c shows the typical subcell development pinned by M_6C particles following irradiation at 510°C. The region at the right of Figure 7.7.2c provides an example of the Mo_2C structure in this condition.

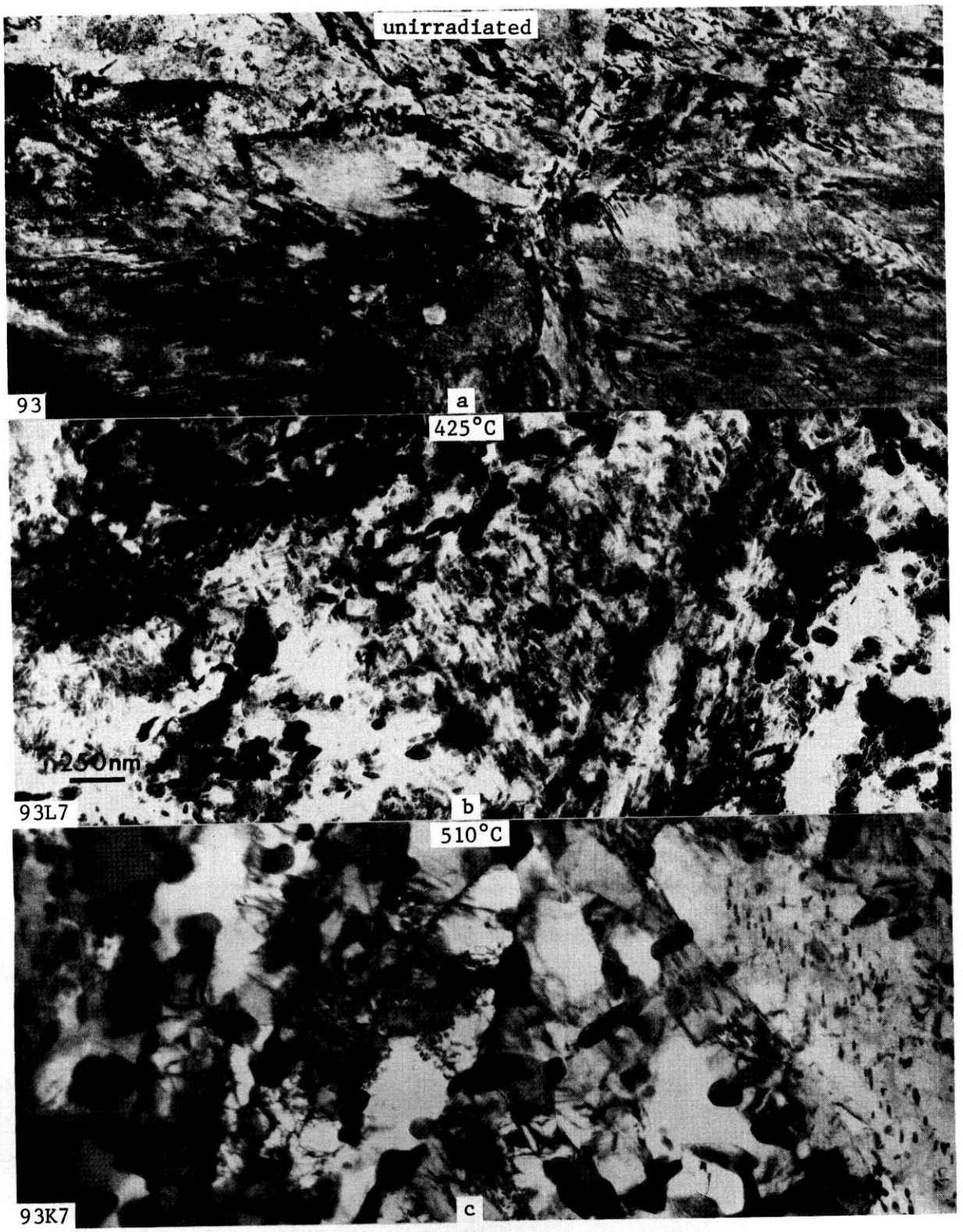

Fig. 7.7.2: Examples of microstructures observed in H-11.

7.7.4.3.3 EM-12. The heat treatment prescribed for EM-12 results in a duplex microstructure of tempered martensite and recovered ferrite. The tempered martensite constitutes a moderately small subgrain size decorated with blocky $M_{23}C_6$ carbide particles whereas the ferrite is precipitate-free with a low density of dislocations randomly distributed. Carbide precipitation is greatest on martensite/ferrite phase boundaries.

Following irradiation at 400°C (condition 98M7) EM-12 is found to have developed a significant void structure and a dislocation structure typical of irradiation induced climb. Voids were found both in the tempered martensite and in the ferrite, but swelling was significantly greater in the ferrite. Void swelling measurements in the ferrite indicated swelling of 0.63%, consisting of truncated octahedral voids with a mean size of 33 nm at a number density of 2.9 x 10^{14} n/cm^3. This is in reasonable agreement with the density change measurement of 0.57% swelling.(1) The dislocation structure in ferrite grains consisted predominantly of straight dislocation segments, similar in structure to that observed following irradiation at 425°C. Also, of note was the observation that precipitation had occurred in ferrite grains during irradiation. The precipitate particles appeared equiaxed, less than 20 nm in diameter and at a fairly high number density. The identity of this precipitate has not yet been ascertained but it has been demonstrated to be different from those which form in EM-12 at higher temperatures and the chromium rich α' body centered cubic phase may be ruled out based on electron diffraction pattern evidence.

Following irradiation at 425°C (condition 98L7) EM-12 develops a microstructure somewhat different from that produced at 400°C. Void and dislocation structures differed primarily in scale. The maximum void sizes were similar but void swelling was less with measurements in ferrite indicating 0.26% swelling consisting of voids of 24 nm mean size at a number density of 2.4 x 10^{22} n/cm^2. This was due to a larger fraction of smaller voids in comparison with the 400°C microstructure. The dislocation structure in ferrite consisted predominantly of straight dislocation segments, pure edge in character and with a Burgers vector of $a\langle 100\rangle$, but $\frac{a}{2}\langle 111\rangle$ Burgers vectors could also be identified. The major difference

observed in comparison with the 400°C condition was as a result of the precipitate structure. Following irradiation at 425°C, precipitation was significantly heavier. In ferrite, it consisted of equiaxed particles as large as 40 nm in diameter. Electron diffraction evidence revealed that this precipitate had a body centered cubic crystal structure with a lattice parameter three times that of the matrix and which formed coincident with the parent lattice. It has been identified therefore as chi phase (Fe-30%Mo-20%Cr) with the orientation relationship

$$\langle 100 \rangle_{\chi} \parallel \langle 100 \rangle_{\alpha}$$
$$\langle 110 \rangle_{\chi} \parallel \langle 110 \rangle_{\alpha}$$

In dislocation contrast, the precipitate particles showed strong fringe contrast which indicated that misfit dislocations were present as required to alleviate a lattice misfit between precipitate and matrix.

Following irradiation at 510°C (condition 98K7) the microstructure of EM-12 was again different. In this condition, no void swelling was found, the dislocation structure was not characteristic of that due to irradiation induced climb and precipitation was observed. However, the precipitate was notably different from that which formed following irradiation at 425°C. Heavy precipitation was observed on all grain and martensite lathe boundaries. Adjacent to these boundaries were 250 nm regions denuded of precipitate, and whenever boundaries were sufficiently separated, within grains heavy precipitation of particles on the order of 100 nm were found. The particles were generally globular in shape but many examples of rod shaped precipitates could also be identified. Again, evidence for misfit dislocations was obtained. Electron diffraction results indicated that again the precipitate had a body centered cubic crystal structure with a lattice parameter three times that of the matrix and therefore the precipitate was chi phase. The reason for the morphological difference was due to a different orientation relationship which could be defined as

$$\langle 111 \rangle_{\chi} \parallel \langle 111 \rangle_{\alpha}$$
$$\langle 0\bar{1}1 \rangle_{\chi} \parallel \langle 1\bar{1}0 \rangle_{\alpha}$$

Thus, eight different orientation variants existed for particles of chi phase following irradiation at 510°C.

Following irradiation at 650°C (condition 98H7) EM-12 was found to be much less complicated. The microstructure was similar to that of over-tempered martensite and ferrite. Precipitates were large and blocky and generally located at grain and subgrain boundaries. However, again the precipitate phase was found to be different. In this case, several examples of particles containing a large number of internal twins were found. Electron diffraction analysis after allowing for the internal twinning revealed that these precipitates were Laves phase (Fe_2Mo). This result was corroborated by L. E. Thomas of HEDL using energy dispersive analysis of x-rays on a JEOL 100 CX scanning transmission electron microscope. The precipitates were found to be rich in iron and molybdenum with lesser amounts of chromium, vanadium and silicon.

Examples of the EM-12 microstructure are given in Figures 7.7.3 and 7.7.4. Figure 7.7.3 provides comparisons of EM-12 microstructures at low magnification following irradiation at 400°C in (a), 425°C in (b), 510°C in (c) and 650°C in (d). Voids can be identified both in ferrite and tempered martensite following irradiation at 400°C in Figure 7.7.3a and at 425°C in Figure 7.7.3b. However, significantly more precipitation is observed in the ferrite grain following irradiation at 425°C. In Figure 7.7.3c, even more precipitation is shown, with continuous layers decorating grain boundaries and heavy precipitation decorating subgrain boundaries. Figure 7.7.3d provides an example of the blocky precipitate morphology decorating grain and subgrain boundaries following irradiation at 650°C. Figure 7.7.4 is constructed to emphasize the differences in precipitate development in ferrite grains following irradiation at 400, 425 and 510°C. The microstructure for each condition is shown and (110) diffraction patterns to demonstrate differences in crystallography are inset in each case. In Figure 7.7.4a, small weakly contrasted particles can be seen in the background whereas in Figure 7.7.4b the particles are larger and in better contrast. Figure 7.7.4c provides examples of the more globular shaped particles formed during irradiation at 510°C but under these imaging conditions, misfit dislocation arrays at particles can be identified; the best examples appear at the left. In order to emphasize chat these

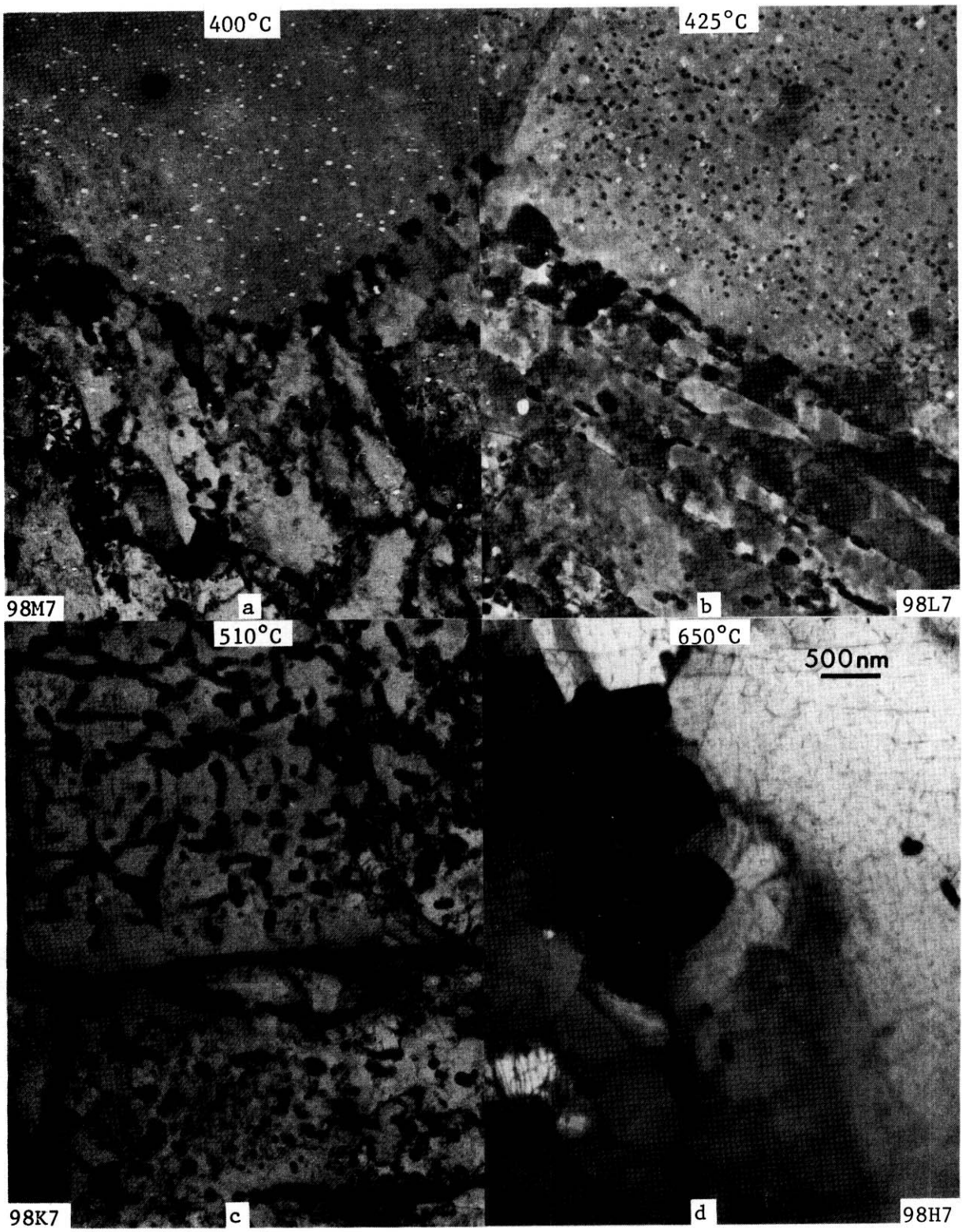

Fig. 7.7.3: Examples of microstructures observed in EM-12.

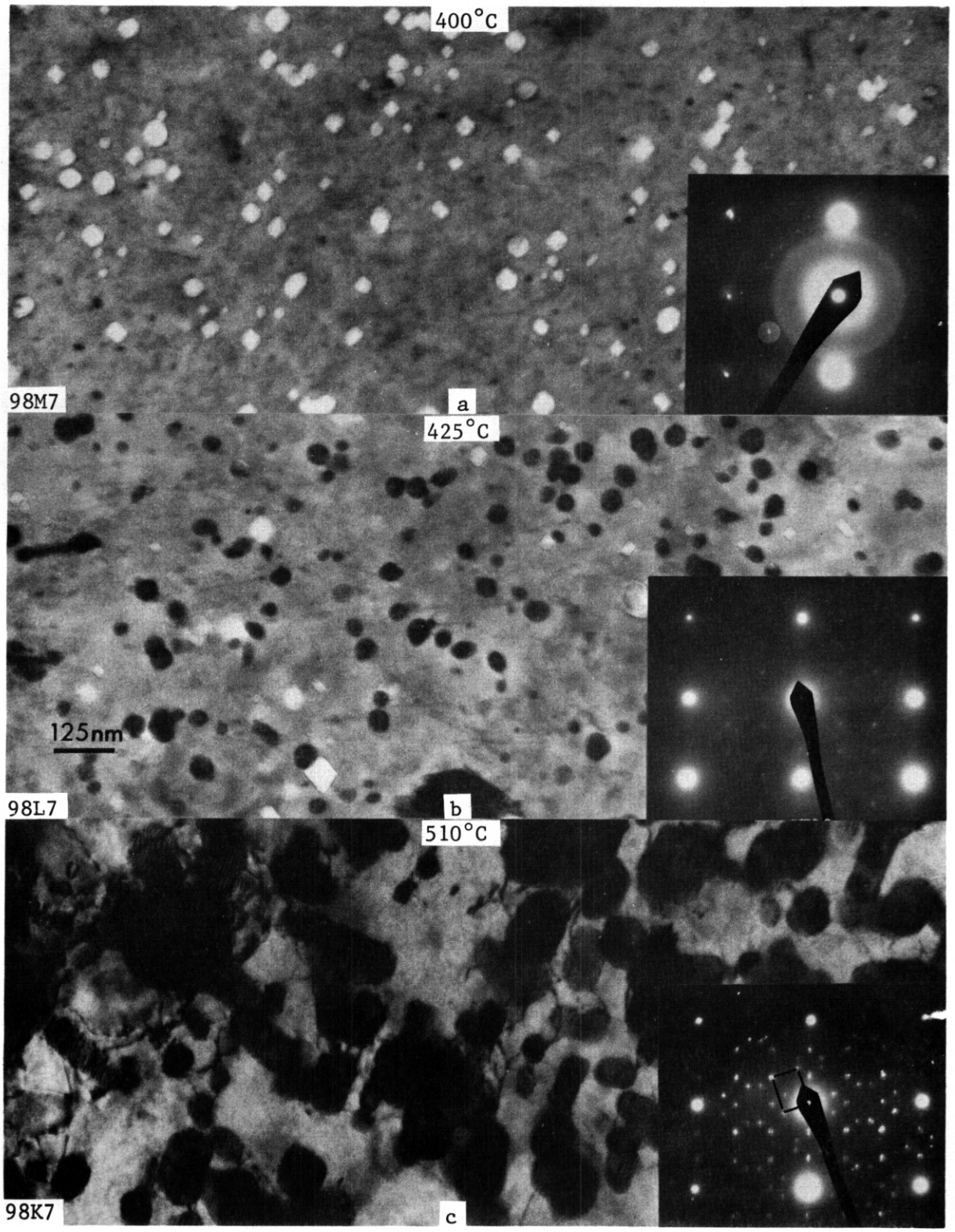

Fig. *7.7.4:* **Comparison of precipitation development in EM-12 following irradiation with (110) diffraction patterns inset.**

precipitates are also chi phase, the diffraction pattern inset in Figure 7.7.4c has been marked to show the chi phase (110) spot array which is rotated 120° from that observed in the diffraction pattern of Figure 7.7.4b.

7.7.4.3.4 416. The heat treatment given to 416 prior to irradiation produced a microstructure which might be described as tempered martensite. The structure appeared to have a subgrain or martensite lathe structure with a very high dislocation density within subgrains and a low density of randomly distributed carbide particles. However, the heat treatment defined for 416 in Table 7.7.2 should have produced an annealed microstructure resulting from slow cooling through the $\gamma \rightleftharpoons \alpha$ transformation. Therefore, it must be presumed that the prescribed heat treatment was not followed. A more likely preirradiation treatment can be surmised as follows 1) warm worked, 2) cold worked and 3) stress relieved at 360°C.

Following irradiation at 425°C (condition 64L7) 416 was found to be highly resistant to radiation induced void swelling. One small void was identified in the material examined. The dislocation structure had recovered from the preirradiation condition to form dislocation arrays characteristic of subgrain boundaries but dislocation tangles typical of radiation induced dislocation climb were not observed. The major effect due to the irradiation was that of precipitation. The precipitation was similar to that observed in EM-I2 following irradiation at 400°C but electron diffraction evidence indicated that both the low temperature EM-12 precipitate and chi phase were forming.

Following irradiation at 510°C, the major change in the microstructure of 416 was that due to formation of a subgrain structure. Unlike the other alloys examined, it was not possible to identify precipitates which had formed during irradiation; large blocky $M_{23}C_6$ precipitates were present but they had also been observed in the structure prior to irradiation. Thus, 416 following irradiation at 510°C represents the most stable alloy microstructure encountered.

Examples of the 416 microstructures are given In Figure 7.7.5. Figures 7.7.5a and 7.7.5b provide comparison of the microstructure of 416 following irradiation at 425°C at low and high magnification respectively.

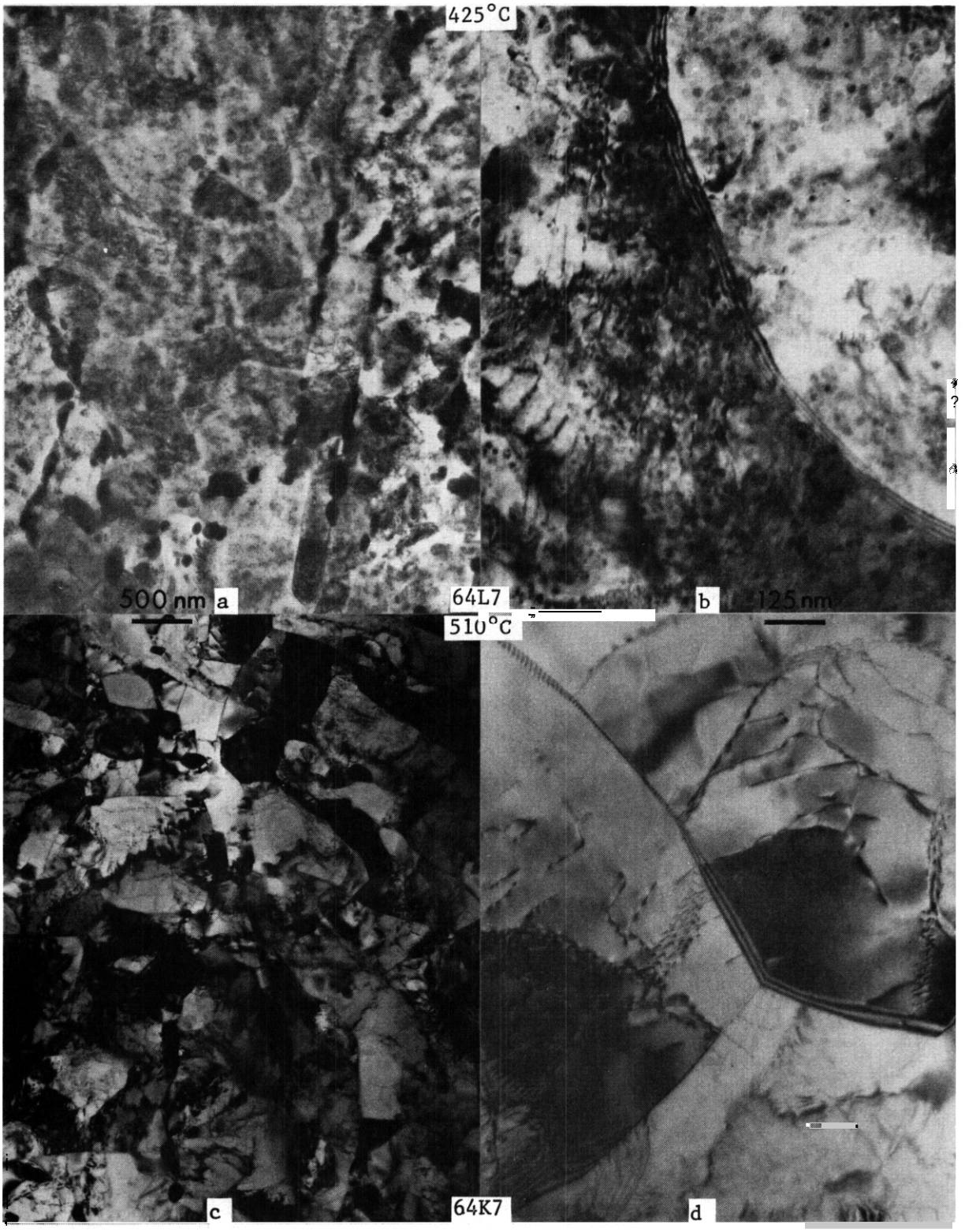

Fig. 7.7.5: Examples of microstructures observed following irradiation in *416*.

In both cases the dislocation structure can be identified as straight parallel lines. The precipitates appear as poorly contrasted equiaxed particles. Figures 7.7.5c and 7.7.5d provide comparison of the microstructure generated in 416 following irradiation at 510°C again at low and high magnification respectively. Subgrain development can be seen to be more clearly defined and precipitation is observed to be much less extensive, The imaging conditions used for Figure 7.7.5d showing the dislocation structure would normally reveal effects of fine precipitation. However, none can be seen.

7.7.4.3.5 430F. The preirradiation heat treatment given to 430F produced a duplex microstructure of ferrite and martensite. AS a tempering treatment was not used, the ferrite was found to be deformed following martensite transformation and the dislocation structure within the martensite plates was very dense.

Irradiation at 425°C (condition 91L7) produced a very different microstructure in 430F. No void swelling was observed and regions of ferrite were distinguishable from those of martensite. The major impact of irradiation was due to precipitation. Boundaries separating ferrite from martensite were thickly coated and boundaries between ferrite grains showed enhanced precipitation on the boundary with adjacent denuded zones. Everywhere else heavy precipitation was observed consisting of globular and equiaxed particles. The precipitate is identified as a', a chromium rich body centered cubic phase, based on analysis of ring electron diffraction patterns. The rings are believed to 'have resulted from an electropolishing artifact; the polish selectively attacked the matrix material, lifting the particles free and creating coatings of particles on foil surfaces.

In comparison, irradiation at 510°C (condition 91K7) produced a microstructure in 430F with much less precipitation, No void swelling was observed and the dislocation structure in martensite had relaxed to form subgrains with blocky $M_{23}C_6$ particles decorating boundaries. In ferrite grains, α' particles on the order of 40 nm in diameter were observed at low number density. That these particles were α' was deduced by the fact that they could only be imaged in dark field using conditions

usually employed for weak beam dislocation imaging.

Examples of 430F microstructures are given in Figure 7.7.6. Figure 7.7.6a and 7.7.6b provide comparison of 430F following irradiation at 425°C at low and high magnification respectively. In Figure 7.7.6a the heavy precipitation coating grain boundaries and developing within ferrite grains can be seen. A martensite region is shown in the upper part of the micrograph. Figure 7.7.6b provides an example of a' precipitation at a ferrite/ferrite grain boundary with the adjacent denuded zones. This structure can be compared with that following irradiation at 510°C as shown in Figures 7.7.6c and 7.7.6d. The more extensive subgrain development in martensite is shown at low magnification in the upper part of Figure 7.7.6c while the globular a' distribution is visible at higher magnification in Figure 7.7.6d.

7.7.4.4 Discussion

This study evolved as a result of an opportunity to take advantage of specimens irradiated to very high fluences in the NCD LMFBR program but no longer needed by that program. The alloys available have provided a complete survey of the ferritic alloy classes which may be employed for intermediate to high temperature use in fusion first wall applications. However, the prime candidate Path E alloy, HT-9, was not included in the materials available and therefore the present study was undertaken only as a brief survey. It is now apparent that the microstructures of these ferritic alloys respond in very complex and different ways, It is the intent of this discussion section therefore to consider the consequences of such behavior for fusion applications.

In order to emphasize the wide range of microstructural development observed in the ferritic alloys which were examined, Table 7.7.3 has been prepared to summarize the microstructural observations made as a function of alloy and irradiation temperature. (To identify situations where microstructural features were observed at low number density, features have been parenthesized.) Review of Table 7.7.3 rapidly reveals that 1) void swelling is not observed at temperatures of 510°C and above and that swelling at temperatures below 510°C is not a straightforward function of composition or precipitation behavior, 2) precipitation is very complex

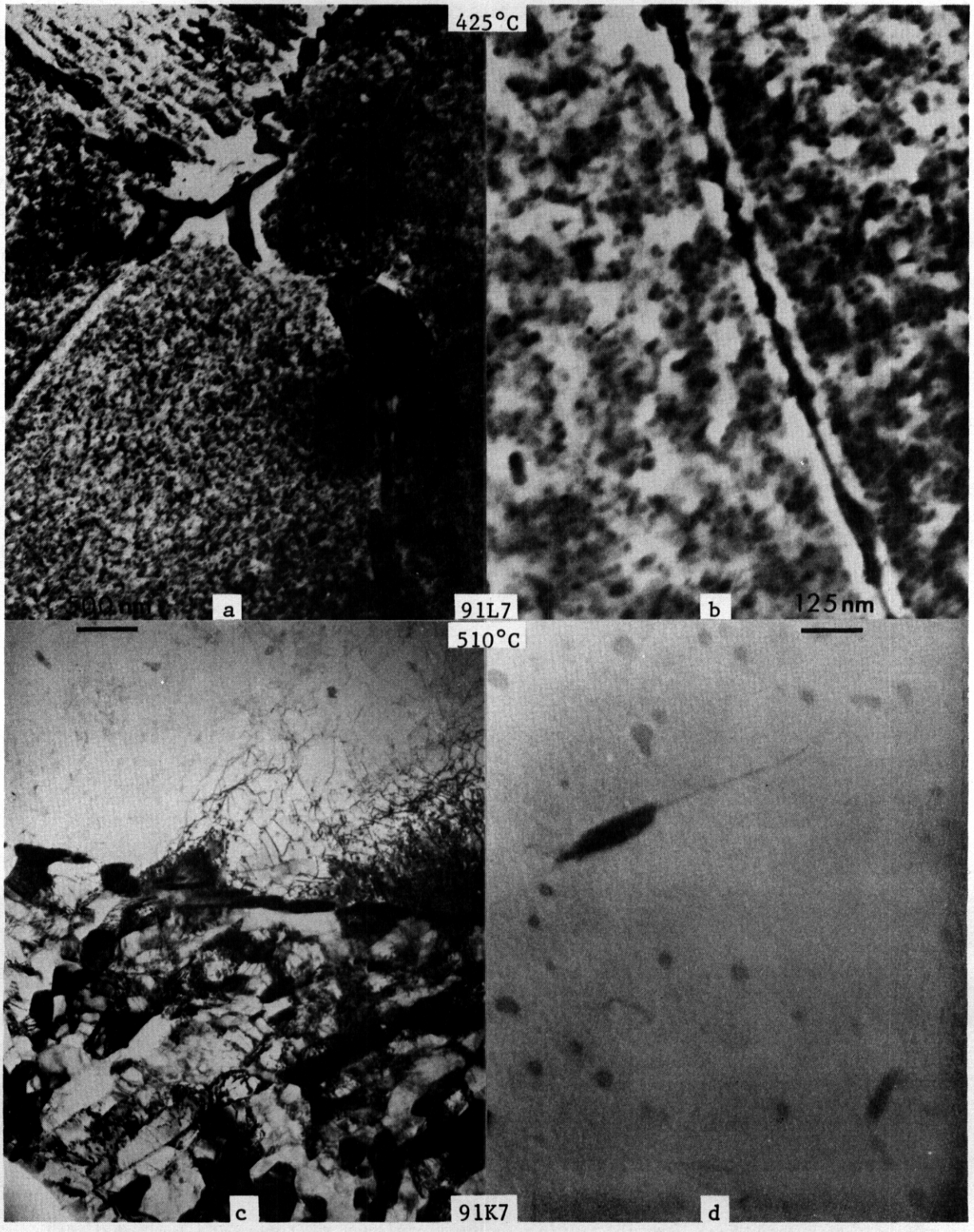

Fig. 7.7.6: Examples of microstructures observed following irradiation in 430F.

Table 7.7.3. Summary of microstructural results obtained in the present study.

Alloy	400"	425°C	510"	650"
2¼Cr-1Mo		Voids M_6C, Mo_2C	M_6C	(M_6C)
H-11		Mo_2C, M_6C	Mo_2C, M_6C	
EM-12	Voids ppts	Voids χ	χ*	(Laves)
416		(Voids) (ppts, $M_{23}C_6$)	($M_{23}C_6$)	
430F		α'	(α', $M_{23}C_6$)	
$\langle 111\rangle_\alpha$	‖	$\langle 111\rangle_{\chi^*}$		
$\langle ii0\rangle_\alpha$	‖	$\langle 0\bar{1}1\rangle_{\chi^*}$		

both as a function of alloy composition and irradiation temperature and 3) the variations in precipitation response are not simply due to variations in the form of the carbide phases which appear.

The present microstructural results confirm that although commercial ferritic alloys can develop void swelling, the swelling is probably not going to represent a design limitation. The maximum swelling observed was less than one percent following irradiation to 67 dpa. The maximum swelling observed was found at the lowest test temperature examined and therefore the possibility exists that higher swelling would develop at still lower temperatures. However, the dislocation and void densities observed in that condition are typical of a material at peak swelling condition rather than above the peak swelling condition and therefore it may be predicted that if higher swelling occurs at still lower temperature, the increase will not be very large.

To speculate on the reason why ferritic alloys swell at a lower rate than similar austenitic alloys is perhaps opportune. Several studies have found that irradiation of ferritic alloys produces dislocations of

Burgers vector $a\langle 100\rangle$.[2-4] Austenitics instead develop Burgers vectors of $\frac{a}{3}\langle 111\rangle$ or $\frac{a}{2}\langle 110\rangle$. However, in most cases the austenitic dislocation structure evolves to one dominated by glissile $\frac{a}{2}\langle 110\rangle$ dislocations. The glissile Burgers vector for ferritics is $\frac{a}{2}\langle 111\rangle$ and the key difference between these materials, it may be hypothesized, is the ability of the irradiation induced sessile dislocations to evolve into a glissile dislocation network with few obstacles. In the case of ferritics, no simple dislocation reaction between $a\langle 100\rangle$ dislocations or $a\langle 100\rangle$ and $\frac{a}{2}\langle 111\rangle$ will lead to a glissile dislocation structure. Instead, the $a\langle 100\rangle$ dislocations will remain as obstacles to dislocation motion thereby reducing dislocation climb. Therefore, the overall swelling rate will be lower.

Previous studies of irradiation effects on ferritic alloys have not emphasized observations of precipitation as has the present study. It is therefore worth noting that such response is predicted by thermal equilibrium phase diagrams and does not necessarily represent an effect of irradiation to high fluence. A wide range of carbide phases have been identified in Fe-Cr-Mo alloys with 0.1 to 0.2% carbon.[5] The published binary iron-chromium phase diagram[6] includes a miscability gap below 520°C wherein the binary mixture decomposes into iron rich and chromium rich (a') regions below 520°C. Therefore, observations of a' in 430F at 425°C and 510°C are predicted by thermal equilibrium. The iron-chromium-molybdenum ternary phase diagram[7] is generally constructed to show the body centered cubic chi phase in the composition range Fe-20%Cr-30%Mo and therefore observations of chi phase in EM-12 and 416 should not be unexpected. The iron-chromium-molybdenum ternary diagram shows the Laves phase Fe_2Mo to form as well. Observation of this phase is perhaps unexpected in an alloy with 10% chromium such as EM-12 but alloying additions such as carbon may be encouraging the Laves development. To emphasize these points, a section of the iron-chromium-molybdenum phase diagram for 650°C compiled by T. Wada[7] is reproduced in Figure 7.7.7 and the compositions of the five alloys in the present study are shown for comparison. From Figure 7.7.7 it can be noted that all alloy compositions lie in the single phase field but the $(a + \chi)$ region is very close to the EM-12 composition and it is not difficult to envision that a lower temperature

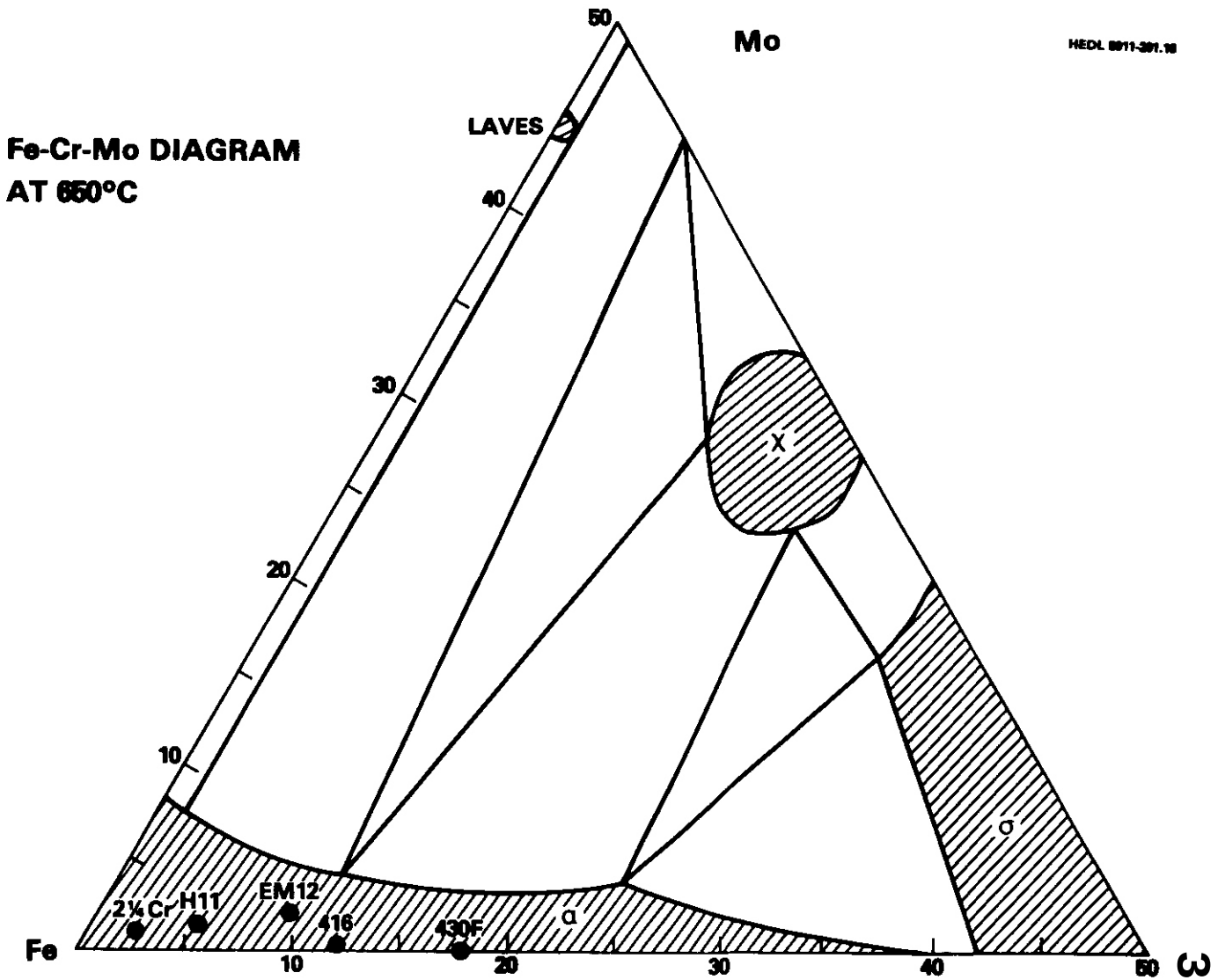

Fig. 7.7.7: A portion of the iron-chromium-molybdenum thermal equilibrium phase diagram showing the compositions of commercial ferritic alloys of interest.

coupled with further alloying additions and irradiation effects would cause the $(\alpha + \chi)$ field to expand.

Observation of extensive precipitation in commercial ferritic alloys can be expected to have bearing on the fusion applicability of these alloys. Precipitation should directly affect postirradiation strength, ductility and toughness. Smidt et al have recently shown that the fracture toughness of HT-9 is degraded significantly as a result of irradiation at 420°C to 1.1 x 10^{22} n/cm^2 (E > 0.1 MeV). [8] The ductile brittle transition temperature was found to shift 103°C due to irradiation. Furthermore, a fine scale precipitation was observed by transmission electron microscopy and therefore one of the explanations given for the degradation was the presence of the precipitate. (It can be noted that the phase found in EM-12 following irradiation at 400°C can be expected to be related to that described by Smidt et al). Furthermore, microstructures such as that shown in Figure 7.7.3c can be expected to have very different mechanical properties than would the preirradiation microstructure. Fortunately, the ADIP Path E reactor experiments have emphasized the need for such data and the experiments have been designed accordingly.

Perhaps, the consequence that must be most emphasized regarding postirradiation mechanical properties in Path E alloys is the impact of irradiation temperature on microstructure. Changes in irradiation temperature were found to produce major differences in precipitate microstructure. Mechanical properties may therefore change markedly with small changes in irradiation temperatures. Therefore, postirradiation mechanical testing matrices must be prepared to test a wide range of irradiation temperature conditions in order to ensure that a particular precipitation response does not create such adverse properties so as to make a given material unusable.

However, the wide range of precipitation response observed as a function of alloy composition suggests that if a phase is found to develop which is particularly detrimental to mechanical properties, it appears possible to eliminate that phase by minor changes in alloy composition,

7.7.5 Conclusions

The commercial alloys 2¼Cr-1Mo, H-11, EM-12, 416 and 430F are found

to be highly resistant to void swelling but prone to a wide variety of precipitation behavior following irradiation over the temperature range 400-650°C to a maximum fluence of 17.6 x 10^{22} n/cm^2 (E >0.1 MeV). Precipitates found included M_6C, Mo_2C, Chi, Laves, $M_{23}C_6$, α' and a low temperature phase as yet unidentified. Gross differences in precipitate development were found not only as a function of alloy composition but also as a function of irradiation temperature for a given alloy. For example, EM-12 was found to develop at least four distinctly different temperature regiemes of precipitation behavior.

7.7.6 Future Work

Specimens of these commercial ferritic alloys will be examined following irradiation at 425°C to the lower fluence of 6 x 10^{22} n/cm^2 (E >0.1 MeV) in order to predict whether changes in mechanical properties due to precipitation will saturate at moderate fluences.

7.7.7 References

1. M. K. Zimmerschied, D. T. Peterson, R. W. Powell, and J. F. Bates, "Immersion Density Analysis of Commercial Alloys Irradiated to a Very High Fluence," this document.
2. B. A. Masters, "Dislocation Loops in Irradiated Iron," *Phil. Mag. 11*, (1965), 881.
3. E. A. Little and B. L. Eyre, "The Geometry of Dislocation Loops Generated in Mild Steel by 1 MeV Electron Irradiation at 550°C," *Met. Sci. J.*, 7, (1973), 100.
4. E. A. Little, R. Bullough and M. H. Wood, "On the Swelling Resistance of Ferritic Steel," AERE-R9678, February 1980.
5. See for example K. W. Andrews, H. Hughes and D. J. Dyson, "Constitution Diagrams for Cr-Mo-V Steels," JISI (1972), 337.
6. See for example R. P. Elliott, "Constitution of Binary Alloys, First Supplement," (McGraw Hill 1965), pg. 345.
7. ASM Handbook, 8th edition, Vol. 8, *Metallography, Structures and Phase Diagrams*, pg. 421.
8. F. A. Smidt, Jr., J. R. Hawthorne and V. Provenzano, "The Fracture Resistance of HT-9 after Irradiation at Elevated Temperature," *Effect*

of Radiation on Structural Materials: Tenth Conference. **ASTM STP** *725,* **D. Kramer, H. R. Brager and J. S. Perrin, eds. ASTM (1981), in press.**

7.8 MICROSTRUCTURAL EXAMINATION OF HT-9 ARCHIVE MATERIAL FROM THE AD-2 TEST - D. T. Peterson (Hanford Engineering Development Laboratory).

7.8.1 ADIP Task

ADIP Program Task, Ferritic Alloy Development (Path E).

7.8.2 Objective

The objective of this work is to evaluate the microstructures of the HT-9 mechanical property specimens in the AD-2 test.

7.8.3 Summary

The HT-9 fracture toughness and miniature Charpy specimens included in the AD-2 test received a different set of thermomechanical treatments (TMTs) than the tensile, crack growth and Grodzinski fatigue specimens. Transmission electron microscopy (TEM) has been performed on material stock representing the four treatments involved. All four treatments produced essentially identical tempered martensite structures.

7.8.4 Progress and Status

7.8.4.1 Introduction

The objective of the AD-2 test is to determine the effect of irradiation on the mechanical properties of the ferritic alloys HT-9, 9Cr-1Mo and 2¼Cr-1Mo. To assess the influence of prior austenite grain size on its mechanical properties two normalization and temper treatments were prescribed for the HT-9 specimens. The first treatment was intended to produce a fine prior austenite grain size while the second treatment was intended to produce a coarse grain size. In order to produce these two microstructures the tensile, crack growth and Grodzinski fatigue specimens were given treatments of 1038°C/4 min/AC + 760°C/0.5 hr/AC and 1038°C/0.5 hr/AC + 760°C/2.5 hr/AC. These treatments produced prior austenite grain sizes of ASTM 6-8 and 4-6, respectively.(1) The fracture toughness and miniature Charpy specimens were fabricated from as-received 33.3 mm round bar. The bar stock was given the following treatment by the vendor: austenitize at a maximum temperature of 1149°C for at least

one hour followed by hot working and a subsequent temper of 750°C for one hour with an air cool. Optical metallography revealed that this treatment, which is referred to as a mill anneal, produced a martensite structure with a prior austenite grain size of ASTM 8-9.[1] Therefore, the as-received condition was used as the first TMT of the fracture toughness and miniature Charpy specimens. Because this material was already in the heat treated condition its grain growth response was different than the sheet specimens which were cold worked prior to heat treating. To produce a coarse grain structure from the as-received material the fracture toughness and miniature Charpy specimens were given a heat treatment of 1050°C/1 hr/AC + 780°C/2.5 hr/AC. This treatment produced a prior austenite grain size of ASTM 3-4.[1] Because of the differences in the TMTs for the two sets of specimens TEM was performed to determine if there were any significant differences in their microstructures.

7.8.4.2 Experimental Procedure

The materials used for the TEM examinations are listed in Table 7.8.1. Treatments 1 and 2 are representative of the tensile, crack growth and Grodzinski fatigue specimens. Treatments 3 and 4 are representative of the fracture toughness and miniature Charpy specimens.

Table 7.8.1. Thermomechanical Treatments of the Materials Examined.

Material	Number	TMT
0.61 mm Sheet	1	1038°C/4 min/AC + 760°C/0.5 hr/AC
0.76 mm Sheet	2	1038°C/0.5 hr/AC + 760°C/2.5 hr/AC
Fracture Toughness Specimen T408	3	Mill Anneal: 1149°C/1 hr minimum followed by hot working and tempering at 750°C/1 hr/AC
Fracture Toughness Specimen T545	4	Mill Anneal + 1050°C/1 hr/AC + 780°C/2.5 hr/AC

To obtain specimens for TEM preparation a 0.25 to 0.38 mm thick slice was cut from the fracture toughness specimens to provide a 2.54 mm wide strip. Disks were then punched from the strips. The sheet stock was ground to a thickness of 0.25 to 0.38 mm. Disks were then punched from the thinned sheet.

The disks were prepared for TEM examination with a Metalthin twin-jet electropolishing unit using a solution of 5% perchloric acid in 95% butyl alcohol. The polishing was done using a moderate pump speed and a voltage of about 90V, with a current of 150-200 mA.

7.8.4.3 Results and Discussion

The microstructures of the four TMTs are compared in Figures 7.8.1 and *7.8.2.* All four treatments produced the characteristic tempered martensite structure. Because of the complexity of this structure it is very difficult to make quantitative comparisons. However, all four conditions have similar carbide distributions with heavy $M_{23}C_6$ precipitation on the prior austenite grain boundaries and the martensite lath boundaries. Some precipitation is also observed within the lathes. No significant amounts of delta-ferrite were observed in any of the conditions.

It is interesting to consider the structure of the mill annealed material in light of the vendor's fabrication procedure. To avoid cracking in large sections of HT-9 the vendor uses a processing sequence that is intended to avoid the martensite transformation. This is accomplished by tempering the material shortly after hot working to prevent it from cooling below the M_s temperature. This process produces a largely delta-ferritic structure. Because the heat treating facilities are at a different end of the plant from the hot working facilities there is a delay between the hot working and tempering steps. In the case of the 33.3 mm round bar this delay is long enough to allow the bar to cool below the M_s temperature. Furthermore, the TEM results indicate that the cooling was rapid enough to avoid the formation of any delta-ferrite. The fine prior austenite grain structure observed is attributed to the hot working which serves to refine the grain size from the coarse structure produced by the high austenitization temperature.

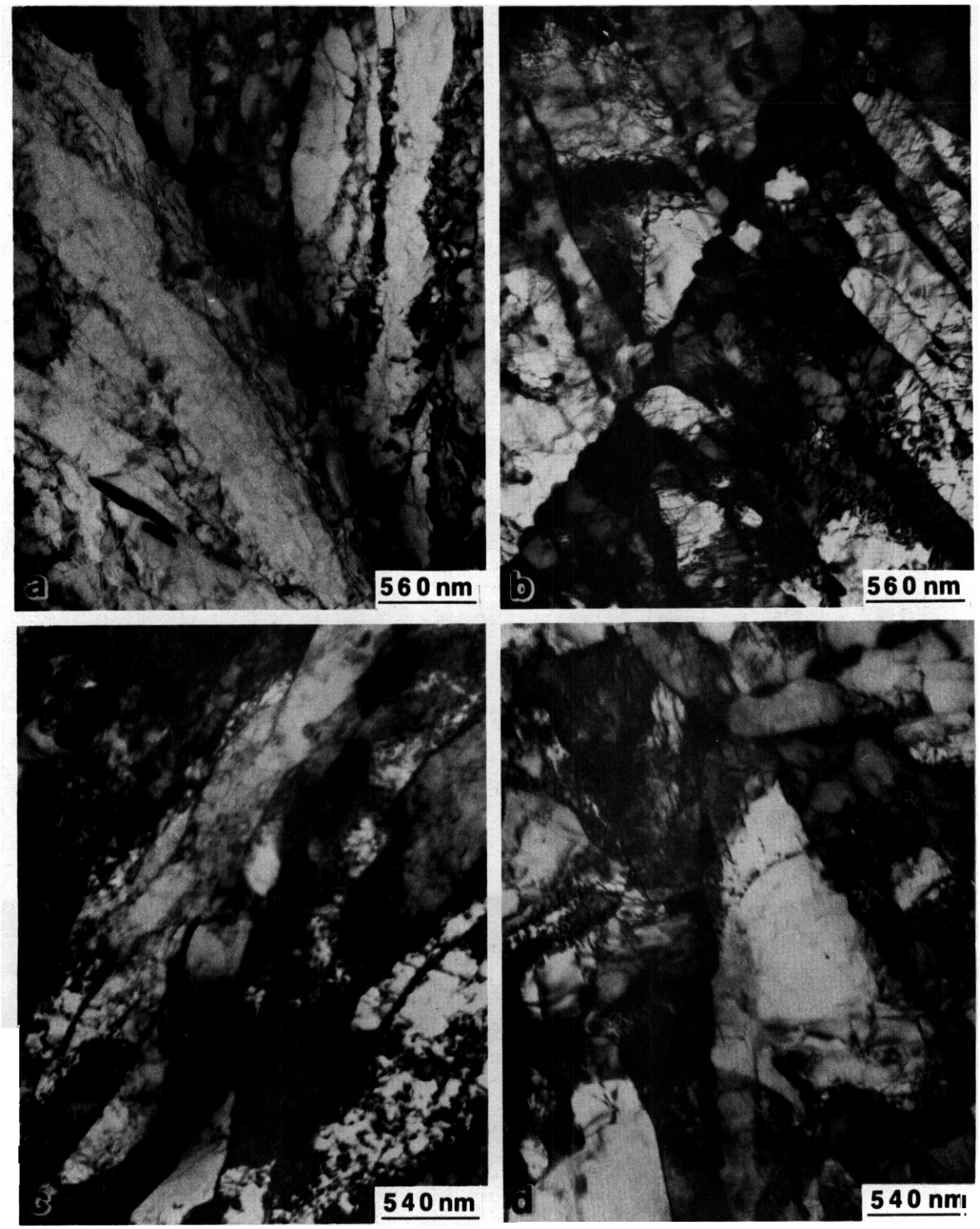

Fig. 7.8.1. Precipitation along prior austenite grain boundaries (a) 1038°C/4 min/AC + 760°C/0.5 hr/AC (b) 1038°C/0.5 hr/AC + 760°C/2.5 hr/AC (c) Mill Anneal (d) Mill Anneal + 1050°C/1 hr/AC + 780°C/2.5 hr/AC.

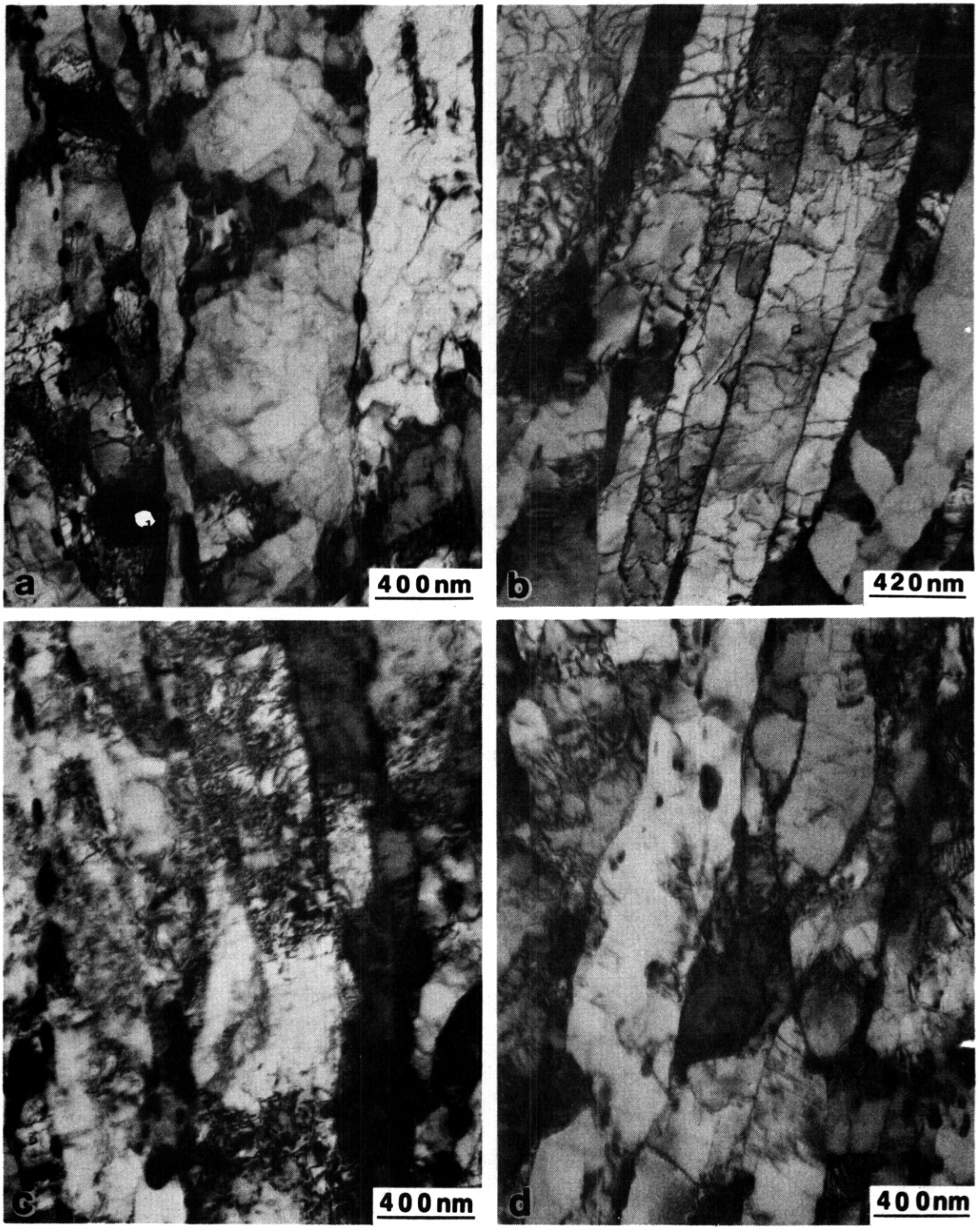

Fig. 7.8.2. The martensite lath structure (a) 1038°C/4 min/AC + 760°C/0.5 hr/AC (b) 1038°C/0.5 hr/AC + 760°C/2.5 hr/AC (c) Mill Anneal (d) Mill Anneal + 1050°C/1 hr/AC + 780°C/2.5 hr/AC.

Thus although the vendor's processing was itended to produce a delta-ferritic structure in actuality it produced a tempered martensite structure comparable to standard normalization and temper treatments.

7.8.5 Conclusion

The fracture toughness and miniature Charpy specimens included in the ***AD-2*** test have been found to have the same tempered martensite microstructure as the other mechanical properties specimens. Nonetheless, due to the differences in microhardness and grain size reported previously,[1]) comparisons of the results from the two sets of specimens must be made with care.

7.8.6 References

1. R. J. Puigh and N. F. Panayotou, "Specimen Preparation and Loading for the ***AD-2*** Ferritics Experiment," ***ADIP*** *Quarterly* Progress Report, April-June, 1980.

7.9 TENSILE PROPERTIES OF FERRITIC STEELS AFTER LOW-TEMPERATURE HFIR IRRADIATION — R. L. Klueh and J. M. Vitek

7.9.1 ADIP Task

ADIP Tasks are not defined for Path E, ferritic steels, in the 1978 program plan.

7.9.2 Objective

The goal of this project is to evaluate the properties of irradiated ferritic steels. Irradiation in the High Flux Isotope Reactor (HFIR) is used to produce both displacement damage and transmutation helium at levels relevant to fusion reactor service.

7.9.3 Summary

Tensile specimens from small heats of ferritic (martensitic) steels based on 12 Cr-1 MoVW, 9 Cr-1 MoVNb, and the low-alloy ferritic 2 1/4 Cr-1 Mo steel have been irradiated to displacement damage levels of up to about 9 dpa in HFIR. The 12 Cr-1 MoVW- and 9 Cr-1 MoVNb-base compositions were irradiated, along with similar alloys to which nickel had been added. Transmutation of the ^{58}Ni during irradiation in HFIR can lead to helium production rates similar to those anticipated in a fusion reactor. Displacement damage is produced simultaneously by the fast neutron flux in the reactor.

During the present reporting period, irradiated specimens from two heats of 12 Cr-1 MoVW and three heats of 12 Cr-1 MoVW with 1 and 2% Ni were tensile tested at room temperature and 300°C. Yield strength and ultimate tensile strength of irradiated samples displayed considerable hardening over the unirradiated condition. The increased strength was accompanied by a decrease in ductility. Indications are that the hardening resulted only from the displacement damage, and was not affected by the transmutation helium formed during irradiation.

7.9.4 Progress and Status

This irradiation experiment (HFIR-CTR-33) was designed to determine the effect of transmutation helium on the tensile properties of

12 Cr-1 MoVW and 9 Cr-1 MoVNb ferritic (martensitic) steels. The 12 Cr alloy has the composition of the commercial Sandvik HT9 alloy, while the 9 Cr steel is the modified 9 Cr-1 Mo steel developed in the breeder reactor program. In this report we will refer to the alloys by generic designations.

Nickel was added to the base-alloy compositions to produce helium during irradiation in the HFIK. These steels with approximately 2% Ni can be irradiated in HFIR to obtain approximately the same helium production rate as the original Cr-Mo alloys would develop during first-wall fusion reactor service with a neutronic wall loading near 3 MW/m^2. The displacement production rate in HFIR is also appropriate for this wall loading.

7.9.4.1 Alloys Irradiated

Details of the chemical composition, heat treatment, and microstructure for the four heats based on 12 Cr-1 MoVW and three heats of 9 Cr-1 MoVNb were given in previous reports.[1,2] These alloys included the 12 Cr-1 MoVW steel (HT9 composition) with 0, 1, and 2% Ni and the 9 Cr-1 MoVNb with 0 and 2% Ni. For both the 12 Cr and 9 Cr steels an additional alloy was prepared with 2% Ni, but with the net chromium equivalent adjusted to be approximately the same as that of the respective steels without the nickel' (i.e., more chromium, molybdenum, and tungsten were added). In addition to these seven alloys, a heat of standard HT9 from the breeder reactor program (heat 91354) and a heat of 2 1/4 Cr-1 Mo steel (heat 72768) were also irradiated.[2] The composition of the alloys discussed in this progress report is given in Table 7.9.1.

7.9.4.2 Experimental Procedure

Sheet tensile specimens in this experiment were of an SS-1 type, with a reduced gage section 20.32 mm long by 1.52 mm wide by 0.76 mm thick (Fig. 7.9.1). Five normalized-and-tempered specimens from heat 91354 and three specimens from each of the 12 Cr and 9 Cr steels (with and without nickel) were irradiated. Six specimens of 2 1/4 Cr-1 Mo steel were irradiated: three of the specimens were normalized and tempered and three were fully annealed.

Table 7.9.1 Composition of 12 Cr-1 MoVW Heats of Ferritic Steels

Element	Alloy Content,[a] wt %				
	HT9 Breeder (91354)	HT9 (XAA-3587)	HT9 + 1% Ni (XAA-3588)	HT9 + 2% Ni (XAA-3589)	HT9 + 2% Ni Adjusted (XAA-3592)
C	0.20	0.21	0.20	0.20	0.15
Mn	0.47	0.50	0.47	0.49	0.32
P	0.004	0.011	0.010	0.011	0.008
S		0.004	0.004	0.004	0.004
si	0.31	0.18	0.13	0.14	0.07
Ni	0.54	0.43	1.14	2.27	2.30
Cr	11.2	11.99	11.97	11.71	13.60
Mo	0.96	0.93	1.04	1.02	1.59
V	0.31	0.27	0.31	0.31	0.30
Nb		0.018	0.015	0.015	0.016
Ti		0.003	0.003	0.003	0.002
co	0.02	0.017	0.015	0.021	0.018
cu	0.04	0.05	0.05	0.05	0.05
Al	0.03	0.030	0.017	0.028	0.018
B	0.0007	<0.001	<0.001	<0.001	<0.001
W	0.5	0.54	0.53	0.54	0.64
As	0.01	<0.001	0.002	<0.002	<0.002
Sn	0.01	0.002	0.001	0.002	0.002
Zr		<0.001	<0.001	<0.001	<0.001
N		0.020	0.016	0.017	0.014
O		0.005	0.007	0.007	0.007

[a]Balance iron.

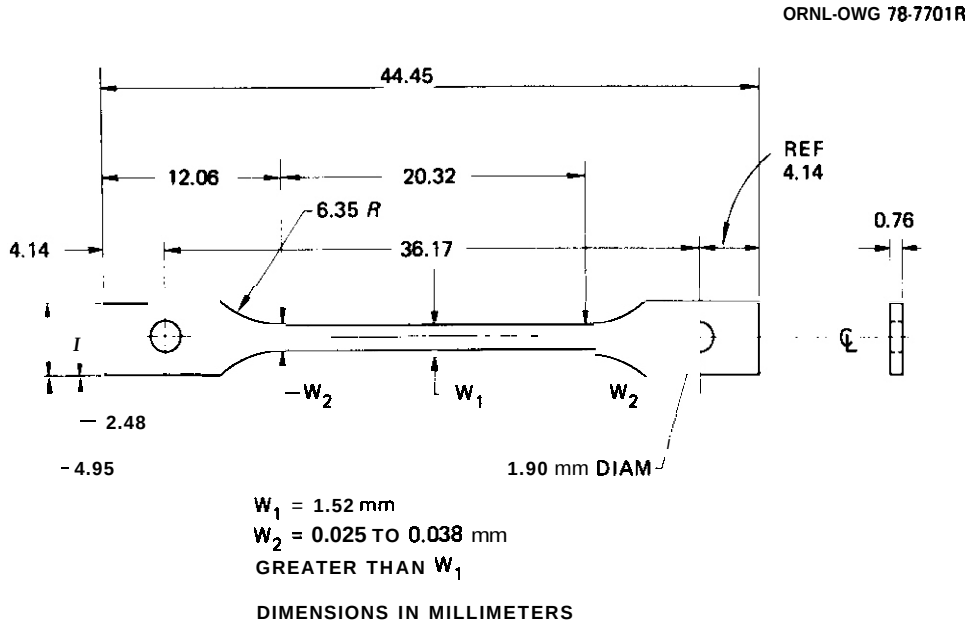

Fig. 7.9.1. The SS-1 Type Tensile Specimen.

The specimens were irradiated at 50°C in an aluminum capsule to a maximum total fluence of 5.0 x 10^{26} neutrons/m^2, and fast fluence of 1.3 x 10^{26} neutrons/m^2 (>0.1 MeV). This irradiation produced a calculated damage level up to 9.3 dpa and helium levels up to about 83 at. ppm (depending on the nickel content of the alloy and its location in the capsule). Details on the capsule loading, irradiation conditions, and the predicted displacement damage and helium production for each specimen in the capsule were given in a previous report.[2]

The specimens were removed from the capsule after irradiation. Immersion density measurements were made on each specimen, after which the specimens were tensile tested at room temperature and 300°C on a 44-kN capacity Instron universal testing machine. A strain rate of 4.2 x 10^{-5}/s was used.

7.9.4.3 Results

There was no detectable change in the density of the specimens caused by irradiation.

Tensile tests at room temperature and 300°C on irradiated and unirradiated (control) specimens are complete for the 12 Cr-1 MoVW alloy series. These results will be reported here. (The chemical composition of the alloys tested is given in Table 7.9.1.) The irradiation parameters, test conditions, and measured tensile properties are given in Table 7.9.2. The following observations summarize the experimental results.

There is essentially no difference in the tensile properties of the breeder heat of HT9 (91354) and the experimental heat melted and used as the base composition for the nickel-doped alloys. This similarity was true for both irradiated and unirradiated properties (Figs. 7.9.2, 7.9.3, and 7.9.4).

We previously discussed the effect of nickel on the tempering characteristics of the 12 Cr-1 MoVW steel.' Because 2% Ni lowered the Ac_1 temperature, it was necessary to use long-time, low-temperature tempering procedures on the 2% Ni alloys. The results for the unirradiated specimens show that after tempering the strength of the 2% Ni and 2% Ni (adjusted) alloys were considerably higher than for the steels with 0 and 1% Ni (Figs. 7.9.2 and 7.9.3). The strength of the 1% Ni alloy was slightly greater than the strength of the steels with 0% Ni.

Table 7 9.2. Tensile Properties of Unirradiated and Irradiated Normalized-and-Tempered[a] 12 Cr-1 MoVW Steels

Fluence, >0.1 MeV, (neutrons/m^2)	Displacement Level (dpa)	Helium Concentration[b] (at. ppm)	Test Temperature (°C)	Strength (MPa)		Strength Ratios[c]		Elongation (%)	
				Yield	Ultimate	R_y	R_u	Uniform	Total
× 10^{25}			12 Cr-1 MoVW (91354)						
0			25	549	716			6.64	9.91
1.3	9.3	26	25	983	987	1.79	1.38	0.31	2.12
0			300	490	647			5.53	8.63
1.2	9.1	20	300	784	800	1.60	1.24	1.36	4.49
			12 Cr-1 MoVW (XXA-3587)						
0			25	553	759			8.06	11.15
1.3	9.3	22	25	980	992	1.77	1.31	0.39	2.89
0			300	483	652			5.10	7.98
1.2	9.1	18	300	783	815	1.62	1.25	1.80	5.08
			12 Cr-1 MoVW-1 Ni (XXA-3588)						
0			25	576	800			7.09	10.64
1.3	9.3	45	25	1115	1134	1.94	1.42	0.56	2.96
0			300	519	761			5.94	9.04
1.2	9.1	41	300	899	931	1.73	1.22	1.11	3.78
			12 Cr-1 MoVW-2 Ni (XXA 3589)						
0			25	719	899			4.63	7.81
1.2	9.1	74	25	1227	1249	1.71	1.39	0.51	2.19
0			300	646	827			3.49	6.18
0.89	8.5	50	300	1019	1128	1.58	1.36	0.83	3.02
			12 Cr-1 MoVW-2 Ni (adjusted) (XAA-3592)						
0			25	769	938			4.76	7.65
1.3	9.3	83	25	1310	1338	1.70	1.43	0.57	2.78
0			300	696	894			3.21	6.29
1.2	9.1	63	300	1056	1094	1.52	1.22	0.65	3.07

[a] All heats were normalized by heating 0.5 h at 1050°C, then rapidly cooled in flowing helium. Heats 91354, XXA-3587, and XXA-3588 were tempered 2.5 h at 780°C; heats XXA-3589 and XXA-3592 were tempered at 700°C for 5 and 8 h, respectively.

[b] Calculated level of helium from ^{58}Ni and ^{10}B. [Each alloy was assumed to contain 0.007 wt % B (total)].

[c] R_y = ratio of irradiated-to-unirradiated yield strengths; R_u = ratio of irradiated to unirradiated ultimate tensile strengths.

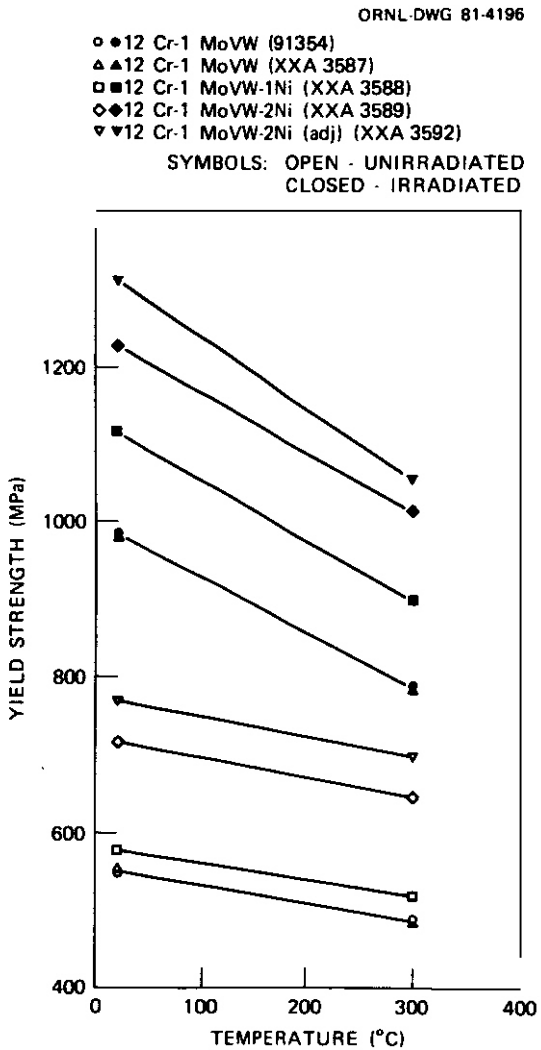

Fig. 7.9.2. The 0.2% Yield Strengths of 12 Cr-1 MoVW Steels Unirradiated and After Irradiation in HFIR to Produce up to 9.3 dpa and 20 to 80 at. ppm He.

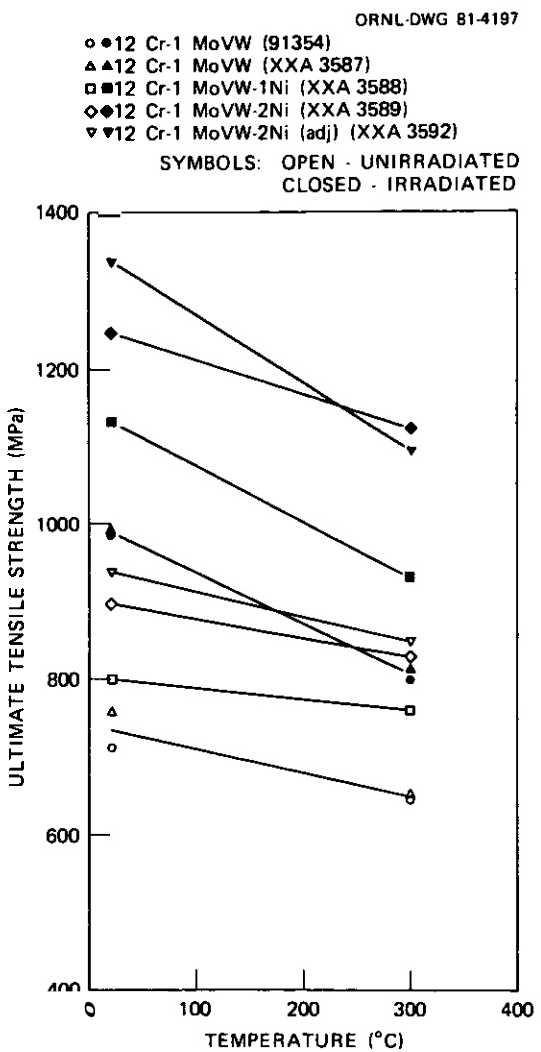

Fig. 7.9.3. The Ultimate Tensile Strength of 12 Cr-1 MoVW Steels Unirradiated and After Irradiation in HFIR.

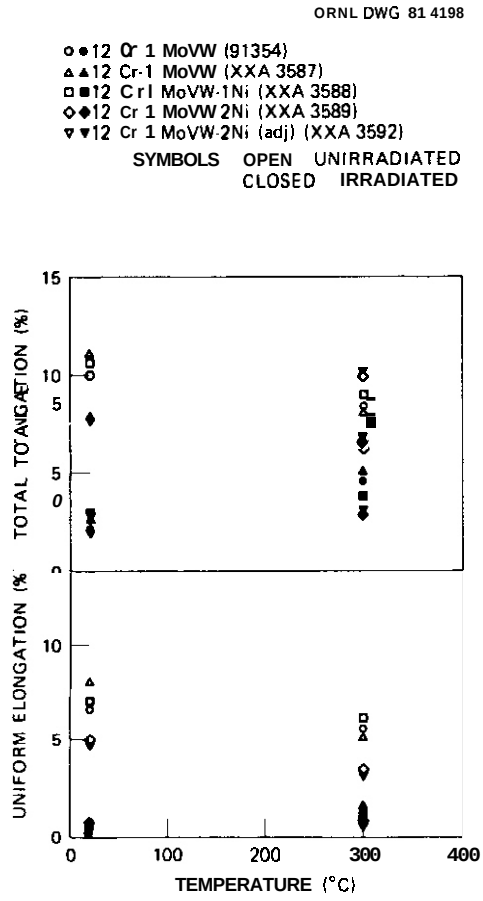

Fig. 7.9.4. The Uniform and Total Elongation of 12 Cr-1 MoVW Steels Unirradiated and After Irradiation in HFIR to Produce Up to 9.3 dpa and 20 to 80 at. ppm He.

With the exception of the alloy containing 2% Ni (XXA-3589), all the room temperature tests were made on specimens irradiated to 9.3 dpa, while the specimens tested at 300°C were irradiated to 9.1 dpa. For the 2% Ni alloy tested at room temperature and 300°C, irradiations were to 9.1 and 8.5 dpa, respectively. The helium concentrations depended on the nickel concentration and fluence (position of the sample in the capsule).

The strength data at room temperature and 300°C were connected by a straight line for each alloy; only one line was used for the two 12 Cr-1 MoVW heats (Figs. 7.9.2 and 7.9.3). An effect of irradiation is immediately obvious. Irradiation increased both the 0.2% yield strength (Fig. 7.9.2) and the ultimate tensile strength (Fig. 7.9.3) and decreased the uniform and total elongation (Fig. 7.9.4). These changes were similar at each test temperature. Also, the rate of decrease in strength with temperature between room temperature and 300°C was greater for the irradiated specimens. The rates were similar (approximately similar slopes) for all five steels.

An examination of the tensile results leads to the conclusion that there is little or no effect of helium on the properties of the steels irradiated under the conditions of this experiment. This follows when the effect of the unirradiated strength differences is eliminated. Qualitatively. this can be seen by calculating the following ratios:

$$R_y = Y_u/Y_i \text{ and } R_u = U_u/U_i ,$$

where Y, and Y_i are the unirradiated and irradiated yield strengths and U_u and U_i the unirradiated and irradiated ultimate tensile strengths.

The value of R_y and R, at a given temperature are reasonably constant for all the steels (Table 7.9.2), regardless of helium content. The only possible deviation was the value of R_y for the 1%Ni alloy. From such a simplified comparison of the effect of irradiation on the steels, the helium appears to have little effect. Essentially all the hardening must result from the displacement damage.

The changes in uniform and total elongation also give no indication of a helium effect (a calculation of the ratio of irradiated to unirradiated ductilities at a given temperature shows little difference for the steels). Note that the strength and ductility of the unirradiated steels both decrease in going from room temperature to 300°C. For irradiated material, the strength again decreases, but the ductility increases between room temperature and 300°C (Fig. 7.9.4).

7.9.5 Future Work

The results for the 9 Cr-1 MoVNb alloys will be reported next quarter.

1.9.6 References

1. M. L. Grossbeck, V. K. Sikka, T. K. Roche, and R. L. Klueh, "Preparation Of Nickel-Doped Ferritic Alloys for HFIR Irradiation to Produce Helium," ADIP *Quart. Prog. Rep. Dec.* 31, 1979, DOE/ER-0045/1, pp. 100-04.
2. M. L. Grossbeck and J. W. Woods, "An Irradiation Experiment to Scope the Tensile Properties of Ferritic Alloys – HFIR-CTR-33," ADIP *Quart. Prog. Rep. June 30,* 1980, DOE/ER-0045/3, pp. 30-34.

7.10 IMMERSION DENSITY ANALYSIS OF COMMERCIAL ALLOYS IRRADIATED TO A VERY HIGH FLUENCE – M. K. Zimmerschied, D. T. Peterson, R. W. Powell, and J. F. Bates (Hanford Engineering Development Laboratory).

7.10.1 ADIP Task

ADIP Task I.C.l, Microstructural Stability.

7.10.2 Objectives

The objective of this work is to provide high-fluence swelling data on commercial alloys of relevance to the ADIP program.

7.10.3 Summary

Immersion density measurements have been performed on a series of high-nickel, refractory and ferritic commercial alloys irradiated in EBR-II to a peak fluence of 17.8×10^{22} n/cm^2 (E >0.1 MeV). The specimens were irradiated at temperatures ranging from 400 to 650°C. All of the alloys exhibit swelling resistance far superior to AISI 316. None of the ferritic alloys exhibited more than 0.6% swelling after this high exposure.

The high-nickel superalloys, Inconel X-750 and Inconel 718, both show a low temperature swelling peak. Inconel X-750 swells more than Inconel 718 at all temperatures and has a peak of 2.4% at 427°C.

The refractory alloys, TZM and Nb-1Zr, both show peak swelling at temperatures at or above 593°C. TZM exhibits the greatest swelling with a peak of 3.6% at 593°C.

7.10.4 Progress and Status

7.10.4.1 Introduction

The alloys being studied were irradiated in the EBR-II reactor as part of the AA-I test of the National Cladding/Duct Materials Development Program. This test, which began irradiation six years ago, consists solely of commercial alloys. During its most recent discharge a number of alloys of interest to the ADIP program were examined. The alloys include the high-nickel alloys Inconel X-750 and Inconel 718; the refractory alloys TZM and Nb-1Zr; and the ferritic alloys AISI 430F, AISI 416, EM-12, H-11 and 2¼Cr-1Mo.

7.10.4.2 Experimental Procedure

Initial material stock was procured from several vendors. The compositions of the alloys are listed in Table 7.10.1. Specimens were machined in the form of 0.3 cm diameter by 1.3 cm long cylinders. The thermomechanical treatments of the specimens are listed in Table 7.10.2.

The specimens were irradiated in capsules B-116 and B-117 of the AA-I test. The capsules were of the B-7a design and contained eight subcapsules. Through gas-gap temperature regulation the subcapsules were designed to run at eight different temperatures. The specimens within the subcapsules were sodium bonded to ensure uniform temperatures. The capsules were irradiated in Row 2 of EBR-II as part of the X-223 subassembly. The peak accumulated fluence of the specimens is 17.8 x 10^{22} n/cm^2 (E >0.1 MeV).

Densities were determined by the immersion density technique. Multiple measurements were made on each specimen with a maximum deviation of ±0.05% being accepted. The swelling was calculated by comparing the densities of unirradiated control specimens with those of the irradiated specimens.

7.10.4.3 Results and Discussion

The swelling results are summarized in Table 7.10.2 and Figures 7.10.1 through 7.10.3. For discussion the results will be grouped by alloy class.

7.10.4.3.1 Path B. No swelling data has yet been generated on the five ADIP path B alloys. However, it is possible to infer their swelling behavior by examining similar commercial alloys. The two superalloys studied in this work were Inconel X-750 and Inconel 718. Inconel X-750 is a γ'-strengthened nickel base alloy very similar to the path B alloy designated B6. Inconel 718 is a γ'/γ''-strengthened nickel base alloy related to alloy B4.

As can be seen in Figure 7.10.1, bothalloys exhibit a low temperature swelling peak. Inconel 718 displays a swelling peak of only 0.35% at 427°C while Inconel X-750 has a peak of 2.38%, also at 427°C. Both alloys exhibit excellent swelling resistance after irradiation to a peak fluence corresponding to about 100 dpa.

Void swelling results have been reported on Inconel 706 irradiated in this same test to a peak fluence of 14.7 x 10^{22} n/cm^2 (E >0.1 MeV). (1)

Table 7.10.1 Alloy Compositions, as Supplied by the Vendor (Weight Percent).

Alloy	Code	I.D.	Heat	Mfg.	Fe	Ni	Cr	Mo	Nb	Ti	Al	Si	Mn	C	Other
2¼Cr-1Mo	94	941A-3	C4337-14S	Lukens	Bal	0.16	2.17	0.93	-	0.02	-	0.21	0.42	0.12	V 0.004
EM-12	98	981A-3	P-12616	Combustion Engineering	Bal	-	9.42	2.02	0.40	-	-	0.28	1.00	0.085	V 0.27
H-11	93	931A-3	D-12099K-11	Universal Cyclops	Bal	0.12	4.97	1.31	-	-	-	0.88	0.37	0.42	V 0.49
AISI 416	64	641B-2	44221	Jones & Laughlin	Bal	0.27	13.36	0.26	-	-	-	0.48	0.42	0.11	
AISI 430F	91	911A-3	G-8821	Universal Cyclops		-	17.64	0.04	-	-		0.50	0.40	0.043	
InX-750	9A	A691A-3	L-2646K14	Universal Cyclops		71.52	15.36	-	+TaTi.06	2.47	0	0.07	0.09	0.045	
In718	76	A761A-3	44F9EY	Huntington Alloys of INCO		52.33	18.57	2.83	+TaT5.28	0.92	0	0.2	0.10	0.04	
Nb-1Zr	82	82 A-2	530126	Wah Chang	<0.005	< 0.002	-	0.002	Bal	<0.004	-	< 0.005	<0.002	0.003	$Ta_{0.095}$
TZM	83	831A-2	8967	Climax Molybdenum	0.003	0.001	-	Bal	-	0.45	-	0.002	-	0.013	Zr 0.09

Table 7.10.2 Thermomechanical Treatment and Swelling

Alloy	Code	Thermomechanical Treatment	T_{irr} ϕt, $X10^{22}$ n/cm^2 (E >0.1 MeV)	400°C 14.0	427°C 15.8	~ 10 %	~ 15.0	~ 17 %	538°C 16.7	593°C 17.8	649°C 17.6
$2\frac{1}{4}$Cr-1Mo	94	1010°C/1 hr/WQ + 843°C/2 hr/WQ		+ 0.12	+ 0.08	+ 0.09	+ 0.10	+ 0.09	+ 0.17		+ 0.12
EM-12	98	1052°C/0.5 hr/AC + 754°C/1.5 hr/AC		+ 0.57	+ 0.32	+ 0.01	- 0.13	- 0.21	- 0.13		+ 0.01
H-11	93	1010°C/1 hr/WQ + 565°C/2 hr/WQ		+ 0.14	+ 0.08	+ 0.09	- 0.02	- 0.03			+ 0.16
AISI 416	64	870°C/FC at 13°C per hr to 593°C/AC		+ 0.25	+ 0.11	+ 0.14	+ 0.08	+ 0.06	+ 0.10		+ 0.10
AISI 430F	91	1066°C/1 hr/WQ		+ 0.19	+ 0.14	+ 0.13	+ 0.17	+ 0.11	+ 0.15		+ 0.13
InX-750	9A	1149°C/2 hr/AC + 843°C/24 hr/AC + 704°C/2 hr/AC		+ 1.09	+ 2.38	+ 1.85	+ 1.15	+ 0.88	+ 0.43	+ 0.02	- 0.03
In718	76	954°C/1 hr/WQ + 718°C/8 hr/FC to 621°C/hold for 18 hrs total/AC		+ 0.28	+ 0.35	+ 0.20	+ 0.18	+ 0.05	+ 0.07	+ 0.05	+ 0.02
Nb-1Zr	82	1204°C/1 hr/vacuum cool		+ 0.34	+ 0.38	+ 0.24	+ 0.18	+ 0.21	+ 0.31	+ 0.32	+ 0.71
TZM	83	1316°C/2.5 hr/vacuum cool		+ 0.14	+ 0.05	+ 0.10	+ 0.12	+ 0.35	+ 0.84	+ 3.57	+ 3.34

SWELLING IN COMMERCIAL ALLOYS: AUSTENITIC ALLOYS (PATH B)

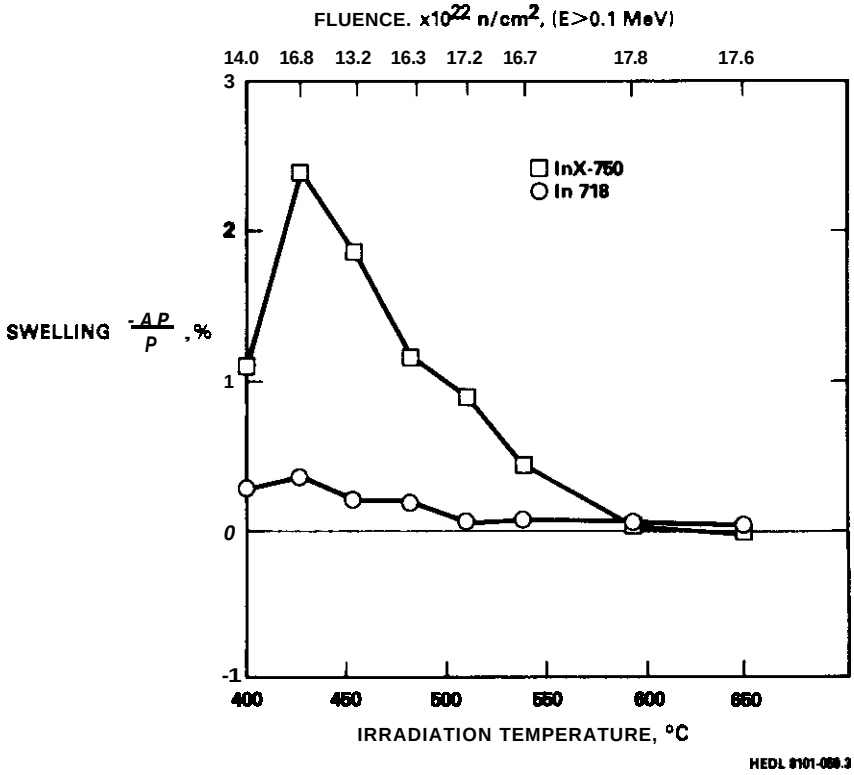

Figure 7.10.1. Swelling in the superalloys Inconel **X-750** and Inconel 718.

Inconel **706** is a γ'/γ''-strengthened iron-nickel base alloy very similar to alloy **B4.** After irradiation to a peak fluence of 14.7 x 10^{22} n/cm^2 (E >0.1 MeV) the maximum void swelling observed was 0.1%. Based on these results it is anticipated that the path B alloys **B4** and **B6** will also be highly swelling resistant.

7.10.4.3.2 Path C. The refractory alloys Nb-1Zr and TZM were previously studied in detail following irradiation to a peak fluence of 14.7 **x** 10^{22} n/cm^2 (E >0.1 MeV). [2] The present data (see Figure **7.10.2)** reveals that **for** the case of Nb-1Zr extremely low swelling is maintained with a peak of 0.71% at **650°C.** Reference to the lower fluence data indicates

SWELLING IN COMMERCIAL ALLOYS: REFRACTORY ALLOYS (PATH C)

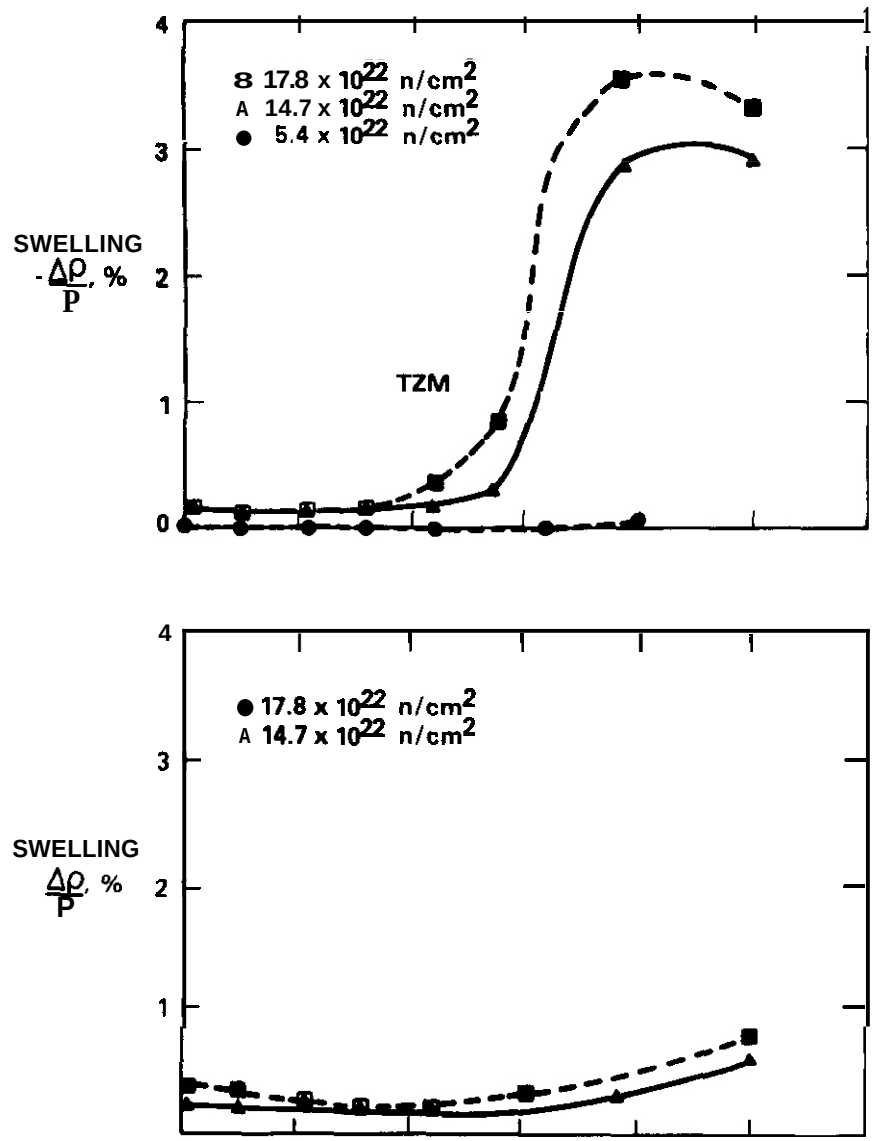

Figure 7.10.2. Swelling in the refractory alloys TZM and Nb-1Zr. The peak fluences are indicated in the legend.

that the swelling has increased slightly, with a rate of $0.02\%/10^{22}$ n/cm^2 at 650°C. This rate is approximately two orders of magnitude lower than the rate of $2.6\%/10^{22}$ n/cm^2 observed in 20% cold worked AISI 316.(3)

In TZM a sharp increase in swelling is observed above 538°C with a peak of 3.6% at 593°C (see Figure 7.10.2). Comparison with the lower fluence data reveals that the swelling has increased at all temperatures above 482°C. At the peak temperature of 593°C the swelling has increased at a rate of $0.18\%/10^{22}$ n/cm^2. This rate is markedly lower than the rate of $0.32\%/10^{22}$ n/cm^2 observed at the lower fluence.

After irradiation to 14.6×10^{22} n/cm^2 (E >0.1 MeV) at 650°C, Gelles and Bates(2) observed void lattice development in TZM. They postulated that if swelling saturation were to occur with continued irradiation the voids in the array must grow to a critical size at which point a stable microstructure could be attained. It is interesting to estimate at what fluence this saturation would take place. Gelles and Bates observed a void density of 1.3×10^{17} cm^{-3} and a maximum void size of 10 nm at 650°C.(2) As Sprague et al observed apparent void coalescence in TZM irradiated at 650°C(4), 8 nm may be a more accurate estimate of the maximum void size. Using a void density of 1.3×10^{17} cm^{-3}, then 10% swelling will be produced if all the voids grow to 8 nm. At the presently observed swelling rate of $0.13\%/10^{22}$ n/cm^2, a fluence of 69×10^{22} n/cm^2 (E >0.1 MeV), or about 250 dpa, would be required to achieve saturation. Therefore saturation would not occur until fluences well in excess of the goal exposures for fusion reactor first walls.

7.10.4.3.3 Path E. Only in the past two years has the fusion program begun to examine ferritic alloys. The three ferritic alloys being studied in the ADIP program are HT-9, 9Cr-1Mo and, to a lesser extent, 2¼Cr-1Mo. These alloys are being irradiated in EBR-II in the AD-2 test. They will not be available at their peak fluence of 6.3×10^{22} n/cm^2 (E >0.1 MeV) until September 1982. This study provides the opportunity to assess the swelling resistance of several ferritic alloys irradiated to a peak fluence (85 dpa) on the order of the anticipated first wall goal exposures.

The five ferritic alloys examined were AISI 430F, AISI 416, EM-12, H-11 and 2¼Cr-1Mo. These alloys encompass a wide range of compositions and structures, which are compared in Table 7.10.3. The microstructures of these alloys have been reported in detail by D. S. Gelles.[5] It should be noted that the heat treatments used produced atypical structures for some of the alloys. In spite of the variations among the alloys, they all were found to be very swelling resistant: the highest swelling observed was 0.57% in EM-12 (see Figure 7.10.3). Thus swelling does not appear to be a problem in the development of the path E alloys.

Table 7.10.3. Comparison of the Nominal Major Element Compositions and Microstructures of the Ferritic Alloys Examined

Alloy	Cr	Mo	C	Structure
AISI 430F	18	0.04	0.05	Duplex - Ferrite/Martensite
AISI 416	13	0.2	0.1	Ferritic
EM-12	10	2.0	0.06	Duplex - Ferrite/Martensite
H-11	5	1.4	0.4	Martensitic
2¼Cr-1Mo	2.2	1.0	0.1	Martensitic

7.10.5 Conclusions

Immersion density measurements have been performed on a series of high-nickel, refractory and ferritic commercial alloys irradiated over the temperature range of 400 to 650°C. After irradiation to a peak fluence on the order of the anticipated goal exposures for fusion reactor first walls, all of the alloys exhibit swelling resistance far superior to cold worked AISI 316.

7.10.6 References

1. L. E. Thomas, "The Stability of γ' and γ'' in Inconel 706 Under Neutron Irradiation," Proceedings of the AIME Symposium on Irradiation Phase Stability, October 5-9, 1980, Pittsburgh.
2. D. S. Gelles and J. F. Bates, "TZM and Nb-1Zr Irradiated to High Fluence," *ADIP Quarterly Progress Report*, January-March, 1980.
3. J. F. Bates and M. K. Korenko, "The *Mk-8* Equation for Stress-Free Swelling of 20% Cold-Worked AISI 316 Stainless Steel," HEDL-TME 80-8.

4. J. A. Sprague, F. A. Smidt, Jr. and J. *R.* Reed, "The Microstructures of Some Refractory Metals and Alloys Following Neutron Irradiation at 650°C," *J. Nuc. Mat.,* 85 and 86 (1979), 739.

5. D. S. Gelles, "Microstructural Examination of a Series of Commercial Ferritic Alloys Irradiated to Very High Fluence," this report.

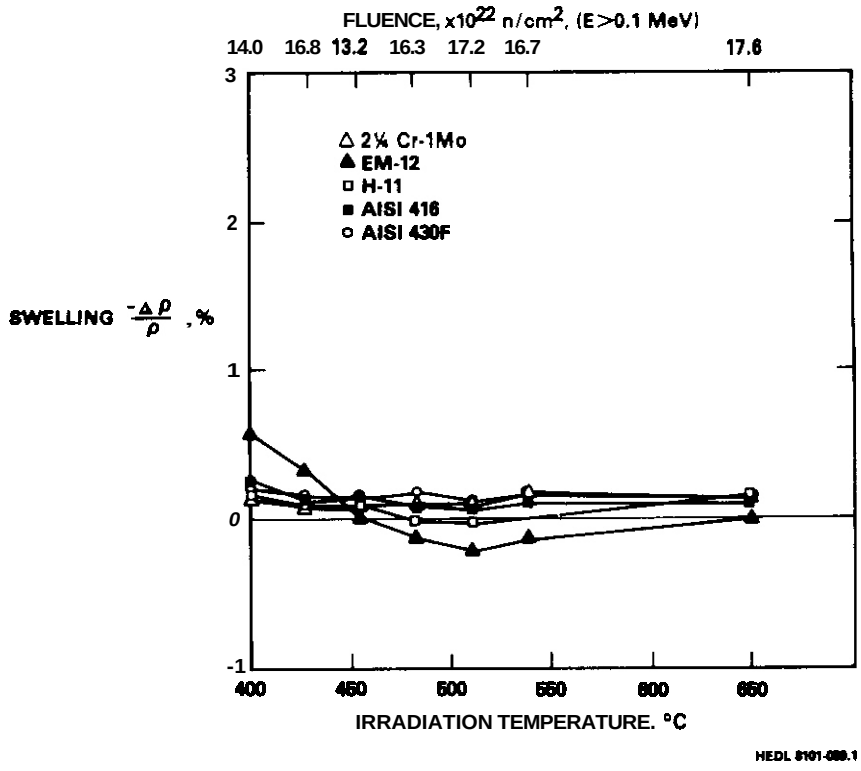

Figure 7.10.3. Swelling in the ferritic alloys.

8. STATUS OF IRRADIATION EXPERIMENTS AND MATERIALS INVENTORY

8.1 IRRADIATION MPERIMENT STATUS AND SCHEDULE

There are a large number of planned, in-progress or completed reactor irradiation experiments that support the ADIP program. Table 8.1.1 presents a summary of the parameters that describe experiments that have been completed. Experiments that have been removed from the reactor only recently, are currently undergoing irradiation, or are planned for future irradiation are included in the schedule bar charts of Table 8.1.2.

Experiments are now under way in the Oak Ridge Research Reactor (ORR) and the High Flux Isotope Reactor (HFIR), which are mixed spectrum reactors and in the Experimental Breeder Reactor (EBR-II), which is a fast reactor.

During the reporting period irradiation was begun on HFIR-CTR-31 and ORR-MFE-5. Experiment HFIR-CTR-31 contains transmission electron microscope disks for bend testing and microstructural analysis of alloys representing all five paths. An experiment to evaluate crack growth in path A alloys is designated ORR-MFE-5. The following three experiments: HFIR-CTR-27, -28, and -33 were removed from the HFIR. Experiments HFIR-CTR-27 and -28 were designed to irradiate the reference heat of type 316 stainless steel to evaluate postirradiation tensile properties. The experiment HFIR-CTR-33 was designed to irradiate path E alloys (ferritic steels) for testing to scope the effect of irradiation on the tensile properties.

Table 8.1.1. Descriptive Parameters for Completed ADIP Program Fission Reactor Irradiation Experiments

Experiment	Major Objective	Alloy	Reactor	Temperature (°C)	Displacement Damage (dpa)	Helium (at. ppm)	Duration (month)	Date Completed
ORR-MFE-1	Scope the effects of composition and microstructure on tensile, fatigue, and irradiation creep	Paths A, B, C	ORR	250–600	2	≤10	4	6/78
ORR-MFE-2	Scope the effects of composition and microstructure on tensile, fatigue, and irradiation creep	Paths A, B, C	ORR	300–600	6	≤60	15	4/80
Subassembly X-264	Effect of preinjected helium on microstructure, tensile properties, and irradiation creep	316, PE-16, V–20% Ti, V–15% Cr–5% Ti, Nb–1% Zr	EBR-II	500–825	8	2–200	4	1/77
AA-X Subassembly X-287	Effect of preinjected helium on microstructure, tensile properties, and irradiation creep	316, PE-16, V–20% Ti, V–15% Cr–5% Ti, Nb–1% Zr	EBR-II	400–700	20	2–200	23	12/78
Subassembly X-217D	Stress relaxation	Titanium alloys	EBR-II	450	2		1	1/78
Pins B285, B286, and B284	Swelling, fatigue, crack growth, and tensile properties	Titanium alloys	EBR-II	370–550	25		14	9/79
HFIR-CTR-3	Swelling and tensile properties	PE-16, Inconel 600	HFIR	300–700	4.3–9	350–1800	3	2/75
HFIR-CTR-4	Swelling and tensile properties	PE-16	HFIR	300–700	2.2–4.5	100–350	2	3/77
HFIR-CTR-5	Swelling and tensile properties	PE-16, Inconel 600	HFIR	300–700	4.3–9	350–1800	3	4/75

Experiment	Major Objective	Alloy	Reactor	Temperature (°C)	Displacement Damage (dpa)	Helium (at. ppm)	Duration (month)	Date Completed
HFIR-CTR-6	Swelling and tensile properties	PE-16, Inconel 600	HFIR	300–700	4.3–9	350–8 00	3	4 75
HFIR-CTR-7	Swelling and tensile properties	PE-16	HFIR	300–700	9–18	12503 000	7	3 77
HFIR-CTR-8	Swelling and tensile properties	PE-16	HFIR	300–700	9–18	12503 000	7	3 77
HFIR-CTR-9	Swelling and tensile properties	316, 316 + Ti	HFIR	280–680	10–16	40–10 00	6	5 77
HFIR-CTR-10	Swelling and tensile properties	316, 316 + Ti	HFIR	280–680	10–16	40001 00	6	5 77
HFIR-CTR-11	Swelling and tensile properties	316, 316 + Ti	HFIR	280–680	10–16	40001 00	6	5 77
HFIR-CTR-12	Swelling and tensile properties	316, 316 + Ti	HFIR	280–680	7–10	20–50 0	4	2 77
HFIR-CTR-13	Swelling and tensile properties	316, 316 + Ti	HFIR	280–680	7–10	20–50 0	4	2 77
HFIR-CTR-14	Fatigue	316	HFIR	430	9–15	40–1 0	7	1 /77
HFIR-CTR-15	Fatigue	316	HFIR	550	6–9	20–4 0	4	1 /78
HFIR-CTR-16	Weld characterization, swelling and tensile properties	316 PE-16 Inconel 600	HFIR	55	6–9	15–2 0	4	8 77
HFIR-CTR-17	Weld characterization	316	HFIR	280–620	7–13	0846 0	5.5	10 77
HFIR-CTR-18	Swelling and tensile properties	316 PE-16	HFIR	280–700	17–27	06–5 600	12	6/78
HFIR-CTR-19	Weld characterization	316	HFIR	280–620	7–10	0050 0	4	12 77
HFIR-CTR-20	Fatigue	316	HFIR	430	6–9	0040 0	4	1/78
HFIR-CTR-21	Fatigue	316	HFIR	550	9–15	0010 00	7	7/78
HFIR-CTR-22	Fatigue	316	HFIR	430	6–9	0040 0	4	3/78
HFIR-CTR-23	Fatigue	PE-16	HFIR	430	6–9	0710 00	3.5	2/79
HFIR-CTR-24	Temperature calibration, and tensile properties	316	HFIR	300–620	2.2	30	1	12/78

Table 8.1.2. Objectives and Schedule for Current and Planned ADIP Program Reactor Irradiation Experiments

Experiment Designation	Major Objective
A. Oak Ridge Research Reactor	
ORR-MFE-3	[1] Effect of irradiation on postirradiation fatigue crack growth in representative path A, B, and C alloys.
ORR-MFE-4	[2] Effect of irradiation on tensile, fatigue, and irradiation creep of path A PCA (Prime Candidate Alloy) and path B base research alloys. Spectral tailoring to maintain correct He/dpa ratio. Irradiation on continuing basis. 330–600°C
ORR-MFE-5	In-reactor fatigue crack growth experiment. 325–460°C

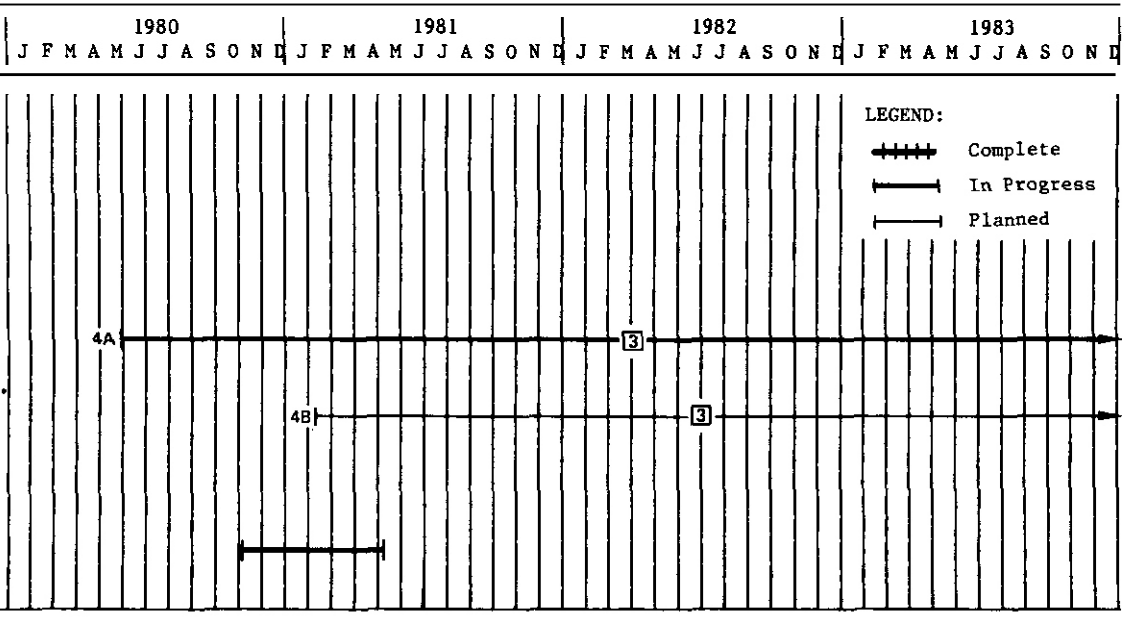

[1] Delayed for undetermined period.

[2] MFE-4A operates at 330 and 400°C. MFE-4B will operate at 500 and 600°C.

[3] Approximate schedule for specimen charge out.

Table 8.1.2 (Continued)

Experiment Designation	Major Objective
B. *Experimental Breeder Reactor (EBR-II)*	
Experiment plan depends on alloy availability. EBR-II space not yet identified.	Effect of irradiation on swelling, tensile, fatigue, and crack growth properties of V and Nb scoping alloys. 370, 450, 550, and 650°C. Position in reactor not finalized, therefore no fluence estimate. [1]
AD-2 (6 pins in separate subassemblies of row 4)	To supplement present EBR-II data on ferritic alloys with data on crack growth, fatigue, and fracture toughness. Temperature 390, 450, 500, and 550°C. 19 and 38 dpa.

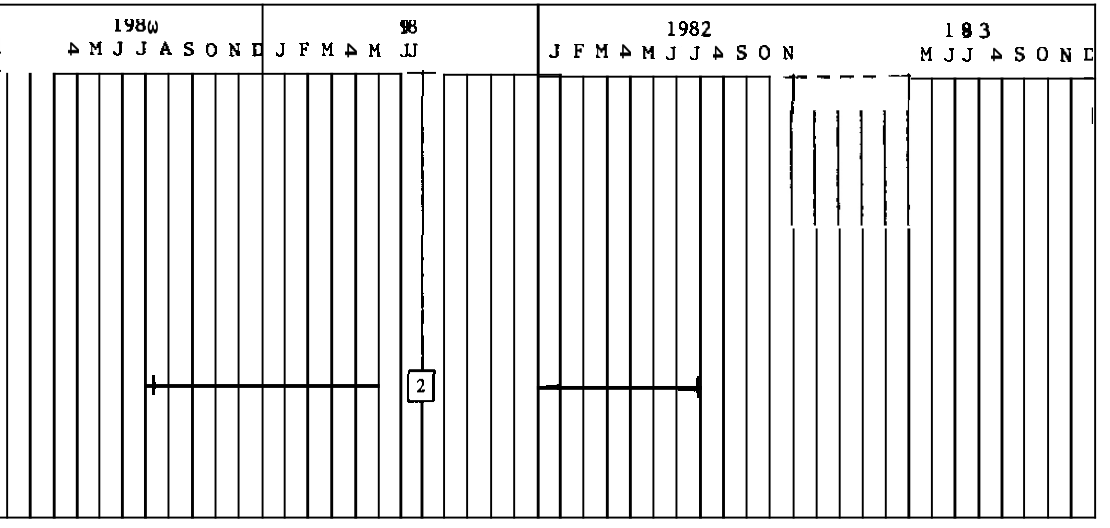

[1] Delayed for undetermined period.

[2] Interim examination. Experiment out of reactor.

Table 8 1 2 (Continued)

Experiment Designation	Major Objective
C. High Flux Isotope Reactor (HFIR)	
HFIR-CTR-25	Temperature calibration, tensile properties of MFE ref. 316, 2.25 dpa, 30 at. ppm He [1]
HFIR-CTR-26	Swelling and tensile properties of MFE ref. 316, 32 dpa, 1900 at. ppm He
HFIR-CTR-27	Swelling and tensile properties of MFE ref. 316, 56 dpa, 3450 at. ppm He
HFIR-CTR-28	Swelling and tensile properties of MFE ref. 316, 32 dpa, 1900 at. ppm He
HFIR-CTR-29	Swelling and tensile properties of MFE ref. 316, 56 dpa, 3450 at. ppm He
HFIR-CTR-30	Swelling and tensile properties, Paths A, B, and D microstructural variations, 40 dpa, 2500 at. ppm He (Path A)
HFIR-CTR-31	Swelling and tensile properties, Paths A, B and D microstructural variations, 20 dpa, 1200 ppm He (Path A)
HFIR CTR-32	Swelling and tensile properties, Paths A, B and D microstructural variations, 10 dpa, 500 ppm He (Path A)
HFIR-CTR-33	Swelling and tensile properties, Path E alloys, 10 dpa, 50°C

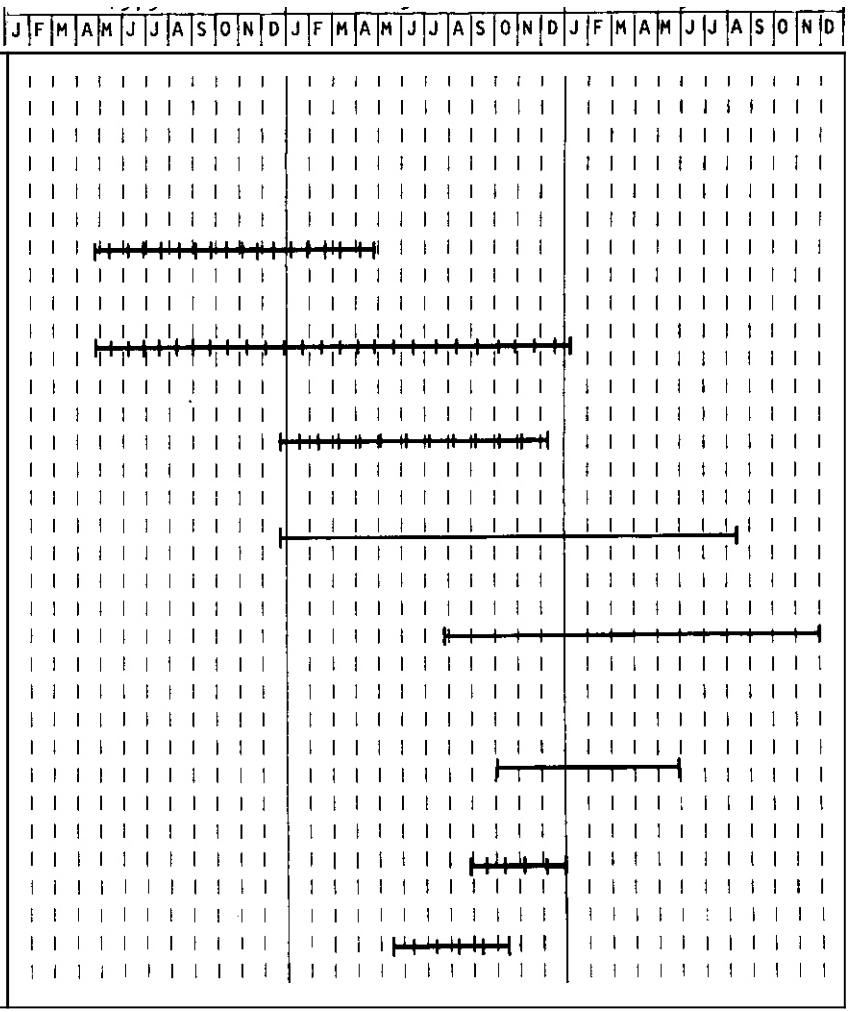

[1] Delayed for undetermined period.

Table 3 1 2 (Continued)

Experiment Designation	Major Objective
HFIR-MFE-T1	Swelling, tensile properties and fatigue of path E alloys. 70 dpa, up to 650 ppm He depending upon alloy, 55°C.
HFIR-MFE-T2	Swelling, tensile properties and fatigue of path E alloys. 10 dpa, up to 75 ppm He depending upon alloy, 55°C.
HFIR-MFE-T3	Impact properties of path E alloys. 10 dpa, up to 75 ppm He depending upon alloy, 55°C.
HFIR-MFE-RB1	Swelling, microstructure, crack growth, fracture toughness, impact, tensile, and fatigue properties of path E alloys, 55°C.
HFIR-MFE-RB2	Similar to HFIR-MFE-RB1.

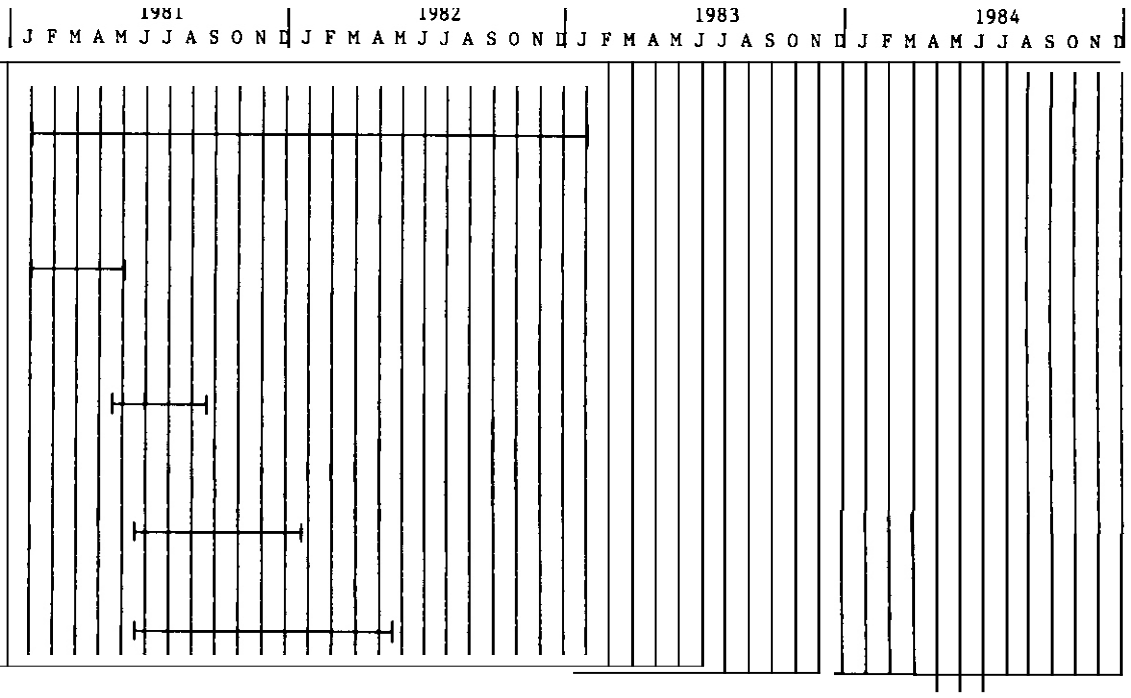

8.2 ETM RESEARCH MATERIALS INVENTORY — F. W. Wiffen, T. K. Roche (ORNL) and J. W. Davis (McDonnell Douglas)

8.2.1 ADIP Task

ADIP Task I.D.1, Materials Stockpile for MFE Programs.

8.2.2 Objective

The Office of Fusion Energy has assigned program responsibility to ORNL for the establishment and operation of a central inventory of research materials to be used in the Fusion Reactor Materials research and development programs. The objective is to provide a common supply of materials for the Fusion Reactor Materials Program. This will minimize unintended materials variables and provide for economy in procurement and for centralized recordkeeping. Initially this inventory is to focus on materials related to first-wall and structural applications and related research, but various special purpose materials may be added in the future.

The use of materials from this inventory for research that is coordinated with or otherwise related technically to the Fusion Reactor Materials Program of DOE, but which is not an integral or directly funded part of it, is encouraged.

8.2.3 Materials Requests and Release

Materials requests shall be directed to ETM Research Materials Inventory at ORNL (Attention: F. W. Wiffen). Materials will be released directly if:

(a) The material is to be used for programs funded by the Office of Fusion Energy, with goals consistent with the approved Materials Program Plans of the Materials and Radiation Effects Branch.

(b) The requested amount of material is available, without compromising other intended uses.

Materials requests that do not satisfy both (a) and (b) will be discussed with the staff of the Materials and Radiation Effects Branch, Office of Fusion Energy, for agreement on action.

8.2.4 Records

Chemistry and materials preparation records are maintained for all inventory material. All materials supplied to program users will be accompanied by summary characterization information.

8.2.5 Summary of Current Inventory and Material Movement During Period Oct. 1 to Dec. 31, 1980

A condensed, qualitative description of the content of materials in the ETM Research Materials Inventory is given in Table 8.2.1. This table indicates the nominal diameter of rod or thickness of sheet for product forms of each alloy and also indicates by weight the amount of each alloy in larger sizes available for fabrication to produce other product forms as needed by the program. Table 8.2.2 lists materials distributed from the inventory during this reporting period. No material was received.

Alloy compositions and more detail on the alloys and their procurement and/or fabrication are given in earlier ADIP quarterly progress reports.

Table 8.2.1 Summary Status of Material Availability in the ETM Research Materials Inventory

Alloy	Product Form: Ingot or Bar,[a] Weight (kg)	Rod,[b] Diameter (mm)	Sheet,[c] Thickness (mm)	Thin-Wall Tubing, Wall Thickness (mm)
Path A Alloys				
Type 316 SS	900	16 and 7.2	13 and 7.9	0.25
Path A PCA[d]	490	12	13	0.25
USSR – Cr-Mn Steel[e]	0	10.5	2.6	0
Path B Alloys				
PE-16	140	16 and 7.1	13 and 1.6	0.25
B-1	180	0	0	0
B-2	180	0	0	0
B-3	180	0	0	0
B-4	180	0	0	0
B-6	180	0	0	0
Path C Alloys				
Ti-64	0	0	2.5 and 0.76	0
Ti-62425	0	63	6.3, 3.2. and 0.76	0
Ti-56215	0	0	2.5 and 0.76	0
Ti-38644	0	0	0.76 and 0.25	0
Nb-1% Zr	0	6.3	2.5, 1.5, and 0.76	0
Nb-5% Mo-1% Zr	0	6.3	2.5, 1.5, and 0.76	0
V-20% Ti	0	6.3	2.5, 1.5, and 0.76	0
v-15% Cr-5% Ti	0	6.3	2.5, 1.5. and 0.76	0
vanstar-7	0	6.3	2.5, 1.5, and 0.76	0
Path D Allays – No Material in Inventory				
Path e Alloys				
HT9	0	0	4.5 and 18	0
HT9 + 1% Ni	0	0	4.5 and 18	0
HT9 t 2% Ni	0	0	4.5 and 18	0
HT9 t 2% Ni + Cr adjusted	0	0	4.5 and 18	0
T-9 modified	0	0	4.5 and 18	0
T-9 modified + 2% Ni	0	0	4.5 and 18	0
T-9 modified ● 2% Ni t Cr adjusted	0	0	4.5 and 18	0
2 1/4 Cr-1 Mo	0	0	f	0

[a] Greater than 25 mm, minimum dimension.

[b] Less than 25 arm in diameter. Same Path A and Path B alloys are available in two different diameters.

[c] Less than 15 arm thick. Some Path A, Path B, and Path C alloys are available, in two or three different thicknesses.

[d] Prime Candidate Alloy.

[e] Rod and sheet of a USSR stainless steel supplied under the U.S.-USSR Fusion Reactor Materials Exchange Program.

[f] Material is thick-wall pipe, rerolled as necessary to produce sheet or rod.

Table 8.2.2. ETM Research Materials Inventory, Fusion Reactor Program, Disbursements 10-1-80 to 12-31-80

Alloy	Heat	Product Form	Dimensions		Quantity		Sent to
			(mm)	(in.)	(m^2)	($in.^2$)	
Path A Alloys — Austenitic Stainless Steels							
Type 316 SS[b]	X-15893	Plate (20% cold worked)	6.4	0.25	0.056	86	NSD[c]
Path A PCA[d]	K-280	Plate	12.7	0.5	0.11	170	Metals Processing Group, ORNL
		Sheet	0.25	0.010	0.42	655	Radiation Effects Group, ORNL
		Sheet	0.76	0.030	0.058	90	Radiation Effects Group, ORNL
Path C Alloys — Reactive and Refractory Alloys							
V–20% Ti	833	Sheet	0.76	0.030	0.017	26	University of Virginia
	832 bottom	Sheet	0.76	0.030	0.11	169	Westinghouse Fusion Power Systems
V–15% Cr–5% Ti	835A	Sheet	0.76	0.030	0.12	182	Westinghouse Fusion Power Systems
Vanstar-7	836 bottom	Sheet	0.76	0.030	0.014	22	Westinghouse Fusion Power Systems
	837	Sheet	0.76	0.030	0.094	146	Westinghouse Fusion Power Systems
Path E Alloys — Ferritic Steels							
HT9	ESR-XAA-3587-4	Plate	5.3	0.210	0.036	55	Radiation Effects Group, ORNL
		Sheet	2.8	0.110	0.034	52	Radiation Effects Group, ORNL
		Sheet	0.76	0.030	0.037	58	Radiation Effects Group, ORNL
HT9 + 1% Ni	ESR-XAA-3588-9	Plate	5.3	0.210	0.027	42	Radiation Effects Group, ORNL
		Sheet	2.8	0.110	0.030	46	Radiation Effects Group, ORNL
		Sheet	0.76	0.030	0.036	56	Radiation Effects Group, ORNL

Table 8.2.2. (Continued)

Alloy	Heat	Product Form	Dimensions		Quantity		Sent to
			(mm)	(in.)	(m^2)	($in.^2$)	
HT9 + 2% Ni	ESR-XAA-3589-9	Plate	5.3	0.210	0.031	48	Radiation Effects Group, ORNL
		Sheet	2.8	0.110	0.028	43	Radiation Effects Group, ORNL
		Sheet	0.76	0.030	0.036	56	Radiation Effects Group, ORNL
HT9 + 2% Ni with chromium equivalent adjusted	ESR-XAA-3592-9	Plate	5.3	0.210	0.032	50	Radiation Effects Group, ORNL
		Sheet	2.8	0.110	0.030	46	Radiation Effects Group, ORNL
		Sheet	0.76	0.030	0.044	68	Radiation Effects Group, ORNL
T-9 modified	ESR-XA-3590-9	Plate	5.3	0.210	0.032	49	Radiation Effects Group, ORNL
		Sheet	2.8	0.110	0.031	48	Radiation Effects Group, ORNL
		Sheet	0.76	0.030	0.043	66	Radiation Effects Group, ORNL
T-9 modified + 2% Ni	ESR-XA-3591-9	Plate	5.3	0.210	0.032	50	Radiation Effects Group, ORNL
		Sheet	2.8	0.110	0.030	46	Radiation Effects Group, ORNL
		Sheet	0.76	0.030	0.036	56	Radiation Effects Group, ORNL
T-9 modified + 2% Ni with chromium equivalent adjusted	ESR-XA-3593-9	Plate	5.3	0.210	0.031	48	Radiation Effects Group, ORNL
		Sheet	2.8	0.110	0.028	44	Radiation Effects Group, ORNL
		Sheet	0.76	0.030	0.044	68	Radiation Effects Group, ORNL

[a]Characteristic dimension — thickness for plate and sheet.

[b]Program reference material.

[c]Hanford Engineering Development Laboratory.

[d]Prime Candidate Alloy.

9. MATERIALS COMPATIBILITY AND HYDROGEN PERMEATION STUDIES

9.1 COMPATIBILITY OF FERRITIC STEELS WITH STATIC LITHIUM AND Li–5 wt % Al — P. F. Tortorelli and J. H. DeVan (ORNL)

9.1.1 ADIP Task

ADIP Task I.A.3, Perform Chemical and Metallurgical Compatibility Analyses.

9.1.2 Objective

The purpose of this program is to determine the chemical compatibility of fusion reactor candidate materials with metallic lithium. Specimens are exposed to static lithium containing selected solute additions to identify the kinetics and mechanisms that govern corrosion by lithium. Specific program objectives are: (1) to determine the effects of N, C, H, and O on apparent solubilities of metals in lithium; (2) to determine the carbon and nitrogen partitioning coefficients between alloys and lithium; (3) to determine the effects of soluble (Ca, Al) and solid (Y, Zr, Ti) active metal additions on corrosion by lithium; and (4) to determine the tendencies for mass transfer between dissimilar metals in lithium.

9.1.3 Summary

Exposures of HT9 to static 500°C lithium for up to 3000 h resulted in negligible weight changes and did not significantly affect the steel's room temperature tensile properties relative to specimens exposed to argon under otherwise similar conditions. Gage sections of 2 1/4 Cr-1 Mo steel specimens exposed for 3000 h to Li–5 wt % Al at 500 and 600°C cracked severely when these specimens were tensile tested at room temperature. Type 316 stainless steel did not deteriorate mechanically when exposed to Li–5 wt % Al for 1000 h at 500°C. Aluminum was incorporated into surface layers on the alloys and appears to have blocked the normal decarburization of 2 1/4 Cr-1 Mo steel in lithium.

9.1.4 Progress and Results

In the preceding quarterly[1] we reported that 500-h exposures of HT9 to 500°C lithium did not cause significant weight changes of the steel or

affect its room temperature tensile properties relative to specimens exposed to argon under otherwise identical conditions. We have continued this study and now have results for HT9 after 1000 and 3000 h of exposure to 500°C lithium. The weight change data are given in Table 9.1.1 together with comparative results for 2 1/4 Cr-1 Mo steel exposed under similar conditions. All the weight changes are relatively small, although the 2 1/4 Cr-1 Mo steel tends to lose weight in lithium slightly more than HT9. This may be attributed to the fact that 2 1/4 Cr-1 Mo decarburizes in molten lithium, whereas HT9 does not. On the basis of analyses of the post-test lithium and changes in tensile properties, carbon transferred significantly1 from 2 1/4 Cr-1 Mo steel to the lithium. In contrast, the tensile properties of HT9 exposed to 500°C lithium for up to 3000 h did not differ significantly from those of HT9 aged in argon at 500°C for similar times (see Table 9.1.2). We thus conclude that there was insignificant carbon exchange between the HT9 specimens and the lithium. This attests to the lower carbon activity of HT9 compared with 2 1/4 Cr-1 Mo steel.[2]

Table 9.1.1. Weight Changes of Normalized and Tempered[a] HT9 and 2 1/4 Cr-1 Mo Steel Exposed to Static Lithium at 500°C

Time (h)	Weight Change,[b] g/m^2	
	HT9	2 1/4 Cr-1 Mo
500	0.0, +0.2, +0.5	-0.2, -0.5
1000	0.0, M.2, +0.5	—0.2, -0.2
3000	-0.2, —0.2, —0.5	—0.9, —1.1

[a]Heat treatments: HT9 — 0.5 h at 1050°C in flowing argon, cooled to room temperature in cold zone, 2.5 h at 780°C in flowing argon; 2 1/4 Cr-1 Mo — 1 h at 930°C in flowing argon, cooled to room temperature in cold zone, 1 h at 700°C in flowing argon.

[b]Three HT9 tests and two 2 1/4 Cr-1 Mo steel tests were conducted.

Table 9.1.2. Room Temperature Tensile Properties of HT9[a] Exposed to Argon and Lithium at 500°C

Time (h)	Yield Strength[b] (MPa)	Ultimate Tensile Strength[b] (MPa)	Elongation[b] (%)
	Argon Exposure		
500	594.4	946.0	8.9
1000	627.4	961.1	10.5
3000	627.4	954.2	7.6
	Lithium Exposure		
500	615.0	967.1	10.5
1000	670.2	968.0	8.5
3000	635.2	986.4	8.1

[a]Normalized and tempered: 0.5 h at 1050°C in argon, cooled to room temperature, and then held for 2.5 h at 780°C.

[b]Average of measurements from two specimens of those exposed to argon and three specimens of those exposed to lithium.

We reported earlier[3] that the addition of aluminum to lithium resulted in the formation of a corrosion-resistant, "aluminized" surface layer on type 316 stainless steel. As the first stage in determining whether we could induce a similar corrosion-resistant layer in lithium-ferritic steel systems, 5 wt % Al was added to lithium in 2 1/4 Cr-1 Mo steel capsules containing tensile specimens of the same composition and heat treatment as the capsule. Data presented in the preceding quarterly' showed that 2 1/4 Cr-1 Mo steel reacted readily with Li—5 wt % Al at 500 and 600°C. However, the reaction led to decreased ductility in subsequent tensile tests.of the steel. Metallographic examinations have revealed very extensive cracking throughout the gage sections fractured in these tensile tests. An example of this in specimens exposed at 600°C is shown in Fig. 9.1.1. It is apparent from the micrographs in

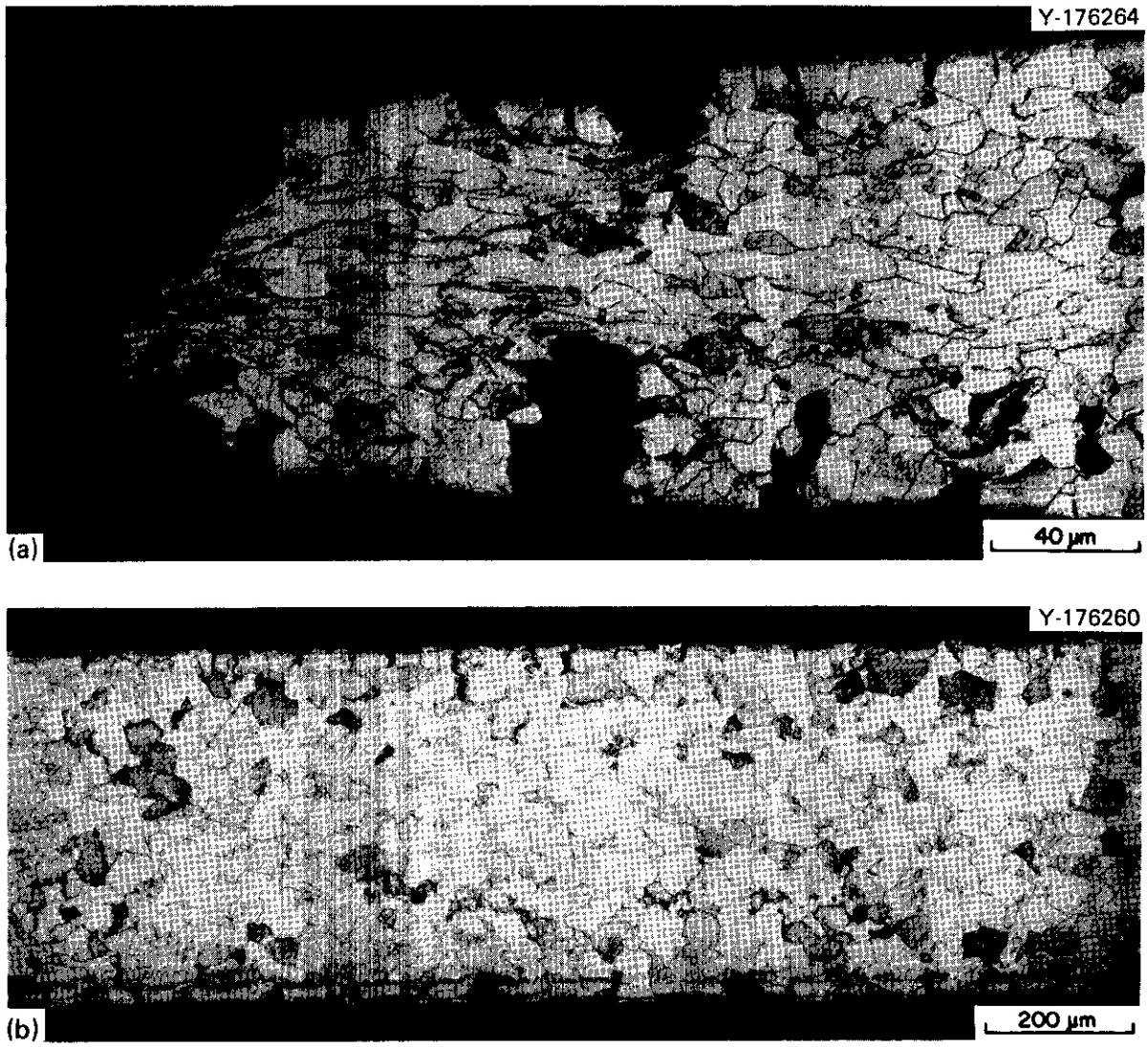

Fig. 9.1.1. Sample of 2 1/4 Cr-1 Mo steel exposed to Li—5 wt % Al for 3000 h at 600°C and subsequently tensile tested in air at room temperature. (a) Fracture area. (b) Away from fracture area.

9.1.5 Conclusions

1. Exposures of HT9 to static 500°C lithium for up to 3000 h resulted in negligible weight changes and did not significantly affect the steel's room temperature tensile properties relative to specimens exposed to argon under otherwise similar conditions. This is in contrast to 2 1/4 Cr-1 Mo steel, which is significantly decarburized in lithium with a resulting degradation of its strength.

2. The gage sections of 2 1/4 Cr-1 Mo steel specimens cracked severely upon tensile testing at room temperature after 3000-h exposures to Li–5 wt % Al at 500 and 600°C. Aside from an obvious association with lithium penetration into the steel, this embrittlement may have been caused by the aluminized surface layer on these specimens, which changed the normal carbon distribution that occurs in this alloy when exposed to pure lithium and thus affected the relative stability of the resultant carbides with respect to the lithium.

3. Exposure of type 316 stainless steel to Li–5 wt % Al for 1000 h at 500°C did not significantly reduce its ductility.

9.1.6 References

1. P. F. Tortorelli, J. H. DeVan, and C. T. Liu, "Compatibility of Static Lithium with Fe-Ni-V and Fe-Cr-Mo Alloys," *ADIP Quart. Prog. Rep. Sept. 30, 2980,* DOE/ER-0045/4, pp. 182–90.
2. K. Natesan and T. F. Kassner, *Calculations of the Thermodynamic Driving Force for Carbon Transfer in Sodium-Steel Systems,* ANL-7646 (December 1969).
3. P. F. Tortorelli, J. H. DeVan, J. E. Selle, and H. D. Upton, "Corrosion Inhibition in Systems of Lithium with Nickel-Bearing Alloys," pp. 1610–13 in *Proc. 8th Symp. Engineering Problems in Fusion Research,* Vol. III, IEEE Publication 79CH1441-S NPS, C. K. McGregor and T. H. Batzer, eds., Institute of Electrical and Electronics Engineers, Inc., New York, 1979.
4. T. L. Anderson, N. J. Hoffman, J. B. Lumsden, and G. R. Edwards, "Intergranular Penetrations of 2 1/4 Cr-1 Mo Weldments by a Lithium-Lead Liquid," paper presented at Second International Conference on Liquid Metal Technology in Energy Production, Richland, Wash., April 21–24, 1980.

9.2 CORROSION OF TYPE 316 STAINLESS STEEL AND A LONG-RANGE-ORDERED Fe-Ni-'J ALLOY IN NATURALLY CONVECTIVE LITHIUM — P. F. Tortorelli and J. H. DeVan (ORNL)

9.2.1 ADIP Task

ADIP Task I.A.3, Perform Chemical and Metallurgical Compatibility Analyses.

9.2.2 Objective

The purpose of this task is to evaluate the corrosion resistance of candidate first-wall materials to flowing lithium in the presence of a temperature gradient. Corrosion rates (in both dissolution and deposition) are measured as functions of time, temperature, additions to the lithium, and flow conditions. These measurements are combined with chemical and metallographic examinations of specimen surfaces to establish the mechanisms and rate-controlling processes for dissolution and deposition reactions.

9.2.3 Summary

Further results on corrosion rates of type 316 stainless steel in lithium-type 316 stainless steel thermal-convection loops (TCLs) are given. The rates in one loop were significantly lower than those measured in several other similar experiments. Comparison of exposed coupons showed that all surfaces experiencing dissolution exhibited porosity, but those with the lower corrosion rates had shallower porous layers. The cause of the lower corrosion rates has not been established but does not appear to be associated with the purity of the lithium. Additionally, data on the corrosion rate8 of long-range-ordered (LRO) alloy Fe—31.8 Ni—22.5 *W*. *4* Ti (wt %) exposed in lithium-type 316 stainless steel TCLs are reported. These rates, which include a contribution from dissimilar-metal transfer of nickel from the alloy, are significantly greater than those of type 316 stainless steel previously exposed in these loops.

this figure that the cracking is not just limited to the aluminized near-surface layer. If the penetration of the steel by aluminum is the cause of the cracking, then the aluminum must have diffused throughout the specimens cross section. Alternatively it is possible that the aluminized layer served as a barrier to retard the decarburization of the steel *so* that the carbon activity of the steel remained at a higher level with the aluminum addition to lithium than without it. At the higher carbon level, it is conceivable that carbides could react with the lithium to cause the observed embrittlement. Other work with 2 1/4 Cr-1 Mo steel in lithium-lead has shown that the potential for attack of this alloy is based on the type(s) of carbide(s) present in the steel. A carbon effect also appears to be associated with our observations of severe penetration only in the heat-affected zones of lithium-exposed 2 1/4 Cr-1 Mo steel. These zones have a different carbide microstructure such that the particular carbides are unstable with respect to pure lithium.

We have recently exposed tensile specimens of type 316 stainless steel to Li—5 wt % Al at 500°C to see if such exposures will embrittle this steel. Preliminary results, shown in Table 9.1.3, indicate that ductility is not reduced after 1000 h. Longer term tests currently under way will prove whether the carbide microstructure of the type 316 stainless steel is indeed resistant to lithium attack.

Table 9.1.3. Weight Changes and Room Temperature Tensile Properties of Type 316 Stainless Steel Exposed to Argon, Lithium, and Li—5 wt % Al for 1000 h at 500°C

Environment	Weight Change[a] (g/m^2)	Yield Strength[b] (MPa)	Ultimate Tensile Strength[b] (MPa)	Elongation[a] (%)
Argon	+0.1	328.2	786.0	40.9
Lithium	-0.2	311.6	758.4	40.5
Li—5 wt % Al	+2.4	321.2	779.1	38.8

[a]Average of data from two specimens.

[b]Average of data from two specimens for Li—5 wt % Al exposures; data from one specimen for argon and lithium exposures.

9.2.4 Progress and Status

We have continued our study of the mass transfer of type 316 stainless steel in flowing lithium using previously described[1] TCLs with accessible specimens. These loops are designed so that lithium samples can be taken and corrosion coupons can be withdrawn and inserted without altering the loop operating conditions. Three loops have operated under nearly identical temperature conditions to develop data on dissolution and deposition processes as a function of time.[2,3] Plugging from mass transfer deposits necessitated replacement of the cold legs in all three loops after 5000 to 10,000 h. Two of these loops have completed 7500 h of additional operation since new cold legs were installed. Fresh coupons were inserted into the refurbished loops (now designated 2B and 3B), and their weight changes have been monitored as a function of time. These data are compared with those from the original three loops in Fig. 9.2.1. The data represent the maximum weight losses measured for each time and were obtained from the coupon located at the maximum temperature position (600°C) in each loop. Four of the data sets are plotted as the solid

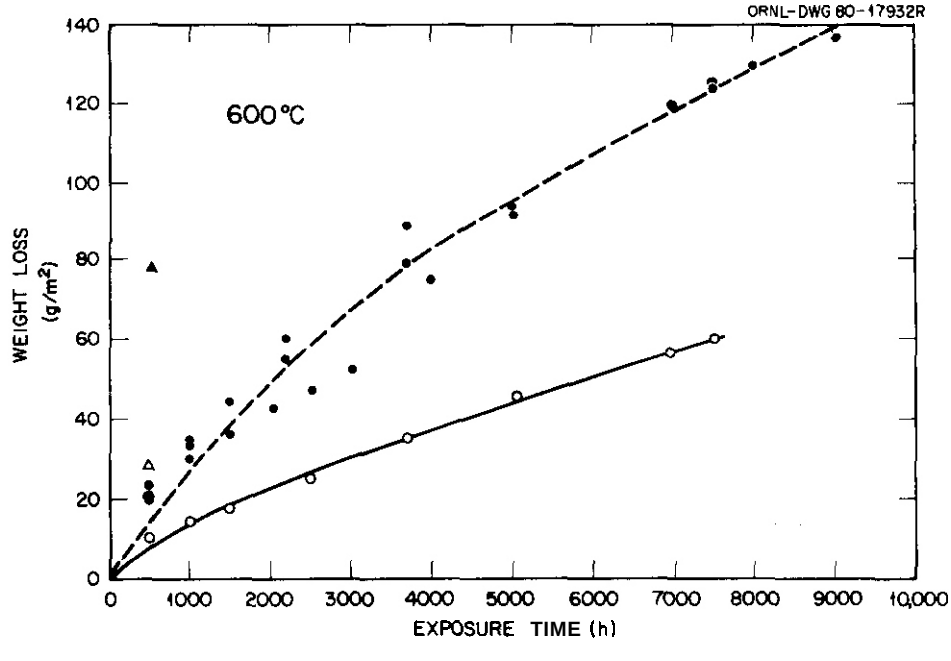

Fig. 9.2.1. Compilation of Weight Loss Data from Experiments with Type 316 Stainless Steel (Circles) and a Long-Range-Ordered Alloy (Triangles) in Lithium-Type 316 Stainless Steel Thermal-Convection Loops.

circles and fall within a small scatter band along the curve represented by the dashed line. Weight losses from one loop experiment (2B), however, have been consistently less than those from the other tests. These are shown as the open circles.

As described in the previous quarterly,[4] the lower weight losses in the latter loop experiment (2B) resulted after replacement of a cold-leg section in a loop that had previously operated for 5000 h. (Data for the previous period fell along the upper curve.) This pattern was not repeated in the second of the loops in which the cold-leg section was replaced (3B). The weight losses versus time in 3B were about the same before and after replacement. The reason for the lower weight loss data from 2B remains unclear. It does not appear to be related to initial impurities in the lithium since such concentrations were similar among all the loops. Recent analyses of the lithium in the two refurbished loops after greater than 7000 h of circulation yielded the following nitrogen and oxygen concentrations:

	Concentration in Lithium, wt ppm	
Loop	Nitrogen	Oxygen
2B	98	120
3B	19	220

These impurity levels are not excessively high and fall within the scatter band of previous analyses. The coupons from both 2B and 3B have now been metallographically examined, and cross sections of the coupons exposed at the 600°C position in the two loops are compared in Fig. 9.2.2. Both specimens have similar underlying microstructures (implying similar starting material and exposure temperatures) and porous near-surface layers, which are characteristic of type 316 stainless steel exposed to flowing lithium.[2] However, the depths of these surface layers on the two specimens are quite different; the specimen exhibiting the higher dissolution rate (that from 3B) has a much more extensive porosity zone of a depth equal to that reported previously[2] for lithium-type 316 stainless steel systems. The depths of the porous surface layers for specimens 2B and 3B differ as a result of the differing initial corrosion rates of the

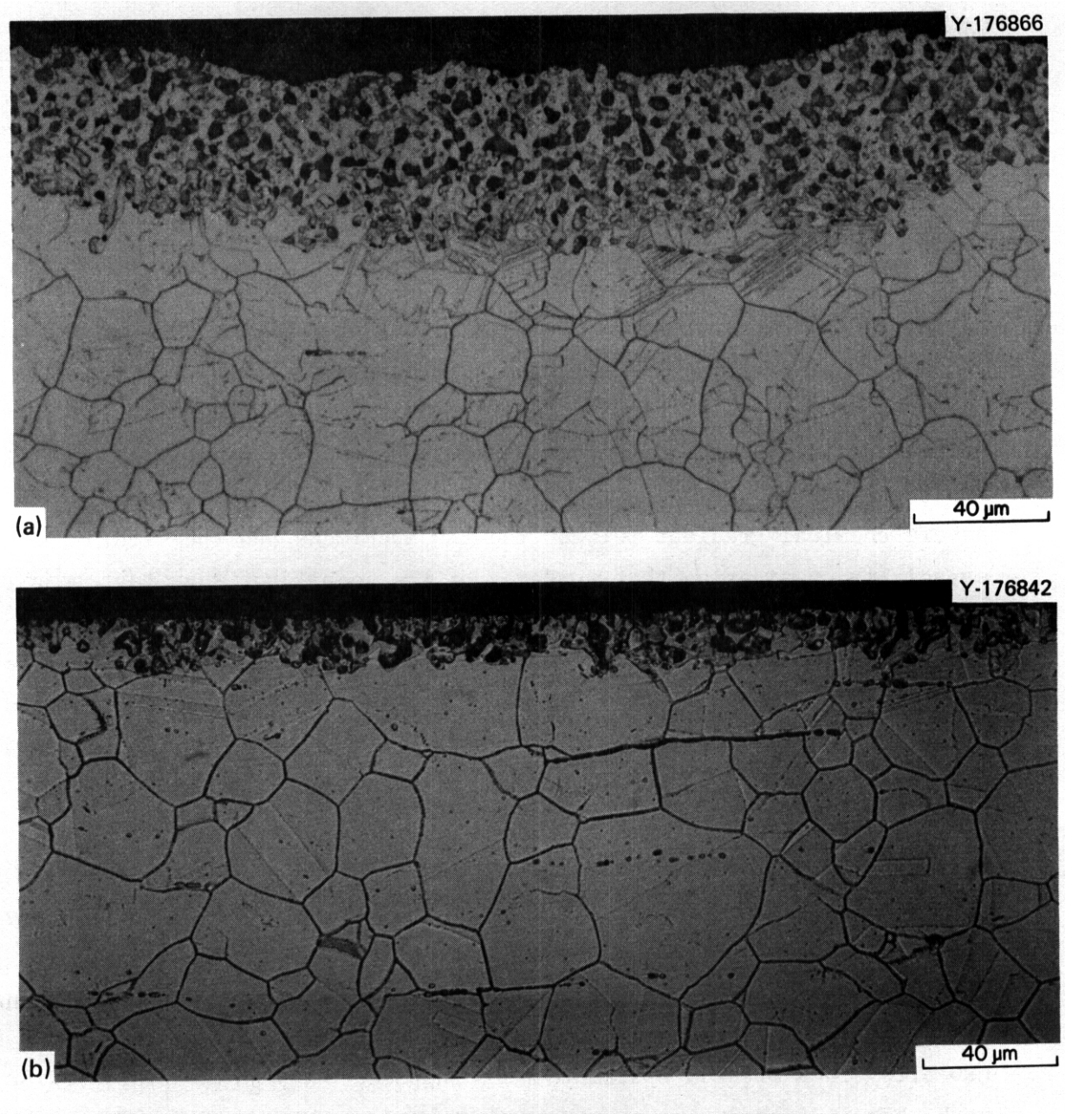

Fig. 9.2.2. Cross Sections of Type 316 Stainless Steel Exposed to Flowing Lithium at 600°C for 7500 h. (a) Typical surface. (b) Surface of coupon from loop in which significantly lower corrosion rates have been measured.

coupons in the two loops; this does not explain why the dissolution in 2B is less than that in 3B and other loop experiments. The chemical compositions of these surface layers will be analyzed to attempt to find the cause of the lower corrosion rates in loop 2B.

It has previously been reported[5,6] that an LRO alloy composed of Fe—31.8 Ni—22.5 *W*. *4* Ti (wt %) has excellent compatibility with static lithium at elevated temperatures, while other alloys with similar and higher nickel concentrations are readily attacked under the same exposure conditions. Recently, we initiated experiments to assess the corrosion resistance of this LRO alloy to flowing lithium. Because of a lack of sufficient LRO material, the tests are being conducted in type 316 stainless steel TCLs. The use of a dissimilar loop material imposes a severe chemical gradient between the LRO specimens and the lithium, especially considering that surfaces of the loops' hot legs have been preferentially leached of nickel from prior exposures to lithium. Such an arrangement provides the worst case for the dissolution of the LRO alloy in flowing lithium. The LRO coupons were placed in the two hottest positions (600 and 570°C) of two type 316 stainless steel TCLs (2B and 3B as described above). The specimens were first weighed after 500 h of exposure, and the resultant weight losses at 600°C are shown as the triangles in Fig. 9.2.1. Relative to the type 316 stainless steel specimens, the 500—h corrosion rates of the LRO alloy are significantly higher. However, because we do not know what fraction of the weight losses can be attributed to dissimilar-metal transfer, we cannot currently make a definitive statement about the relative corrosion resistance of the LRO alloy in a lithium system totally composed of this material. Prior work[7] has indicated, though, that the transfer of nickel from fresh austenitic (~10 wt % Ni) surfaces to the ferritic walls (~1 wt % Ni) of the loops' hot legs was minimal. Further work is planned to enable us to examine the corrosion of the LRO alloy in these loops in more detail.

As illustrated by the data in Fig. 9.2.1, the weight losses of the LRO alloy in 2B were less than those exposed in 3B. Since this trend is consistent with the one discussed above for type 316 stainless steel specimens in these loops, the cause of the discrepancy in the corrosion rates can be attributed to conditions in the respective loops rather than any differences between specimens of the same alloy.

9.2.5 Conclusions

1. Specimens in the hot zone of one lithium-type 316 stainless steel TCL have consistently lower dissolution rates than those measured in several other similar loop experiments. These specimens exhibited a porous corrosion layer that was shallower but otherwise microstructurally similar to the more highly corroded coupons. As yet, unknown differences in loop conditions must account for the discrepancy in the corrosion rates. However, it did not appear to be associated with the nitrogen and oxygen levels of the lithium.

2. The corrosion rates of a LRO alloy composed of Fe-31.8 Ni-22.5 V-0.4 Ti (wt %) in lithium-type 316 stainless steel TCLs are significantly greater than those of type 316 stainless steel previously exposed in these loops. The higher corrosion rates of the LRO alloy do include a contribution from dissimilar-metal transfer of the nickel component.

9.2.6 References

1. J. H. DeVan and J. R. DiStefano, "Thermal-Convection Loop Tests of Type 316 Stainless Steel in Lithium," *ADIP Quart. Prog. Rep. Mar. 31, 1978*, DOE/ET-0058/1, pp. 200-08.
2. P. F. Tortorelli and J. H. DeVan, "Thermal-Gradient Mass Transfer in Lithium-Stainless Steel Systems," *J. Nucl. Mater.* 85 & 86(II,A): 289-93 (1979).
3. P. F. Tortorelli and J. H. DeVan, "Mass Transfer Deposits in Lithium-Type 316 Stainless Steel Thermal-Convection Loops," paper presented at Second International Conference on Liquid Metal Technology in Energy Production, Richland, Wash., April 21-24, 1980.
4. P. F. Tortorelli and J. H. DeVan, "Mass Transfer of Type 316 Stainless Steel in Lithium Thermal-Convection Loops," *ADIP Quart. Prog. Rep. Sept. 30, 1980*, DOE/ER-0045/4, pp. 191-94.
5. P. F. Tortorelli, J. H. DeVan, and C. T. Liu, "Compatibility of Static Lithium with a Long-Range-Ordered Fe-Ni-V Alloy and 2 1/4 Cr-1 Mo Steel," *ADIP Quart. Frog. Rep. June 30, 1980*, DOE/ER-0045/3, pp. 328-36.

6. P. F. Tortorelli and J. H. DeVan, "Corrosion of Fe-Ni-Cr and Fe-Ni-V Alloys in Static Lithium," *ADIP* Quart. *Prog. Rep. Dec. 31, 1979,* DOE/ER-0045/1, pp. 152–57.

7. P. F. Tortorelli and J. H. DeVan, "Corrosion of Type 316 Stainless Steel and Alloys B1 and B3 in Lithium Thermal-Convection Loops," *ADIP Quart. Prog. Rep. Dec. 31, 1979,* DOE/ER-0045/1, pp. 158–65.

DOE/ER-0045/5
Distribution
Category
uc-20, 20c

DISTRIBUTION

1-4. Argonne National Laboratory, 9700 South Cass Avenue, Argonne, IL 60439

L. Greenwood
V. Maroni
D. L. Smith
H. Wiedersich

5-6. Battelle-Pacific Northwest Laboratory, P.O. Box 999, Richland, WA 99352

J. L. Brimhall
D. Dingee

7. Brookhaven National Laboratory, Upton, NY 11973

C. L. Snead, Jr.

8. Carnegie-Mellon University, Schenley Park, Pittsburgh, PA 15213

J. C. Williams

9-204. Department of Energy, Technical Information Center, Office of Information Services, P.O. Box 62, Oak Ridge, TN 37830

For distribution as shown in TID-4500 Distribution Category, UC-20 (Magnetic Fusion Energy), and UC-20c (Reactor Materials)

205-210. Department of Energy, Office of Fusion Energy, Washington, DC 20545

M. M. Cohen
T. C. Reuther, Jr. (5 copies)

211. Department of Energy, Oak Ridge Operations Office, P.O. Box E, Oak Ridge, TN 37830

Office of Assistant Manager for Energy Research and Development

212. General Atomic Company, P.O. Box 81608, San Diego, CA 92138

D. I. Roberts

213—221. Hanford Engineering Development Laboratory, P.O. Box 1970, Richland, WA 99352

H. R. Brager
D. G. Doran
F. A. Garner
D. S. Gelles
G. L. Wire
R. E. Nygren
E. C. Opperman
R. W. Powell
J. L. Straalsund

222—224. Lawrence Livermore Laboratory, P.O. Box 808, Livermore, CA 94550

E.N.C. Dalder
M. Guinan
C. M. Logan

225—228. Massachusetts Institute of Technology, Cambridge, MA 02139

O. K. Harling
N. J. Grant
D. J. Rose
V. B. Vander Sande

229—230. McDonnell Douglas Astronautics Company, East, P.O. Box 516, St. Louis, MO 63166

J. W. Davis
D. L. Kummer

231—233. Naval Research Laboratory, Washington, DC 20375

Superintendent, Materials Science and Technology Division
J. A. Sprague
H. Watson

234—267. Oak Ridge National Laboratory, P.O. Box X, Oak Ridge, TN 37830

Central Research Library (2 copies)
Document Reference Section
Laboratory Records Department (2 copies)
Laboratory Records Department, RC
ORNL Patent Section
E. E. Bloom (10 copies)
D. N. Braski
J. H. DeVan
T. A. Gabriel

M. L. Grossbeck
M. R. Hill (3 copies)
R. L. Klueh
K. C. Liu
P. J. Maziasz
C. J. McHargue
T. K. Roche
J. L. Scott
K. R. Thoms
P. F. Tortorelli
J. M. Vitek
F. W. Wiffen

268—269. Sandia National Laboratories, Livermore Division 8316, Livermore, CA 94550

J. Swearengen
W. Baller

270. University of California, Department of Chemical, Nuclear, and Thermal Engineering, Los Angeles, CA 90024

R. W. Conn

271. University of California, Santa Barbara, CA 93106

G. R. Odette

272. University of Missouri, Department of Mechanical and Aerospace Engineering, Columbia, MO 65211

M. Jolles

273. University of Virginia, Department of Materials Science, Charlottesville, VA 22901

W. A. Jesser

274. University of Wisconsin, 1500 Johnson Drive, Madison, WI 53706

W. G. Wolfer

275. Westinghouse Electric Company, Fusion Power Systems Department, P.O. Box 10864, Pittsburgh, PA 15236

R. E. Gold

☆U.S. GOVERNMENT PRINTING OFFICE: 1981-740-062/5